REPUBLIQUE DU CAMEROUN
Paix – Travail – Patrie
****
UNIVERSITE DE YAOUNDE I
FACULTÉ DES SCIENCES
DEPARTEMENT DE SCIENCES DE LA TERRE
****
CENTRE DE RECHERCHE ET DE FORMATION DOCTORALE EN SCIENCES, TECHNOLOGIE ET GÉOSCIENCES
LABORATOIRE DE GEOSCIENCES DES FORMATIONS PROFONDES ET APPLICATIONS

REPUBLIC OF CAMEROUN
Peace – Work – Fatherland
****
UNIVERSITY OF YAOUNDE I
FACULTY OF SCIENCE
DEPARTMENT OF EARTH SCIENCES
****
POSTGRADUATE SCHOOL FOR SCIENCES, TECHNOLOGY AND GEOSCIENCES
LABORATORY O

LITHOSTRATIGRAPHY, GEOCHEMISTRY, GEOCHRONOLOGY AND STRUCTURAL GEOLOGY OF THE NKOUT IRON DEPOSIT (SOUTH CAMEROON)

Thesis submitted in fulfilment of the requirements for the degree of Doctor of philosophy (Ph.D)

Par : **EKAH NZUME NDIME**
M.Sc. in Earth Sciences

Sous la direction de
NZENTI Jean Paul
Professor

Année Académique : 2020

b

DECLARATION

I hereby declare that this thesis is submitted for the degree of Doctor of Philosophy in Geology, at the University of Yaoundé I.

Apart for the help recognised, this work is my own effort and has not been submitted to another University for degree.

Signature

Mr. Ekah Nzume Ndime

DEDICATION

This dissertation is dedicated to the Almighty God.

TABLE OF CONTENT

LIST OF FIGURES

LIST OF TABLES

LIST OF ABBREVIATIONS AND SYMBOLS

Abbreviations	Full name
Amp	Amphibole
Bt	Biotite
Chl	Chlorite
Cpx	Clinopyroxene
Ep	Epidote
Grt	Garnet
Hem	Hematite
Hld	Hornblende
Ilm	Ilmenite
Kfs	K-feldspar
Mag	Magnetite
Mus	Muscovite
Opx	Orthopyroxene
Opq	Opaque mineral
Pl	Plagioclase feldspar
Qtz	Quartz
Th/Pb	Thorium Lead ratio
Th/U	Thorium Uranium ratio
Th	Thorium
U	Uranium
U/Pb	Uranium lead ratio
Zir	Zircon

Abbreviations	Full name
ACM	Active continental margin
ALS	Australian lab services
BIF	Banded iron formations
BRGM	Bureau de Recherches Géologiques et Minières
CH	Centre hole
CRM	certified reference material
EH	East hole
GPS	Global positioning system
Gnt	Granulite
ICP-MS	Inductively Coupled Plasma-Mass Spectrometry
ICP-AES	Inductively Coupled Plasma-Atomic Emission
Km	Kilometre
Km^2	Square kilometres
LA-ICPMS	Laser ablation inductively coupled mass spectrometry
LOI	Loss of ignition
LREE	Light rare earth element
Ma	Million years
mm	Millimeter
Mm:	Micrometre
MREE	Middle rare earth element
NCC	North China Craton
NNE-SSW	Northnortheast-southsouthwest
N-S	North-south
NW-SE	Northwest- southeast
PM	Passive margin
Ppm	Parts per million
QA/QC	Quality control and quality assurance
REE	Rare earth elements
S-E	South-east
Se	External schistosity
Si	Internal schistosity
SRTM	Shuttle radar topographic mission
SW	South West
T^oc	Temperature
TTG	Tonalite, trangemite, granodiorite
USGS	United States Geological Society
WH	West hole
WNW-ESE	Westnorthwest-eastsoutheast
XRF	X-ray fluorescence

ACKNOWLEDGEMENTS

I am particularly grateful to the management staff of '**IMIC /CAMINEX SA'** for their permission, field and logistic support during field work and making access to their deep level of drilled core that were sampled for this study.

Special thanks go to **Professor Nzenti Jean-Paul** for suggesting this project, and for his guidance and encouragement throughout its completion.

Thanks to **Professor Suh Emmanuel C.** of the University of Buea for his help; I knowledge his advice, patience and assistance throughout the dissertation, a particular interest during things concerning analytical portion of the project.

I am grateful to **Associate Professor Ganno Sylvester** who co-supervised this work; he pre-read the manuscripts, made useful advices, valuable criticisms, wonderful suggestions, insights, interest and patience in the research project.

Special thanks go to all the staff and fellow post graduate students of the **Department of Earth Sciences** of the University of Yaoundé I for their direct and indirect support, most especially to the head of Department, **Professor NDJIGUI Paul-Desire.**

Special thanks go to all the staff and friends of the **Department of Geology** of the University of Buea for their assistance.

Special thanks go to the **CAMICO** team who supported me at the beginning of the profession especially to **Doctor GEORGE Mafiny.**

Finally, I am indebted to my parents for providing me with unlimited educational opportunities, and all my family members, **Madam Rufina Njume, Madam Eboh Bridget Mayer, Mr Evaristus Elime Njume, Madam Ekume Prisca Mbulle, Mr. Nkwelle Norbert Njume, Madam Marie-cle Ngwesses, Mr. Elime Mbe Cletus Njume and Mr. Epie Mbe Protus Njume** for always believing in my little strength and abilities.

Thanks also go to my friends **Mr. Engombi Godlove; Mr. Awah Elivs** for all their love, support, patience and encouragement during this project.

This acknowledgement is complete by recognising the immense contribution of my wife **Senge Hannah Mesumbe** during the final stage of the work.

ABSTRACT

The Nkout banded iron formations (BIFs) is located in the northwestern margin of the Congo Craton (CC) and is hosted within the high-grade metamorphic Ntem complex. Nkout iron deposit is subdivided into three prospects namely; East, Centre and West deposits.

Petrographically, the Nkout iron oxide facies is composed of four types of which are strongly deformed and were metamorphosed under relative low (greenschist) to medium (amphibolite) metamorphic grades. The gneissic rocks are composed of four types namely which were subjected under relative medium (amphibolite) to high (granulitic) metamorphic grades. The litho-package from the top to the base of Nkout comprises of iron-rich member and the gneissic member containing nine litho units. The upper unit is ~200m deep and consists of oxidized (haematite) and un-oxidised (fresh BIF) ore types. The middle unit is approximately 150m thick and consists of fresh BIF with minor intercalation of biotite gneiss. The lower unit is made up of gneiss which represents the footwall of the deposit. The units reveal both thicknesses and depth variations from West to the East, inferring a folded structure of the Nkout deposit. Their occurrence supports the fact that BIFs deposition took place on a basin-wide scale.

The rocks have undergone polyphase tectonic evolution with four stage of deformation. The deformation phase 1 (D_1) comprises of F_1 fold and S_1 mineral foliation with E-W trend. This stage took place under low grade green-schist metamorphic facies condition. The later D_2 event affected the previously deformed E-W (D_1) structures accompanied by the development of F_2 folds and S_2 schistosity and C_2 shear plane. The F_2 folding is marked by inclined similar folds verging towards north. The C_2 shear planes show both dextral and sinistral shear movement. We interpreted this tectonic event as the major stage of deformation. The D_3 event is a phase of tectonic superimposition with NW-SE trend. It is accompanied with the development of schistosity (S_3), shear planes (C_3) and fold (F_3). The F_3 was as a result of refolding of the F_2 folds. The resulting geometry is type 1 and 3 interferrence pattern. D_4 is a phase of brittle tectonism. Structural evolution is the main controlling factor in the localization and preservation of high grade ore.

The area comprise of granite, granodiorite and tonalite. These plutonic rocks are peraluminous and metaluminous. They show characteristic I-type igneous rock affinity that has evolved by fractional crystalisation of the mantle source with crustal contamination. The negative Nb, Zr, Ti, Sr and Yb anomalies in all the rock types interpret the contribution of the continental crust to the genesis of the rock. They are characterized with low REE abundance, positve Eu anomalies, LREE enrichment and HREE depletion.

The gneissic rocks are derived from mafic igneous protolith characterised with gabbroic to dioritic composition. They show low REE abundance, negative to no Eu anomalies, LREE-enrichment and HREE-depletion. Their strong negative Ti, Yb, Ta and Zr anomalies indicates that the continental crust and the mantle participated in the genesis of this rock.

The meta-sedimentary are from Fe-derived sand and quartz arenitic protolith represented by magnetite BIF and garnet BIF. The magnetite BIF shows high SiO_2 and Fe_2O_3 and low Al_2O_3, TiO_2, HFSE and ΣREE contents similar to detritus-free chemical sediments. In contrast, their high concentrations in garnet BIF indicate clay-rich-contaminated input. The BIFs are depleted in CaO + MgO, suggesting a near absolute absence of calcite and dolomite.

Whole-rock Pb isotope composition is roughly on average of 2.0 ppm, suggesting a hydrothermal Pb source. The Pb-Pb dating yielded an isochron age of 2679 Ma interpreted as the Neoarchean metamorphic event, attributed to high-K granitoid emplacement in the Ntem complex.

Keywords: *Petrography and litho-stratigraphy; Geochemistry and Geochronology; Structural control mineralisation; Nkout deposit; Southern Cameroon.*

RÉSUMÉ

Les formations ferrifères rubanées de Nkout (BIF) sont situées dans la marge nord-ouest du craton du Congo (CC) et appartiennent au métamorphisme de faibles à moyens degré du complexe Ntem. Le fer de Nkout est respectivement subdivisé en trois zones de gisements : gisements Est, Centre et Ouest.

Sur le plan pétrographique, l'oxyde de fer de Nkout est composé de quatre types de faciès pétrographiques qui sont fortement déformés et métamorphisés sous des degrés de métamorphismes relativement faibles (schistes verts) à moyens (amphibolite). Ces roches gneissiques sont composées de quatre types, à savoir ceux qui ont été soumis, dans des milieux relatifs (amphibolite), à des teneurs métamorphiques élevées (granulitiques). Le log lithographique réalisé dans le secteur de Nkout comprend du haut vers le bas, une unité riche en fer et l'autre essentiellement gneissique subdivise neuf unités lithographiques. L'unité supérieure (200 m de profondeur) constituée de minerais de types oxydes (hématite) et non oxyde (BIF frais). L'unité centrale d'environ 150 m d'épaisseur constituée de BIF frais avec une intercalation mineure de gneiss à biotite. Enfin l'unité inférieure marquée par des variations d'épaisseurs et de profondeur allant de l'Ouest à l'Est, induisant des pliées du gisement de Nkout, ce qui confirme le fait que les dépôts de BIFs ont eu lieu à l'échelle du bassin.

Les roches ont subi une évolution tectonique polyphasique avec quatre phases de déformation. La phase de déformation (D_1) marquée par un pli P_1 et une schistosité minérale S_1 avec une orientation E-W. Cette phase s'est déroulée dans des conditions de faciès métamorphiques de schistes verts à faible degré. La phase de déformation D_2 est caractérisée par un événement métamorphique qui a affecté les structures E-W (D_1) précédemment déformées, accompagnées du développement des plis P_2, d'une schistosité S_2 et d'un plan de cisaillement C_2. Les plis P_2 sont marquées par des plis orientés vers le nord. Les plans de cisaillement C_2 montrent un mouvement dextre à sinistre. Cet événement tectonique est interprété comme une phase majeure de la déformation. La phase D_3 est une phase tectonique de superposition avec pour orientation NW-SE. Elle s'accompagne du développement de la schistosité (S_3), des plans de cisaillement (C_3) et du pli (P_3). Le P_3 est le résultat du repli des plis P_2. La géométrie résultante est un motif d'interférence de types 1 et 3. Enfin la phase (D_4) est une phase de tectonique fragile. L'évolution structurale est le principal facteur déterminant de la localisation et de la préservation du minerai à haute teneur.

La région de Nkout comprend les granites, les granodiorites et les tonalites. Les granitoïdes sont hyperalumineux à métallumineux. Ils présentent une affinité caractéristique des roches ignées de type I qui ont évolué par cristallisation fractionnée du manteau avec contamination de la croûte terrestre. Les anomalies négatives de Nb, Zr, Ti, Sr et Yb dans tous les types de roches est interprétée comme la contribution de la croûte continentale à la genèse de la roche. Ils se caractérisent par un faible enrichissement en terres rares, des anomalies faiblement positives en Europium, un enrichissement en terres rares légères et un appauvrissement des terres rares lourdes.

Les roches gneissiques de Nkout dérivent d'un protolithe igné mafique caractérisé par une composition gabbroïque à dioritique. Ils présentent un faible enrichissement en terres rares, une absence d'anomalies en Europium, un enrichissement en terres rares légères et un appauvrissement en terres rares lourdes. Leurs fortes anomalies négatives en Ti, Yb, Ta et Zr indiquent que la croûte continentale et le manteau ont participé à la genèse.

Les métasédiments des roches proviendraient des protolithes arénitiques de sable et de quartz dérivés de Fe, représentés par les BIFs à magnétite et les BIFs à grenat. Les BIFs à magnétite présentent des teneurs élevées en SiO_2 et Fe_2O_3 et en Al_2O_3, TiO_2, HFSE et REE similaires à celles de sédiments chimiques non détritiques. En revanche, les concentrations élevées dans les BIFs à grenat indiquent un apport en argile. Les BIF sont appauvris en CaO + MgO, suggérant une absence quasi absolue de calcite et de dolomite.

La composition isotopes en Pb de la roche entière est d'environ 2ppm en moyenne, ce qui suggère une source de Pb hydrothermale. La datation Pb-Pb a donné un âge isochrone de 2679 Ma interprété comme un événement métamorphique Néoarchéen, attribué à la mise en place des granitoïdes de type potassique élevé dans le complexe du Ntem.

Mots-clés: *Pétrographie et Lithostratigraphie; Géochimie et Géochronologie; Minéralisation; Dépôt de Nkout; Sud Cameroun.*

GENERAL INTRODUCTION

1. INTRODUCTION

Precambrian banded iron formations (BIFs) are typically thinly banded or laminated iron-rich (Fe >15%) sedimentary rocks of marine origin, commonly composed of iron oxides (magnetite and haematite) and gangue (quartz) minerals (James, 1954). Four main types of metamorphosed BIFs have been distinguished based on their iron mineralogy. They include; oxide-, carbonate-, silicate- or sulfide-type, among which the oxide-type is the most important (James, 1954). Banded iron formations are distributed throughout the geologic record around the world, with depositional peak at ca. 2.7-2.5 Ga, and ca. 1.85, with an exception of a few Neoproterozoic iron formations between 0.8 to 0.6 Ga (Klein, 2005; Bekker et al., 2010). They are commonly associated with greenstone belts and other Precambrian supracrustal sequences (James, 1992; Zhai and Santosh, 2011; 2013).

Banded iron-formations (BIFs) can be divided into Algoma-type, Superior-type, and Rapitan-type based on depositional environment and geotectonic settings (Gross, 1980).

Algoma type BIFs are associated with volcanic arcs and are typically found in Archean greenstone belts. In the Congo Craton, the Algoma type is located within the Ntem complex in the Bikoula area (Teutsong et al., 2017), and in the Meyomessi area (Ganno et al., 2018).

Superior type BIFs or continental margin BIFs are located on stable continental platforms and are mainly deposited in Paleoproterozoic times, while Rapitan type BIFs are exclusively Neoproterozoic in age and are associated with a glacially influenced depositional environment (Gross, 1983: 1993; Klein and Beukes, 1992). The Superior-type iron formations are laterally very extensive and constitute a major iron ore resource world-wide, with major deposits being located in the Hamersley Basin in Australia (Barley et al., 1999; Lascelles, 2006); the Superior Province (Abitibi belt) in North America (Trendall, 2002; Pufahl, 2010); the Amazon Craton of Brazil (Spier et al., 2003; 2007); the Kaapvaal Craton of South Africa (Beukes and Klein, 1992); and the North China Craton (NCC) (Zhang et al., 2011).

Metamorphosed BIFs are not only important sources of iron ore for industry, but due to the fact that their deposition has been linked to significant compositional change in the earth's atmosphere, they play an important role in understanding the evolution of life, oceans, and the atmosphere in the Archean and Proterozoic times (Poulton et al., 2010; Bekker et al., 2010; Young, 2013; Tang and Chen, 2013; Ganno et al., 2015).

The Nkout iron deposit is located in the northern margin of the Congo Craton (CC) within the Ntem complex. This complex hosts many iron ore deposits in Cameroon such as Mbalam (Suh et al., 2008; Nforba et al., 2012, Chombong et al., 2013; Ilouga et al., 2013,) Elom (Ganno et al., 2015a), Zambi BIF (Ganno et al., 2015b), Kouambo BIF (Ganno et al., 2017), Bikoula deposit (Teutsong et al. 2017) and Nkout iron deposit (Suh et al., 2009; Kelvin et al., 2014; Ndime et al., 2018), and the Kpwa-Atog Boga BIF deposited in an active continental margin tectonic setting (Soh et al., 2018). In other area of the northern portion of the Congo craton (CC), it hosts other

huge deposits in Congo such as Avima, Nabeba, Badondo Zanaga, Mayoko deposit and Gabon such as Belinga, Baniaka deposit (Caen Vachette et al., 1988). Most of these deposits are not yet well studied and very little is known of BIFs in the Congo basin.

The Nkout deposit is divided into three prospects namely: Nkout-East, Nkout-Centre and Nkout-West. All three deposits (9km long) are of northwest plunging isoclinal fold composed of iron ore of economic importance which occurs in close association with BIFs.

The Nkout mining project currently undertaken by Caminex SA is part of the emerging iron ore province in central Africa, situated some 240 km SE of Yaoundé in Cameroon. It comprises of vast quantity of iron ore deposit (http://www.imicplc.com/Nkout.aspx).

In this study, we take the advantage of the intense drilling activity of Nkout iron ore deposit to improve the understanding of litho-stratigraphy, geochronology, geochemistry and deformation which is established on the basis of data generated from boreholes of deeper drill targets, with interest in the overlying Archaean BIF succession.

2. BACKGROUND OF THE RESEARCH

The country's mineral endowment potential is well known internationally and the bulk of its iron is located within the northern portion of the Archean Congo Craton in the south region. The history of mineral resources in Cameroon has been dormant until when the government reviewed the mining code and regulation to attract mineral investors for mineral exploration, exploitation and production during the last mining convention completed in August 2014. The availability of investors and investment for mineral exploration has provoked political, economic and scientific studies to be carried out for better understanding and efficient production. In-spite of the long lasting dormant history of mineral activities, iron is now becoming one of the most precious and primary mineral endowment of the country.

The increasing need for iron in the world market indicates that iron has been the back bone for the development of emerging nations. China, Brazil, Russia, India and South Africa with other emerged nations have been the main consumers of iron. Though the price for iron in the world market is fluctuating, other developing nations wish to emerge with Cameroon by 2035. Cameroon therefore, as a prospective emerging nation needs to develop their present emerging iron ore province within the national territory (from exploration, till production and consumption) for their successful emergence.

Out of the several iron ore deposits in the central-west Africa, the most important iron deposits hosted in banded iron formations (BIFs) within the Cameroon national territory are Mbalam, Nkout, Bikoula, Kouambo, Mamelles. The Nkout deposit being located at the heart of the rapidly emerging iron ore, comprises of vast quantity of iron ore deposits, evolving to be a large iron ore producer with a metal value of 1.8billion tones at 32.6% Fe indicated, 0.9billion tones at

30.3% Fe inferred, includes high to medium grade cap (45% Fe cut off), totalling 127.2 million tones at 53.1% Fe Indicated and 5.7million tones at 50.9% Fe Inferred (http://www.imicplc.com/Nkout.aspx). The Nkout iron deposit is presented as the most important of Cameroon, ahead of the Mbalam-Nabeba (in the East). IMIC's largest asset (100%-owned subsidiary Caminex) has planned for 35 million tonnes per year of production over the 20 year life of the mine, in conjunction with African Iron Ore Group (AIOG), which is currently engaged to work in Cameroon to develop the multi-user, multipurpose infrastructure, and which will unlock not only Nkout, but will form the backbone of a wider economic development opportunity in the region.

3. PROBLEM DEFINITION

Since the last decade, emerged countries (China, India, South Africa, Russia and Brazil) have experienced increasing economic activities. They are interested in iron for their development. The immediate consequence is the increasing international demand for iron. To solve this problem, the discovery and studies of new iron deposits all around the world is imperative.

The countries within the Precambrian basement in general and cratonic formations have become more interesting, because the main iron ore deposits around the world are hosted in metamorphosed BIFs within Archean greenstone formations (Trendall and Morris, 1983). The Archean Congo Craton is one of the iron mineralized areas. It trends along the southern border within the Cameroon national territory and continued in Congo, Gabon, and Central Africa Republic. This Craton hosts iron deposits in Congo (Nabeba, Zananga, and Avima deposits), in Gabon (Minkebe, Mitizic, Belinga, Boka Boka (Suh et al., 2008). Unlike other iron mineralized Archean Craton of the country, the northern limit is less explored and studied. Notwithstanding, small scale deposits occur and major mineral iron deposits with their iron potential are not fully assessed in Metamorphosed BIFs.

In Cameroon, the southern part of the Ntem complex constitutes the northern border of the Congo Craton. This part of the Congo Craton hosts most of the large and important iron deposits located in Congo (Avima, Nabeba, Badondo Zanaga, Mayoko), Gabon (Belinga, Baniaka), and Cameroon (Mbalam, Nkout, Bikoula, Kouambo, Mamelles, Caen Vachette et al., 1988; Suh et al., 2009; Kevin et al., 2014; De Waele et al., 2015, Ganno et al., 2017; Teutsong et al., 2017, Ndime et al., 2018). Most of these deposits are not yet studied and very little is known in the Congo basin.

In the Nkout area, the only available work done on iron formation is that presented by the authors, who have shown the presence of high grade haematite deposit of the Nkout hill (Djoum area). Previous studies on Nkout deposit were focused on mineralogy and ore-textures of high-grade haematite ore (Suh et al., 2009; Kelvin et al., 2014; Nsoh et al., 2014).

Little is known on the origin, the genetic models, the tectono metamorphic event, the stratigraphy of the Nkout deposit, and the depositional environment of BIF. Little has been studied in the area structurally; the events of deformation, the structural control mineralisation and ore forming processes.

4. OBJECTIVES

The main objective of the study is to characterize the litho-stratigraphical, geochemical, geochronological, and structural features of the Nkout iron deposit. This is with the view to investigate the genesis of the deposit, the metamorphic age, reconstruct the litho-stratigraphy of the area, and elucidate the structural control mineralisation and deformation.

Other minor objectives of the study describe the regional geologic setting and provide a geologic background for which metamorphosed BIFs forming processes are evaluated. However, it lays emphasis on the geological conditions that may favour the enrichment of iron ore from banded iron formations (BIFs).

In this study, after both field mapping and a detailed logging of nine representative diamond drilled holes, three on each of the individual deposits (Nkout-West, Nkout-centre and Nkout-east), were provided;

(1) Petrographic and litho-stratigraphic data

(2) Structural data

(3) geochemical and geochronological data

We provide petrographic data with the aim to describe metamorphic and magmatic rock types; and discriminate between enriched iron ore, barren species, and siliceous BIF types, and to evaluate the different metamorphic grades.

We provide litho-stratigraphic data with the aim to construct a synthetic stratigraphic column of the Nkout basin and to constrain the basin structure with its depositional setting; to also construct possible depositional environment for the studied iron rich units.

We provide geochemical data that consists of whole-rock geochemical analyses, which was performed with the aim to investigate the genetic model of Nkout BIFs; and to evaluate the context of mineral deposit in relation with the available geochemical data.

We provide Pb-Pb isotopic compositions and dating of Nkout metamorphosed magnetite BIF was performed with the aim to elucidate the metamorphic resetting age.

We provide structural data with different deformation events that affected the mineralisation and the overprint of various episodes of brittle to ductile phase deformation on representative diamond drill core and on outcrops. This was performed with the aim to constrain a synthetic structural control mineralisation and hydrothermal alteration of the Nkout basin. Also to evaluate the possibilities of the secondary enrichment processes.

5. STRUCTURE OF THE THESIS

The thesis is structured in the following way:

- *General introduction*: introduction, background of the research, the problem statement, objectives and the structure of the thesis.

- *Chapter one* is made up of literature review, which consists of regional and local geologic settings. It describes the geology of the studied areas from a regional to a depositional point of view based on literature.

- *Chapter two* consists of material and methods of study, which includes field and laboratory technics. It explains the analytical methods of geochemistry, optical microscopy and geochronology used in this research including the general sample preparation.

- *Chapter three* is the Litho-stratigraphy and Petrography study.

It summarises the results of the field work carried out and takes a detailed look at the geology in the Nkout area

-*Chapter four* gives Structural study of the Nkout deposit

-*Chapter five* is made up of Geochemistry and geochronology of the studied BIFs

- *Chapter six* deals the discussion. It discusses the main findings of the research.

In this chapter, (i) the stratigraphic correlation and interpretation, depositional environment and tentative model of basin deposition and comparative geochemical aspects are discussed. (ii) The detrital input, mineral paragenesis and effects of metamorphism, the origin of the Nkout west BIFs and metamorphic resetting age is discussed. (iii) Deposit morphology and spatial attributes, origin of mineralisation, structural control and ore mineralisation are also discussed.

- General conclusion

- References

CHAPTER I. LITERATURE REVIEW

I.1 GEOGRAPHICAL SETTING

I.1.1 LOCATION OF THE STUDY AREA

The Nkout ridge is one of the largest iron ranges in the Republic of Cameroon (Suh et al., 2009), and it is one of the largest in the Congo Craton (Milesi et al., 2006). It is about 0.5Km to 0.7Km wide and 9Km long. The Nkout area is located some 27.5Km due south-east of Djoum town in the Southern region of Cameroon at the approximate location between latitude 2.575^0N-2.596°N and longitude 12.76°E-12.81°E as shown in figure 1.

It is situated around 280 km southeast of the capital city Yaoundé. The road from Yaoundé incorporates 170km of macadam or tar road and 110Km of laterite road which is under construction. The study locality covers a surface area of approximately 64.5km^2.

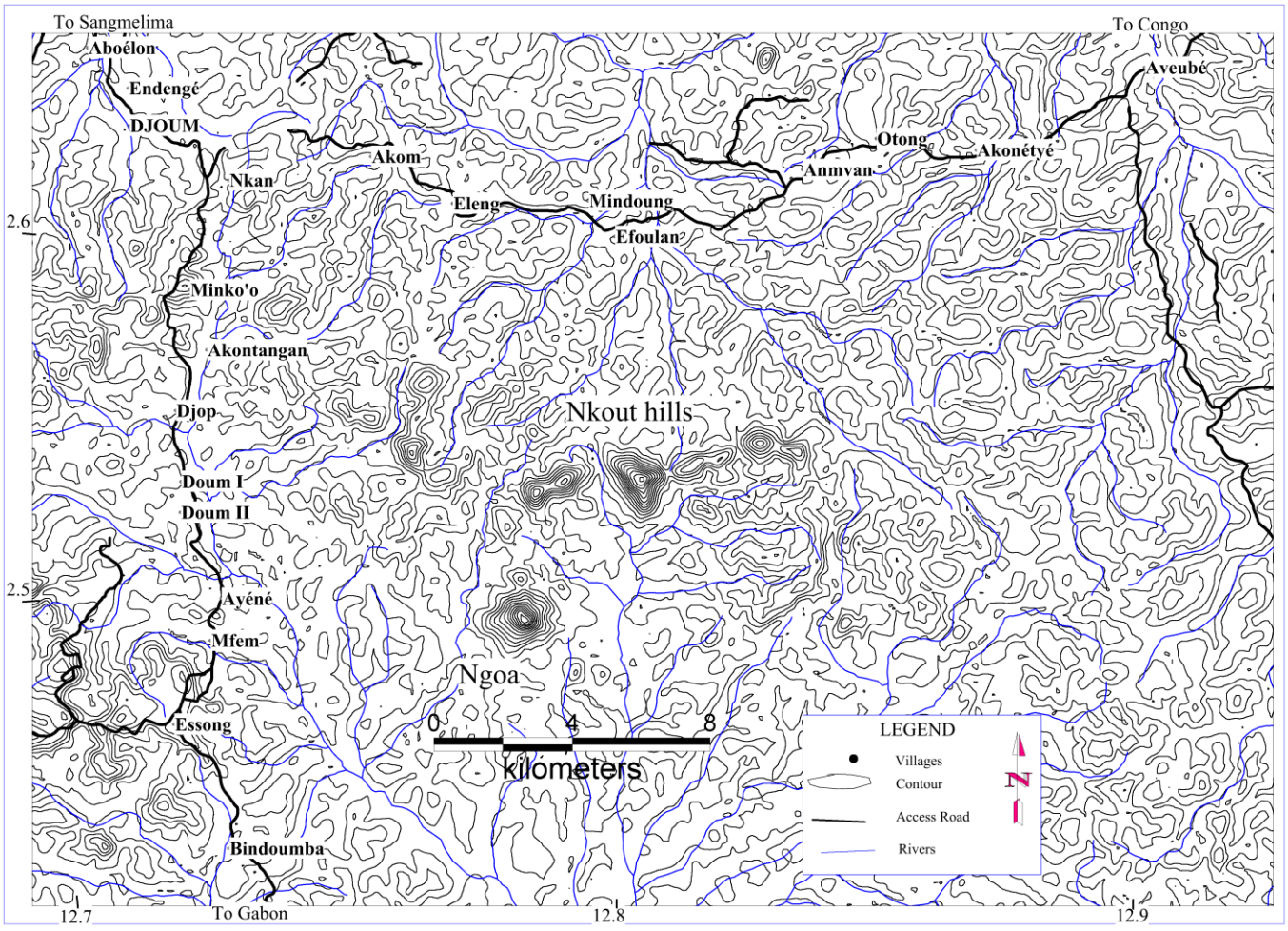

Figure 1: Topographic map of Djoum area showing the location of Nkout hill (contour generated from SRTM image of Nkout area)

I.1.2 PHYSIOGRAPHY

Based on the topographical map (Fig. 1) and SRTM image, the relief of this region consists of two hills, namely: Nkout hill, and Ngoa hill **(Fig. 2).** The altitudes of the Nkout hill is 910m while that of Ngoa is relatively 900m. With respect to the basic topographic map of the region,

there is a strong dendritic drainage pattern following N-S direction while the sub streams have strong E-W direction drainage patterns.

The research area is covered by a tropical rain forest with small scale agriculture near the road. In this relatively virgin area, the forest is comprised of a number of levels, tall trees (approximately 40m high) form the highest stratum, beneath which stands smaller trees with leaves clustered at their top. The terrain of the Nkout area is locally characterised by tree covering hills at the average elevation between 200m and 600m above sea level **(Fig. 1).** The forest bed has little vegetation, resulting from the shielding effects of the sunlight by high forest canopy. The vegetation in this whole region is represented by a jungle with very dense undergrowth that is difficult to cover on foot without cut paths through the undergrowth.

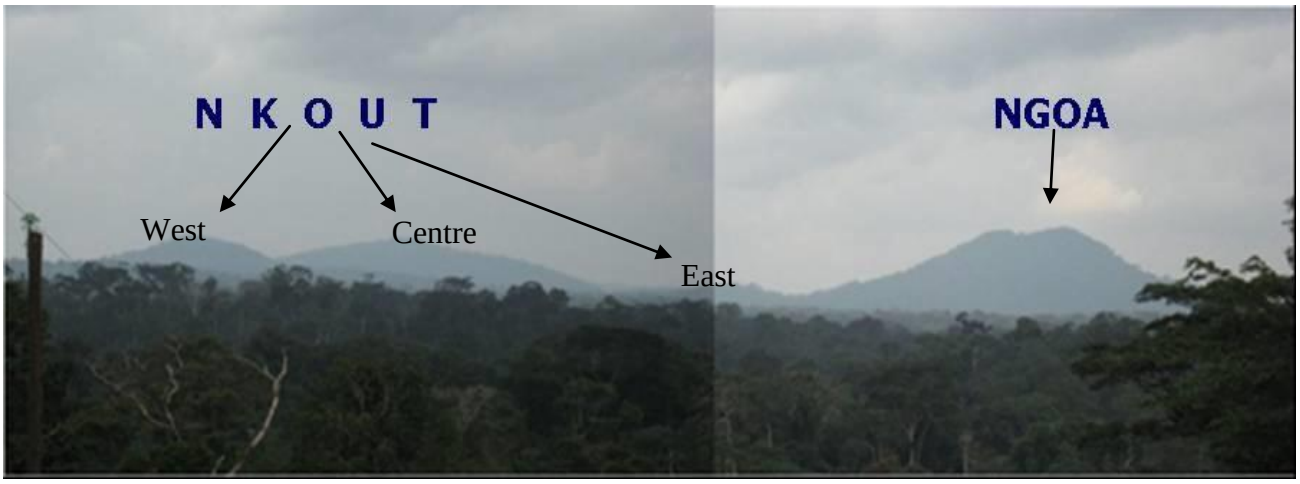

Figure 2: Panoramic view of the study area (photo taken SE of Nkout and Ngoa hills) Afferro-Mining, 2010

I.1.3 CLIMATE

The climate of southern Cameroon is equatorial in type, with four seasons: a long dry season that lasts for six months; from December to May. This is followed by a short rainy season from May to June, a short dry season from July to August and a heavy rainy season from mid-September to the end of November (Suchel, 1987; Tab. 1; **Fig. 3).**

Humidity is high, and precipitation averages between 1500mm and 2000mm per year. The mean annual rain fall in the Nkout area is around 1570mm and has less than 100mm of rain fall during the driest months. Precipitation is the main factor determining vegetation in this area (Suchel, 1987; Bagnouls and Gaussen, 1959).

Temperature is relatively high with average between 27.0°C to 31.5°C **(Tab. 1).** In the Nkout hill temperature is uniform throughout the year with an average of 19.14°C. August is the coolest month with monthly minimum of 27.0°C and a maximum of 27°C. January is the hottest

month with an average minimum temperature of 31.55°C and an average maximum temperature of 30°C.

Table 1: Monthly rainfalls/temperature average for Djoum in mm/T°

Month	Jan	Feb	Mar	Apr	May	Jun	Jul	Aug	Sep	Oct	Nov	Dec	Mean/ Total
T°c	31.5	31.5	30.7	30.1	29.1	27.6	29.4	27	28	27.19	28.27	29.1	29.14
mm	38	54	129	184	194	146	78	88	216	252	130	47	1556

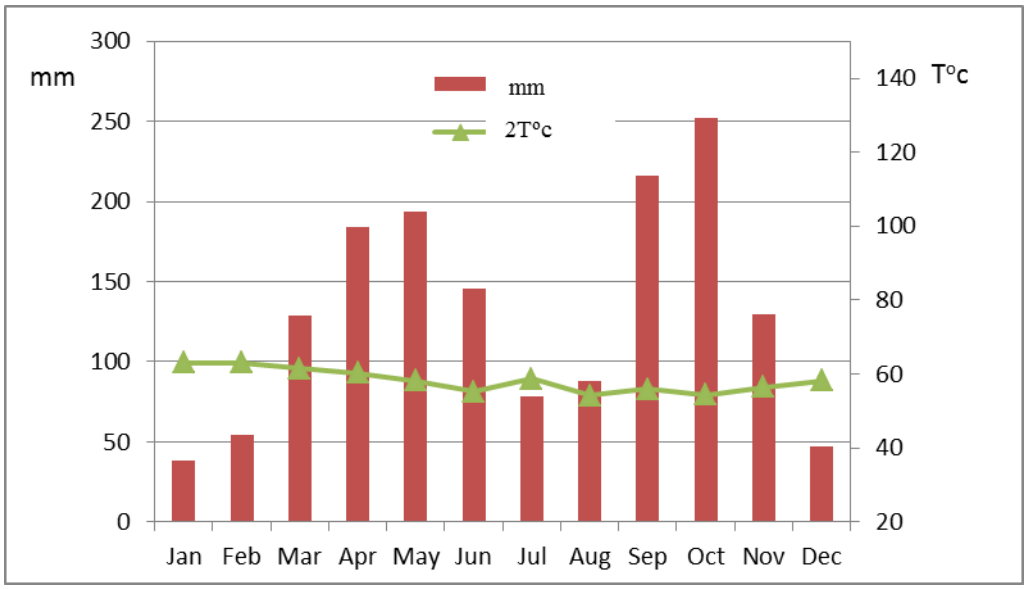

Figure 3: Annual average rainfall of the study area (Djoum) is in mm and annual average temperature of the study area (Djoum) is in T° C (after Bagnouls and Gaussen, 1957)

I.1.4 VEGETATION AND FAUNA

The Nkout area is part of the South East Cameroon forest bloc with a low altitude forest. The vegetation is a dense evergreen rainforest. It alternates with semi deciduous forests. This forest type is marked by a high tree density per hectare. Among these trees, there are several valuable species with a canopy height between 40-50 meters. Floral variety is huge, with the most dominant families being*: meliaceae*, *sterculiaceae*, *combretaceae*, and ochnaceae which lose their foliage in the dry season (Kamdem -Toham et al., 2003).

Among the species found in this area (Kamdem -Toham et al., 2003) are: Moabi (*Baillonnella toxisperma*), Padauk (*Pterocarpus soyauxii*), Movingui (Distemonanthus benthamianus), Tali (*Erythrophleum suaveolens*), Sapele (*Entandrophragma cylindicum*), Sipo (*Entandrophragma utile*), Bibolo (*Lovoa trichilioides*), Iroko (*Chlorophora excelsa*), Kossipo (*Entandrophragma candolei*), Okan (*Cilicodiscus gabonensis*), Ilomba (*Pycnanthus angolensis*), Frake (*Terminalia superba*), Bilinga (*Nauclea diderrichii*).

The hydrography in the valleys has had an impact on the vegetation which in these cases becomes a temporarily flooded marshy forest along water bodies which themselves are most hemmed by steep banks.

Among the numerous Non-Timber Forest Products *(*NTFPs) found in the Nkout area are: rattan, bamboo, *maranthaceae* leaves and eru (*Gnetum africanum*). Equally identified in the Djoum Community Forest Management Plan are several trees for domestic use such as: Bush mango *(Irvingia gabonensis),* Njangsa *(Riccinodendron heuidolotti),* and Moabi *(Baillonella toxisperma).*

In the area, a large variety of animal species had been identified amongst which are : monkeys *(Cercopithecus spp),* duikers *(Cephalophorus spp),* giant pangolins *(Manis gigantea),* wild hogs *(Potamochoerus porcus),* giant forest hogs, porcupines, grass cutters *(Thryonomis swinderianus),* tortoises, pythons locally called boa snake, vipers (*Bitis gabonensis*), etc.

Big mammals that were noted about 60 km away from the villages have disappeared from the community forest (which lies adjacent to the exploration site) because of intense poaching. Among them are, forest elephants (*Loxodonta africana cyclotis*), gorillas and chimpanzees (*Pan troglodytes*). Fish abound in the rivers and fishing is done mostly by women who use the damming technique. The Kaka tribe does large scale fishing in the Ayna and Dja Rivers (Kamdem -Toham et al., 2003).

I.1.5 SOIL

Red to reddish brown lateritic soil is found in this area. In some cases, the soil can be yellowish brown in colour. The thickness of the laterite can reach several meters depending on the relief (Suchel, 1987; Fig. 2). The nature of the laterite is also correlated with the bedrock geology. Precipitation and humidity is one of the prominent factor affecting bedrock thereby, enhancing physical alteration of the underlying and subsurface geology.

I.1.6 DEMOGRAPHY AND ECONOMIC ACTIVITIES

There are two main ethnic groups here: the Fang (majority) and the Zamane. Other minorities also found here are the Baka (Pygmies), the Kaka and the Ndjem. They are spread over some thirty villages and hamlets (Nzooh, 2003).

The population of Djoum subdivision can be estimated at 20,000 inhabitants. This population is mostly rural, given that Djoum town has only 6,000 inhabitants. The town's population is composite and constitutes not only the above mentioned tribes but other Cameroonian tribes including the Bamileke, Bamoun, Ewondo, Bassa, etc.

The Economic activities in the area include the primary, secondary and tertiary sectors. Primary sector activities include agriculture, fishing, hunting and gathering of non-timber forest products (NLFP, Nzooh, 2003).

Agriculture is the main economic activity of the area. Both food crops and perennials are cultivated. Farming is extensive and characterised by human labour mainly by family and small or medium sized farming units. The most common food crops are groundnuts, plantains, roots and tubers (cassava, coco yams, sweet potatoes, yams, etc.), corn and melons. Agricultural output is rather low, given the small amounts of cultivated land. The output is meant for feeding the producer's family with any surpluses being sold. The low agricultural output is reflected in the scarcity of foodstuff in local markets, especially in Djoum or the stalls along villages in Nkout area.

Hunting is widespread in the area, being a tradition among local communities. Hunting has become the target of a highly developed illegal trade in the area (Fondo, 2005). The most common hunting techniques in the area are the use of fire arms (modern and traditional hunting guns). Rearing is not very developed in the area. Animals are reared traditionally, i.e. they are allowed to roam and feed. Flocks, herds and flights are small and constitute rustic bird species (chicken, ducks), pigs, sheep, and goats.

Fishing is an artisan activity done by both men and women, during the dry season, fishing is done in big rivers (Miete etc.) using hooks, nets and sometimes damming. The landed catch is mostly carps, tilapia, and mudfish. Their catch is usually destined for the fisherman's consumption as well as for sale, before or after drying. Community forestry is well developed in the Nkout area. Local exploitation mainly targets species like Moabi and Iroko.

I.2 -GEOLOGIC SETTING

I.2.1 GENERAL GEOLOGIC SETTING

In Cameroon, Archean rocks are found in the southern parts of the country representing the northern edge of the Congo Craton (Fig. 4). The Congo Craton is a large sub-circular Craton of about 511,000 km^2 in area, and has a diameter of about 2,500 km, comprising Archaean crust early to mid-Proterozoic fold belt and Proterozoic cover (Goodwin, 1991; Shang et al., 2010). However, the Pan-African foreland belt surrounds and partly indents the Congo Craton (Fig. 4). The Congo Craton is almost entirely surrounded and is partly indented by circumjacent Pan-African foreland belts: Mozambique belt to the east, Damara-Katanga-Zambezi belt to the south-west, Congo-Kimezian belt to the west, and the North Equatorial fold belt to the north. The north-western margin of the Archaean Congo Craton in Southern Cameroon is represented by the Ntem complex (Maurizot et al., 1986; Nédélec et al., 1990; Goodwin, 1991; Fig. 5).

The Ntem complex is divided into two main structural units: the Archean Ntem unit (where Nkout is located Fig. 6A), and the Paleoproterozoic Nyong unit in the western area (Toteu et al., 1994; Tchameni et al., 2001; Penaye et al., 2004; Lerouge et al., 2006; Ndema et al., 2014), is bordered in the north by the Yaoundé Group (e.g. Nzenti et al., 1988; Barbey et al., 1990; Mvondo et al., 2003), of the Pan-African orogenic belt in Central Africa.

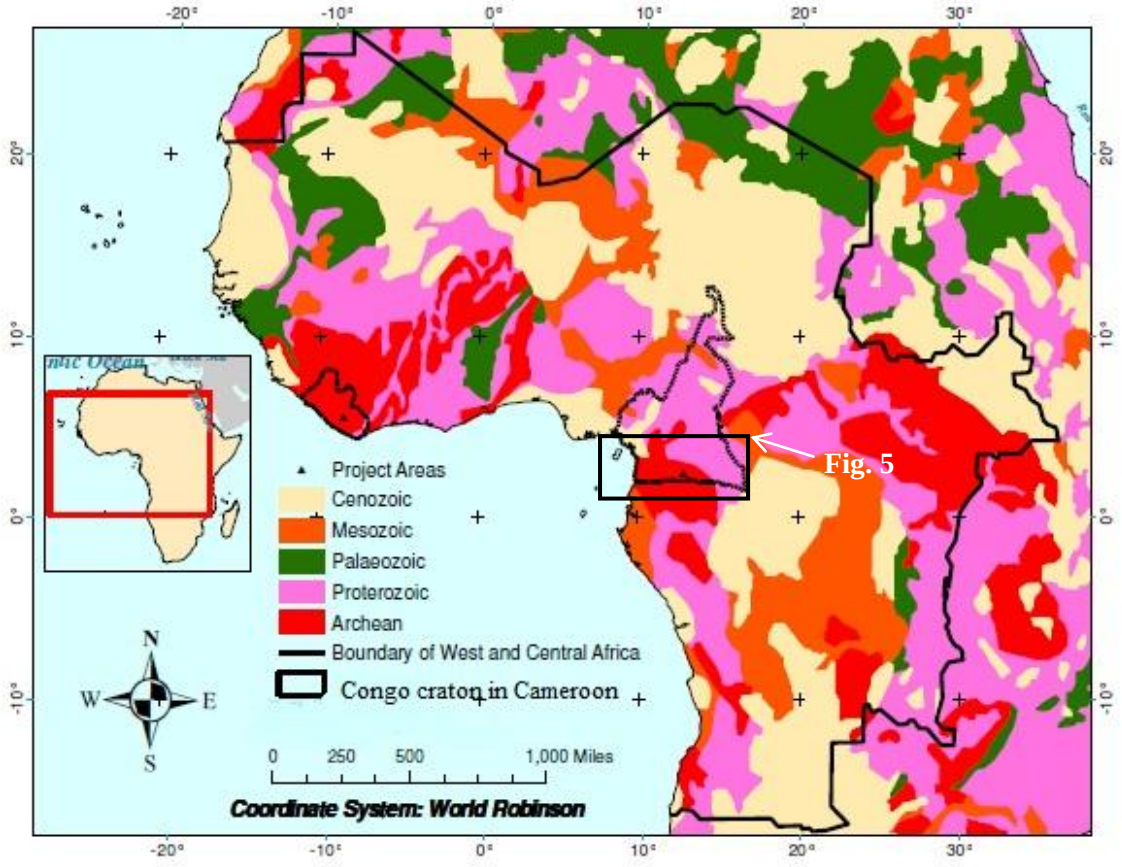

Figure 4: Regional geological maps of West and Central Africa (modified from Taylor et al., 2009)

The Yaoundé Group is in the southern part of Cameroon and comprises of two series, the Yaoundé series and the Mbalmayo-Bengbis series, which is marked by deformed metasedimentary rocks and migmatites (Nzenti et al., 1988; Fig. 6A), that overthrusted the Ntem complex and dips gently northwards (Fig. 5 and 6A). Rock types in the Yaoundé series includes schists and high-grade gneisses, thought to be derived from pelites and greywackes either in a continental margin or in a passive margin environment (Nzenti et al., 1988; 1999).

I.2.1.1 Archean Congo craton formation in Cameroon

The Ntem group (>2500Ma) is part of the large complex of the Archaean age of the Congo Craton in Cameroon (Fig. 6A). The Ntem group is made up of two units, the Ntem unit in the south-central area, and the Nyong to the northwest end (Fig 5B). The two units were reactivated during the post Archean orogeny (Toteu et al., 1994; Lasserre and Soba, 1976).

-Ntem unit

The Ntem unit represents the north-western part of the Archaean Congo Craton in Central Africa-Cameroon **(Fig. 5**; Maurizot et al. 1986; Nédélec, et al. 1990; Goodwin, 1991). It is limited in the north by a major thrust that marks the contact with the Pan-African orogenic belt (Yaoundé group, Nzenti et al., 1988; Barbey et al., 1990; Ngnotue et al., 2012) and is composed of massive

and banded plutonic rocks of the charnockite suite and by intrusive tonalites, trondhjemites and granodiorites (Nédélec et al. 1990; Shang et al., 2004) constituting the greater part.

The charnockite, granodiorite, and tonalite, make up this Trondhjemite-Tonalite-Granite (TTG) unit (Pouclet et al., 2007). The tonalitic suite which is strongly mylonitized and retrogressed along the faulted boundary with the Pan-African orogenic belt is located to the north of the Craton (Nsifa et al. 1993). The granodiorites form distinct massifs within the dominantly charnockitic southern zone while the banded iron formation and the paragneisses represent remnants of greenstone belts which forms xenoliths in the TTG (Nsifa et al., 1993). Late- to post-tectonic granitoids and syenites intruded the TTG (Nédélec, 1990; Tchameni, 1997; Tchameni et al., 2000; Shang et al. 2001). The Late Eburnean (*ca.* 2.1 Ga) doleritic dykes (Toteu et al., 1994; Vicat et al., 1996) represent the final magmatic activity in the Ntem complex. Three major episodes of deformation occurred in the Ntem complex (Maurizot et al., 1986; Feybesse et al., 1998). (i) The first deformation episode is characterized by vertical foliation, stretching and vertical lineation and isoclinal folds (Ne´de´lec et al., 1990; Vicat, et al., 1996; Shang et al., 2001; Tchameni et al., 2001). These structural features were correlated with the granitoids emplacement in the early to mid-Archean times (Tchameni, 1997; Tchameni et al., 2000; Shang, 2001); (ii) The second tectonothermal episode was marked by the development of N–S, NE–SW to ESE–WSW sinistral and dextral shear planes trending north-south (Nsifa et al., 1990; Tchameni et al., 2000) with partial melting of the TTG and the greenstone belt country rock which occurred between 2400 Ma and 1800 Ma (Lasserre and Soba 1976). Toteu et al. (1994) dated the peak of this metamorphism at about 2050 Ma and was confirm by Rb-Sr biotite ages of 1997 ± 19 Ma, 2064 ± 20 Ma, and 2299 ± 22Ma (Shang et al., 2004) for the Sangmelima TTG; (iii) The third deformational was evident to the overthrusting Pan-African schistose formations to the craton, a multifold structure of the Pan-African origin are observed in TTG rocks at the thrusting front.

The Ntem unit bears overprints of D_1 shearing deformation in association with M_1 metamorphic facies (Maurizot et al., 1986; Nsifa et al., 1990; Tchameni, 1997). The D_1 is marked by E-W orientation S_1 foliation and isoclinal fold. The S_0 structural surface is basically NW-SE in the charnockitic suite, NNE-SSW to almost E-W in the tonalitic suite and E-W to WNW-ESE in granodiorites, indicating structural discordances and suggesting a polyphase structural set-up in the Sangmelima TTG (Shang et al., 2001). The TTG group bears strong imprints that is characterised by mylonitization in the Mbalmayo-Bengbis schistose series. The lineation and subordinate foliation defined by alternating mesocratic and leucocratic bands fabrics are hosted Ntem charnockites and granodiorite in with variable orientation and intermediate dips (Kankeu et al., 2017). The foliation $S_{1/2}$ trends E-W with intermediate to steep dips and NW-SE intermediate to steep dips are broadly parallel with the tectonic boundary. The D_3 brittle deformations were

marked by E-W trending fractures and joints, structures with either sinistral or dextral sense of shear (Kankeu et al., 2017).

Brittle deformation of the Congo Craton was therefore more intensely enhanced by the effect of the Pan-African orogeny than by the effect of the Eburnean orogeny (Shang et al., 2001). Shang et al., (2007) interpreted this as Pan-African collision metamorphism imprints that intensively affected the northern margin of the Congo Craton.

-Nyong unit

The Nyong unit is initially defined as Neoproterozoic, or a Paleoproterozoic-reactivated NW corner of the Archean Congo Craton (Lasserre and Soba, 1976), that shows a well-preserved granulitic unit of the WCAB resting as an Eburnean nappe on the Congo Craton (Toteu et al., 1994, Fig. 6A). This series consists of metasedimentary and metavolcanic rocks, as well as syn-to late-tectonic D_2 granitoids and syenites (Pouclet et al., 2007). The Meta-sedimentary rock consists of quartzite and banded iron formations (BIFs; Lerouge et al., 2006). Metasediments have the composition of shale and close to those of continental or near-shore argillaceous sediments (Fig 6A andB; Ndema et al., 2014).

Meta-igneous rocks exhibit the compositions of intermediate to basic tholeiitic and calc-alkaline rocks derived from continental igneous protoliths varying from granites to gabbros (Ndema et al., 2014). The granodiorites are massif (Lerouge et al., 2006) while the syenite suites is the most abundant (Lasserre and Soba, 1976).

The unit displays three age groups (Toteu et al., 1994; Lasserre and Soba, 1976; Lerouge et al., 2006); (1) the oldest were the Archaean, U-Pb ages rocks (2500–2900 Ma) which were obtained from detrital zircons in metasedimentary rocks, and magmatic zircons in charnockites and migmatitic gneisses; (2) the rock of the Palaeoproterozoic age were obtained from U-Pb zircon (ca. 2050 Ma) corresponding to a thermometamorphic event associated with an important crustal melting and emplacement of granite and syenite massifs, (3) the age of the Neoproterozoic rock were obtained from U-Pb zircon (626 ± 26 Ma) corresponding to the metamorphic effect of Pan-African thrusting.

The Nyong Group is a reactivated portion of the Archean Ntem complex (Lasserre and Soba, 1976; Maurizot et al., 1986) during a Paleoproterozoic or the Pan-African orogeny. Ndema et al. (2014) indicated that the western border of the Congo craton and central domain of the fold belt represent an ancient continental domain which has been reworked during the later events of the Pan-African orogeny and the Paleoproterozoic orogeny. The rocks of the Nyong series were thrust in the South and in the East, forming the Oubanguides Nappe in the Central Africa Republic and in NE Brazil in the Borborema province (Ndema et al., 2014).

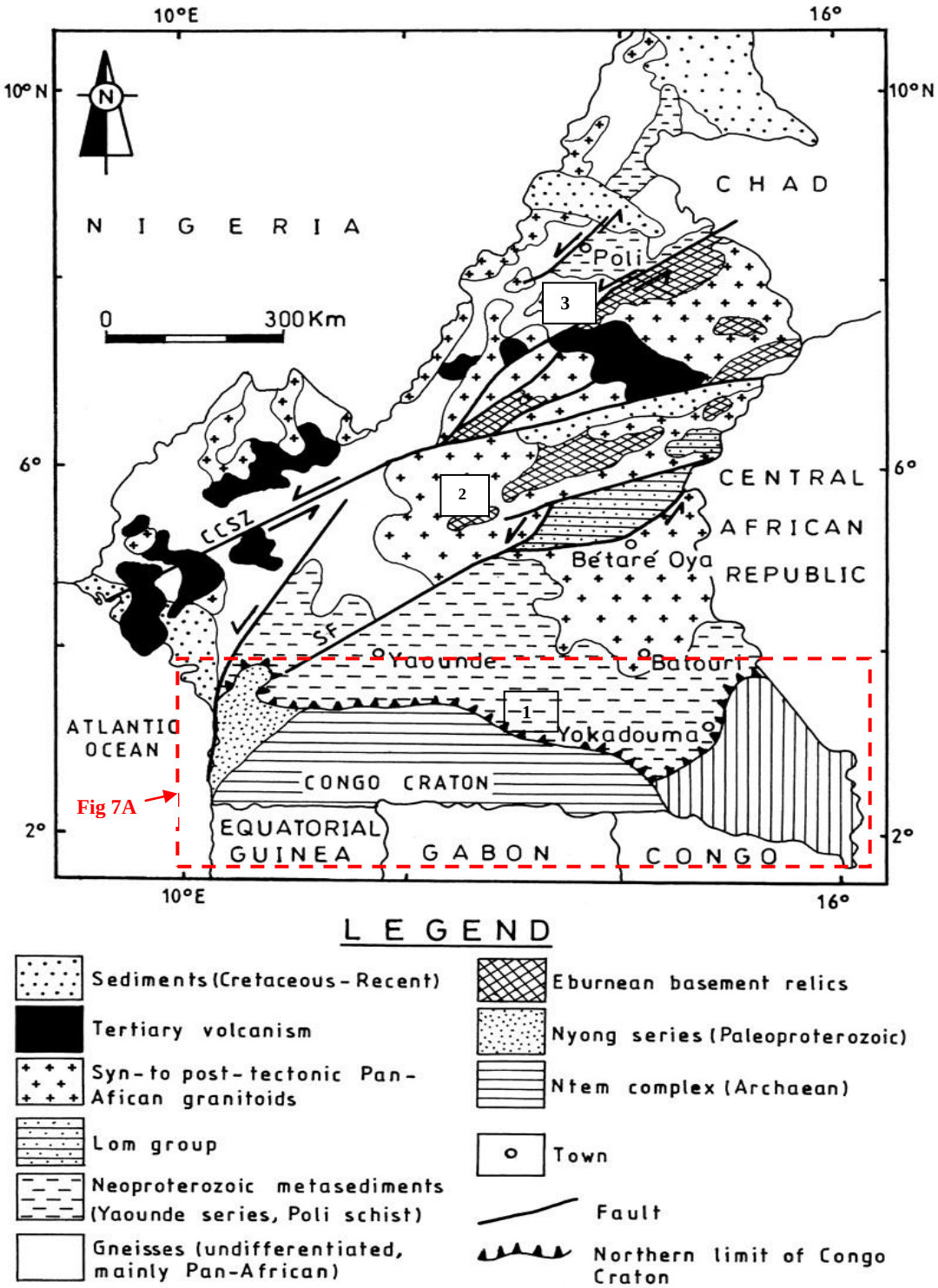

Figure 5: Geological map of Cameroon with the three main domains of the Pan-African North-Equatorial fold belt (Nzenti et al., 2010): (1) southern domain corresponding to the Yaoundé series thrust on the Congo Craton, (2) Central domain, (3) Northern domain, CCSZ: Central Cameroon Shear Zone; SF: Sanaga fault.

This reactivation interpretation was widely supported by Nd isotope data on whole rocks and U-Pb on zircons (Lerouge et al., 2006). It was also supported by SHRIMP analyses on detrital zircons from metasediments from the Craton, which yielded Mesoarchean to Paleoproterozoic ages (2423 ± 4 Ma; Lerouge et al., 2006). Toteu et al. (1994) by U-Pb and Sm-Nd whole rock method and Lerouge et al. (2006) by Rb–Sr, U–Pb and Sm–Nd isotopic dating method, suggested that the Nyong Group is a Paleoproterozoic unit that was deposited at the edge of the Congo Craton and

was subsequently involved in the Eburnean orogeny, before being locally overprinted by later Pan-African events.

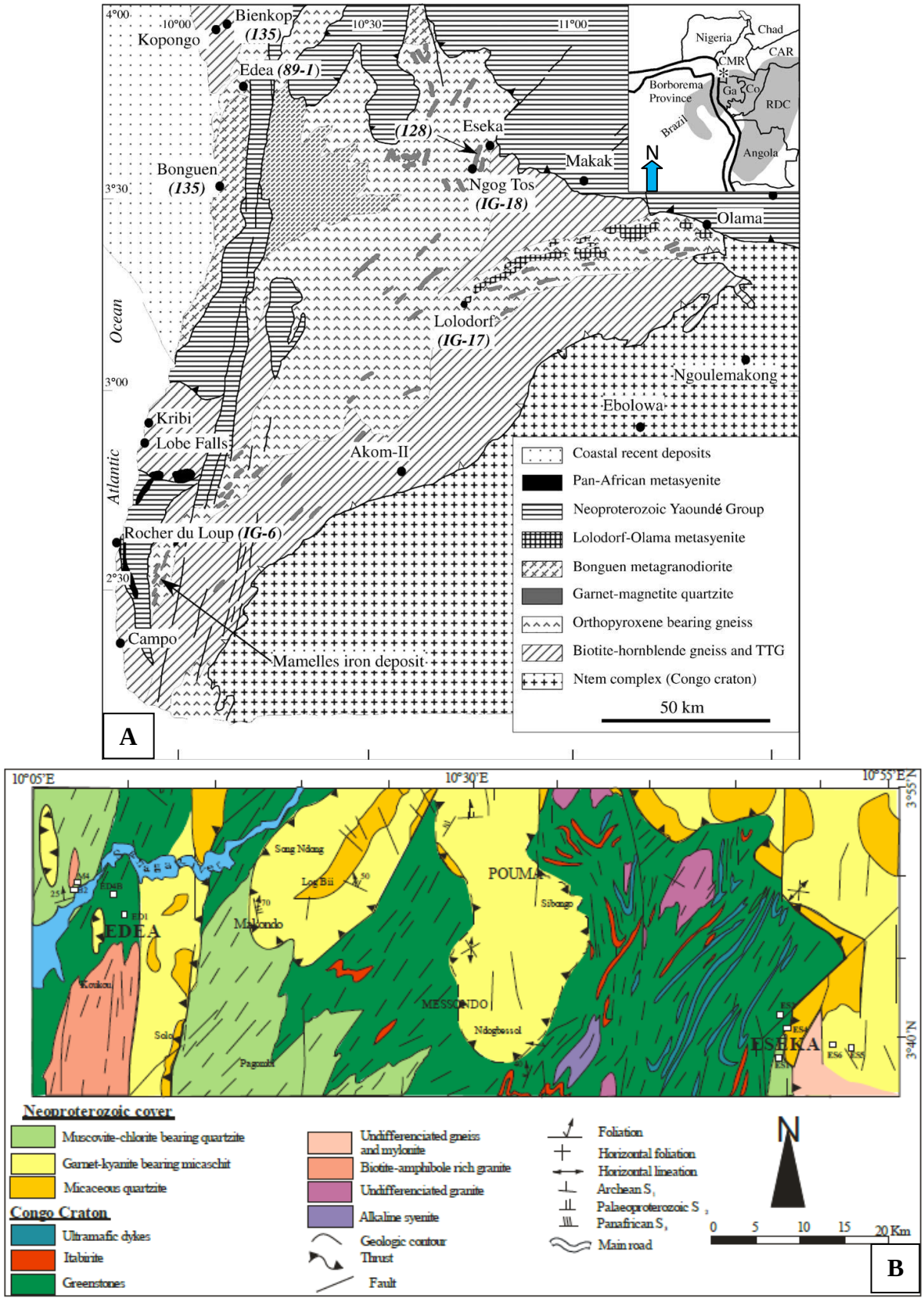

Figure 6: A) Geological sketch map of the Nyong Group (after Maurizot, 2000); B) Geological map of Nyong (Edéa and Eséka, after Ndema et al., 2014)

I.2.1.2 Geodynamic characteristics of the Congo Craton

The geodynamic evolution of the northern region of the Congo Craton was divided in to Archean and the Paleoproterozoic age.

-Archean evolution

The Ntem in Cameroon is tectonically overlain by Paleoproterozoic rocks (Nyong, Toteu et al., 2001; Feybesse et al., 1998; Tchameni et al., 2000; Shang et al., 2004). The Archean evolution comprises of two phases: (i) crustal formation and (ii) emplacement of the protolith to the volcano sedimentary formations (greenstones).

Between 3.32Ga and 2.9Ga (Sm-Nd and Rb-Sr methods), the processes of accretion corresponded to the emplacement and the recycling of the volcano sedimentary formations (Caen-Vachette et al., 1988; Toteu et al., 1994; Pouclet et al., 2007; Tchameni et al., 2004). The Trondhjemite-Tonalite-Granite (TTG) rock formations were emplaced by fractional crystallization of magma issued from melting and recycling of an oceanic crust as residual phase. These first two periods marked the pre- D_1 tectonic event. The period of 2.6 Ga to 2.5 (U-Pb, Sm-Nd and Rb-Sr methods) marked the geothermal activity of the area, leading to migmatisation at localized areas; the development of the Trondhjemite-Tonalite-Granite (TTG) and the formation of the orthogneiss.

The emplacement of granite (granitisation) and charnockite (charnockitisation) in the Ntem complex represents the crustal recycling processes in the end of the Archean evolutions (Toteu et al., 1994). The Archean fabric in the Ntem shows successive emplacement of diapiric granitoids during the D_1 deformation phase with sub-vertical lineation and isoclinal folds. Thus the diapiric intrusion for TTG granitoids could explain Archean geodynamic evolutions.

The Archean Ntem complex comprises of charnockites (from Palaeo-archaean, Meso-archaean, to late-Archaean ages), greenstone formations (Meso-archaean age), TTG basement (late Archaean age), dolerite dykes and high-K granites (Tchameni et al., 2000; Shang et al., 2001, Shang et al., 2004a; 2006; 2010; Pouclet et al., 2007). The rock group contains, (i) Trondhjemite-Tonalite-Granite (TTG) and banded gneisses at 3186 ± 75 Ma to 3120 Ma by Rb–Sr method (Caen-Vachette et al., 1988) (ii) The Meta-sedimentary rocks and greenstone belts, including Banded Iron Formations (BIFs) and mafic-ultramafic rocks that pre-date 3 Ga. (iii) The intrusive rocks which include TTG charnockites and associated greenstones are of 2950-2800 Ma by U-Pb method on zircon (Caen-Vachette et al., 1988; Toteu et al., 1994), and (iv) the late magmatic rocks (K-rich granitoids, syenogranites) which are dated at 2800-2500 Ma. The TTG suite is made up of tonalites, granodiorites and high-K granites, some of which are charnockitic (Pouclet et al., 2007). The igneous plutons of supracrustal rocks were interpreted as remnants of greenstone belts and dated at ca. 3.1 Ga by Pb-Pb method on whole rock (Tchameni et al., 2004).

The Ntem complex was affected by two major reactivation periods of deformation related to syntectonic plutonism and coeval metamorphism in the Eburnean and Pan-African times (Lasserre and Soba 1976; Toteu et al., 1994; Lerouge et al., 2006).

The first episode of deformation was successive diapiric emplacements of the Mesoarchean charnockites (~2.900 Ma) and TTGs (~2830 Ma) which were marked by vertical foliation and lineation, stretching and isoclinal folds (Shang et al., 2004a; Toteu et al., 1994). Tchameni (1997) synchronized this episode with a regional granulite-facies metamorphism. After the Archean event then followed the Paleoproterozoic, which was characterized by deformation phase marked by the development of N-S to NE-SW trending sinistral shear zones and brought about partial melting of the TTG suite and the greenstone belt and granites (Shang et al., 2007).

During the second tectonic episode (Tchameni et al., 2001), the late syenitic plutons (~2.3 Ga) intruded the complex. The Eburnean metamorphism affected all the Archean and Paleoproterozoic formations and was dated at ~2.05 Ga (Toteu et al., 1994) which brought about the amphibolite-facies metamorphism re-activated fingerprints occurrences in the Ntem complex. Lasserre and Soba (1976) suggested recrystallization between 2,400 Ma and 1,800 Ma from Rb–Sr whole rock data; Toteu et al., (1994) reported a U–Pb zircon metamorphic ages from the Nyong series of ca. 2050 Ma, a similar Rb–Sr biotite age reported by Shang et al. (2004a), dated this metamorphism at 2,064 Ma; whereas Lerouge et al. (2006) re-interpreted these ages as syntectonic plutonism ages.

This indicates that the Pan-African orogeny has more pronounced imprints on the Congo Craton. Palaeoproterozoic U-Pb zircon ages of ca. 2050 Ma (Lerouge et al., 2006) corresponded to a thermo-metamorphic event associated with an important crustal melting and emplacement of some granite and syenite massifs (Tchameni et al., 2001).

A major thrust fault of Pan-African age separated the Ntem complex and the Yaoundé Group of the Pan-African orogenic belt in Central Africa (Nzenti et al. 1988; Nédélec et al. 1986; Ngako et al. 2008; Fig. 7A). The Ntem unit constitutes the immediate margins of the Congo Craton with the Pan-African orogenic belt (Shang et al. 2004a, b). During the Pan-African orogeny (~600Ma), the Yaoundé series drifted southward and collided with the Ntem complex, forming a major nappe structure with peak granulite-facies metamorphism (Nzenti et al. 1984; 1988; Nedelec et al., 1986).

-Paleoproterozoic evolution

The Paleproterozoic evolution of the northern region of the Congo Craton is characterized by polyphase deformation (Fig. 7A), which was enhanced by subduction during the collision with the Pan-African orogenic belt (Toteu et al. 2001 and 2006, Fig. 7A).

This has reactivated the subducted part, which is corresponding to a metacratonization process (Shang et al. 2010). The reactivated process suggests that the Ntem complex represents the

northern metacratonic boundary of the Archaean Congo Craton, thus being a partly destabilized segment of the Congo Craton that has retained only some cratonic characteristics (Shang et al. 2010). The TTG group bears imprints of strong mylonitization and retrogression interpreted as Pan-African collision metamorphism imprints. Shang et al. (2004b), reported zircon U–Pb lower intercept Pan-African ages on charnockitic and granodioritic TTG of the Sangmelima region-Ntem complex indicated that the Pan-African orogeny as affected more intensively the northern margin of the Congo Craton. The D_1 foliations are essentially sub vertical as a result of the compressive phase. The D_2 phase consists of the rotational non-coaxial shearing structure and was accompanied by amphibolite facies metamorphism (Nsifa et al. 2013). Regional compression led to D_3 that overprints the D_2 as a result of the compressional phase (Toteu et al. 1994). The D_4 phase is a brittle phase. This episode ended with thermal and hydrothermal events. The Proterozoic episode ended at about 1.8Ga with thermal and hydrothermal events.

I.2.2 GEOLOGY AND STRATIGRAPHY OF IRON DEPOSIT

The Nkout iron deposit is located on the Ntem complex, an emerging iron ore province in West and Central Africa. Previous works indicate that the Nkout area comprises of Trondhjemite-Tonalite-Granite (TTG) granite, charnockitic gneiss, schist, amphibolite, and metamorphosed banded iron formations also known as itabirite (Suh et al. 2009; Shang et al. 2010; Ndime et al. 2018; Ganno et al., 2015; Fig. 7B). The deposit is comprised of beds of magnetite-bearing quartzite that are concordant with the country rock which is composed of granite-charnockite assemblage in the north and greenstone, gneissic rocks in the south (Suh et al., 2009). Caen Vachette et al. (1988) attributed itabirite rocks in the Ntem complex to be Archaean in age similar to their host country rocks. The deposit has an E-W ($N70^0E$) trending (9km long) ridge that defines the northwest plunging isoclinal fold structure. It is subdivided into West, Centre and South deposits (Kelvin et al., 2014; Ndime et al. 2018; Fig. 7B).

The Nkout-West, Nkout-Centre and Nkout-East deposits are the focus of this work (Fig. 8). It is bounded by N-S and NE-SW striking faults and approximately 9km long and 400-500m wide (Suh et al. 2009). The bulk deposit is magnetite-rich iron formation. The hanging and footwalls comprise of the country rock which is made up of biotite gneiss, biotite-garnet gneiss, and pyroxene-biotite gneiss (Fig. 8).

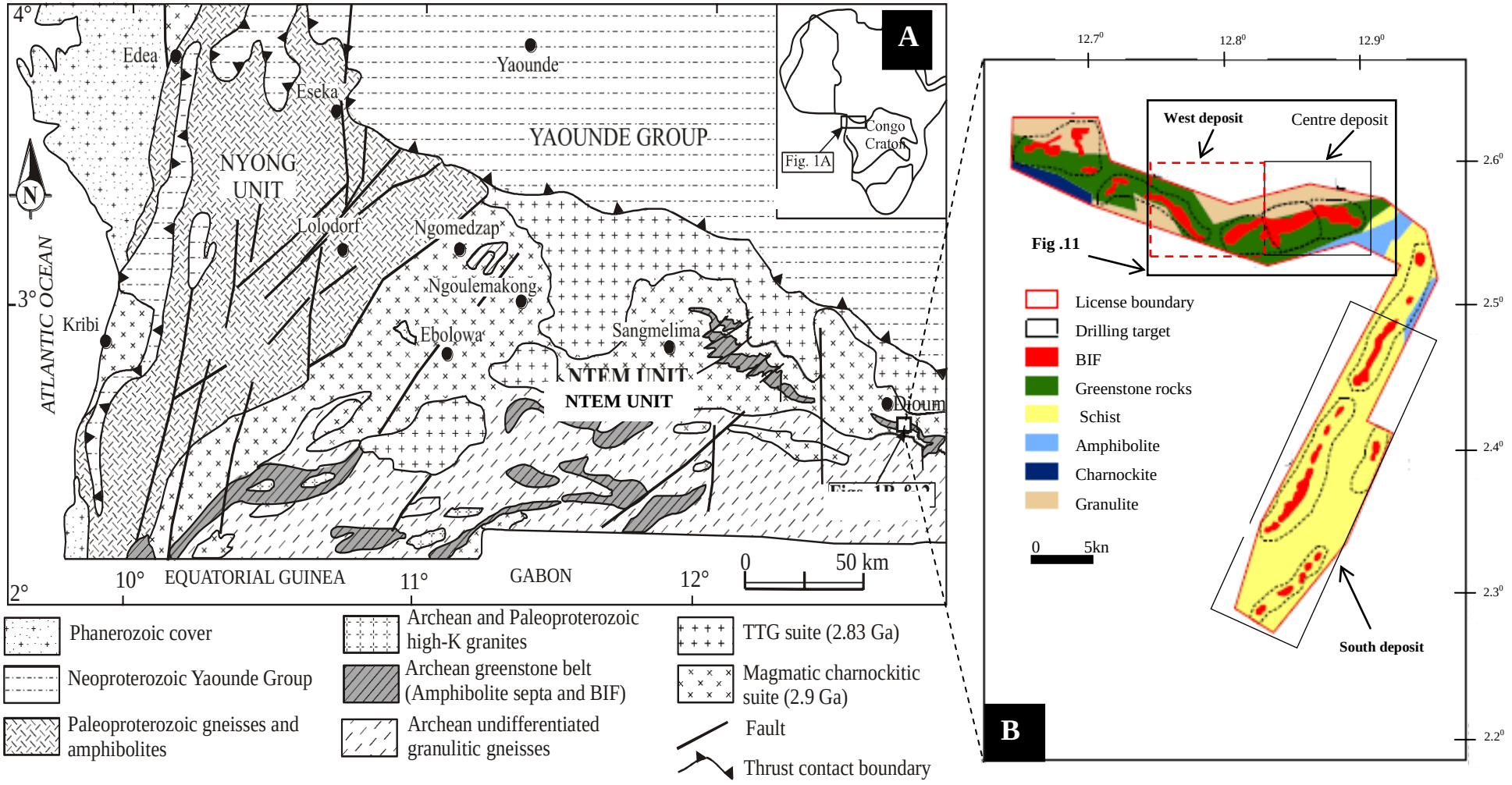

Figure 7: A) Simplified geologic map of south west Cameroon (Maurizot et al., 1986); B) Local geological map of Nkout banded iron deposit (after Kelvin et al., 2014)

CHAPTER II. MATERIALS AND METHODS OF STUDY

II.1. FIELD MATERIALS

This chapter deals with the details of things that are critical to bring out a meaningful and accurate report in obtaining the goals and objectives on this study. Field materials consist of the following:

II.1.1. GLOBAL POSITIONING SYSTEM (GPS)

The Global positioning system (GPS) is an electronic appliance which communicates with the satellite and gives the location of a point in three dimensions. It appropriately records the coordinates in longitude, latitude and altitude. On each point on the field where we made some observations and collected samples, we recorded the Global positioning system (GPS) coordinates with the aim to project the points on the topographic map, in order to establish a geological map.

II.1.2 TOPOGRAPHIC AND AEROMAGNETIC MAPS

The topographic map permitted us to quickly locate the area of study by its geographical coordinates. This provided us with geomorphological field information such as landforms and altitude (hill, valleys), rivers, streams, villages and road networks. However, it is on the topographic map that we momentarily plotted observation and sample coordinates gotten from the GPS. The aeromagnetic map permitted us to locate the areas of high magnetic signature. We later delimited the rock boundaries on the topographic map, which permitted us to develop and establish the geological map.

II.1.3 COMPASS CLINOMETERS

Besides the topographic map, the compass permitted us to well orient and organise ourselves on the field by the use of the four cardinal points. The clinometer was employed to sample outcrop orientation and measure the different structural elements such as the foliation plans, schistosity, lineations, shearing, dips and strikes of planner surfaces.

II.1.4. GEOLOGIC SLEDGE HAMMERS

Geologic hammer (1Kg) is one of the instruments available to chip identified rock types and petrographic facies for samples. It also permitted us to collect both hard rock and friable samples. Due to rock resistance and compatibility of certain rocks that show smooth plain surfaces without fracture, we used the geologic hammer of about 5Kg to collect samples for geochemistry and thin section.

II.1.5. DIGITAL CAMERA

For a good petrographic and structural description, both field (core and outcrop sample photos) and laboratory (thin section for petrography) photos were made. Each photograph was collected with a scale on it. These scales were represented as pen, coins, hammers, compass, meter tape and humans at the back ground of the photographs, while others were represented as scale bars. The use of the scale allows us to estimate the size of the object in the photographs.

II.1.6 MARKER, SAMPLE BAGS

To avoid confusion and contamination of the different samples collected, we took time to provide each sample with a plastic sample bag and with labels by the use of marker. Each number indicates the period, location of field work and the order of sampling. On the field note book, we recorded very important information (location, GPS coordination, rock description, structural measurement, photo number, and sample number). After this, the samples were then safe to be transported to the laboratory.

II.1.7 HAND LENS AND MAGNETIC PROPERTY PENS

The magnification (20X) lens is a hand held convex magnifying lens permitted us to observe minerals in rocks. Before the description of each rock type, we first observed the rock samples with the portable hand lens and took valuable petrographic information in our note books. The magnetic pen permitted us to test the magnetic property of the rock. This allowed us to know the statues of the magnetic property of the rock, which also permitted us to distinguish between the magnetite mineralised rock and barren species. These also allowed us to establish a precise dataset and to compare our data with that released in the laboratory.

II.1.8. MEASURING TAPE

The measuring tape was instrumental during field work as it was used to appropriately measure the dimension of outcrop as observed on the field and the drill depths during lithological and structural core logging. This permitted us to produce the lithostratigraphic column. We then synchronised the depths of the lithological and structure logs, and we were able to construct the north-south cross-section.

II.2 METHODS OF STUDY

The Method of study is classified in to field methods and laboratory methods. To conduct this study, fieldwork was followed by laboratory investigations.

(i) Field work investigations;

In field work investigations, a list of materials was made and the field methods were designed to carry out the fieldwork in the Nkout area.

(ii) Laboratory investigations:

The laboratory methods were carried out in many phases;

- The preparation and observation of thin sections for the petrographic study,
- The preparation and analyses of samples for geochemical study,
- Sample preparations and analyses for geochronological study.

II.2.1 FIELD METHODS

The field methods consisted of bibliographic research and investigation, interpretation of preliminary field data (topographic and aeromagnetic maps) on the Nkout prospect, a mineral

exploration property owned by Caminex SA (a subsidiary of International Mining and Infrastructure Corporation (IMIC) PLC, a British-London based company).

The field work started with the primary and fundamental phases which were field observations that gave us a better understanding of the Nkout area. From 2011 to 2014, we made several field trips, amongst which were two official field campaigns that lasted for two weeks (14 days) with Prof Nzenti of the University of Yaoundé I, assisted by Dr Ganno of the University of Yaoundé I. During the first week of the field trips, we established alongside a legend for geological mapping (on the different petrographic types with different lithographic facies, different lithostratigraphic units, and different sampling protocols) in the Nkout area. This legend was updated as more rock types were encountered with more detailed differentiations of the main rock groups.

We then created a database for the dataset in the entire project. This consists of the following:

The GPS waypoints consist of the coordinates date, time and number of observation points that were made on the field;

The field data consists of a table for the observed outcrop points. All geologically observed data and data that are obtained from instruments are stored in the field data. On GPS waypoint, we can have one or more field observation points. The field observation point number was introduced because in some cases, the geological observations and measurements can be made at the contact of two different rock types;

The sample data contains all sample information collected on the field. One observation point can have more than one sample;

The photographic data contains all observation points that are being documented with digital camera, usually three photographs are made; large scale, small scale and detail. One observation point can have more than one set of three photographs;

The analytical data from the laboratory consists of the data table where the geochemical and geochronological data are being stored. This data shows a one to one relationship with the sample data. We adapted standard symbols at the start of the geological mapping exercise.

II.2.1.1 FIELD MAPPING

During the field work, surface and subsurface field mapping exercises were done with the aid of the topographic map on the studied area.

II.2.1.1.1 Surface field mapping

The surface field mapping exercise was in two phases: random and systematic field mapping exercises.

The random field exercise consists of mapping along surface exposure. We were able to identify and map outcrops on exposed surfaces like horizontal road surface, vertical road cuts, quarries, hill slopes, river and stream beds, which were of great priority. It consists of observing rock on both outcrop scale and hand held specimen scale.

In the outcrop scale, we explore outcrops on each surface exposure with description made in our field note book. We took note of the scale of the outcrop, which permitted us to define its form or morphology (dome shape), outcrop azimuth (E-W or N-S direction) and identified most importantly the structural elements (such as foliation, folding, faulting and shearing).

In the hand held specimen scale, we observed the nature of the rock and the different petrographic facies. We also identified the different structural elements (foliation, schistosity, lineation, folding, shearing and boudinage), their orientation and chronologies. In cases where the petrologic observations were not clear as in weather rock surfaces, we used the geologic hammer to chip fresh surfaces. This aided us to find the true nature of the rock and the possible petrographic facies.

During the systematic surface field mapping exercise, a 0.5km long N-S grid lines of 200m line spacing by 100m observation points offset programme was conducted and mapped over across, on areas of higher magnetic signatures situated on the deposit. Based on preliminary information from the topographic and aeromagnetic maps, outcrops as well as float materials were searched around the gridlines, and around high altitudes. This was in an effort to increase on the quantity and quality of geological data acquired from the field mapping. Outcrops on this area were identified and described from the regional scale, down to hand specimen in the geologic field note books.

II.2.1.1.2. Subsurface field mapping (Core logging)

The subsurface field mapping exercise consists of core logging. Nine diamond drilled holes spatially distributed in three sections of Nkout area were chosen. Three representative holes within a cross-section were selected from a multitude of different drill holes from each of the prospects (Nkout west, centre, and east).

- Lithological logging

The different lithologies were studied on the field by observing core materials. The cores were logged lithologically at their respective depth intervals. We described the rock material in the different sequences (lithology, grain size, colour, texture, fabric, stratigraphy, and weathering). The lithologic units were distinguished by the different litho assemblages. These different litho assemblages were recorded as interval data, which is the depth from where a particular lithology starts to where it ends. This was studied for the construction of lithological log and cross section.

- Structural logging

The different structural regimes were studied on the field by observing the different structural elements. Structural data was acquired directly from the surfaces of gneissic rocks, BIFs outcrop and drill core materials. These features include bedding surfaces, fault surfaces, shear surfaces, joint and veins, faults plans, cleavages, and fold axis. Structural features were recorded as point data with their point depths and the corresponding structural features. The number of variations of the features such as fracture indexes and fracture frequencies were recorded. More detailed point data base on structural orientation of rock fabrics were also obtained. We took note of the thicknesses, weathering and shear strength of clay infills and the presence of shear surfaces, which could indicate movement. We also used the clinometers and recorded outcrop direction and orientation of structural features, with respect to their dips and strike values (lineation, foliation, fault plane, fold limbs, and fold axial plane etc). The measurements of the different structural elements were done for the goal to stereographically study the orientation of the main deformation phase.

II.2.1.2 FIELD SAMPLING

- Random (Outcrop) sampling

During field mapping, grab and in-situ outcrop samples were collected. We used the Global position system (GPS) to obtain coordinates for the locations of outcrop and samples on the field. Rocks of different lithologies were selected and set apart for analyses.

- Systematic core sampling

Half and quarter core samples were systematically collected from the representative drill holes with respect to their lithology and texture. The drill core samples were carefully selected so that they were representatives of the deposit alongside detailed core logging.

Representatives of quarter core saprolite, laterite and fresh BIF samples were selected based on their bulk chemistry, size and textural characteristics of the BIF being investigated. They were based on a thorough understanding of the geology; general petrography, geochemistry, geochronology and mineralogy. These include ore (iron-mineralized rocks) and un-mineralized zones (barren species). This is to ensure that the full variability of the BIF samples have been represented as they need to reflect the geology and ore of the deposit. Rock chips were carefully observed and data recorded in a note book. Care was taken during sample preparation and transportation from site to the laboratory to avoid cross contamination and confusion.

A total of 106 samples were collected out of 256 outcrop locations and 9 drill holes that were observed. Selected samples were placed in plastic bags and were sealed up. Labels and codes were given to the samples which were written on the bags. Selected samples were protected from contamination before analysis. Each sample rock type was cut in to four pieces, which were

distributed into the laboratories for thin section production, geochemical and geochronological analysis. A piece was kept for backup and reference.

II.2.2 LABORATORY METHODS

In this work, the bibliographical study consists of reviewing previous geology work, research theses and scientific publications.

The bibliographic research encompasses the following sub-phases:

(i)The studies of all available documents were made. This includes all published and unpublished papers, topographic maps, geological maps of the Nkout area, etc.

(ii)The collection of remote sensing data was made. Besides literature and printed maps, the following satellite scenes that cover the study area were acquired: SRTM (Shuttle Radar Topography Mission).

II.2.2.1 THIN SECTIONS

Thin section is a piece of rock sample which is being polished to render it transparent and translucent, so that it could be observed with the petrographic microscope under transmitted and reflected light. The production of thin section consists of several steps; making a rock slice, gluing the rock on the microscopic slide, polishing the rock slice, protecting the slice with cover slip.

a). Preparation

After field work, samples collected (51) were sent to the laboratory for thin section preparation. Thin sections of different rock types (granite basement and charnockite, BIFs and gneiss) for petrographic study were prepared in Geotech Lab Vancouver (Canada) from diamond drilled cores and out crop samples. Good thin sections preparation and finishing were made in the following manner: A thin slice of rock is cut with a diamond saw and trimmed to fit onto a microscopic glass slide. The slice is glued on the microscopic slide with clear 5-minute epoxy or similar glue. The slides are then mounted on a special holder and ground on a diamond lap. When thicknesses of 0.03mm are reached, the thin sections are completed and ready for examination under the microscope. The thickness of the sections were usually measured with a digital micrometre or estimated by sight. With experience, a good estimation can be made by visual examination of the section and final checking with a microscope. A cover slip is placed on the mount to protect the specimen from water and other mechanical risks.

b). Observation

After the preparation of the thin sections in the laboratory, the thin sections were then observed under the microscope. Thin section study consisted of mineral identification, manual point counting and mineral dimension estimation. The thin sections were studied in a standard optical microscope in transmitted and reflected light, to constrain mineral assemblages, texture and

abundance in the different mappable units. We observe 47 thin sections in the Laboratory of Petrology and Structural Geology in the University of Yaoundé I, using a binocular microscope OPTIC IVYMEN SYSTEM. The minerals were observed under plane polarized light (PPL), cross polarized light (XPL) and reflected light (RL). The minerals were distinguished in plane polarized light by certain mineralogical characteristics (morphology, relief, cleavages, pleochroism). In cross polarized light, we were able to distinguish other mineralogical characteristics. We were able to determine at every time the mineral phases in equilibrium (paragenesis), the microstructure (foliation, schistosity, kink band, micro-fold, micro fault, micro shearing), and the precise mineral phase (syn, pre, or post tectonic). Other observed microscopic features were mineral zonation and mineral inclusion.

After the observation of thin sections under the petrographic microscope, we made photomicrographs of samples under plane polarized light (PPL), cross polarized light (XPL) and reflected light (RL).

II.2.2.2 WHOLE ROCK GEOCHEMISTRY METHODS

Whole-rock analyses were done using the pulp by Inductively Coupled Plasma-Atomic Emission (ICP-AES) for major elements and by Inductively Coupled Plasma Mass Spectrometry (ICP-MS) for trace elements and REE at ALS Minerals Global Group Vancouver (Canada).

The samples (40) were pulverized and 50-60 grams were obtained for the analyses. 0.2 g of rock powder was fused with $LiBO_2$ and dissolved in 100 mm^3, 5% HNO_3. 63 Elements were obtained by various leaching technic and Inductively Coupled Plasma Mass Spectrometry (ICP-MS). The leaching technique involved Ionic Leaching with Ammonium Acetate which is slightly stronger than water and the highly sensitive ICP-MS to achieve (ppt) detection limits. Carbon and sulphur by combustion in furnace was used for whole rock geochemistry to quantify the major elements. The majority of these analytes have a lower detection limit of 0.01%, with the exception of Na_2O (0.05%) and P_2O_5 (0.005%). Loss on ignition ("LOI") was determined by 0.5 g, ignited for two hours at 1000ºC and then weighed again.

Trace elements and REE digestions were done with lithium borate ($LiBO_2$) and fusion. Four acid digestions were done for the base metals and an aqua regia digestion for the volatile gold related trace elements. Analysis precision for REE is estimated at 5% for concentration >10ppm and 10% when lower.

II.2.2.3 LEAD ISOTOPE METHOD

The Pb isotope method was done as an add-on to the trace level four acid digestion methods at ALS Minerals Global Group Vancouver (Canada). In the default method, eight (8) samples were prepared 0.5g each was digested with four acids ($HClO_4$, HF, HNO_3 and HCl) to dryness followed

by leaching with HCl. After cooling, the resulting solution is diluted to volume (25 ml) with 10% HCl, mixed and analyzed with HR ICP-MS Isotope analysis method. The ICP-MS instrument was carefully tuned to rapidly scan the isotopes of interest and provided a level of precision that was fit for purpose of age determination.

Six Pb isotope ratios are reported ($^{206}Pb/^{204}Pb$, $^{207}Pb/^{204}Pb$, $^{208}Pb/^{204}Pb$, $^{208}Pb/^{207}Pb$, $^{208}Pb/^{206}Pb$, and $^{206}Pb/^{207}Pb$). The detection limit was 0.01 for $^{206}Pb/^{204}Pb$, $^{207}Pb/^{204}Pb$, $^{208}Pb/^{204}Pb$ and 0.001 for $^{208}Pb/^{207}Pb$, $^{208}Pb/^{206}Pb$, and $^{206}Pb/^{207}Pb$.

Precision and accuracy were monitored using certified Pb isotope and internal rock standards. The age determination was calculated and plots were prepared using Isoplot 4.15 program (Ludwig, 2011) according to the Pb-evolution model of Stacey and Kramers (1975).

RESULTS

CHAPTER III. PETROLOGY AND LITHO-STRATIGRAPHY

INTRODUCTION

The geology of Nkout area consists of magmatic and metamorphic rock units. The Magmatic unit consists of the granitic rocks while the metamorphic unit consists banded iron formation (BIF) in association gneiss country rock.

In order to carry out this study, drill core were logged and samples were collected from both units and thin sections were produced in Geotech lab in Vancouver Canada.

The chapter systematically describes the lithostratigraphy and petrographical study of the different formation in the Nkout area.

The field work on petrographical study in the area is presented in distinctly two petrographic domains: the magmatic unit (40% vol) and the metamorphic unit (60% vol). The study was done by means of optical microscopy (plain polarised light PPL and cross polarised light XPL). It presents the petrographical characteristic of the samples based on the macroscopic and microscopic texture as observed on the field and in the thin section respectively. On the microscopic scale, a more detail description of the mineral on the thin section is made with regards to the mineralogical phases and the rock is presented.

The lithostratigraphy study presents the different lithologic units. The studied litho-units were described according to their inferred stratigraphic position from bottom to top of the succession. Mappable units were defined based on litho-facies using primary lithology, texture, field occurrences (estimation of the thickness or volume of the unit) and relation with other units (observed and inferred) and correlation was made possible by litho-stratigraphic facies. Description of the rock types were supported by macroscopic and microscopic samples observation. This finally constrains a depositional model for the formation.

III.1. PETROGRAPHY

III.1.1 MAGMATIC ROCK UNIT

The magmatic unit within the Nkout area consists of the granitoid rock which is the most abundant plutonic rocks.

III.1.1.1 GRANITOID ROCK

The granitoid rock of the Nkout area consists of biotite granite and amphibole granite

III.1.1.1.1 Biotite granite

Biotite granite occurred as boulders of 3 to 4 m high and 7 to 10 m wide and occurs close to the contact with the banded iron formation northeast of the deposit (Fig. 13). They are medium to coarse-grained, not foliated equigranular microstructure in hand specimen (Fig. 8A). It consists mainly of plagioclase (25 - 30%), K-feldspars (20 - 25%), biotite (15 - 20%), quartz (15 - 20%), and pyroxene (3 - 5%). Biotite granite displays heterogranular microstructures (Figs. 8BandC).

Plagioclases occur as large to small subhedral to anhedral grains, commonly showing granulitic texture (Fig. 8B). Plagioclase grains are commonly medium- to coarse-grained (0.12-0.49mm) in sizes. Myrmekyte (intergrowth of plagioclase and quartz) occurs on rims of larger grains (Fig. 8B). Biotite granite is associated with subhedral K-feldspar, quartz, biotite and pyroxene.

K-feldspars display subhedral to euhedral grains and it is medium to coarse grained. They show granular texture and consist of grain-size of 0.19-0.45mm, and are in association with biotite, quartz, plagioclase and pyroxene.

Anhedral to subhedral biotite crystals (0.1-0.25mm) occur as flakes. Secondary greenish chlorite mineral have been transformed from biotite. They are associated with quartz, plagioclase and pyroxene crystals.

Quartz grains are subhedral to anhedral and are medium to coarse-grained (dominantly showing granulitic texture. Quartz crystals show variable grain sizes 0.02-0.46mm). These grains exhibit interlocking grain boundaries with biotite minerals and intergrowth with K-feldspar (Fig. 8C). They are associated with biotite, pyroxene, K-feldspar and plagioclase. Quartz shows the lack of alteration and non-uniform domain extinction.

The orthopyroxene grains are subhedral to anhedral with crystal sizes of 0.1-0.28 mm. They are medium to coarse-grained and are associated with plagioclase, biotite, K-feldspar, quartz (Fig. 8B).

III.1.1.1.2 Amphibole granite

Amphibole granite occurs as boulders some 2m high and 5m wide and 10m in extension. They occur to the north of the banded iron formation (Fig. 13). Amphibole granite is medium to coarse-grained, equigranular, not foliated rock. (Fig. 8D). It is composed of plagioclase (20 - 25 %), K-feldspars (20 - 25 %), quartz (15 - 20 %), biotite (15 - 20 %), Amphibole (5 - 10 %) and pyroxene (5 - 10 %). Amphibole granite is heterogranular in microstructures (Figs. 8E and 8F). Plagioclase is subhedral to euhedral with various sizes (0.05 - 0.25 mm) and commonly showing granulitic texture.

It is often associated with biotite, K-feldspars, amphibole and quartz and show characteristic twinning (Fig. 8E and 8F).

K-feldspars display subhedral to euhedral grains in forms and are in association with amphibole, biotite, quartz, plagioclase and pyroxene. They are forming intergrowth with quartz and are of various sizes (0.19 - 0.51 mm). Some are rimmed by quartz aggregates

Quartz grains are subhedral to anhedral and mostly medium to coarse-grained (0.01-0.2 mm). They show granulitic texture with interlocking grain boundaries K-feldspars. This is associated with biotite, K-feldspars, plagioclase, and pyroxene minerals (Fig. 8F).

Biotite crystals occur as anhedral to subhedral flakes of various sizes (0.05 - 0.2 mm) and mainly show a granulitic texture, without transformation. They are often associated with, quartz, K-feldspars, plagioclase, and pyroxene.

Amphibole crystals are euhedral to subhedral grains. Megacrysts of amphibole are of various sizes (0.05 - 0.12 mm). They are associated with biotite, quartz, plagioclase, K-feldspars and pyroxene. Pyroxene crystals are subhedral to euhedral in form. Megacrysts are of various sizes (0.02 - 0.15 mm). They are associated with biotite, K feldspars, plagioclase and quartz.

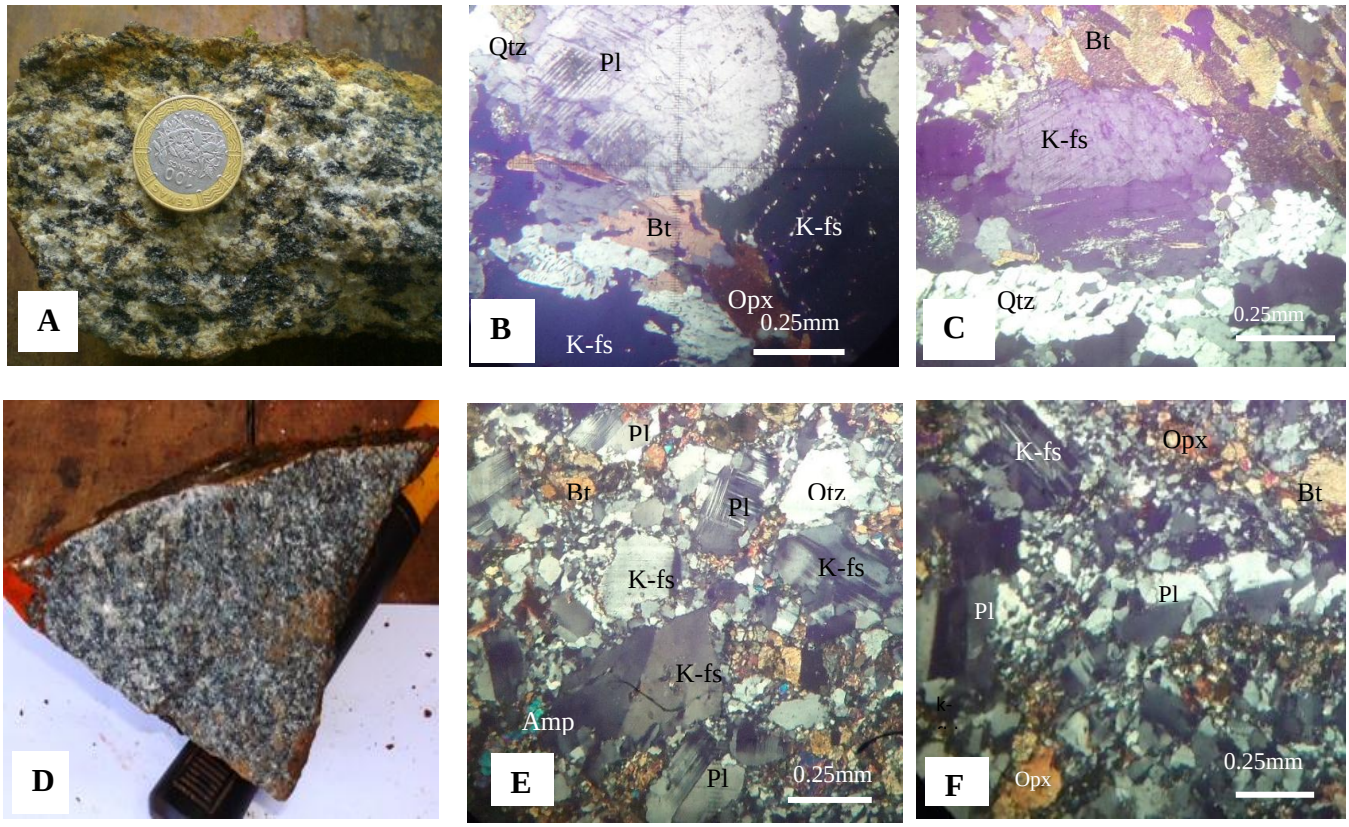

Bt: biotite; Kfs: potassium feldspar; Qtz: quartz; Pl: plagioclase; Amp: amphibole; Opx: ortho pyroxene

Figure 8: Hand specimen and photomicrographs of granitic country rock: A. hand sample photo of biotite granite; B, C (plane polarized light PPL) photomicrographs showing granulitic microstructure and mineral assemblage of biotite granite: D. hand sample photo of amphibole granite; E, F (PPL) photomicrographs showing granulitic microstructure and mineral assemblage of amphibole granite.

III.1.2 METAMORPHIC UNIT

The metamorphic unit consists of gneiss country rock and banded iron formation (BIF).

III.1.2.1 GNEISSIC COUNTRY ROCK

The gneiss country rock consists of biotite-rich gneiss, garnet-magnetite micaschist, garnet-biotite gneiss and pyroxene-biotite gneiss.

III.1.2.1.1Biotite-rich gneiss

Biotite-rich gneiss samples were collected from the upper contact between gneiss and metamorphosed BIF. Biotite-rich gneiss sample shows gneissic structure with alternating millimetric quartzo-feldspathic and ferromagnesian layers in hand specimen (Fig. 9A), and displays heterogranular granoblastic microstructure on thin sections (Fig. 9B and 9C). It consists mainly of potassium feldspar (K-feldspars) (25 - 30 %), quartz (20 - 25 %), biotite (15 - 20 %), Plagioclase (10 - 15 %) and magnetite (5 - 10 %).

Potassium feldspar (K-feldspars) are anhedral to subhedral in shape and measures up to 0.15-0.24 mm in crystal sizes, indicating granoblastic texture (Fig. 9B). Potassium feldspars in biotite gneiss show interlocking grain boundaries with quartz crystals. They are often associated with biotite, quartz and magnetite crystals.

Quartz crystals are the most abundant minerals in the gneiss assemblages with equigranular coarse-grain sizes, and are dominantly granoblastic in textures. Quartz crystals (0.06 to 0.20 mm) are anhedral to subhedral, exhibit polycrystalline ribbons or single crystals with undulatory extinction and the coarse-grained domains occur as megacrystals. The deformational features are indicative of dynamic recrystallization. The interlocking grain boundaries shared with the other minerals are smoothly curved (Fig. 9C). Quartz crystals are mostly in association with feldspar, magnetite and biotite.

Biotite crystals occur as anhedral to subhedral flakes (0.16 mm) commonly altered to secondary greenish-blue chlorite minerals. They share grain boundaries that are straight or smoothly curved with the other minerals. The biotite crystals present in biotite-rich gneiss are porphyroblastic. Biotite porphyroblasts are of various sizes (0.05 - 0.16 mm), and mainly show a granoblastic texture (Fig. 9B). They exhibit interlocking grain boundaries with quartz and are often associated with magnetite crystals, quartz and feldspar.

Plagioclase crystals are commonly medium to coarse-grained (0.01 - 0.05 mm) and euhedral to subhedral with polysynthetic twins. Plagioclase crystals are mostly in association with K-feldspar, magnetite and biotite.

Magnetite crystals occur as large subhedral to anhedral grains which measure up to 0.21 mm, showing granoblastic textures (Fig. 9C). The magnetite crystals are dark-grey and are commonly surround by other coarse-grained minerals (K-feldspars and quartz crystals). It exhibits interlocking grain boundaries with quartz. It is in association with biotite, quartz, Plagioclase and feldspars.

The biotite-rich gneiss shows medium amphibolite facies mineral assemblage, which is made up of feldspars, quartz, biotite, magnetite and plagioclase.

III.1.2.1.2 Garnet-magnetite micaschist

This rock is medium to coarse-grained with gneissic structure in hand specimens (Fig. 9D). It consists mainly of garnet (25 - 30 %), quartz (20 - 25 %), biotite (15 - 20 %), magnetite (10 - 15 %), and secondary chlorite (05 - 10 %). The garnet-magnetite micaschist displays heterogranular and granoblastic microstructure under the petrographic microscope (Fig. 9E and 9F).

Garnet porphyroblasts show micro-fractures due to deformation and display disseminated fine-grained (0.20 mm) quartz inclusions that developed in micro-cracks (Fig. 9F). Euhedral to subhedral garnet porphyroblasts exhibits interlocking grain boundaries with quartz and biotite as neighbouring crystals. The garnet porphyroblasts are often surrounded by a schistose matrix that mainly consists of chlorite, biotite and quartz minerals. Garnet crystals are associated with biotite, magnetite and quartz.

Quartz grains are subhedral to anhedral and mostly medium to coarse-grained (0.1 - 0.8 mm) with wavy extinction. They are often associated with biotite, magnetite, and garnet grains. Granoblastic texture of quartz mainly occurs as recrystallised mineral aggregates with equiangular triple points. They exhibit interlocking curved grain boundaries at contacts between neighbouring minerals. Quartz is associated with biotite, magnetite and garnet.

Anhedral to subhedral biotite crystals (0.60 mm) are partially to completely alter to light-green chlorite minerals. Individual biotite crystals are commonly medium to coarse-grained in sizes with the long axis of biotite flakes that define a direction which is parallel to schistosity. Biotite is associated with quartz, magnetite and garnet crystals and show interlocking grain boundaries with quartz and garnet.

Magnetite grains occur as subhedral to anhedral, coarse to medium- grains (0.025 mm average), dominantly showing granoblastic textures. They are mainly surrounded with other coarse-grained minerals and often occur in the interstices of biotite and quartz, showing interlocking grain boundaries.

The mineral assemblage of garnet-magnetite micaschist is quartz-garnet-magnetite-biotite, which is consistent with medium amphibolite grade metamorphism.

III.1.2.1.3 Garnet-biotite gneiss

Garnet-biotite gneiss samples were collected from an interlayer of gneiss (Fig. 9G).The rock is dark-grey in colour and medium to coarse-grained. The garnet-biotite gneiss samples are rich in garnet minerals, and show gneissic structure in hand specimen with alternating millimetre quartzo-feldspathic and mafic minerals layers (Fig. 9G). Under the petrographic microscope, garnet-biotite gneiss displays heterogranular and granoblastic microstructure, and is composed mainly of garnet (30 - 35 %), quartz (25 - 30 %), biotite (20 - 25%) and feldspar (5 – 10 %), magnetite (2 – 5 %).

Large euhedral to subhedral crystals of garnet porphyroblasts with average crystal sizes of 0.20 mm are rich in fine-grained quartz and biotite inclusions (Fig. 9H and 9I). The garnet present in garnet-biotite rich gneiss is surrounded by a foliated matrix of secondary chlorite, biotite and quartz (Fig. 9I). They exhibit smooth curved interlocking grain boundaries with quartz and biotite. Garnet crystals are associated with quartz, feldspars and biotite crystals.

Quartz crystals are the most abundant minerals in the gneiss assemblages with variable grain sizes. It occurs as coarse- to fine-grained subhedral to anhedral crystals and also exhibit granoblastic texture. Some quartz grains are ribbon with undulose extinction, a deformational feature indicative of recrystallization while others are undeformed. They exhibit interlocking curved grain boundaries at contact with other neighbouring crystals. Quartz crystals are in association with garnet, biotite, magnetite and feldspars.

Anhedral to subhedral biotite crystals occur as flakes of various dimensions (0.05 - 0.08 mm) and orientations, some of which are partially altered to light greenish blue chlorite (Fig. 8I). Biotite crystals are commonly medium to coarse-grained and occur as individual grains in a foliated matrix. They exhibit interlocking grain boundaries with quartz grains, some of which are straight while others are smoothly curved.

Feldspar porphyroblasts are about 0.05 - 0.125 mm in sizes, and are often in association with quartz, biotite and garnet crystals.

Magnetite crystals are euhedral to subhedral (0.01 - 0.025 mm), and are coarse to medium grain in sizes. Magnetite is the main Fe-oxide mineral component of garnet-biotite gneiss and is associated with quartz, biotite and garnet crystals.

The garnet-biotite gneiss shows amphibolite facies mineral assemblage, which is made up of garnet, quartz, biotite, feldspar, and magnetite.

III.1.2.1.4 Pyroxene-biotite gneiss

This rock is medium to coarse-grained with gneissic structure in hand specimen (Fig. 9J). It consists mainly of plagioclase (25 - 30%), biotite (25 - 30%), feldspars (20 - 25%), quartz (10 - 15%), and pyroxene (3 - 5%). Pyroxene-biotite gneiss displays heterogranular granoblastic microstructures (Figs. 9K and 9L).

Plagioclase in pyroxene-biotite gneiss occurs as large to small subhedral to anhedral grains, commonly showing granoblastic texture (Fig. 9L). Plagioclase grains are commonly medium- to coarse-grained (0.12 - 0.19 mm) in sizes. Plagioclase crystals display twinning and are associated with biotite, quartz and pyroxene.

Anhedral to subhedral biotite crystals (0.05 - 0.23 mm) occur as flakes with infilled cleavages parallel to their long axis.

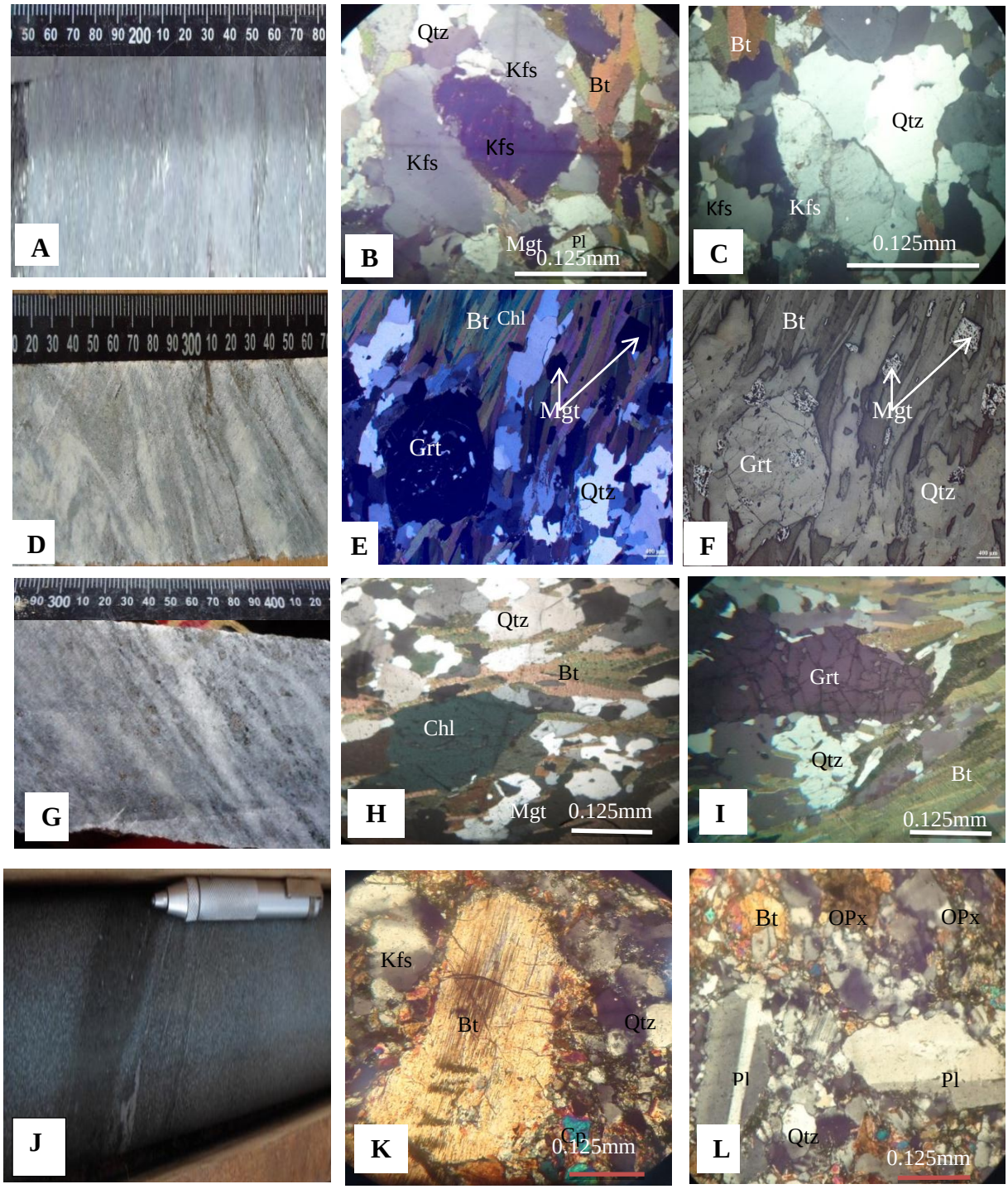

Bt: biotite, Kfs: potassium feldspar, Qtz: quartz, Pl: plagioclase, Amp: amphibole, Cpx: clyno pyroxene, Grt: garnet, Chl: chlorite, Mgt: magnetite

Figure 9: Hand specimen and photomicrographs of country rock: A. drill core photo of biotite rich gneiss; B, C (Plane polarized light PPL) photomicrographs showing granoblastic microstructure and mineral assemblage of biotite rich gneiss. D. drill core photo of garnet-magnetite micaschist; E, F(PPL) photomicrographs showing granoblastic microstructure and mineral assemblage of garnet-magnetite micaschist; G. drill core photo of garnet-biotite rich gneiss; H, I(PPL) Photomicrographs showing granoblastic microstructure and mineral assemblage of garnet-biotite rich gneiss; J. drill core photo of pyroxene-biotite gneiss; K, L (PPL) Photomicrographs showing granoblastic microstructure and mineral assemblage of pyroxene-biotite gneiss.

Equigranular fine-grained biotite, quartz and pyroxene disseminatedly surround the rims of biotite porphyroblasts with intergrowth (Fig. 9K). They are associated with quartz, plagioclase and pyroxene crystals.

Feldspars porphyroblasts display subhedral to euhedral grains in forms and consist of an average grain-size of 0.19mm, and are in association with biotite, quartz and pyroxene.

Quartz grains are subhedral to anhedral and mostly medium to coarse-grained (0.02 - 0.04mm), dominantly showing granoblastic texture with wavy extinction. Quartz crystals in the pyroxene-biotite gneiss assemblage with variable grain sizes (Fig. 9L), some of which occur as both reduced aggregates and individual grains. These grains exhibit interlocking grain boundaries at contacts between neighbouring minerals, such as biotite, pyroxene, and plagioclase which are often in association.

Clinopyroxene crystals are subhedral to anhedral in form and consist of grains that measure up to 0.140 mm. Large subhedral clinopyroxene crystals (0.05 - 0.1 mm) are present with inclusions of quartz. The clinopyroxene grains in pyroxene-biotite gneiss are transformed into amphibole/chlorite minerals (Fig. 9K).

The orthopyroxene grains are subhedral to anhedral in form with an average crystal size of 0.12 mm. They are medium to coarse-grained that are well preserved (Fig. 9L).

The pyroxene-biotite gneiss shows amphibolite facies mineral assemblage, which is made up of plagioclase, biotite, feldspars, quartz, and pyroxene.

III.1.2.2. BANDED IRON FORMATIONS (BIFs)

BIFs commonly display alternating micro (1 - 5 mm) - to meso (1 - 1.5 cm) -bands of Fe- and Si-rich layers. The iron-rich bands are mainly composed of iron oxides (magnetite with minor haematite) and silicate minerals (chlorite, garnet and biotite), whereas the Si-rich bands are mainly composed of quartz. Based on the mineral content and composition, BIFs have been subdivided into four types, magnetite-rich BIF, amphibole-rich BIF, garnet-biotite BIF and garnet-amphibole BIF.

III.1.2.2.1 Magnetite-rich BIF

The medium- to coarse-grained magnetite-rich BIF samples show schistose structures (Fig. 10A) and are composed primarily of magnetite (25 - 30 %), quartz (20 - 25 %), biotite (20 - 25 %), chlorite (15 - 20 %) and heterogranular and granoblastic microstructures prevail in this rock type (Figs. 10B and 10C).

Magnetite is the main iron minerals of the Nkout magnetite BIF and occurs in both magnetite-rich bands and silica-rich bands (Fig. 10C). Magnetite occurs as large subhedral to

anhedral grains (0.1 - 0.6 mm) dominantly showing granoblastic texture. Magnetite exhibits an interlocking grain texture with curved grain boundaries. These grains are distributed uniformly and are interconnected to form aggregates of different sizes. They occur around quartz and other mafic minerals (Fig. 10C).

Quartz crystals are one of the most abundant mineral in the magnetite-bearing BIF assemblage with variable grain sizes. It is medium to coarse-grained (average 0.25 mm) which locally exhibit undulose or wavy extinction and recrystallization. Quartz grains occur as large to small subhedral to anhedral grains, dominantly showing granoblastic texture and exhibit curved interlocking grain boundaries. Fine magnetite grains (0.02 mm) occur as inclusions in quartz porphyroblasts.

Biotite crystals are subhedral to anhedral. They are flakes of various dimensions (0.1-0.4mm), some of which are commonly transformed to chlorite (Fig. 10C). They are in association with magnetite, quartz and chlorite crystals.

Chlorite minerals are anhedral to subhedral crystals (average grain size 0.013 mm) which are light-green within schistose structure (Fig. 10B). They are commonly surrounded by magnetite coarse-grained minerals and often occur in the interstices of minerals. Most of the secondary chlorite grains are derived from the transformation of biotite minerals. These grains exhibits interlocking grain boundaries at contacts between neighbouring minerals and are in association with magnetite, biotite and quartz crystals.

The mineral assemblage of magnetite BIF is magnetite, quartz, biotite, and chlorite consistent with greenschist facies metamorphism.

III.1.2.2.2 Garnet-biotite BIF

The garnet-biotite rich BIFs are medium to coarse-grained foliated rocks (Fig. 10D) composed of garnet (25 – 30 %), quartz (20 – 25 %), biotite (15 – 20 %), magnetite (10 – 15 %), and chlorite (0 – 5 %). They display heterogranular and granoblastic microstructures (Figs. 10E and 10F).

The garnet crystals occur as euhedral to subhedral porphyroblastic grains that measure up to 0.23 mm in sizes, and are surrounded by a foliation matrix made up of magnetite, biotite and quartz minerals (Figs. 10E and 10F). Garnet porphyroblasts (0.05 - 0.23 mm) contain mineral inclusions of magnetite and quartz some of which are within developed micro-fractures. Garnets grains in garnet-biotite BIF exhibit interlocking curved grain boundaries.

Quartz grains are one of the main components in the biotite-garnet BIF and occur as euhedral or subhedral, fine-grained sizes (0.04 - 0.2 mm) crystals. Most of the quartz grains show wavy extinctions (Figs. 10E and 10F) which are indicative of micro-deformation and recrystallization. Quartz crystals in biotite-garnet BIF occur as both aggregates with equiangular

triple points and individual grains, exhibiting curved grain boundaries commonly showing granoblastic texture.

Biotite grains occur as flakes of various dimensions and also forms euhedral inclusions in garnet (Fig. 10E). Subhedral to anhedral biotite crystals (0.02 - 0.16 mm) display magnetite and quartz inclusions (Fig. 10F). Fine-grained magnetite (0.01 - 0.04 mm) inclusions occur in biotite porphyroblasts. Biotite aggregates surround and occur at the rims of garnet porphyroblasts. Biotite grains show interlocking grain boundaries at contacts between garnet and quartz, some of which are smoothly curved surfaces whereas others are straight.

Magnetite is the main Fe-oxide mineral component of biotite-bearing BIF. They are subhedral to anhedral, exhibiting both individual grains and aggregates which are disseminated with the rims of garnet, and as inclusions within the biotite porphyroblasts (Fig. 10F). Magnetite grains (0.01 - 0.06 mm) exhibit curved rough to smoothly interlocking grain boundaries, and dominantly exhibit granoblastic texture. Some magnetite grains occur as interstitial aggregates in coarse-grained quartz and garnet.

Secondary chlorite flakes (0.01 - 0.10 mm) result from alteration of biotite. The mineral assemblage of garnet-biotite BIF is made up of quartz, magnetite, garnet and biotite.

III. 1.2.2.3 Garnet-amphibole BIF

Garnet-amphibole BIF samples were collected from the contact between gneiss and BIF. The garnet-amphibole rich BIF is a medium to coarse-grained foliated rock (Fig. 10G). It is composed of garnet (30 – 35 %), amphibole (20 – 25 %), quartz (10 – 15 %), magnetite (10 - 15 %), biotite (5 - 10 %) and Pyrite (2 – 5 %). It is heterogranular and granoblastic in microstructures (Figs. 10H and 10I).

Garnet is one of the main mineral components at the lower units of Nkout metamorphosed BIF. It dominantly shows granoblastic texture. Garnet porphyroblasts (0.2 - 0.72 mm) are largely anhedral to subhedral in shape, rich in quartz inclusions, embedded in biotite, quartz and amphibole foliated matrix. Garnet grains show typical microstructures produced through brittle deformation, with two phases of micro-cleavages that are typical on garnet porphyroblastic crystals. These micro-cracks are at right angle to each other. The first phase of micro-cleavage is parallel to the foliation matrix (biotite and quartz) which is parallel to the direction of maximum elongation. The second phase of micro-cleavages is characteristically shorter, and is at right angle to the former. The micro-cleavages are generally restricted to the garnet crystals only, and propagation into the surrounding foliated matrix is not evident. The majority (50 – 60 %) of the garnet crystals show intense fragmentation**,** although a few crystals remained intact which are the late stage crystallisation.

Subhedral amphibole crystals (0.2 - 1.5 mm) are associated with biotite, magnetite, garnet and quartz.

Quartz grains have been one of the most ubiquitous minerals in all the occurrences, although the proportions and grain sizes are highly variable. Quartz crystals are euhedral or subhedral (0.03 - 0.24 mm), dominantly showing a granoblastic texture. They occur as inclusions disseminated within the garnet porphyroblasts; as subhedral to anhedral grains (Figs. 10H and 10I). Some quartz grains show wavy extinction and recrystallization.

Biotite occurs as fine to coarse subhedral to anhedral grains, dominantly showing an inequigranular granoblastic texture (Figs. 10H and 10I). Some of the biotite grains are partially altered to chlorite. Subhedral biotite crystals (0.02 - 0.21 mm) are associated with magnetite, garnet and quartz. Biotite grains exhibit textural interlocking curved grain boundaries.

Magnetite is the main Fe-oxide mineral components of garnet-amphibole-rich metamorphosed BIF. They occur as subhedral to anhedral aggregates disseminated within the rims of garnet and interstitial aggregates in coarse-grained garnet (Fig. 10I). Magnetite grains (0.05 - 0.15 mm) exhibit curved interlocking grain boundaries which dominantly show granoblastic texture.

Sulfides in the Nkout metamorphosed BIF are comprised of pyrite. Pyrite is light-yellow and is commonly surrounded by coarse-grained garnet, amphibole and quartz minerals and often occurs in the interstitial spaces. Pyrite crystal occurs as subhedral to euhedral (0.1 – 1 mm) and displays smoothly curved contacts with the other minerals (Fig. 10I).

The garnet-amphibole metamorphosed BIF shows amphibolite facies mineral assemblages composed of quartz, garnet, amphibole and biotite.

III. 1.2.2.4 Amphibole-rich BIF

The amphibole-rich BIFs consist of two varieties, cummingtonite-rich BIF and hornblende-rich BIF.

Cummingtonite-rich BIF shows foliated structures and are medium to coarse-grained with alternating millimetric to centimetric iron and siliceous layers (Fig. 10J). It is composed of magnetite (30 - 35 %), quartz (25 - 30 %), biotite (20 - 25 %), and cummingtonite (15 - 20 %). Cummingtonite-rich metamorphosed BIFs are heterogranular and granoblastic in microstructures (Figs. 10K and 10L).

Magnetite crystals occur in both Fe-rich bands and quartz-rich bands as grains and aggregates (Figs. 10K and 10L), with subhedral to anhedral shape ranging from 0.21 - 0.30 mm in sizes, and exhibiting granoblastic texture. Their grain boundaries with other minerals are straight to smoothly curve.

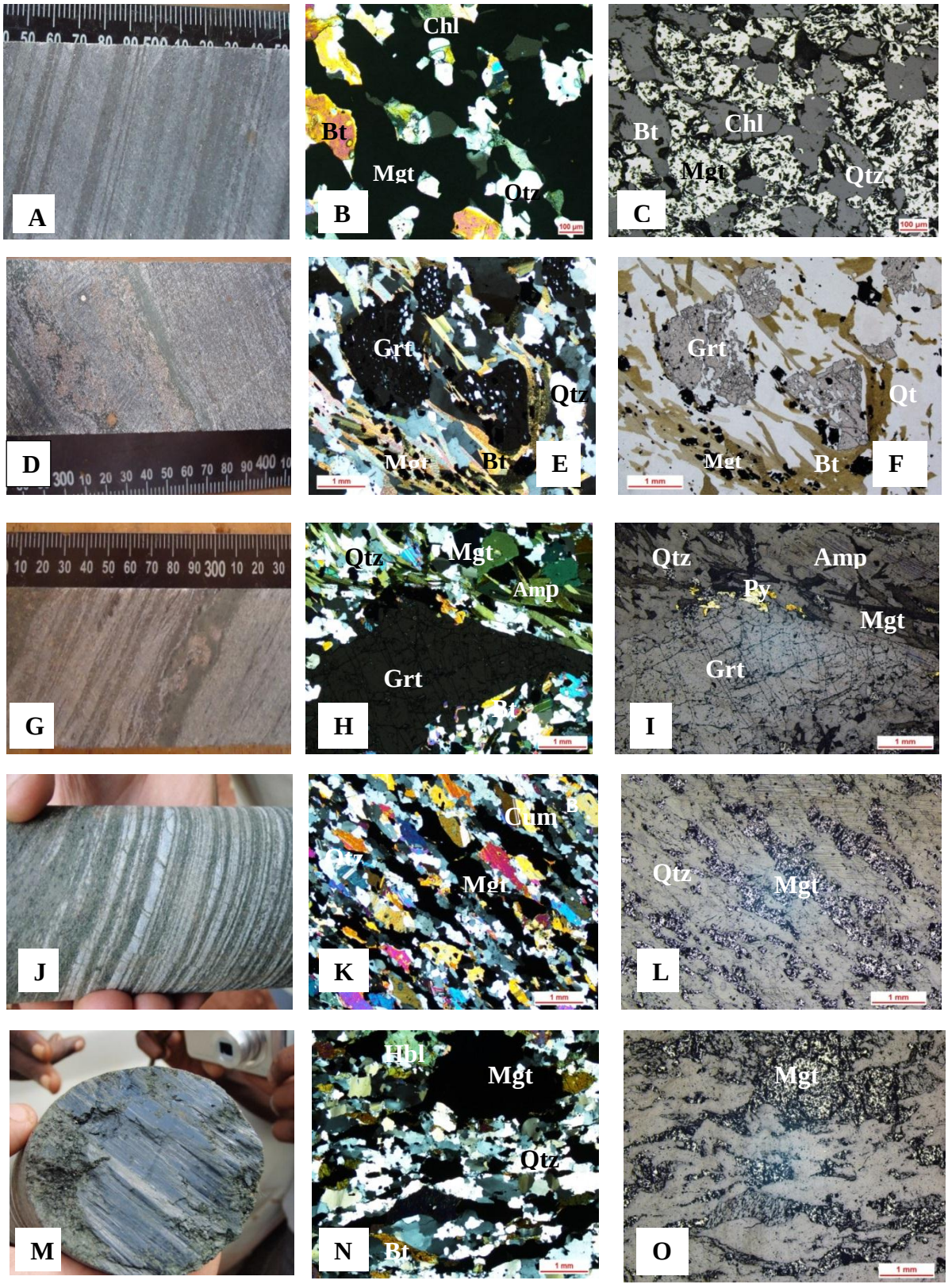

Bt: biotite, Hbl: hornblende, Qtz: quartz, Amp: amphibole, Cum: cumingtonite , Grt: garnet, Chl: chlorite, Mgt: magnetite, Py: pyrite.

Figure 10: Hand specimen and photomicrographs of BIFs: **A**. drillcore photo of Magnetite-rich BIF; B (plane polalised light PPL, C (Reflected light RL) photomicrograph showing granoblastic microstructure and mineral assemblage of magnetite- BIF; **D**. drillcore photo of garnet-biotite BIF; **E** (PPL), **F**(RL) **p**hotomicrograph, granoblastic microstructure and mineral assemblage of garnet-biotite BIF; **G**. drillcore photo of garnet-amphibolite BIF; **H**(PPL), **I** (RL) Photomicrograph, granoblastic microstructure and mineral assemblage of garnet-amphibolite BIF, **J, M**. drillcore photo of amphibole BIF; **K** (PPL), **L**(RL) Photomicrograph,

granoblastic microstructure and mineral assemblage of cummingtonite BIF and **N(**PPL**)**, **O(**RL**),** Photomicrograph, granoblastic microstructure and mineral assemblage of hornblende BIF.

Magnetite grains occur as interstitial aggregates in coarse-grained quartz and cummingtonite bands. Magnetite crystals are often associated with quartz, cummingtonite, and biotite. Cummingtonite BIF shows amphibolite grade mineral assemblage mainly consisting of quartz, cummingtonite, magnetite and biotite.

Quartz crystals occur as large subhedral to anhedral grains (0.02 - 0.24 mm), dominantly showing granoblastic texture (Figs. 10K and 10L). Most quartz grains are recrystallized, displaying wavy extinctions and exhibiting inequigranular texture (Fig. 10L).

They occur mainly as both aggregates and individual grain and exhibit interlocking grain boundaries. Quartz grains occur as interstitial aggregates in coarse-grained cummingtonite parallel to the long axis of mineral foliation. Their pronounced deformational features are indicative of dynamic recrystallization.

Biotite grains are partially transformed to chlorite with an average crystal size of 0.16mm and are associated with quartz, cummingtonite and magnetite.

Cummingtonite crystals in occur as large to small subhedral to anhedral grains (0.03 - 0.20 mm), dominantly showing granoblastic texture. They are the main components that occurs mainly as individual grains, associated with biotite, magnetite and quartz. They exhibit smooth curved grain boundaries showing elongated coarse to medium-grained crystals. The long axis of recrystallized cummingtonite aggregates defined a stretching lineation which is parallel to the direction of foliation.

Hornblende-rich BIF is a medium to coarse-grained foliated rock (Fig. 10M) composed of magnetite (25 - 30 %), quartz (20 - 30 %), hornblende (20 - 25 %) and biotite (10 - 15 %). This rock displays heterogranular and granoblastic microstructures (Fig. 10N and 10O).

Magnetite crystals occur in both magnetite-rich bands and quartz-rich bands as either individual grains or aggregates. They occur around quartz and other mafic minerals, and exhibit interlocking grain boundaries with other minerals that are smoothly curved (Fig. 10O). They occur as large subhedral to anhedral shape (0.05 - 0.55 mm), dominantly showing granoblastic texture. Fine magnetite grains (0.05 mm) occur as inclusions in quartz and biotite porphyroblasts.

Quartz grains are the main component in the hornblende-rich metamorphosed BIF, and show both aggregates with equiangular triple points. Quartz grains (0.01 - 0.15 mm) display undulose extinction and curved to smooth interlocking grain boundaries.

Biotite flakes occur in various dimensions (0.02 - 0.1 mm) and are anhedral to subhedral commonly showing granoblastic texture. Grain boundaries are straight to smooth curve with other minerals (Fig. 10N). Biotite is associated with quartz, magnetite and hornblende.

With an average grain size of 0.013 - 0.1 mm, hornblende crystals are subhedral. They exhibit interlocking grain boundaries at contacts between neighbouring minerals (quartz and magnetite).

Hornblende-rich metamorphosed BIF is an amphibolite facies metamorphic grade which consists of mineral assemblage mainly made up of magnetite, quartz, biotite and hornblende.

III.1.2.3 ORE TYPES

Nkout iron ore can be broadly divided in to five field categories namely lateritic (indurated) ore type, goethite-martite (soft) ore type, haematite in breccias (brecciated) ore type, Magnetite/haematite (massive) ore type and quartz/magnetite (hard laminated) metamorphosed BIF.

III.1.2.3.1 Laterite ore type

Laterite ore type is found mostly at the surface of the study area. It blankets the iron ore deposit and occurs in 5 to 15 m thickness from surface. It is the weathering and erosion products of earlier formed laminated and massive ores which contained hard to friable material in nature. Laterite ore is reddish brown to brownish iron oxides~~,~~ composed mainly of goethite (Fig. 11A).

III. 1.2.3.2 Goethite ore type

The most important ore in Nkout is the laminated (vuggy) ore in the weathering zone and which is formed by the removal of gangue minerals. This ore type is soft laminated ore. Individual lamellae measure from a few millimeters to centimeters in thickness and is highly porous and fragile (Fig. 11B).

III. 1.2.3.3 Haematite in breccias type

The Nkout deposit hosts fault breccias and fault related hydrothermal breccias that are characterized by fine haematite and medium to coarse-grained structure (Fig. 11C). This ore type is moderately porous and permeable. The possibilities for the origin could either be (i) Lump breccia of un-oxidized haematite metamorphosed BIF that underwent mechanical fracture and transportation into the zone of high oxidation with a “powdery” iron oxide that consolidated them; (ii) The metamorphosed BIF might have occurred at fault zone, thus representing a fault breccia (Fig. 11C).

Figure 11: Field photographs of Nkout drill core showing: (A) ferrigenous lateritic ore (indurated); (B) haematite-quartz with preserved banding (Friable soft); (C) quartz-haematite Breccia (fault breccias).

III. 1.2.3.4 Magnetite/haematite ore type

Magnetite/ haematite ore is massive, compact and dense with packed haematite minerals and appear to be the precursor of martite ore. The ore is generally dark grey iron (Figs. 12DandE). In this type of ore, haematite crystals are fine grained and tightly packed forming a compact mass (Fig. 12E).

III.1.2.3.5 Quartz/magnetite ore type

The high-grade iron ore in Nkout is hosted in quartz-martite (i.e., haematite pseudomorphs after magnetite) metamorphosed BIF. The un-oxidized metamorphosed BIF is observed below the weathering front, characterized by alternating bands/laminations with quartz. The thickness of an individual band, however, varies between few millimeters and 10 cm and does not extend more than 30 m before they pinch and merge with other bands (Fig. 12F-J).

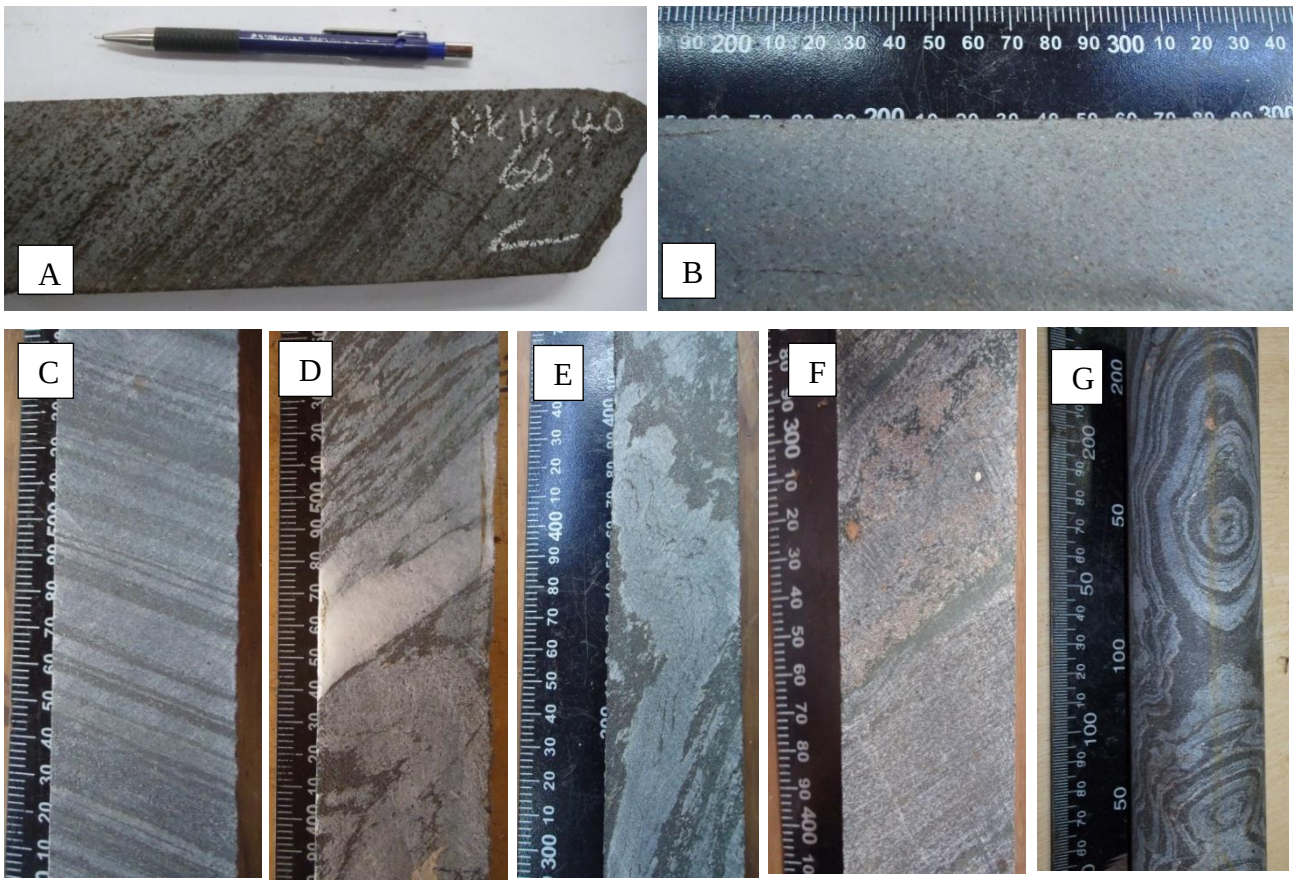

Figure 12: Field photographs of Nkout drill core showing: (A) magnetite-quartz ore, enrichment as a result leaching of gangue mineral (biscuity); (B) haematite ore (massive, without visible banding developed); (C) compositional laminated BIF; (D) distorted band quartzite intercalation; (E) irregular banded BIF bearing amphibole; (F) diffused banding bearing garnet; (G) folded magnetite BIF.

III.2 LITHOSTRATIGRAPHY

This section presents the lithostratigraphy of Nkout BIF deposit. It is subdivided into three main prospects, Nkout East, Nkout Centre, and Nkout West (Fig. 7B). The detail logging of 9 boreholes enabled us to identify all the mappable members and units of the entire Nkout BIF deposit (Fig. 13). The members are (i) metamorphosed banded iron formation (BIF) and (ii) gneissic country rock or gneissic member. These units are distinguished by the mineral abundance and metamorphic grade. The banded iron formation dips approximately 50 to 65° to the north, while gneissic formations display a sharp transition to gradational contact with the iron-rich member, and forms both footwall and hanging wall in the deposit. The gneissic member is typically foliated and directly in association with the banded iron formation member in the stratigraphy.

III.2.1. NKOUT WEST AREA

This section is based on the results of three representative drilled holes (WH3, WH4, WH8) selected from 52 completed diamond drilled holes at Nkout West prospect (Fig. 13). The depths of the different holes are 459m, 527m, 80m respectively for WH3, WH4, and WH8.

III.2.1.1 Banded Iron formation member

The iron formation member has different thicknesses that vary from one hole to another. The first interception of iron formation is located at depth of 85m below surface. The total thicknesses along section vary between 85-467 m and 111-510 m (WH3, WH4), with the largest thickness being approximately 400 m (Fig. 14A). These formations were subjected to various metamorphic grades (greenschist to amphibolite facies). It is composed of three lithological units on the mineral abundance basis. These units include magnetite-bearing iron unit, garnet and biotite-bearing iron unit, and garnet and amphibole-bearing iron unit.

The magnetite-bearing iron unit is distinguished from the other units by the magnetite abundance. It is found at sharp hanging wall contact with biotite-bearing gneiss unit and has an overall thickness of 236 m. The magnetite-bearing iron unit is coarse to medium-grained, with limited lateral extension and composed mainly of quartz, iron oxide (magnetite, haematite) and chlorite. It is a low grade (greenschist) metamorphic unit.

The garnet and biotite-bearing iron unit is rich in biotite and garnet. It is a medium to coarse-grained rock unit (dark grey in colour and located at various depths of the deposit's stratigraphy).This unit lies between the magnetite-bearing unit and garnet and amphibole-bearing metamorphosed BIF unit at various intervals. This unit is found at the footwall contact which is made up of garnet and biotite-bearing gneiss of the gneissic member. It is in sharp contact with the biotite-bearing gneiss at the bottom of the iron-member.

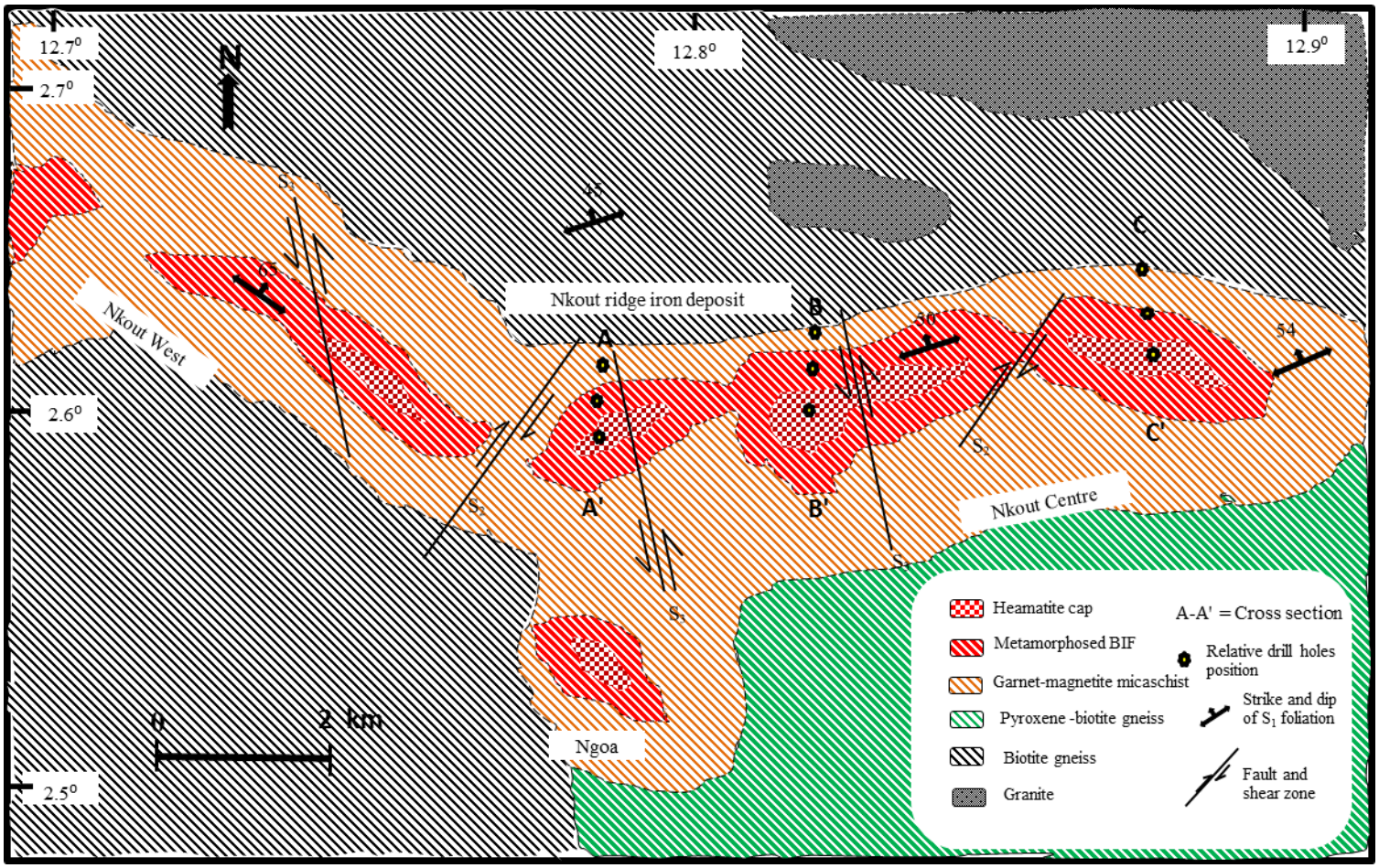

Figure 13: Local geological map of Nkout study area

.

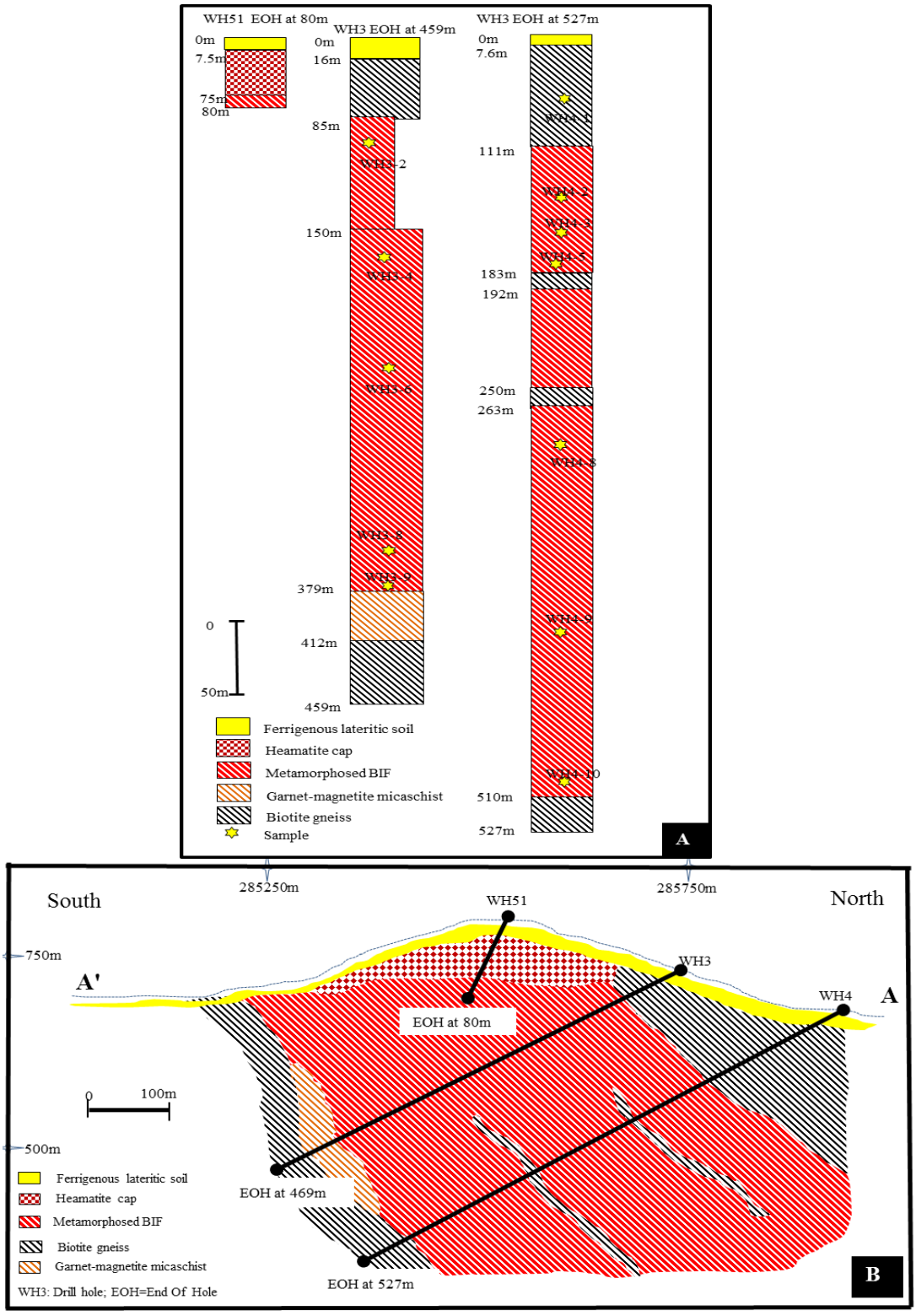

Figure 14: **A)** Stratigraphy log of Nkout-West deposit A-A' in Fig. 13) with sample location; B) Geological S-N (dip) cross-section (A-A' in Fig. 13) of Nkout-west deposit (looking west)

Garnet-amphibole-bearing iron unit and amphibole-bearing iron unit are found at the contact of the footwall of gneissic members. They are medium to coarse-grained rocks, dark grey in colour. They show foliation similar to that of garnet and biotite iron unit. These units are overlaid by the garnet and biotite-bearing unit with a sharp contact.

III.2.1.2 Gneissic formation member

Gneiss at the hanging wall was intercepted just below the lateritic surface (at varying depths of 5 to 16 m) while the footwall contacts were intercepted at 412 m and 510 m respectively at different holes (WH3, WH4). Minor intercalations (1 to 5m) were intercepted at various depths, 250 m and 390 m. The total gneissic formation thicknesses along the section vary between 85 m and 111 m (WH3, WH4), with the largest thickness being ~120 m (Fig. 14A). The gneissic formation member is composed of three main units (biotite-bearing gneiss unit, garnet-magnetite-bearing gneiss unit and garnet-bearing gneiss unit).

The biotite-bearing gneiss unit is medium to coarse-grained foliated rock unit and generally leucocratic. It forms sharp contacts between the iron-rich members, occupying both footwall and hanging wall contacts. It is overlain by lateritic layer at the upper layer and is underlain by magnetite-rich iron unit of the lower layer in the stratigraphy.

This unit occupies a total depth of 110 m in the stratigraphy and is intercepted at the interval depths ranging from 7.6 m to 111 m, 192 m to 200 m, and 510 m to 527m. The mineral assemblage is mainly made up of biotite, quartz, feldspars, which is consistent with medium amphibolite facies metamorphism.

Garnet-magnetite-bearing micaschist unit is medium to coarse-grained rock unit, characterising a transitional boundary between the iron-rich member and the biotite-rich gneiss unit on the footwall sharp contact. It is intercepted at depths of 379 m to 412 m, occupying a total interval of 32 m in the stratigraphic column and is sandwiched between the garnet-biotite iron unit and the biotite-rich gneissic unit.

The garnet-bearing gneiss is in sharp contact between the iron-rich members and occupies the footwall of the deposit. This unit is medium to coarse-grained, with gneissic foliation characterised with alternation of grey and dark bands.

The stratigraphic relationship between the iron-rich member and the country rock (gneiss) lithology is shown on the lithostratigraphic section (Fig. 14A). It lies within the Nkout-West prospect and on the AA cross section (Fig. 14B).

III.2.2 NKOUT CENTRE AREA

This section is based on the results of three representative drilled holes (CH24, CH7 and CH4) selected from 110 completed diamond drilled holes at Nkout Centre. The depths of the

different holes are 440m, 540m, 80m respectively (Fig. 15A). Figure 15B presents the Nkout Centre lithological section (BB' cross-section in Fig. 13).

III.2.2.1 Banded Iron formation member (BIF)

The iron member of Nkout Centre area shows different thicknesses. It was initially intercepted at the depths of 76 m below surface on CH7 and 112 m on CH24. The total iron formation thicknesses across-section varies between 85 - 390 m and 112-400 m respectively, with the largest thickness being approximately ~400 m (Fig. 15A). Three litho-assemblage units, magnetite-bearing iron unit, garnet-biotite-bearing iron unit, garnet-amphibole-bearing iron unit were observed.

The magnetite-bearing iron has the similar lithological characteristics to that of the West prospect. It is found at sharp hanging wall contact with biotite-bearing gneiss unit and has an overall thickness of 227 m. The garnet-amphibole-bearing iron unit is the least extended of all the iron-rich units of the Nkout Centre prospect. It displays a fairly consistent pattern of an increased metamorphic grade and is found at depths of 228m in drill hole CH7 and 252 m in drill hole CH24. The garnet-amphibole-bearing iron unit lies between biotite-bearing gneiss of the gneissic member. It is found at the contact of the footwall of gneissic members in drill hole CH7. It is a medium to coarse-grained foliated rock, dark grey in colour. This unit is intercalated between biotite-bearing gneissic units with a sharp contact in drill hole CH24.

III.2.2.2 Gneissic formation member

Hanging wall gneissic formation member displays sharp contacts with the iron-rich member, which was intercepted below the lateritic surface (at varying depths of 10 m to 20 m), while the footwall contacts are intercepted at 390 m and 400 m respectively. Minor intercalations (1 m to 10 m) were intercepted at various depths. The total thicknesses along section vary between 220 m and 265 m, with the largest thickness being approximately ~265m (Fig. 15A).

This member is composed of the biotite-bearing gneiss unit, garnet and magnetite-bearing gneiss unit and pyroxene and biotite-bearing gneiss unit. The biotite-bearing gneiss unit is characterised by the hanging wall in sharp contact between the iron-rich members.

This unit is overlain by a lateritic layer which in turn is underlain by magnetite-bearing iron unit. It occupies a total depth of 70 m to 100 m respectively and was intercepted at different depths intervals that vary in the drill hole. The garnet and magnetite-bearing micaschist unit characterized transitional and gradational boundaries between the magnetite-bearing iron unit and the pyroxene and biotite-bearing gneiss unit at the footwall. This unit shows compositional banding marked by magnetite and garnet layer and quartz-rich layer. It is intercepted at depths of 405 m to 503 m, occupying a total interval of 98 m in the stratigraphic column.

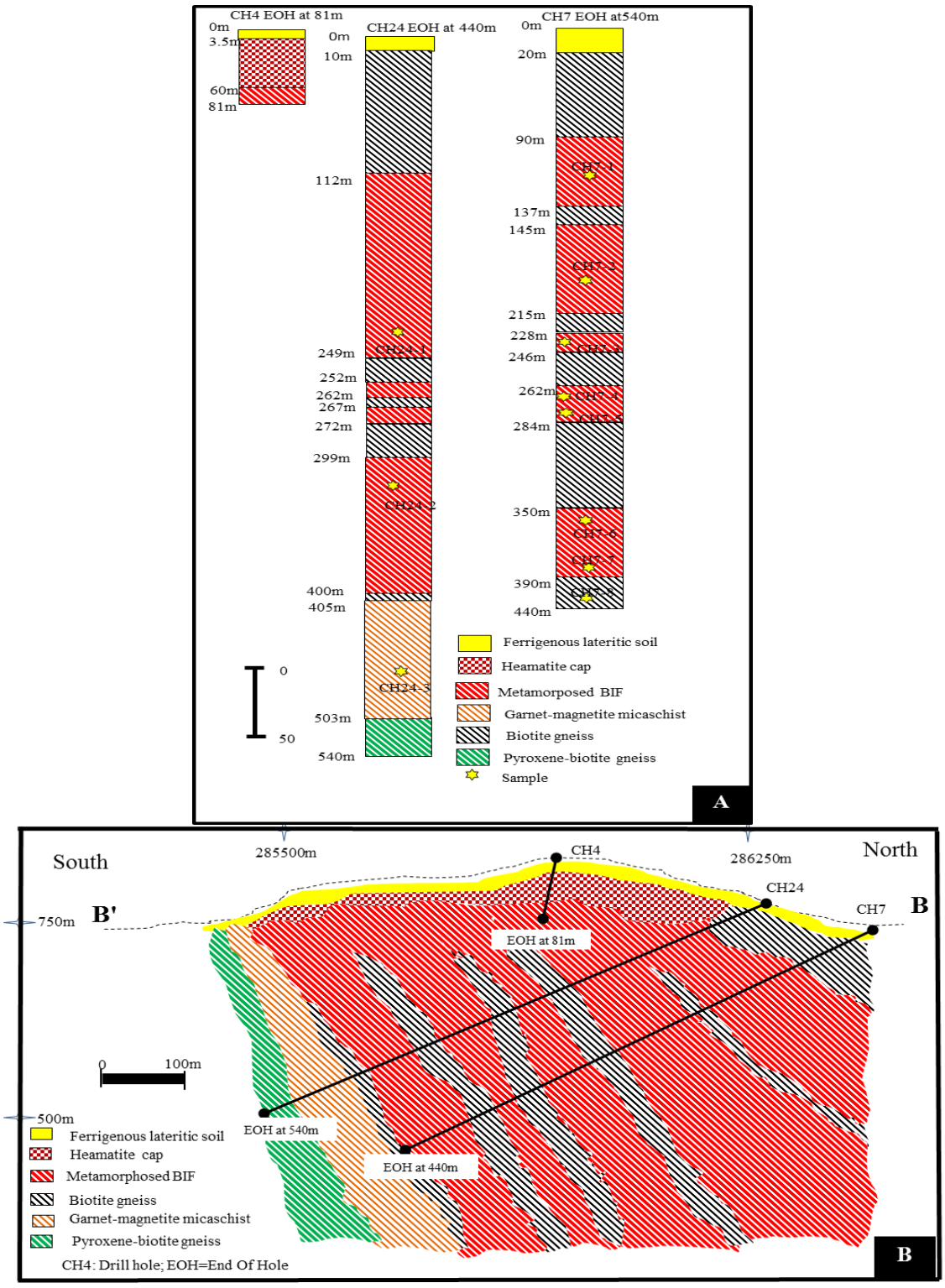

Figure 15: Stratigraphy log of Nkout-Centre deposit A) Stratigraphy log of Nkout-Centre deposit (Centre B-B' in Fig.13) with sample location; B) Geological S-N (dip) cross-section (B-B' in Fig. 13) of Nkout-Centre deposit (looking west)

The pyroxene-biotite-bearing gneiss unit is in sharp contacts between the garnet and magnetic unit and characterised the footwall of the deposit. It is medium to coarse-grained rock unit, with gneissic foliation characterised by the alternation of grey and dark bands. It was intercepted at depths of 503 m to 540 m, making a total interval of 37m. The stratigraphic relationship between the hanging and footwalls country rock (gneiss) and the iron-rich member lithology is shown on the lithostratigraphic section (Fig. 15A) and on the BB cross section (Fig. 15B, Fig. 13).

III.2.3. NKOUT EAST AREA

Three representative drill holes (EH2, EH4, and EH7) with depths of 305 m, 565 m and 120 m respectively, were selected from about 200 completed diamond drilled holes at Nkout East prospect (Fig. 16). Detailed logs of these drill holes revealed that the Nkout East prospect has two iron-rich units (magnetite-bearing iron unit and amphibole-bearing iron unit) and three gneissic units.

III.2.3.1Banded Iron formation member (BIF)

The first interception of iron formation is located at depth of 62 m below surface (EH2). The total iron formation thicknesses across-section vary between 62 to 152 m and 234 to 389 m (EH2, EH4), with the largest thickness being approximately ~150 m (Fig. 16A).

The magnetite-bearing iron units are found at sharp hanging wall contact with biotite-bearing gneiss unit and have an overall thickness of ~80 m. The amphibole-bearing iron units are found at the contact of the footwall of biotite-bearing gneiss unit. This unit is overlaid by biotite-bearing gneiss unit with a sharp contact.

III.2.3.2 Gneissic formation member

The interception of gneiss formation at the hanging wall is located just below the lateritic surface (at varying depths of 14 m to 57 m). The footwall contacts are intercepted at 152 m and 420 m respectively (EH4 and EH2). Minor intercalations (1 m to 10 m) were intercepted at various depths, 90m, and 259m. The total gneissic formation thicknesses along section vary between 68m and 270m, with the largest thickness being ~270 m (Fig. 16A). The Nkout East lithological section is shown on the figure 16B (CC cross-section on figure 13).

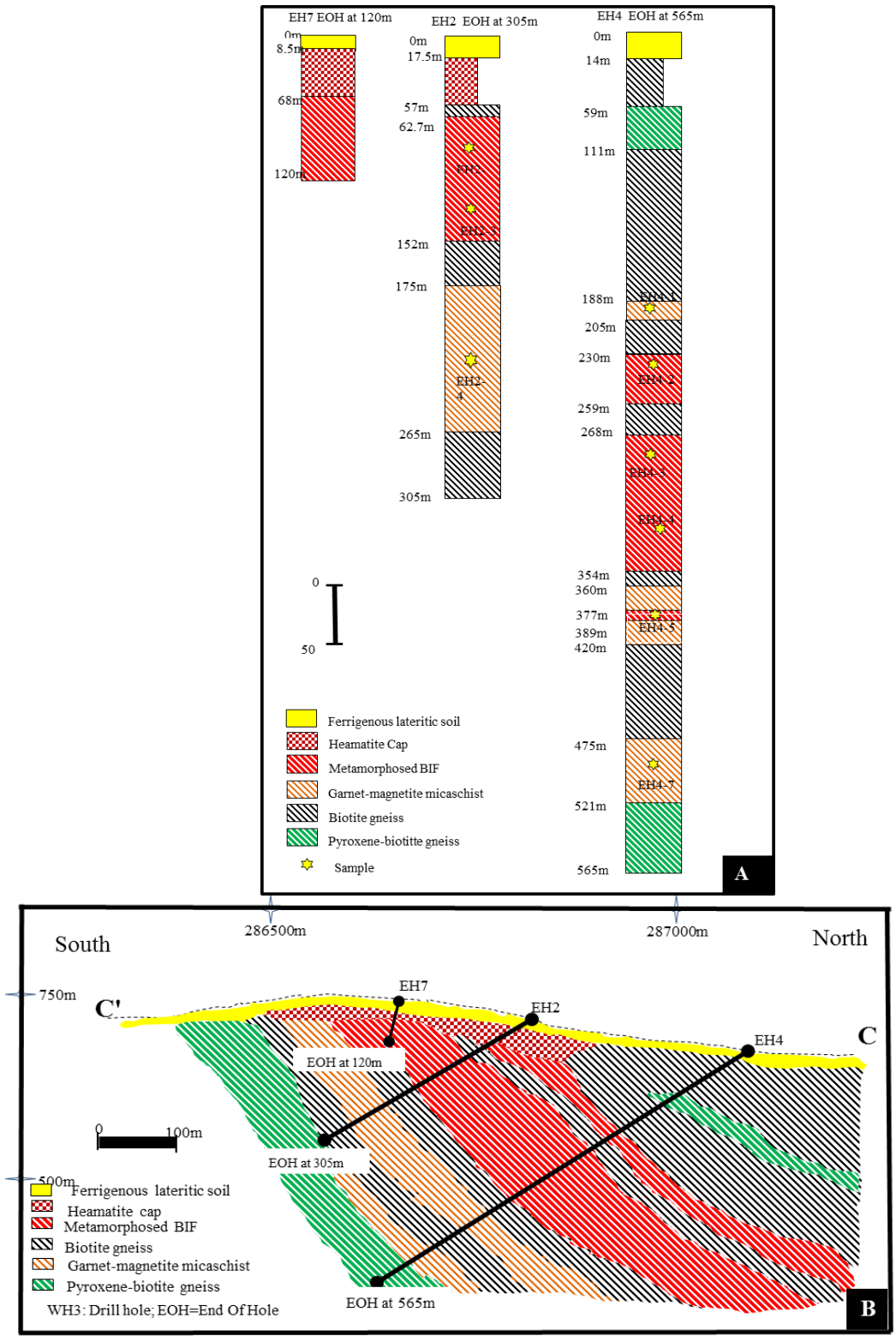

Figure 16: A. Stratigraphy log of Nkout-East deposit (C-C' in Fig. 13 with sample location; B) Geological S-N (dip) cross-section (C-C' in Fig. 13) of Nkout-East deposit (looking west)

CONCLUSION

The petrographical study reveals and confirms both field magmatic and metamorphic units. The magmatic unit consists of granitoid rocks as the most abundant plutonic rocks. The metamorphic unit consists of gneissic country rocks and banded iron formation (BIF). The petrographic studies have permitted us to show the different lithologies, therefore their characteristic are summarised in the table below.

Table 2: Mineral association and main petrographic characteristics of Nkout formation

Lithology	Rock type	Associated mineral	Microstructure	Metamorphic grade
Magmatic unit	Biotite granite	Pl + Kfs + Bt + Qtz ± Px	Heterogranular	
	Amphibole granite	Pl + Kfs + Qtz + Bt + Amp ± Px	Heterogranular	
Metamorphic unit	Biotite gneiss	Kfs + Qtz + Bt + Pl + Mgt	Heterogranular granoblastic	Amphibolite facies
	Garnet-magnetite micaschist	Grt + Qtz + Bt + Mgt± Chl	Heterogranular granoblastic	Amphibolite facies
	Garnet-biotite gneiss	Grt + Qtz + Bt + Kfs ± Mgt	Heterogranular granoblastic	Amphibolite facies
	Pyroxene-biotite gneiss	Pl + Bt +Kfs + Qtz ± Px	Heterogranular granoblastic	Amphibolite facies
	Magnetite-rich BIF	Mgt + Qtz + Bt + Chl	Heterogranular granoblastic	Greenschist facies
	Garnet-biotite BIF	Grt + Qtz + Bt + Mgt ± Chl	Heterogranular granoblastic	Amphibolite facies
	Garnet-amphibole BIF	Grt + Amp + Qtz+ Mgt + Bt ± Py	Heterogranular granoblastic	Amphibolite facies
	Amphibole BIF	Mgt + Qtz + Bt + Cum ± Hbl	Heterogranular granoblastic	Amphibolite facies
	Massive haematite ore	Hem + Mgt + Qtz ± Gib ± Goe	Haematite rich.(haematite >> quartz with no banding, poor porosity and permeability, medium grained	
	Quartz/magnetite ore	Qtz + Hem + Mgt	Quartz ~ haematite and magnetite distinct banding, low porosity and permeability, medium-grained	
	Goethite ore	Hem + Mgt + Goe + Gib + Qtz	Quartz + haematite, diffused banding, porosity, and permeability medium-grained	
	Laterite ore	Hem + Qtz + Mgt ± Goe	Iron oxides ± haematite, high porosity and permeable , medium-grained	
	Haematite in breccias ore	Hem + Qtz + Mgt ± Goe	Fault brecciated, high porosity and permeable, medium-grained	

Amp: amphibole, Bt: biotite, Chl: chlorite, Cum: cummingtonite, Hbl: hornblende, Hem: haematite, Grt: garnet, Gib: gibbsite, Goe: Goethite, Kfs: potassium feldspar, Mgt: magnetite, Pl: plagioclase; Pl: plagioclase; Px: pyroxene, Py: pyrite, Qtz: quartz;

The mineral association of both magmatic and metamorphic assemblages are identified. This indicates that they evolved under the same metamorphic condition and were probably generated for the same protolith. The geochemical characteristics will verify this hypothesis.

The metamorphic mineral assemblages of the different petrographic type correspond to following: amphibolite facies for amphibole BIF, garnet-amphibole BIF and garnet-biotite BIF all the gneissic rock, except magnetite BIF which greenschist facies.

From the detailed litho-stratigraphic section in the chapter, certain generalisation could be made from the stratigraphy point of view. The footwall and the hanging walls are made up of gneiss intercalated with BIF.

CHAPTER IV. STRUCTURAL ANALYSIS

INTRODUCTION

This chapter deals with the analysis and description of the different structural features that have been recorded in the different rock types of the Nkout area. The detail geometric, kinematics and chronology of the structures allowed us to recognize four different phases of deformation, the first three ((D_1**,** D_2 and D_3**)** been ductile and associated with metamorphic recrystallization while the last (D_4) been the brittle phase.

The structural elements in the studied area are planer structures (foliation, schistosity, shear and fault planes), and folded structures (folds). This study is therefore our best contribution to the knowledge of the different structural configuration in the area, which may permit us to integrate the tectonic evolution in the Congo Craton.

The folds of different generations were formed due to different phases of deformation. Superposed folding has given rise to different morphologies of the folded surface, which were classified into three broad classes of Ramsay (1967). In the studied area we have observed two types of superposed folds.

IV.1 MACROSCOPIC STRUCTURAL ELEMENT IN METAMORPHIC UNIT

Rocks in the Nkout area were subjected to polyphase deformation. These involve metamorphic rocks (BIF and gneiss) with three ductile deformation events (D_1 - D_3) and a later brittle (D_4) event. Foliation is the most prominent planar structure within the metamorphic units, over which the later major and minor folds of different generations were developed. They are made up of layering and preferred orientation of mineral (schistosity).

IV.1.1 D_1 DEFORMATION EVENT

The D_1 phase is associated with the development of S_1 foliation, and F_1 folds in BIFs and gneissic rocks.

IV.1.1.1 Planar structure

IV.1.1.1.1 S_1 Foliation

The S_1 is here interpreted to be the dominant primary fabric characterised by layer in outcrop, resulting in the transposition of primary bedding plane (S_0) of BIFs.

It is characterized in BIFs with banding or layering (alternation of dark and light layers) and preferred orientation of minerals (Figs. 17A-C). These minerals are haematite, magnetite, garnet, amphibole, quartz, feldspars, pyroxene in BIFs and gneiss.

The S_1 foliation plane marked by layering and preferred mineral orientation strikes roughly N55-70°E with gentle dips (10-70°) in BIFs and a moderate dips (45-55°) in gneiss mainly to the NW. The S_1 foliation marked by layering and schistosity was observed locally in BIFs (Figs. 17G and H). The S_1 schistosity is underlined by the disposition of preferred orientation of quartz and magnetite.

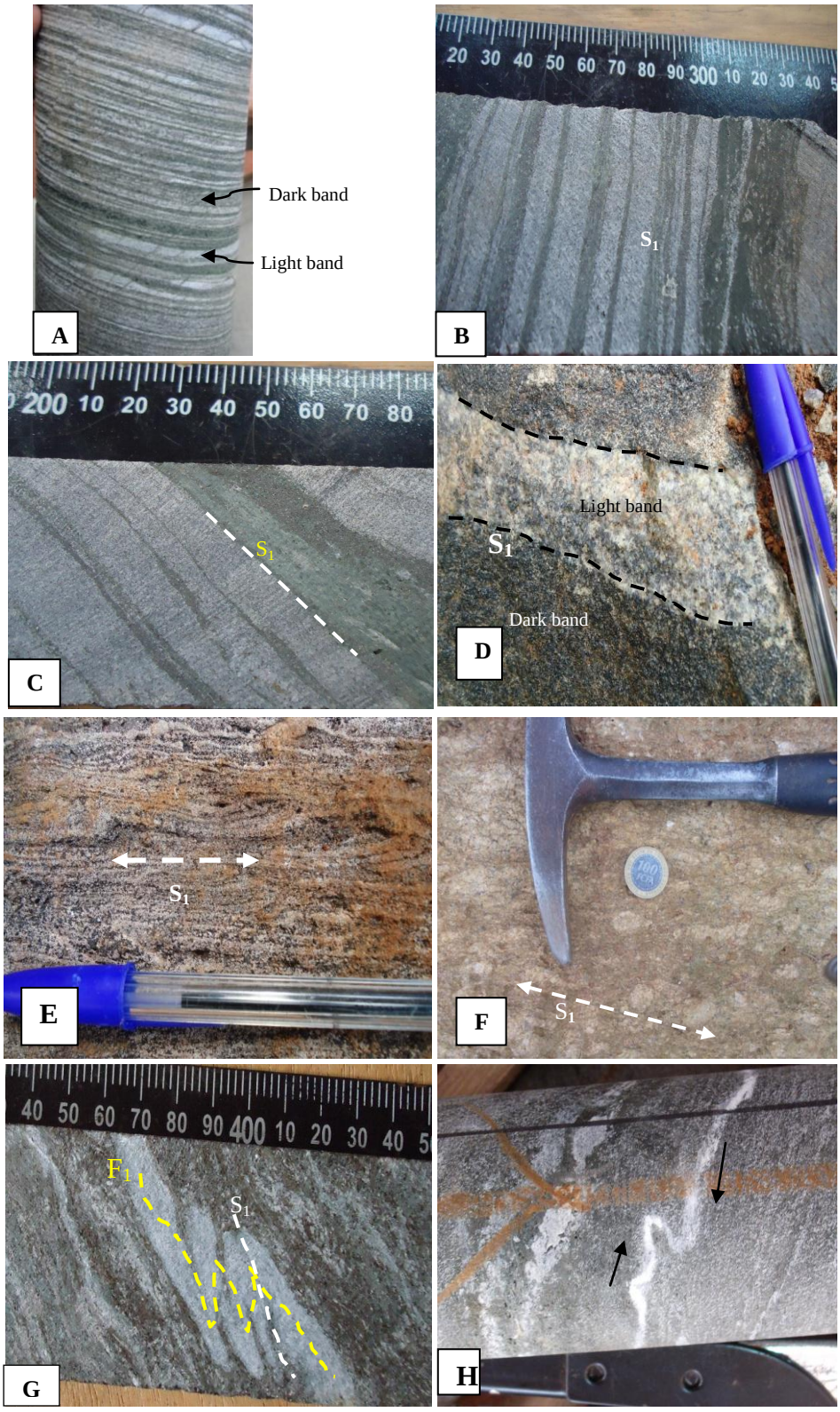

Figure 17: Field view of D_1 structural elements, gneiss and BIF with lithological banding and compositional banding (A ,B and C): S_1 banding or layering in BIF (D) S_1 banding or layering banding in gneiss (E) S_1 banding or layering in BIF (F) preferred orientation of quartz in gneiss (G,H) F_1 fold in BIFs and Gneiss.

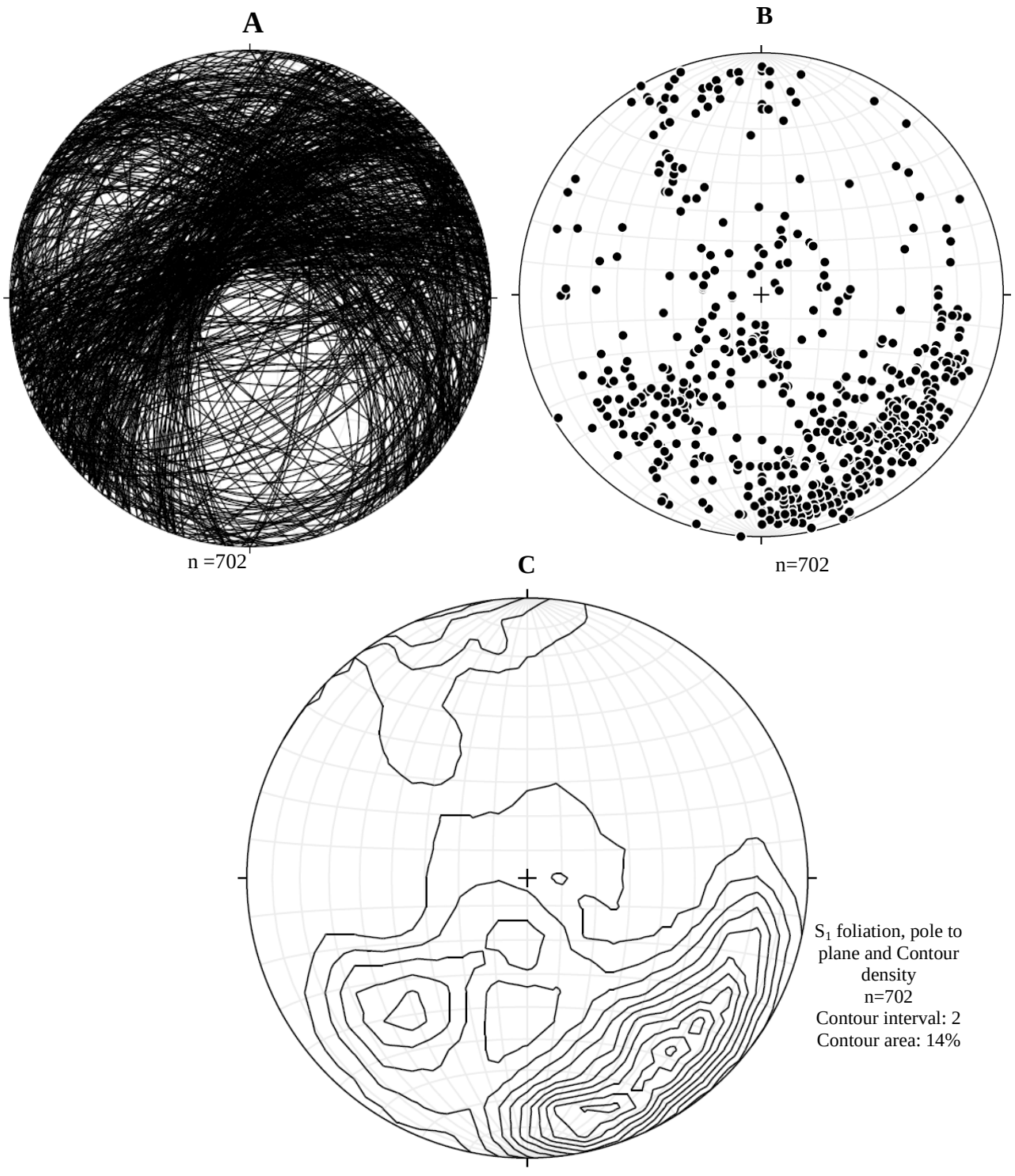

Figure 18: Stereographic projection of S_1 foliation. A) Plane B) Pole and C) Contour in Nkout area

The S_1 planes stereographic projection of layering and schistosity show variable spatial orientations throughout the study area (Fig. 18).

In the regional scale, the Nkout area shows asymmetric poles to S_1 planes confirming that the planes generally strike NE-SW, NW-SE and dip to the NW/NE.

IV.1.1.2 F_1 Folding

Minor F_1 isoclinal folds have been developed during the D_1 event **(**Figs. 17G-H). The F_1 folding is marked by quartz folding. They are asymmetric and isoclinal tight fold in BIFs. The folds show S_1 schistosity which strikes N55-70°E with gentle dips (10-70°) to the NW (Fig. 17G and H).

CONCLUSION

In conclusion, the D_1 deformation event is made up of S_1 foliation marked by banding and preferred orientation of minerals (schistosity) and fold F_1.

The S_1 foliation is characterised by layering and preferred orientation of minerals. The minerals that underline the S_1 schistosity are haematite, magnetite, garnet, amphibole, quartz in BIF and feldspars, pyroxene in gneiss. This foliation shows an average NE-SW/NW-SE direction which dip to the NW. The poles to S_1 foliations show that the D_1 formation event was associated with the NE-SW NW-SE tectonic movement. The F_1 folding is characterised by quartz folding in gneiss.

IV.1.2 D_2 DEFORMATION EVENT

The later D_2 deformation is accompanied by the development of (i) F_2 folds, (ii) planar structure (S_2 axial planar schistosity and C_2 shear plane), and with minor fault sets.

IV.1.2.1 F_2 Folding

The F_2 folding is marked by inclined similar folds verging towards north, which collectively forms a major inclined and overturned fold that defines the shape of the deposit. Two sub-generations were distinguished.

The earliest fold (first-generation F_{2a}) structure is marked by asymmetric close to tight isoclinal folds with E-W striking axial planes, dipping to the north (Fig. 19A). The first order antiformal E-W fold axis plunge to the W at a sub-horizontal to low angles plunge direction.

The late fold (second generated F_{2b}) is marked by asymmetric open to tight folds with N-S, NW-SE axial plan S_2 schistosity. The second order antiformal and synformal N-S to SE-NW fold appears as recumbent to upright, asymmetrical open to tight folds in profile with their wavelength ranging between few centi-meters to tens of meters (Fig. 19B-C). These folds show a northwest-plunging fold axis, sub-vertical to steeply-dipping axial plane. The fold axial plane strikes N90-170°E and dips 40-88° to the NE.

In the Ngoa hill, the NNE-SSW strike F_2 folds show asymmetrical shape, unequal limbs of dip angles which partly characterize the recumbent asymmetric folds. The long and short limbs are tilted in the clockwise direction and the thickness was the same with the width of the hinge. The fold axial-plane strikes N15-30ºE and dips 60-65° to the NW (dip direction being 286°). The F_2 folds also show NW steeped dipping (70° to 80°) S_2 axial-planar foliation (Fig. 19).

IV.1.2.2 Planar structure

The later D_2 deformation is accompanied by the development of S_2 axial planar schistosity and C_2 shearing.

IV.1.2.2.1 S_2 Schistosity

S_2 foliation is an axial plane schistosity marked by preferred orientation of quartz and iron mineral along the F_2 fold axial plane in BIFs. The S_2 schistosity roughly strikes N-S to SE-NW and shows vertical to steep westerly dipping (Figs. 19A-C).

The first order axial plane schistosity of the antiformal E-W fold strike N60-70°E and dip (70 to 80°) to the N.

The second order axial plane schistosity S_2 of the antiformal and synformal N-S to SE-NW fold strike N90-170°E and dips 40-88° to the NE.

IV.1.2.2.2 C_2 Shearing

The C_2 shear planes are marked by discontinuous planes that truncate the S_1 foliation in BIFs (Figs. 19D-E). These C_2 planes are parallel to the S_2 axial plane schistosity of the F_2 folds, with both dextral and sinistral shear movement (Figs. 19F-G).

They strike N-S and NW-SE with vertical to steep westerly dipping. Drill core of the study area, revealed both asymmetric forms of Z-shaped and S-shaped drag folds.

The high clockwise rotation that constructed the Z-shaped drag fold reflects a right-handed shear, specifically a dextral displacement and S-shaped drag fold reflects a left-handed shear showing sinistral movement.

Other features associated with C_2 shearing in mylonitized BIFs include strain-slip, which appears as a single deformation that led to the enhancement of flattening and shearing of the BIF layering.

The strain-slip structures are commonly observed in mylonitized BIFs. In the shear band, the mineral grains are much finer than the mineral grains outside of the shear band (showing grain size reduction**,** Figs. 19H and I). Moderately foliated BIF locally contain such mylonitic zones defined both quartz and magnetite grain size reduction (Figs. 19H and I). A strongly mylonitized BIF with an incipient S_2 mylonitic foliation is indicative with extremely reduction in fine grain size. The result of "pulverization" occurred during strain slip (Figs. 19H and I).

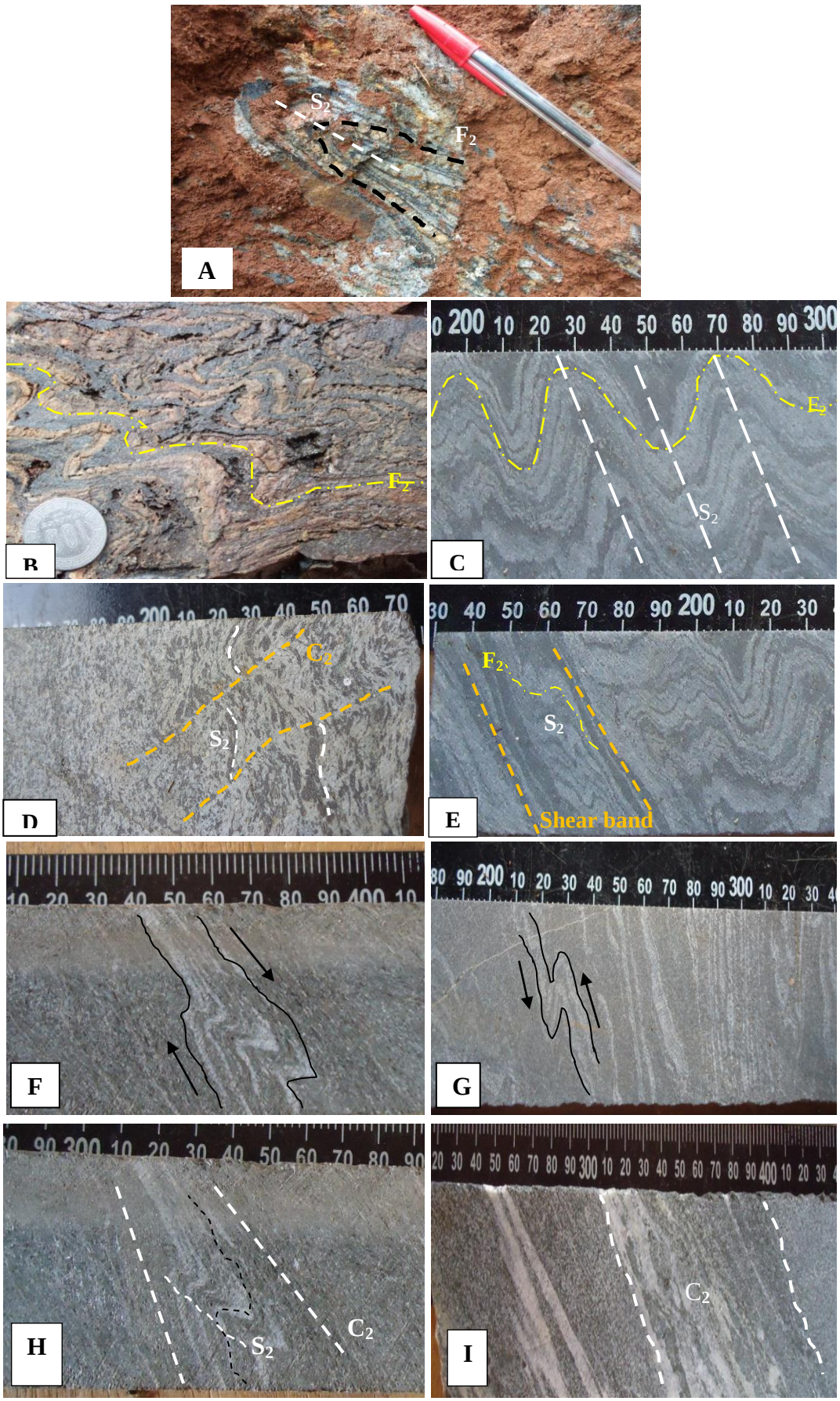

Figure 19: Field view of D_2 structural elements in BIFs; (A, B and C) F_2 folding and related S_2 schistosity in BIFs, (D) C_2 Strain-slip (F and G) dextral and sinistral shear movement (H and I) shear band showing grain size reduction.

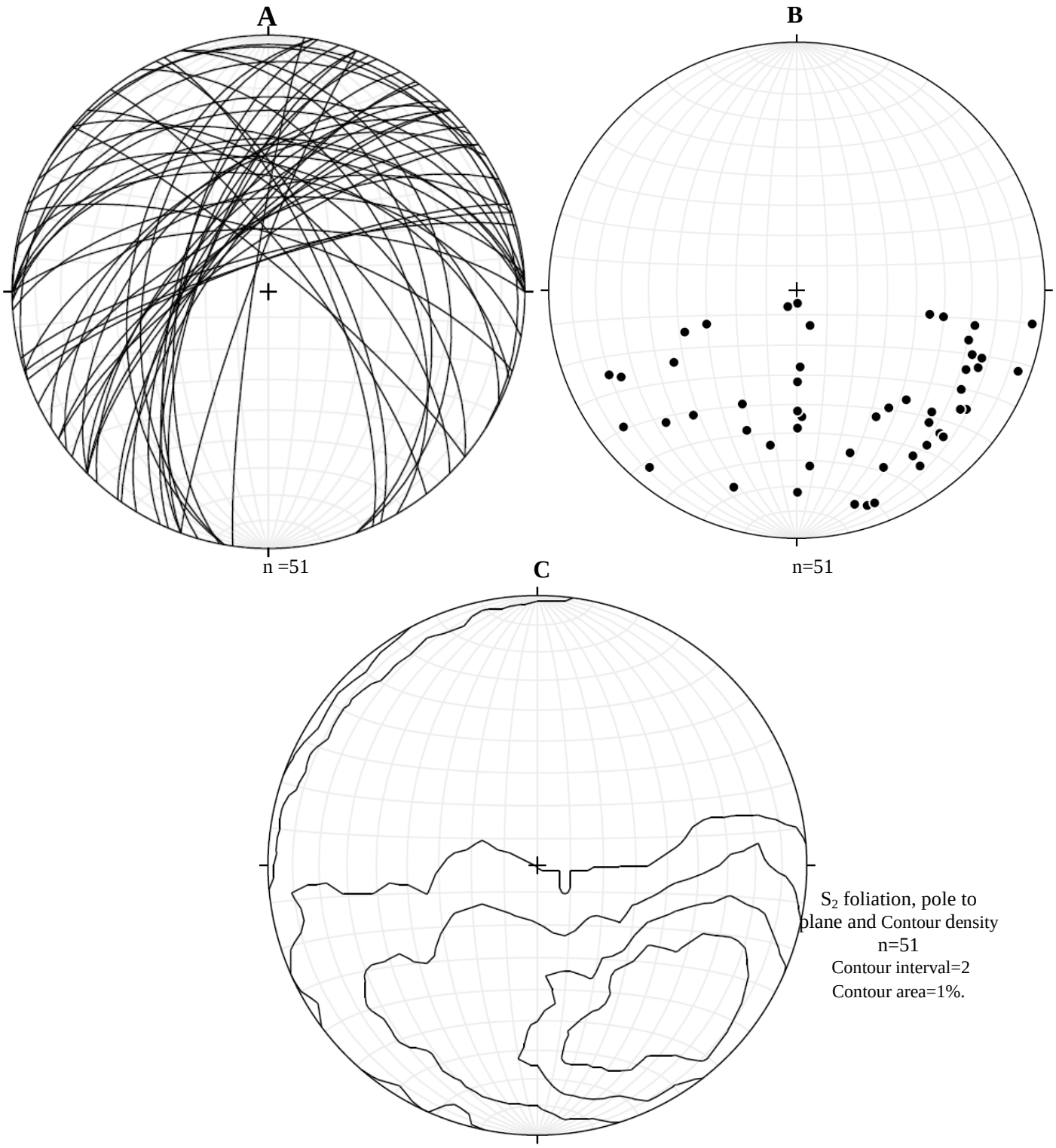

Figure 20: Stereographic projection of S_2 foliation in study area A) plane, B) pole and C) contour

The sets of shear bands in the BIFs have developed the subparallel bands to boundaries of shear band zone which are subparallel to foliation surfaces (Fig. 19H). Hence, the oblique nature directly reflects the orientation of the strain ellipsoid, making the fabrics a reliable shear sense indicator in the BIFs. Based on the strain-slip, both sinistral and dextral sense of shear is apparent (Figs. 19F and G). They indicate shear displacement in N-S trending strike-slip shear zones.

The stereographic diagram of the D_2 deformation phase was constructed with the aim of obtaining the major specific orientation of the S_2 surfaces.

The Nkout study (Fig. 20A) shows a symmetric display of the poles to S_2 axial plane schistosity. The plotted poles to plane indicate either NW-SE to NE-SW striking S_2 surface, and dips oriented between NE and NW.

CONCLUSION

The D_2 deformation event is made up of planar structure characterised by the development of S_2 schistosity and C_2 shearing. The S_2 axial plane schistosity of the F_2 fold, the C_2 planes are parallel to the S_2 axial plane schistosity. C_2 shearing planes show both dextral and sinistral shear movements. This confirms the asymmetrical drag fold. Within the D_2 structural elements, the F_2 fold structures are the most representative. They represent the S_2 surface that is synformal and antiformal folded in the NE-SW an NW-SE axial direction. The D_2 is the major tectonic event in the area. The mechanism of the deformation was simple shearing.

IV.1.3 D_3 DEFORMATION EVENT

The D_3 event occurs in a brittle-ductile regime with the development of shear zones, which is marked by the overprint of the early deformation phase (D_1 and D_2) with a similar E-W and NE trending structures. The D_3 deformation is accompanied by the development of S_3 foliation, C_3 shear planes and F_3 folds. It is typically a phase of superimposed folding and the structures associated to this phase of deformation are a result of the transposition and reorientation of the D_2 structures with a large-scale close fold of a N-S-striking fold axis and associated parasitic folds (Fig. 21A-C).

IV.1.3.1 F_3 folding

F_3 folds are typical interference fold pattern that occurs as a result of the development of the late minor folds across the earlier formed structure; by the refolded of F_2 folds in the last folding event. F_3 folds display small scale asymmetric or symmetric shapes depending on their hinge or limb zones location on the large scale F_2 folds. The overprint F_3 folds show asymmetrical ‘S’ and ‘Z’-shapes on the limb due to passive shearing and symmetric M-or W-shapes on the hinge zone. The fold axis of F_3 are parallel (Figs. 21A-C) to the F_2 fold axis depending upon their location in the large F_2 folds.

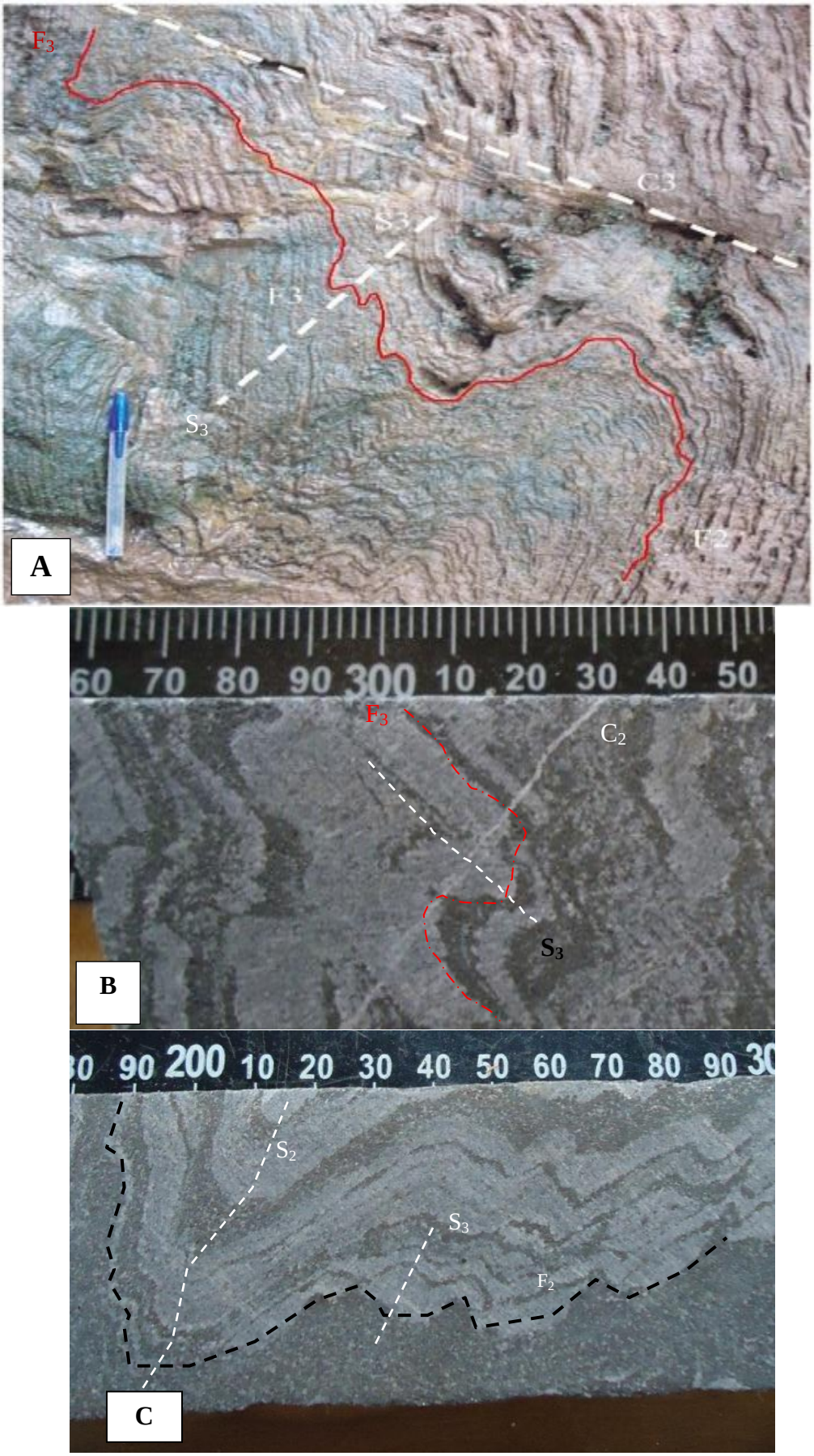

Figure 21: Outcrop and drill core view of the main D_3 structures of (A) F_2 and F_3 folds affected by C_3 shearing in BIFs outcrop (B) F_3 folds affected by C_3 shearing. (C) F_2 and F_3 folds.

IV.1.3.2 Planar structures

IV.1.3.2.1 S_3 foliation

S_3 foliations in the Nkout BIFs are marked by preferred orientation of quartz and magnetite along the fold axial plane of F_3 folds (Figs. 21A-C). The S_3 fold axial plane schistosities overprint the pre-existing S_2 planes (strikes N100-160°E, dips 70-80° steeply toward the NE) which are visible in the fold axial plane of the F_3 folds.

In the Ngoa hill, the S_3 fold axial plane schistosities overprint the pre-existing S_2 schistosities which strikes range from N20-30ºE and steeped dipping 60º to 80º to the NW (dip direction being 280°) are visible on the F_3 fold axial planes. F_3 folds are typical interference fold pattern that occur as a result of the development of the late minor fold across the earlier formed structures. The overprint F_3 folds show asymmetrical 'S' and 'Z' with 'M' and 'W'-shape. The fold axis of F_3 are parallel to the F_2 fold axis.

IV.1.3.2.2 C_3 shearing

C_3 shear planes in BIFs are marked by in-fill of iron oxides (magnetite and haematite) that have affected both the F_1/F_2 folding. The C_3 shows both sinistral/dextral movement (strikes N90-160°E and dips 50° to the south to southwest). The shear planes are parallel to S_3 foliations; these usually displace the ore-bodies vertically, particularly at localities where the strike continuations of the BIFs are offset, mainly around the margin of the planes within the BIFs.

CONCLUSION

The D_3 deformation is a fundamental phase of superimposed tectonism as a result of the transposition and reorientation of the D_2. It is essentially made up of S_3 foliations, C_3 shear planes and F_3 folds. The fold structures show N-S to SE-NW striking fold axis, with the development of parasitic folds. The S_3 fold axial plane schistosities are parallel and subparallel to the pre-existing NW-SE S_2 plane on F_3 axial planes.

IV.1.4 D_4 DEFORMATION EVENT

The fourth phase of deformation (D_4) is regrouped into penetrative and none penetrative elements observed on both outcrop and core samples in BIFs and Gneiss.

IV.1.4.1 Planar structure

The last phase of the deformation (D_4) is characterized by a brittle regime and shear zone, resulting in the fracturing of rocks (BIFs and gneiss) marked by open and in-filled fractures, space cleavages, joints, cracks, veins and faults. The polyphase brittle stage started with the development of sub-vertical tension gashes, primarily within the BIFs as a result of extensive compression and extension.

IV.1.4.1.1 Fracture

The NE fractures are infilled with iron oxide (magnetite and haematite) and calcite, which trends N50-60°E with a sub-vertical dip ranging from 70-80° towards the NW. These structures are in conformity with the D_4 compressional phase deformation roughly oriented N-S to NW-SE. Tension fractures displacement are perpendicular to bedded plane (tension gashes) and are quartz infilled within magnetite domain and vice versa, which occur at the inner rim of folded structures (Figs. 22A-B).

IV.1.4.1.2 Cleavage

The N-S sub-vertical spaced cleavages and joints overprinted D_3 structures. These structures are considered to represent a late structural phase. The late stage deformation joint sets are open fractures with no displacement (Figs. 22C-E), usually perpendicular or parallel to the foliation plane.

IV.1.4.1.3 Fault

The fault appears as discontinuous displacement in brittle zones. These faults are marked by dip-slip and strike-slip movement components which offset the BIF sequence, with the development of tectonic breccia. The presence of tectonic breccia and cataclasite favours local thrust imbricate settings which involve movements contained between faults, resulting in the up throwing of the hanging wall. Many of the thrust faults are rectilinear, but a few are curved (Fig. 22). Some of the faults show no apparent displacement as they mainly occur when vertical faults with principally dip-slip movements cut horizontal structures. These faults cut the BIFs banding at different angles and measure up to 5-100 cm wide in length.

The WNW and NE trending reverse faults are frequent and are marked by amphibole infills (Figs. 22D and 22E). The earlier generations of these faults are developed as a result of an E-W compression. The NE reverse faults strike 0-30° and dips 48° NW (dip direction = 320°) while the WNW reverse faults strike 340-360° and dips SW (dip direction = 260°).

A second generation of these faults are developed as a result of NE-SW compression. It trends N110°-160°E and dips 50° to the NE (dip direction = 40°). They are characterized by precipitation enriched in calcite, and magnetite within the fault planes (Figs. 22C, 22G, 22H)

A late oblique fault type is characterized by an average spacing displacement that ranges from 20 to 40 cm with quartz and iron oxide (magnetite) infills. It strikes N70°-110°E and dips up to 80°NE (dip direction = 20°) and was generated by N-S compression.

An earlier NE to ENE generation of normal faults as a result of an E-W extension with sub-horizontal planes that strike N0-40°E and dips 16-45°NW (dip direction = 310°). The fault planes are mineralized with iron oxide (magnetite), quartz infill and disseminated sulphides.

Fault breccias of several metre thicknesses are restricted to the upper part of the stratigraphy. A later NW normal fault strikes N328-0°E and dips 20-48° to the SW. They are marked by calcite

cementation, quartz and partly with iron oxide mineral (magnetite) from aqueous solution that were leached along the fault planes (Fig. 22B). Some of the late stage deformations are usually cataclastic (Figs. 22D and 22F), commonly without infill and are termed open faults.

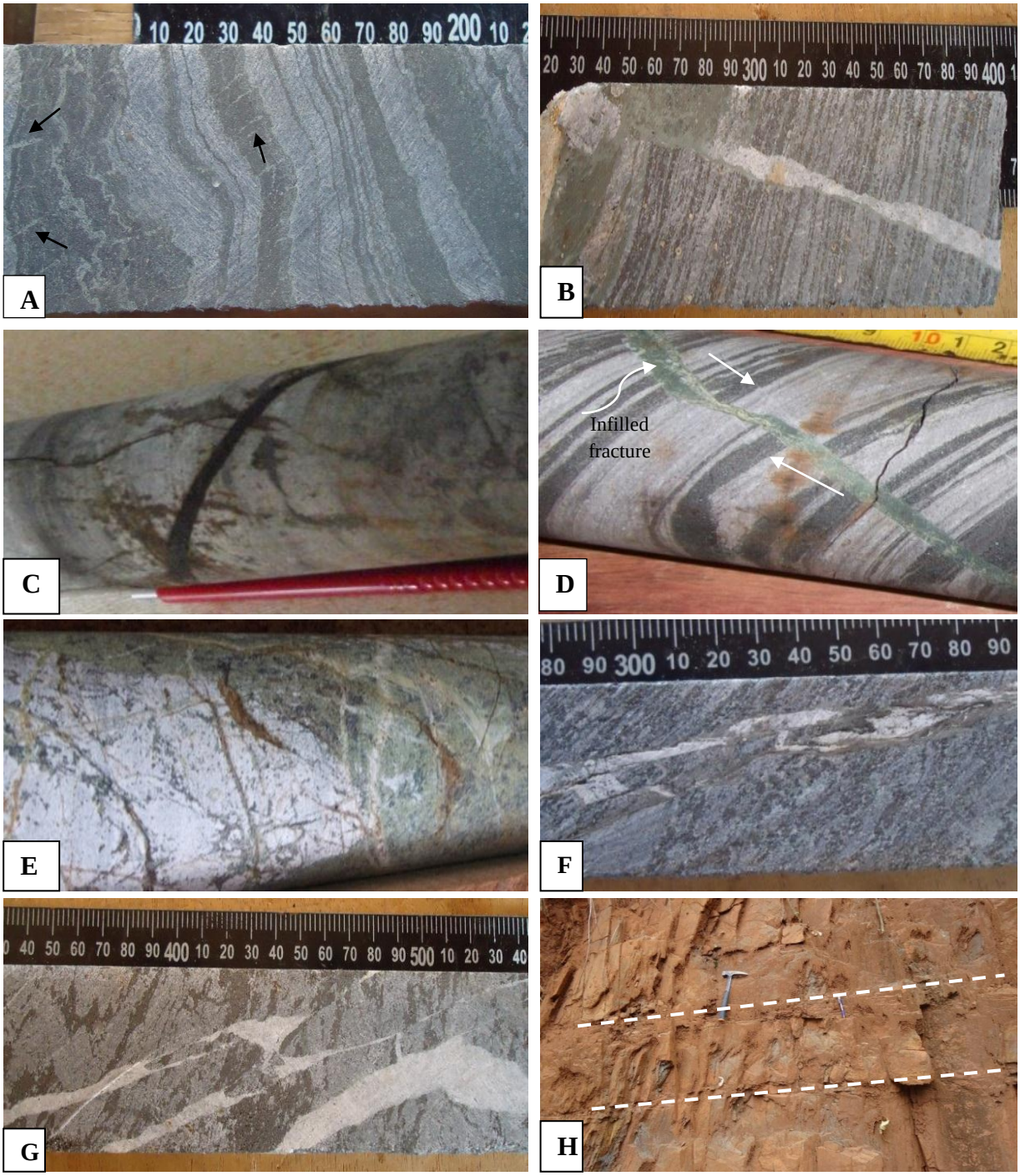

Figure 22: Macroscopic view of the main D_4 structural features. (A and B) Tension gashes, (C and D) fracture infill with quartz in BIFs and infill with amphibole in quartzite respectively, (E) Cataclasite in quartzitic gneiss, (F and G) Fractures infill with quartz and amphibole in BIFs showing slight displacement, (H) strike-slip with low angle faults.

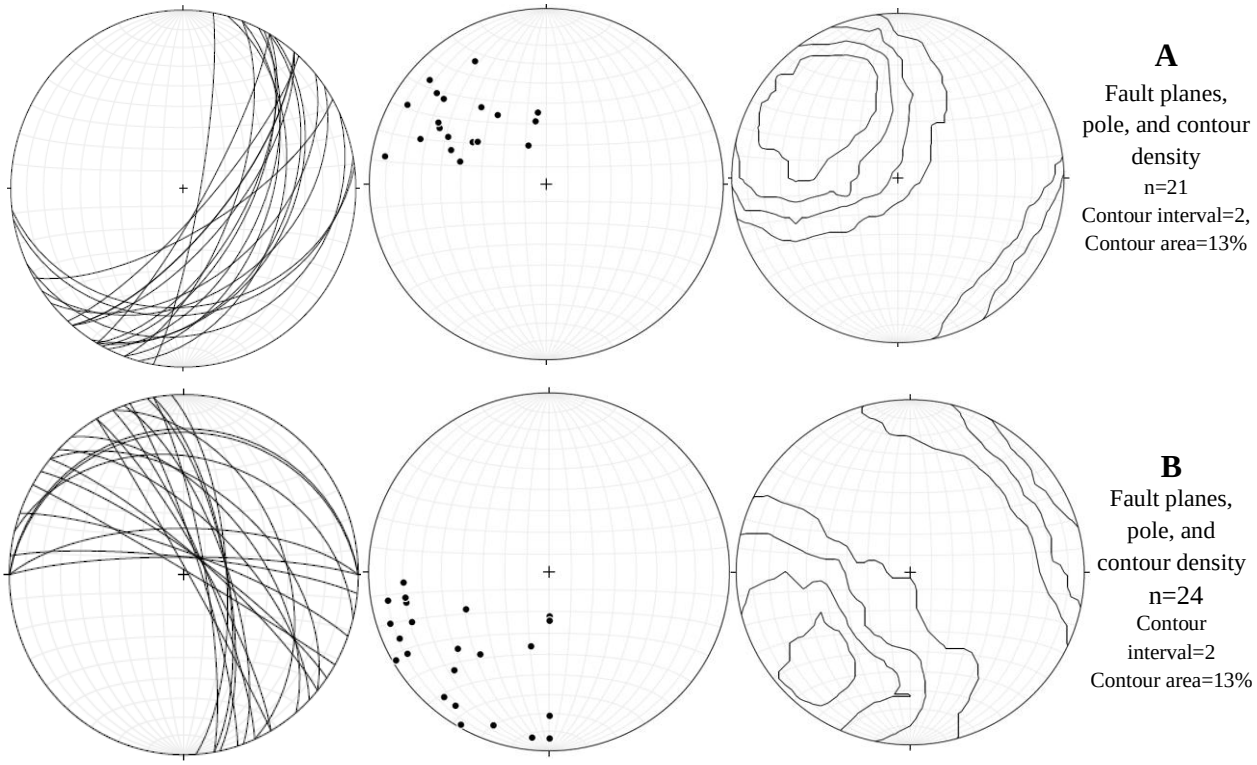

Figure 23: Stereographic projection of structural elements in the studied BIFs, A) Open faults dip-slip thrust B) Open faults strike-slip (planes, poles, and contour density of poles to fault plane).

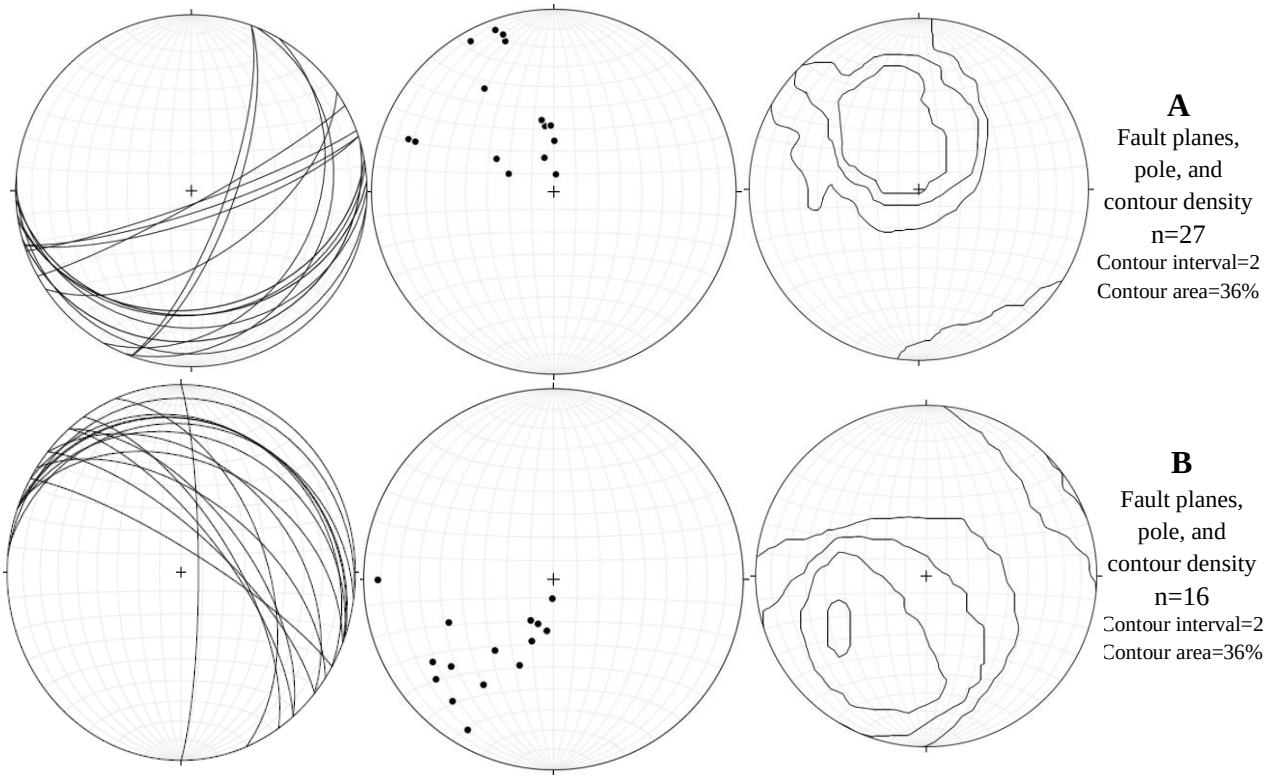

Figure 24: Stereographic projection of structural elements in studied BIFs, (A) Infilled faults QV dip-slip; B) Infilled faults QV strike-slip (planes, poles, and contour density of poles to fault plane).

The veins contain quartz, magnetite, and calcite minerals as in-fills, and cross cut the S_1 compositional banding in BIFs (Fig. 22). F_2 fold type is numerous within the BIFs and was affected with vein in the later stage of the deformation.

The stereographic diagram of D_4 deformation phase was constructed to determine the major orientation of the faulted surfaces. These plotted poles to fault planes confirming NW-SE strike that dip to the NE, NE-SW strike and dip to the SE, NW-SE strike and dip to the SW respectively (Fig. 23 and 24).

IV.2. FOLD INTERFERENCE PATTERN

Three distinct types of folds have been recognised in the studied area, which are the outcome of polyphase deformations. The formation of successive fold structures represents the deformation history of the area. Superposed folding may have given rise to different morphologies of the folded surface, which have been classified after Ramsay (1967). In the studied area we have observed certain types of superposed folds on drill cores. However, the small scale structures observed in the drill cores often give a reliable indication of the style and attitude of associated larger structures.

The earliest fold type is the first-deformation isoclinal close to tight fold (F_{2a}) structures with E-W striking axial planes gently dipping to the North.

The major fold (F_{2b}) is a second generation refold of earlier isoclinal folds (F_{2a}). The second phase of folds (F_{2b}) with axial planes striking in N-S/NW-SE direction and gently dipping W/SE has modified the geometry of the earlier folds. These folds are recumbent to upright, asymmetrical open to tight folds showing both synformal and anitformal closure in many places (Figs. 25A and B). The majority of the traced F_2 fold axial planes orthogonally overprint F_1 folds.

The late minor fold (F_3) is the third-deformation refolding of the earlier fold (F_{2a} and F_{2b}) with similar axial planes striking in the N-S/NW-SE direction, gently dipping W/SE. The traced F_3 fold axial planes parallel to subparallel overprint F_2 folds.

The different types of interference fold patterns produced by successive phases of deformation are well observed. However, all three folds of different generations i.e. the first, second and third generation fold structures are noticed together in a single complex fold (Fig. 25). D_2 and D_3 have together produced two types of fold interference patterns observable in local drill cores.

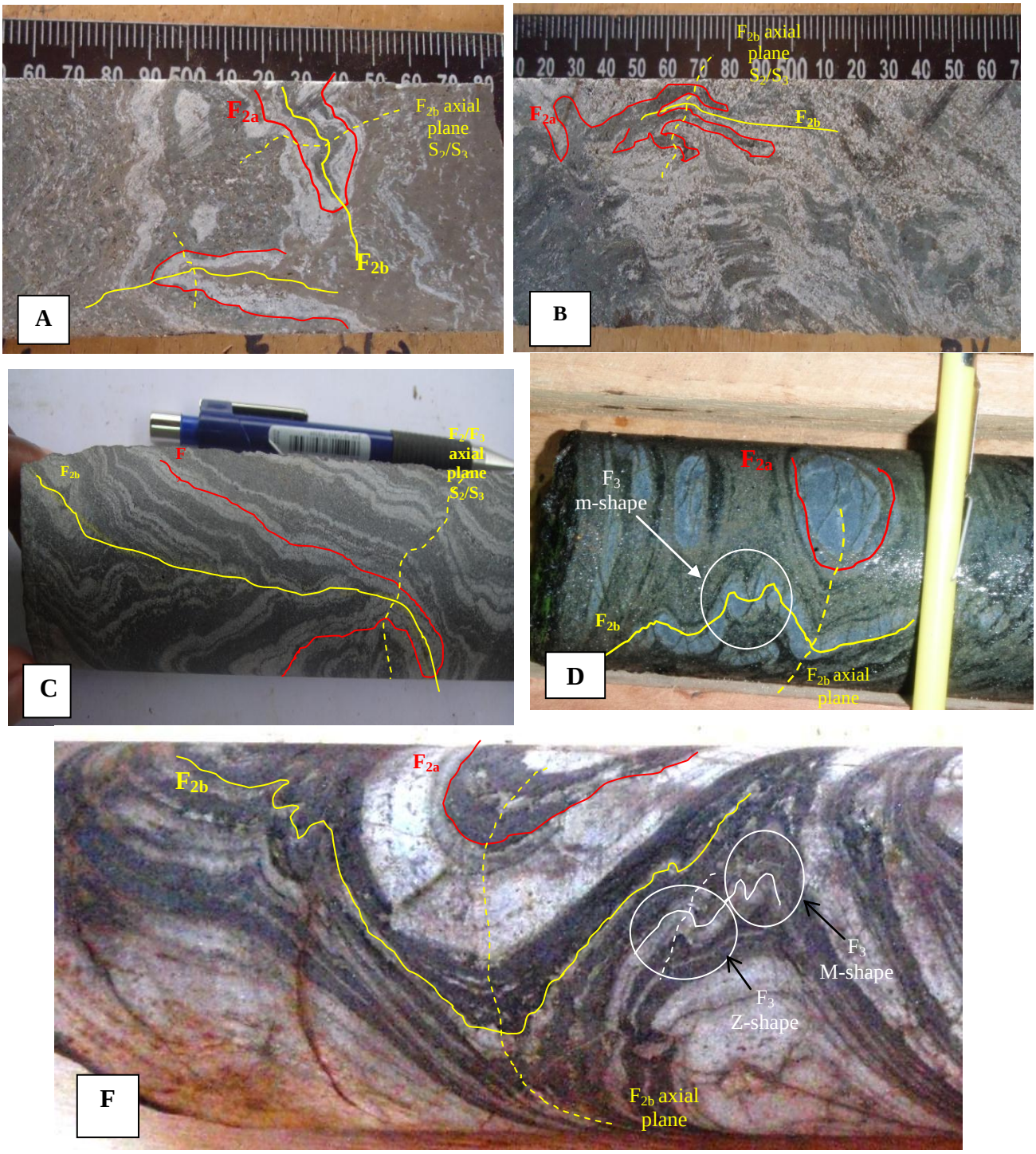

Figure 25: Field photograph showing evidence of folding and refolding in the studied area (drill half and whole cores). (A, B and C) Folding of F_{2a} and refolding of F_{2b}/F_3 (note with incipient type-3 fold pattern of Ramsay, 1967). (D, F) F_{2a} fold and F_{2b}/ F_3 re-fold (note: distinct type 1 fold pattern of Ramsay, 1967).

- Hook fold

Superimposition of the first generation F_{2a} and the second generation F_{2b} are parallel to each other, gave rise to Type-3 fold interference pattern. Here, the low lying first generation isoclinal fold axial plane F_{2a} folds are overprinted by F_{2b} upright folds producing the fold interference

pattern indicating a “zig-zag fold” shape. These folds were superimposed by the late D_3 event of F_3 folding. The fold is non-plane, cylindrical fold in which hinge of F_{2a} is straight, but axial surface is curved. This type of coaxial deformation gives rise to a Hook-shaped. The curve axial trace of F_{2b} folds is due to the interference of F_{2b} generates hook shape folds (Type-3 of Ramsay, 1967) of double closures (Figs. 25C).

- *Dome and basin patterns*

A second type of fold interference pattern was recognized in the studied area. This pattern is associated with the steeply inclined isoclinal F_2a and F_3 folds interfering with F_{2b} folds (Fig. 25). It is suggested that F_{2a} structures with planar axial surfaces and highly curved F_{2b} fold axial surface are developed as a result of strong later compression of F_{2b} fold. The minor (‘S’, ‘Z’, ‘W’and ‘M’) fold shapes related to the third deformations have been traced in the studied area (Fig. 25F). As a result, varieties of combine shapes have been developed during the superposition of the later folds on the earlier ones, giving rise to an enveloping surface that shows Dome and Basin structures or Type-1 patterns of Ramsay (1967). The fold is Plane Non-cylindrical Fold, in which axial surface of early fold F_2 remains planar, but the hinge line is curved within that plane. The outcrop pattern is eye-shaped with antiformal and synformal culmination and depression.

IV.3. STRUCTURAL MAPPING

In the regional scale, the major directions of all the structural elements of Nkout include the variable foliation strike and dip and the disruption by faults of the BIFs (Fig. 26). The studied BIFs occur as a roughly east-west trending ridge.

The S_1 foliation in the studied area is a lithology parallel foliation that is particularly well developed within the BIFs. Within this unit, the S_1 foliation is highly variable in strike and dip due to later refolding. The major direction of the S_1 foliation structure strikes roughly E-W (N55-70°E) mainly dipping to the NW (10-70°).

The study has shown the presence of multiple folding events that affect the geometry of the deposit. The F_{2a} upright asymmetric, isoclinal E-W tight fold dip to the North in combination with the F_{2b} antiformal and synformal N-S to SE-NW fold, have confirms the shape of the deposit. The relative N-S cross (AA’) section through Nkout west and Ngoa (Fig. 25) show an E-W tight isoclinal fold dip to the North. It is folded around a variably oriented NE striking fold axis or axial planes on account of later refolding. Moreover, the North-East longitudinal (DD’) section of the studied area (Fig. 27) demonstrates antiformal and synformal structure, folded around an N-S to NW-SE and NE-SW striking fold axis.

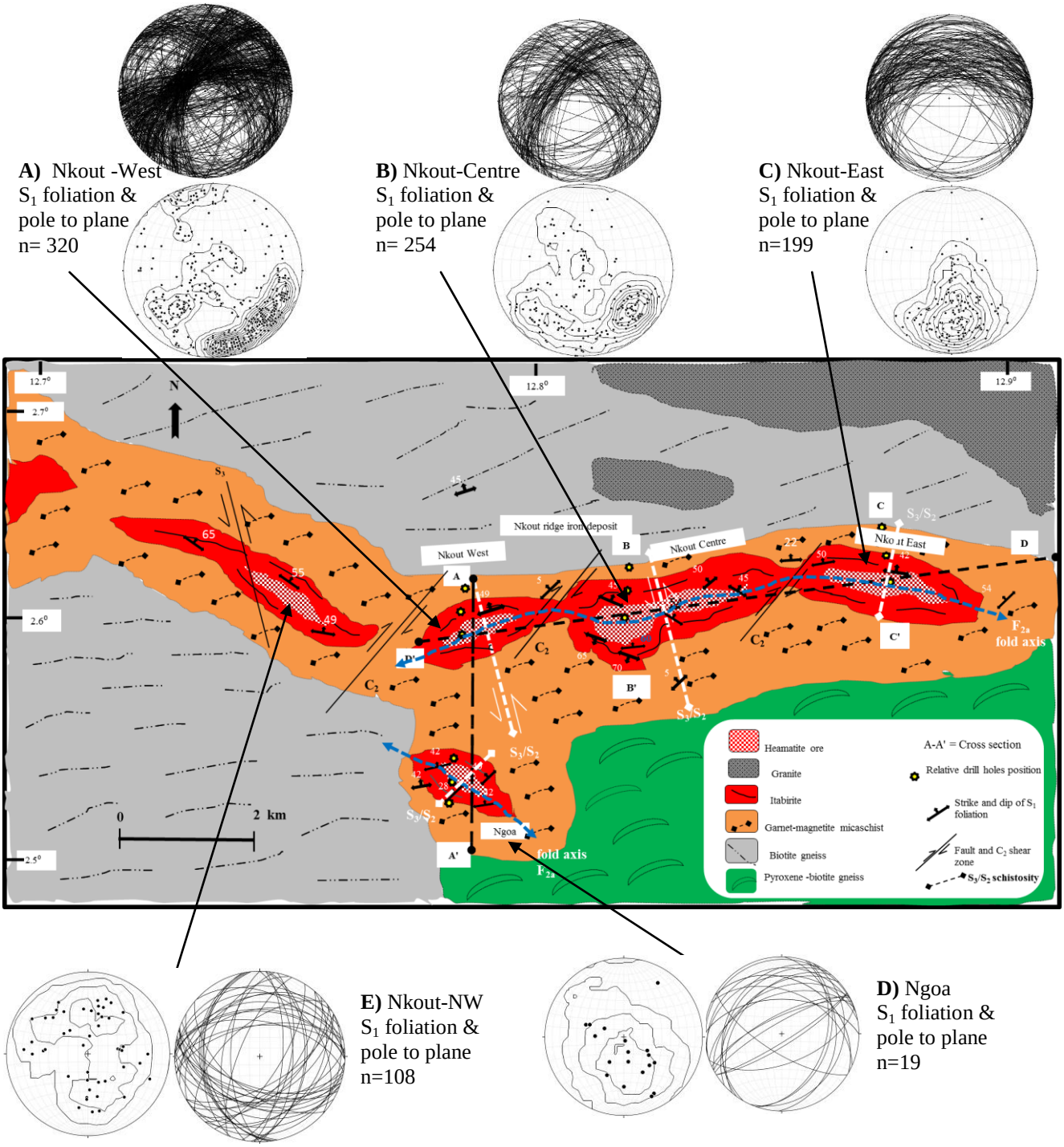

Figure 26: Structural map of the individual deposit of the study area (A) Nkout-west, (B) Nkout-centre and (C) Nkout-east, (D) Ngoa, (E) Nkout-NW).

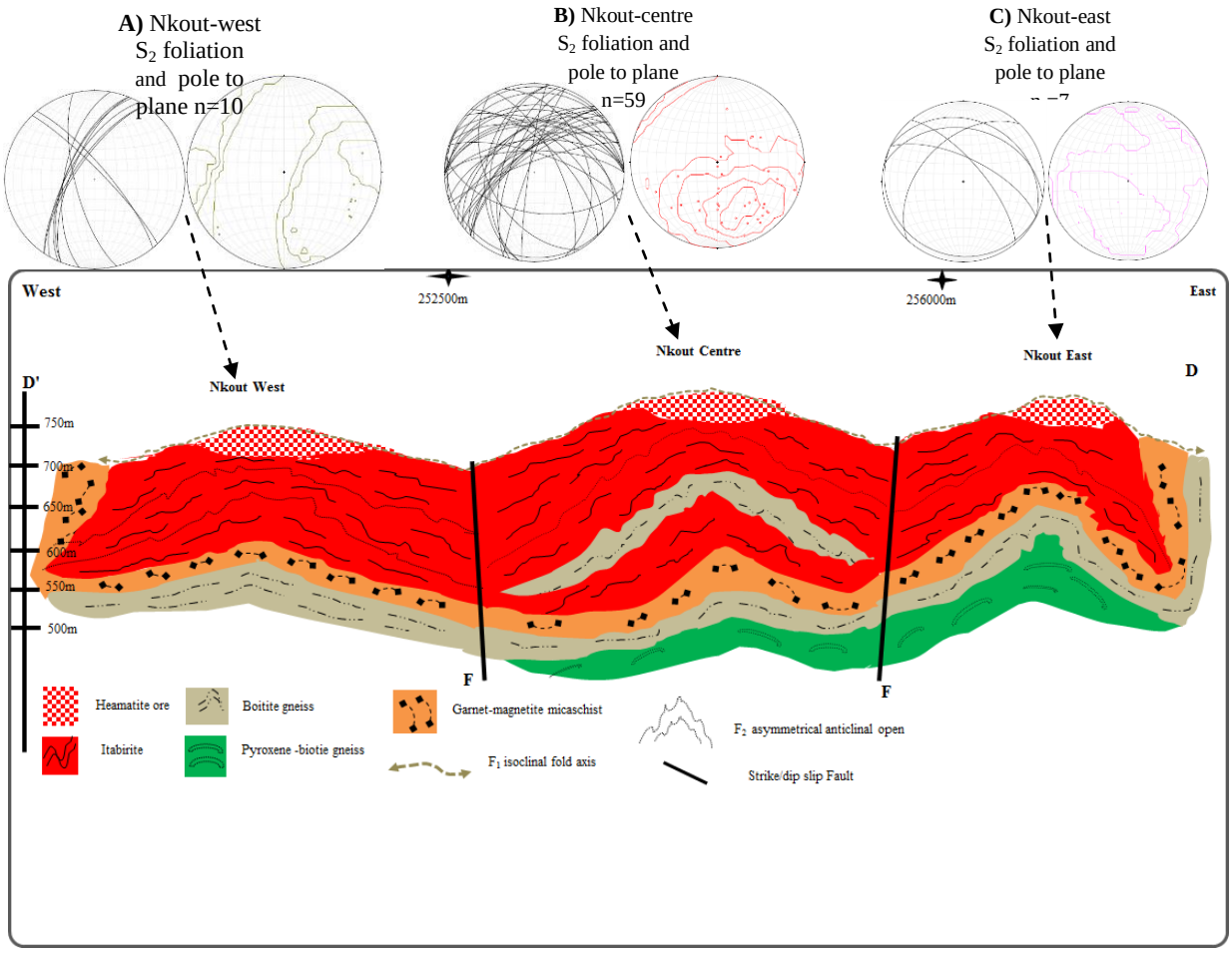

Figure 27: East-West longitudinal section (D-D' in **Fig 26**) with S_2 foliation and pole to plane stereographic projection showing the individual deposit indicating NE-SW, N-S, and NW-SE F_{2b} antiformal fold axis in the study area (A) Nkout-west, (B) Nkout-centre and (C) Nkout-east.

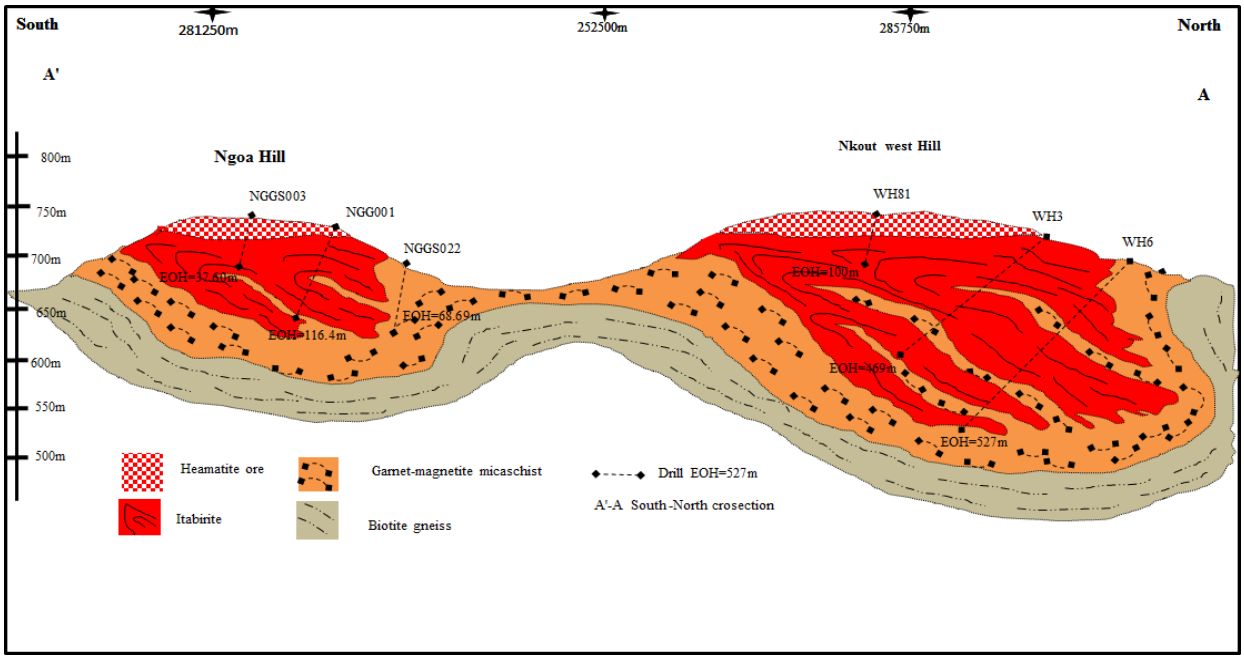

Figure 28: North-South cross-section (A-A' in **Fig 26**) of the study area showing E-W F_{2a} isoclinal fold axis.

The F_2 folding and F_3 refolding have brought about 3D 'dome, oval' shape and 2D lenses shape of Nkout and Ngoa. Nkout show triangular topographic morphological outlines reminiscent of fold interference structures as a result of the refolding of early sinuous E-W isoclinal folds by later N-S trending fold which equally brought about the development of dome-basin structures. The Ngoa area equally shows ellipsoidal morphology as a result of the fold interference pattern, the refolding of the NW-SE isoclinal folds by later NE-SW trending folds.

The stereographic projection of S_1 foliation and schistosity planes show variable spatial orientations in the individual deposit throughout the studied area (Fig. 26).

In the Nkout-west deposit the pole to S_1 planes show asymmetric display and are concentrated on the second, third and fourth quadrant confirming that the planes generally strike NE-SW, NW-SE and dip to the NW (Fig. 26A).

The Nkout-centre shows symmetric display of poles to S_1 planes, concentrated on the SE and SW quadrant NE-SW, NW-SE (Fig. 26B).

In the Nkout-east, the pole to S_1 foliation shows a single display of concentrated on the second and third quadrant in the SE and SW confirming that the plans generally strike NE-SW and dip to the NW (Fig. 26C).

The Ngoa deposit shows pole to S_1 foliation concentrated on the second and third quadrant (SE and SW) indicating that the planes generally strike NE-SW, NW-SE and dip to the NW/NE (Fig. 26D).

The Nkout-NW shows concentrated of poles to S_1 planes scattered throughout all quadrants (Fig. 26E).

S_2 foliation and schistosity planes show variable spatial orientations on stereographic projection in the individual deposit (Figs. 27and28).

The Nkout-west deposit shows a symmetric display of the poles to plane of the S_2 surfaces. The plotted pole to planes are concentrated on the SE and SW quadrants confirming either N-S to NW-SE, NNE-SSW striking S_2 surface, and dips oriented between NE and NW. (Fig. 27A).

In the Nkout-centre deposit, the pole to planes of the S_2 are concentrated on the SE and SW quadrants, indicating NW-SE, NNE-SSW striking S_2 surface dipping to the NE and NW (Fig. 27B).

The pole to S_2 planes of the Nkout east are concentrated on the SE and SW quadrants, indicating NW-SE, NE-SW striking S_2 surface dipping to the NE and NW (Fig. 27C).

The major faults identified in the study area are shown schematically with numerous map-scale faults recorded in BIFs. The faults are typically rectilinear and a few are curved. In the regional scale, the major directions of the fault structures were of the NE, N-S strike slip and the NW dip-slip faults movement components which mainly separate the deposit into three fault blocks

(Fig. 27). The faults are typically 1 - 3 mm as they cut the BIFs at different angle. The intensity of these deformations along faults is known to have truncated the BIFs resulting in thinning up lithology on the local scale.

IV.4 MINERAL ASSEMBLAGES AND DEFORMATION EVENT

The Nkout study area is characterised by tectonic and metamorphic event. It shows traces of history with the succession of paragenesis of prograde and retrograde. This indicates that there was a complete metamorphic cycle in the Nkout area which is characterised by high-pressure and high-temperature metamorphic type.

The successive mineral phases in association with the different state of deformations are as follows:

The D_1 event:

The D_1 deformation is characterized by S_1 foliation marked by banding and preferred orientation of mineral in BIFs. The mineral assemblage underlines the S_1 are iron-oxide (magnetite and haematite), quartz, biotite, chlorite in BIFs and feldspars, pyroxene in gneiss (Fig. 17). The S_1 foliation planes generally strike roughly E-W with gentle dips mainly to the NW. The D_1 mineral assembly develop during M_1 metamorphism characterised by greenschist facies metamorphism (magnetite, quartz, biotite, and chlorite).

The D_2 event:

The D_2 deformation is characterized by S_2 foliation, marked by preferred orientation of mineral in BIFs. The mineral assemblage underlines the S_2 schistosity are iron-oxide (magnetite and haematite), biotite, quartz and garnet. The D_2 mineral assembly developed during M_2 metamorphism characterised by medium grade amphibolite facies metamorphism (quartz, magnetite, garnet, amphibole and biotite).

The D_3 event:

The D_3 deformation event is characterized by superimposed refolding as a result of the transposition and reorientation of the D_2 structures associated with parasitic folds. The D_3 deformation is characterised by refolding of S_2 surfaces, characterised by S_3 schistosity marked by preferred orientation of minerals. The mineral assemblage that underlines the S_3 schistosity is iron-oxide (magnetite and haematite), biotite, quartz, amphibole and garnet. The D_3 mineral assembly developed during M_3 metamorphism, characterised by medium grade amphibolite facies metamorphism (magnetite, haematite, garnet, biotite and quartz, amphibole).

The D_4 event:

The D_4 event is brittle deformation, characterised by faulting and fracturing marked by open and in-filled features. The mineral assemblage that underlines D_4 phase deformation the iron oxide (magnetite and haematite), sulfides (pyrite), calcite and amphibole

Table 3: Tectonic and metamorphic relationship in the study area

Deformation event	Structural element	Petrographic type	Microstructure	Associated mineral	Metamorphic grade
D_1 deformation event	S_1 mineral foliation and axial plane schistosity, and F_1 isoclinal fold	Magnetite-Haematite BIFs	Heterogranular granoblastic	Iron oxide (Magnetite, Haematite), Quartz, Biotite & Chlorite	Greenschist facies
D_2 deformation event	S_2 axial plane schistosity, and, F_2 isoclinal, synformal and antiformal folds	Magnetite - Haematite BIFs	Heterogranular granoblastic	Iron oxide (Magnetite, Haematite), Garnet, Biotite & Quartz	Amphibolite facies
D_3 deformation event	S_3 axial plane schistosity, , and F_3 parasitic folds	Magnetite-Haematite BIF	Heterogranular granoblastic	Iron oxide (Magnetite, Haematite), Garnet, Biotite, Quartz, & Amphibole	Amphibolite facies
D_4 deformation event	Fractures, cleavages, joints, cracks, veins and faults			Sulfides (pyrite), iron oxide (magnetite /Haematite), calcite & amphibole (cummingtonite/ hornblende).	

CONCLUSION

In the Nkout area, the deformation range from ductile D_1, D_2 and D_3 to brittle D_4 deformation.

The D_1 deformation event consists of the S_1 foliation marked by layering and preferred orientation of minerals. The minerals that underline the S_1 schistosity are haematite, magnetite, garnet, amphibole quartz, feldspars, and pyroxene in BIFs and gneiss. Asymmetric and isoclinal tight F_1 folds occur in BIFs and gneiss which show S_1 axial plane schistosity.

The D_2 tectonic event is characterised by an earliest fold (first-generation F_{2a}) structure, marked by asymmetric close to tight isoclinal folds with E-W striking axial planes, dipping to the north. The late fold (second generated F_{2b}) is marked by asymmetric open to tight folds with N-S, NW-SE axial plane S_2 schistosity. The C_2 shearing is both dextral and sinistral sense. The mechanism of deformation during the D_2 event was simple heterogeneous shearing.

The D_3 tectonic event is fundamentally a superposed phase tectonic event. The F_3 folds are as a result of the refolding of the F_2 folds, with S_3 schistosity, and shearing C_3. The D_3 event occurs as brittle-ductile regime with the development of shear zones C_3, which are marked by the overprint of the early deformation phase with a similar N-S, NW-SE axial plane S_3 schistosity.

The successive phases of deformation produced two main interference patterns. The results in forming a combination of the individual folding event, let to the development of hook shaped folds (‘zig-zag fold’ Type-3 of Ramsay, 1967) and a wide spread dome and basin patterns (‘egg box’ Type-1 of Ramsay, 1967).

The D_4 tectonic phase is a brittle phase deformation event and is marked by several generations of fractures and faults of different compression and extension events resulting in reverse and normal fault systems. These fractures are roughly oriented in the N-S and NE-SW. In the regional scale the major direction of the structure were the NE reserve strike-slip and the NW dip-slip fault which separate deposits.

CHAPTER V. GEOCHEMISTRY AND GEOCHRONOLOGY

V.1 GEOCHEMISTRY

INTRODUCTION

Field work and petrographic studies (Chapter III) have permitted us to distinguish the different formations in the Nkout area. In this chapter we bring out principal geochemical characteristics of the formation which permitted us to research the possible protolith and to define their geotectonic characteristics. Chapter III shows that the geology of Nkout area is made up of magmatic and metamorphic units. The magmatic units within the Nkout area consist of abundant plutonic rocks. The metamorphic rock unit is mde up of banded iron formation (BIF) in association with gneiss country rock intruded by magmatic rocks.

In order to determine the geochemistry of metamorphic and magmatic units, rock samples selected were analysed for major, trace and REE. Seven samples (7) were collected and analysed for plutonic rocks while eight samples (8) were for gneiss whereas fourteen BIF samples (14) and ten iron ore samples (10) where collected and analysed.

The results of the data obtained are presented in this chapter. The geochemical characterisation of the different lithologies were done with the gold to determine, firstly, the different rock protolith or the nature of their origin and secondly, to appreciate the context of geologic setting and geodynamics of the rocks.

The petrography as well as the geochemical classification of Debon and Le Fort (1983) permitted the sub-classification of plutonic rocks. The geochemical diagram of De La Roche (1965) permitted the protolith reconstruction, whereas the geochemical diagram of Roser and Korsch (1988) confirmed and established the classification of the gneissic rock.

The geochemical diagram of Herron (1988) also permitted the protolith reconstruction of BIF. The nature of iron ore protolith rocks were determined by comparative study of major element oxide geochemical characteristics of BIF composition. In this chapter, we compare our data with the average values of Archean-Proterozoic granitoid (Le Maitre, 1976, Divakara-Rao et al., 1999, Frost et al., 2006, Almeida et al., 2010, Mikkola et al., 2014, Moyen et al., 2003), average values of Archean-Proterozoic igneous rocks (Le Maitre, 1976, Shervais et al., 2008, Tokhi et al., 2016, and Ibrahim et al., 2015), average composition values of Precambrian Fe-sand (Mishra et al., 2012, Elzien et al., 2014, Ramachandran et al., 2016, Abu et al., 2017, McLennan, 2001, and Taylor et al., 1985), and average composition of Precambrian BIFs (Adekoya et al., 2012, Gross et al., 1980, Klien 2004, and Prasad et al., 2010).

V.1.1 PLUTONIC ROCKS

The geochemical studies permitted us to characterise the plutonic rocks of Nkout and to determine the nature of magma and show evidence of the different genetic type of the rocks, and to determine the source of the possible magma. This information permitted us to define the geochemical context and the emplacement of the magma. In this study, seven (7) rock samples where geochemically analysed.

Major, trace and rare earth elements (REEs) data are employed to constrain these objects. The rare earth elements are chondrite-normalised to the value of Evensen et al. (1978) and the trace elements in the multi-element diagram to the values of Thompson et al., (1984).

Their whole rock major, trace and rare earth elements (REEs) data are presented in Table 3. The geochemical classification diagram of Debon and Le Fort, (1983) for plutonic rocks is shown in figure 29. On the Q=Si/3-(K+Na+2Ca/3) vs. P = (K-(Na+Ca)) classification diagram of Debon and Le Fort (1983), the studied samples correspond to granite, granodiorite and tonalite (Fig. 29).

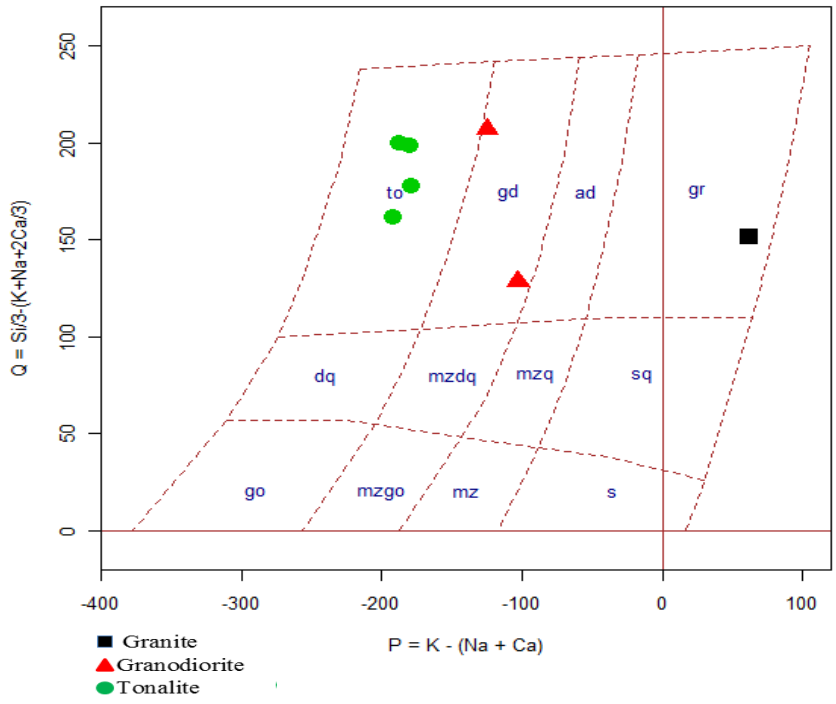

Figure 29: The geochemical classification diagram Q=Si/3-(K+Na+2Ca/3) vs. P = (K- (Na + Ca)) of Debon and Le Fort (1983), position of study plutonic rocks.
Legend = (go: gabbro; mzgo: monzogabbro; mz: monzonite; s: syenite; dq: quartz diorite; mzdq: quartz monzodiorite; mzq: quartz monzonite; sq: quartz syenite; to: tonalite; gd: granodiorite; ad: adamellite, gr: granite)

Table 4: Major, trace and REEs geochemical composition of study plutonic rocks

	Granite	Granodiorite		Tonalite			
Wt.%/Samples	MN02	DJO2	NKR1	DJO1	DJO3	MN01	MN04
SiO_2	71.9	73.8	65.7	71.3	69.3	73.1	73.4
TiO_2	0.02	0.28	0.78	0.33	0.37	0.31	0.22
Al_2O_3	13.9	13.7	14.9	15.25	15.5	14.4	14.7
Fe_2O_3	0.91	2.62	6.75	4.09	3.56	3.49	3
MgO	0.04	0.59	1.12	0.88	0.88	0.79	0.64
MnO	0.01	0.04	0.08	0.04	0.03	0.06	0.04
CaO	0.44	2.62	3.15	3.3	3.54	3.02	3.45
Na_2O	2.68	3.87	3.8	4.62	4.8	4.6	4.53
K_2O	7.34	2.18	3.58	1.39	1.21	1.07	0.96
P_2O_5	0.01	0.03	0.24	0.06	0.13	0.09	0.06
LOI	0.47	0.46	0.32	0.56	0.54	0.18	0.3
Total	98.59	100.39	100.58	101.99	99.96	101.17	101.39
A/NK	1.13	1.57	1.47	1.67	1.68	1.65	1.73
A/CNK	1.06	1.02	0.94	1.01	0.99	1.01	1.00
K_2O/Na_2O	2.74	0.56	0.94	0.30	0.25	0.23	0.21
Fe_2O_3/MgO	22.75	4.44	6.03	4.65	4.05	4.42	4.69
Al_2O_3/TiO_2	695.00	48.93	19.10	46.21	41.89	46.45	66.82
Trace (Ppm)							
Ba	67.9	13.05	17.15	24.3	13.1	5.63	5.29
Co	0.053	0.112	0.375	0.202	0.131	0.153	0.129
Cr	5.44	5.99	6.31	7.57	6.68	7.21	7.46
Cu	0.13	0.41	1.79	0.33	0.26	0.24	0.23
Fe	1820	2730	3580	5310	3380	4400	4240
Ga	bdl	0.06	0.08	0.09	0.07	0.07	0.05
Ge	0.022	0.03	0.037	0.053	0.031	0.043	0.042
Hf	bdl	bdl	0.002	bdl	bdl	bdl	bdl
Li	1.57	0.28	0.55	0.47	0.4	1.49	0.68
Mo	0.042	0.052	0.072	0.103	0.075	0.093	0.11
Nb	bdl	0.0011	0.001	0.0024	0.0009	0.0008	bdl
Ni	0.28	0.33	0.45	0.54	0.47	0.42	0.61
Pb	1.52	1.195	1.01	0.778	1.02	0.285	0.175
Rb	1.7	0.492	2.59	0.616	0.569	0.834	0.327
Sb	0.0021	0.0011	0.0019	0.0015	0.0006	0.0024	0.0029
Se	0.1	0.03	0.09	0.13	0.11	0.09	0.03
Sr	7.26	1.9	1.68	2.45	1.755	1.115	1.61
Ta	bdl	bdl	bdl	bdl	bdl	bdl	bdl
Te	bdl	bdl	bdl	bdl	bdl	bdl	bdl
Th	0.286	0.338	1.06	0.539	1.005	0.266	0.138
U	0.0723	0.0104	0.0526	0.0126	0.0112	0.0619	0.0054
V	0.97	1.14	1.37	1.56	1.33	1.33	1.27
W	0.009	0.006	0.01	0.009	0.009	0.006	0.009
Zn	1.31	1.99	2.61	1.25	1.7	1.55	1.85
Zr	0.002	0.003	0.045	0.003	0.002	0.007	0.004
REE (Ppm)							
La	0.1195	0.257	2.4	1.765	1.075	0.774	0.226
Ce	0.191	0.426	4.3	3.06	1.91	1.555	0.404
Pr	0.0196	0.0444	0.412	0.281	0.1885	0.172	0.0428
Nd	0.0803	0.1485	1.395	0.829	0.608	0.592	0.154
Sm	0.0141	0.0187	0.178	0.0668	0.0629	0.0754	0.0296
Eu	0.0083	0.0068	0.0167	0.0102	0.0057	0.0041	0.0037
Gd	0.0106	0.0165	0.107	0.0292	0.0425	0.0557	0.0221
Tb	0.0013	0.0015	0.0127	0.0029	0.0034	0.0068	0.0023
Dy	0.0078	0.0084	0.056	0.0107	0.0136	0.0311	0.0106
Y	0.039	0.0372	0.269	0.0497	0.0612	0.1415	0.0473
Ho	0.0013	0.0016	0.0113	0.0017	0.0023	0.0058	0.0013
Er	0.0037	0.0045	0.0255	0.003	0.0053	0.0151	0.0041
Tm	0.0007	0.0004	0.0024	0.0005	0.0005	0.0018	0.0005
Yb	0.0065	0.0044	0.0207	0.0039	0.0031	0.0142	0.0045
Lu	0.001	0.0006	0.0029	0.0005	0.0006	0.0019	0.0006
∑REE	0.5047	0.9765	9.2092	6.1141	3.9826	3.4464	0.9534
Eu/Eu*	2.076	1.183	0.370	0.706	0.337	0.193	0.442
$(La/Yb)_{CN}$	12.409	39.425	78.258	305.472	234.065	36.791	33.899
$(Ce/Sm)_{CN}$	3.270	5.500	5.832	11.059	7.331	4.979	3.295
$(Gd/Yb)_{CN}$	1.318	3.030	4.177	6.051	11.079	3.170	3.969

$Eu/Eu^* = Eu_{CN}/(Sm*Gd)_{CN}^{1/2}$, A/CNK: $Al_2O_3/(CaO+Na_2O+K_2O)$, A/NK: $Al_2O_3/(Na_2O+K_2O)$, bdl: below dictection

V.1.1.1. GRANITE

The granite is represented in the plutonic rocks of the studied samples (MN02). The geochemical composition is represented in table 4.

V.1.1.1.1. Major Element Oxides (MEO)

The rock sample shows rich silica whole-rock content (71.9 wt % SiO_2; Tab. 4) which shows that the rock is felsic in composition similar to that of granite (SiO_2 = 71.3 wt. %, Le Maître, 1986). The Fe_2O_3 (0.91 wt. %) content is closely similar when compared to that of granite (Fe_2O_3 = 1.21) after Le Maître, (1986), Indian Shield (Fe_2O_3 = 1.46) after Divakara-Rao et al. (1999), Central Wyoming (Fe_2O_3 = 1.44) after Frost et al. (2006), Rio Maria terrane-Brazil (Fe_2O_3 = 1.13) after Almeida et al. (2010), Surmansuo-Eastern Finland (Fe_2O_3 = 2.4) after Mikkola et al. (2014), and Dharwar Craton-India (Fe_2O_3 = 2.23) after Moyen et al. (2003).

The Al_2O_3 content (13.9 wt. %) is relatively similar to that of granite (Al_2O_3 = 14.32 wt. %, Le Maître 1986; 14.40, Divakara-Rao et al. 1999; 14.5, Frost et al. 2006;15.4, Almeida et al. 2010; 14.9, Mikkola et al. 2014; 14.45, Moyen et al. 2003).

The MgO contents (0.04 wt. %) in the studied sample is in trace amount and is relatively similar to the average concentration of granite (0.7, Le Maître 1976, 0.35, Moyen et al. 2003), while the CaO contents does not exceed 0.44 wt. % and relatively low (1.84, Le Maître 1976; 1.47, Divakara-Rao et al., 1999; 2.12, Frost et al., 2006; 1.8, Almeida et al., 2010; 0.8, Mikkola et al. 2014; 2.01 Moyen et al., 2003).

The alkaline contents (Na_2O and K_2O) are 2.68 wt. % and 7.34 wt. % relatively moderate respectively, showing an alkaline nature of the granite rock. The Na_2O concentration is relatively lower while the K_2O concentration is relatively higher compared to that of granite (3.68 and 4.07, Le Maître, 1986; 3.62 and 4.57, Divakara-Rao et al., 1999; 3.4 and 3.5, Frost et al., 2006; 4.6 and 3.9, Almeida et al., 2010; 3.9 and 5.1, Mikkola et al., 2014; 4.2 and 3.7, Moyen et al., 2003).

The contents of Na_2O are slightly lower than that of K_2O. The K_2O/Na_2O ratio (2.7) in the sample is relatively higher to that of the average granite values (1.1, Le Maitre 1976). The total alkali content ($Na_2O + K_2O$=10.02 wt. %) is closely similar to the average granite value (7.75, Le Maitre, 1976; 8.19, Divakara-Rao et al., 1999; 7.1, Frost et al., 2006; 8.4 Almeida et al., 2010; 9.9 Mikkola et al., 2014; 7.9, Moyen et al., 2003), indicate the association of feldspars mineral in granite.

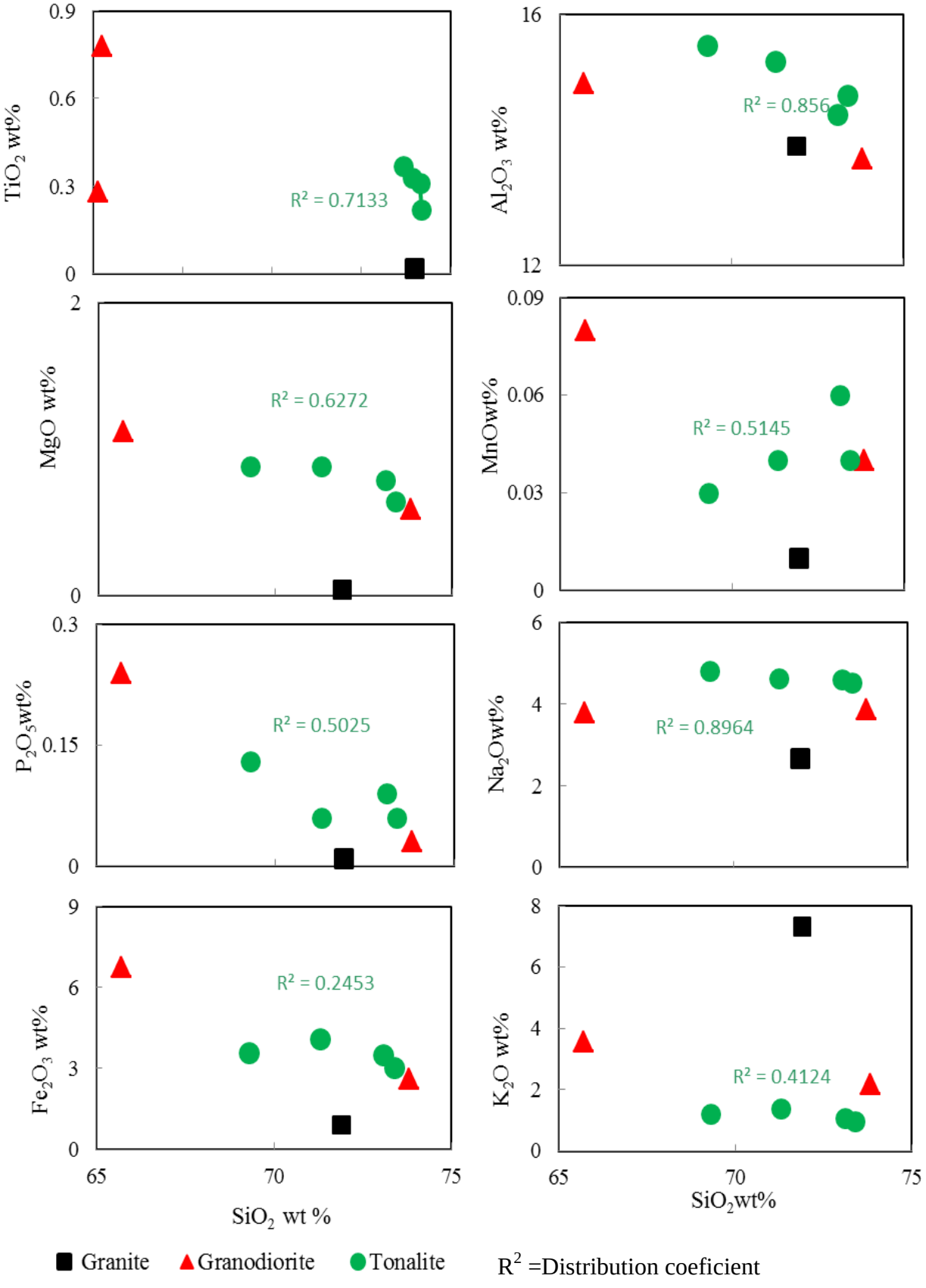

Figure 30: Binary plots for major element oxide variation with SiO_2 for Nkout Plutonic rocks (granite, granodiorite and tonalite).

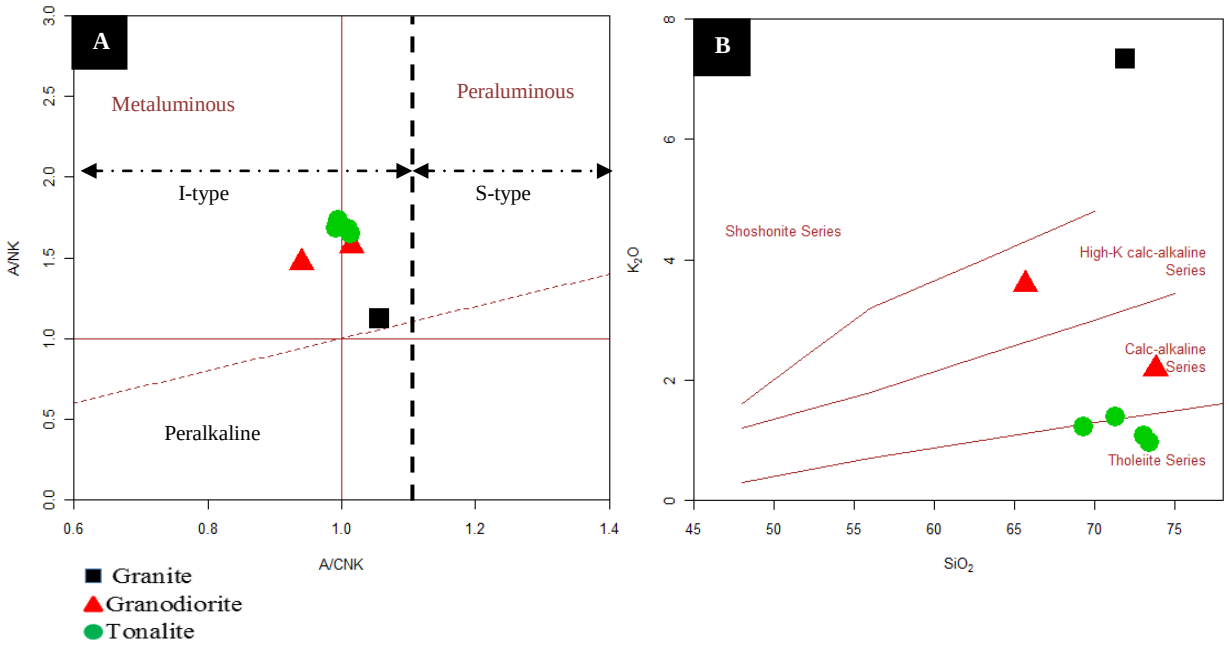

Figure 31: Geochemical characterization of Nkout plutonic rock (granite, granodiorite and tonalite): (a) Al_2O_3/ ($CaO+Na_2O+K_2O$) versus Al_2O_3/ (Na_2O+K_2O) moles% diagram showing metaluminous composition and (b) K_2O versus SiO_2 showing low-high K_2O (Peccerillo and Taylor 1976)

The TiO_2 concentration in the sample does not exceed 0.02 wt. % and is similar to average granite value (0.31, Le Maître 1986; 0.25, Divakara-Rao et al. 1999; 0.24, Frost et al. 2006; 0.19, Almeida et al., 2010; 0.49, Mikkola et al., 2014; 0.35, Moyen et al., 2003). The Al_2O_3/TiO_2 ratio (695) is slightly high while the Fe_2O_3/MgO (22.75) is slightly lower to the average value (Le Maitre 1976) which characterises a magnesian series.

The content of MnO (0.01 wt. %) and P_2O_5 concentration (0.01 wt. %) are relatively similar compared to that of granite (0.12 and 0.05, Le Maître 1976; 0.13and 0.07, Divakara-Rao et al. 1999; 0.01 and 0.05, Frost et al., 2006; 0.02 and 0.08, Almeida et al., 2010; 0.04 and 0.09, Moyen et al.. 2003), whereas they are averagely the same in the studied samples (0.03 and 0.04, Shang et al., 2007).

The major element contents of the studied samples are similar to that of the average granite contents (Le Maître, 1976; Divakara-Rao et al., 1999; Frost et al., 2006; Almeida et al., 2010; Mikkola et al., 2014; and Moyen et al. 2003).

The rock is slightly peraluminous on the A/NK= $\{Al_2O_3/(Na_2O+K_2O)\}$ vs. A/C NK=$\{Al_2O_3/(CaO + Na_2O + K_2O)$ mol %$\}$ diagram of Shand (1943) and plots in the I -type igneous domain (Fig. 31A), with shoshonitic composition as revealed by the K_2O vs SiO_2 diagram (Fig. 31B).

V.1.1.1.2. Trace Elements (TE)

The studied samples show variable low concentration of Ba (67.9ppm), Zn (1.31ppm), Ni (0.28 ppm), Cr (5.44ppm), Rb (1.7ppm), V (0.97ppm), Y (0.039ppm), Th (9.8 ppm), U (9.8 ppm), Sr (1.0 ppm), and Zr (0.0005 ppm), while the concentration of Hf (below detection limit), Te (below detection limit), Ta (below detection limit) are below detection limit. The values of the studied samples are similar to the concentration of trace element in granite (Haïmeur et al., 2004; Divakara-Rao et al., 1999; Frost et al., 2006; Almeida et al., 2010; Mikkola et al., 2014; and Moyen et al., 2003).

The Rb/Sr ratios (0.23) are relative low and similar to that granite (1.3, Shang 2007; 0.12, Moyen et al., 2003; 0.35, Almeida et al., 201; 00.7, Frost et al., 2006; 0.39 Mikkola et al., 2014), equally the Th/U ratios (3.95) are relatively very low and closely similar to granite (3.8, Somarin 2017; 6.48, Mikkola et al., 2014).

The Rb/Ba ratio (0.025) is similar to that of granite (0.45, Shang 2007, 5.0 Haïmeur et al. 2004; 0.039 Almeida et al. 2010; 0.20, Mikkola et al., 2014).

The other element in trace amount Zr (0.002 ppm), Co (0.053 ppm), and Sr (7.26 ppm) show moderately low contents and variable while Cu (0.13 ppm) Hf (below detection limit) content are very low similar to that of the average composition of granite.

The large ion lithophile elements (LILE) compositions in the studied samples show relatively low concentration. These include Rb (1.7 ppm), Th (0.286 ppm), U (0.0723 ppm), Ba (67.9 ppm) and Sr (7.26 ppm).

The concentration of high field strength elements (HFSE) such as Zr (0.0002 ppm show uniform distribution; V (0.97 ppm); and Hf (below detection limit) are very low.

The Zr/Y (0.051) ratios are lower compared to granite (5.3, Haïmeur et al. 2004; 3.0 Almeida et al. 2010; 11.0, Frost et al. 2006; 16.7, Mikkola et al. 2014).

The Nb/Y (below detection limit) ratios are also relatively low (0.2, Shang 2007; 1.2, Haïmeur et al. 2004; 0.57, Almeida et al. 2010; 0.31 Frost et al. 2006; 0.7, Mikkola et al. 2014). The Zr/Y ratios are higher when compared to the Nb/Y ratios as the value of Nb falls below detection limit.

The transition elements abundances within the studied sample, such as, Cr (0.002 ppm), and Ni (2.66 ppm) are also low suggesting the depletion of mafic minerals.

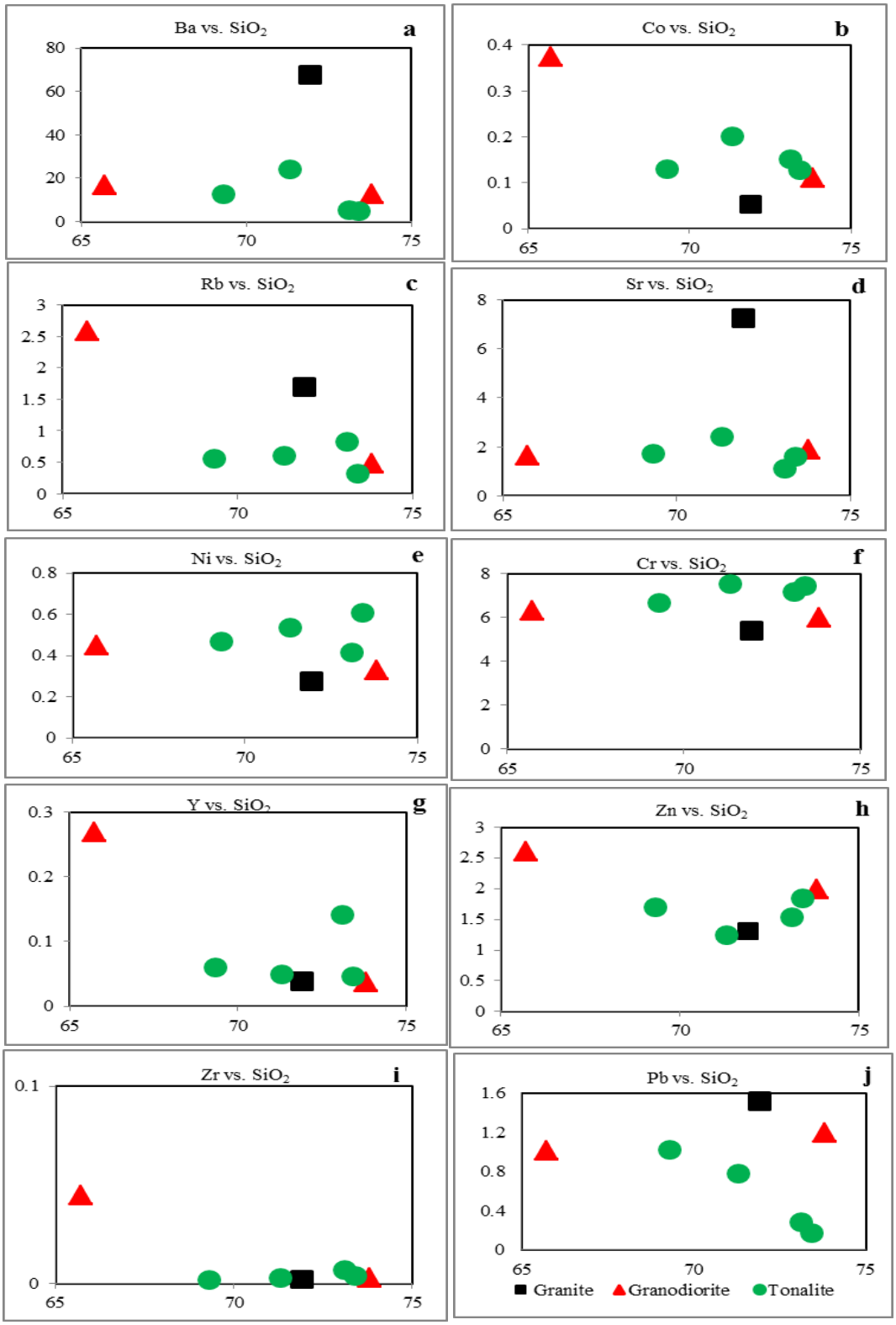

Figure 32: Binary diagram for some trace element variation with SiO_2 for Nkout plutonic rocks

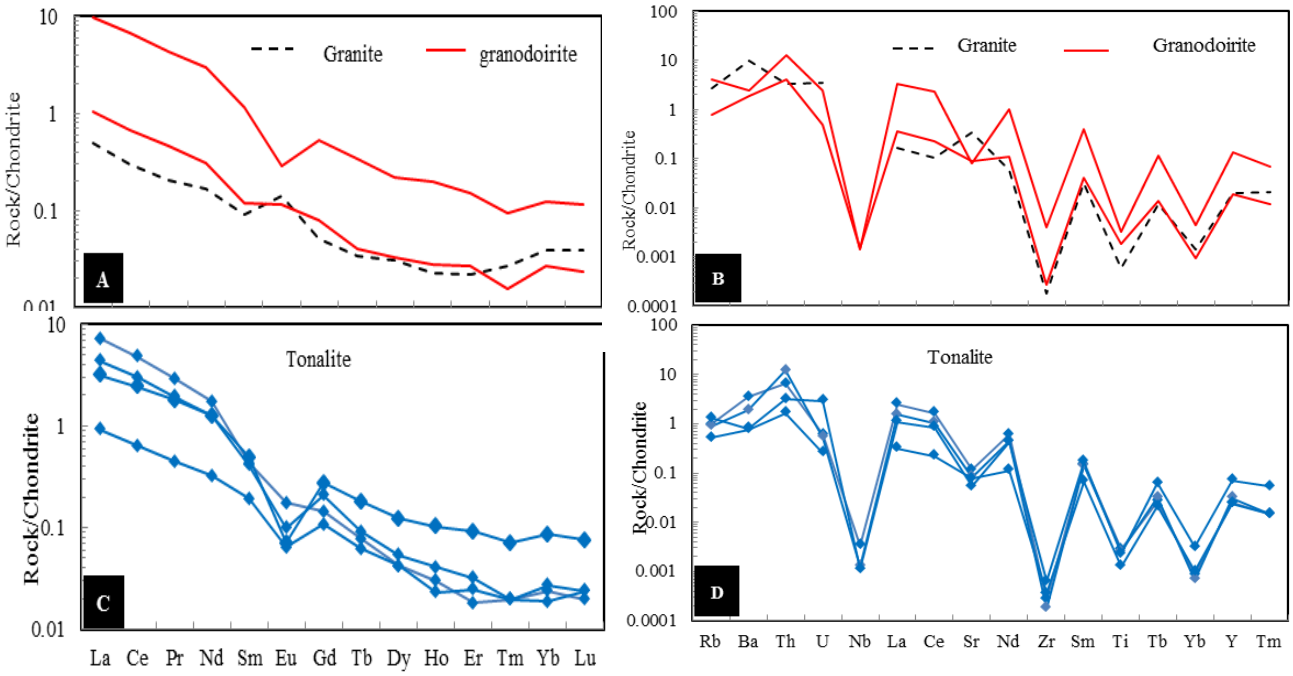

Figure 33: Multi-element and rear earth elements (REEs) diagrams of Nkout plutonic rocks (granite, granodiorite and tonalite). Values for normalisation are after Evensen et al. **(**1978**)** and Thompson et al. (1982) respectively

V.1.1.1.3. Rare Earth Elements (REEs)

The rear earth elements (REEs) abundance of the studied sample is low (0.50**,** Table 3). The results show that the concentrations of La and Lu are 0.0007 and 0.119 ppm respectively.

The results are lower when compared to the average values of granite in central Maroco (ΣREE= 39.75 - 57.44, average = 48.5, Haïmeur et al., 2004), Mongolia (ΣREE= 86.2 - 185.14 average = 135.67, Buriánek et al., 2012), Indian Shield (ΣREE=156) after Divakara-Rao et al., (1999), Central Wyoming (ΣREE=133) after Frost et al. (2006), Rio Maria terrane-Brazil (ΣREE=127) after Almeida et al. (2010), Surmansuo-Eastern Finland (ΣREE=243.92) after Mikkola et al. (2014), and Dharwar Craton-India (ΣREE=694) after Moyen et al. (2003).

The results were chondrite-normalised to the values of Evensen et al**.** (1978). The fractionation is characterized by a significant enrichment in light rear earth elements (LREEs) over heavy rear earth elements (HREEs).

The chondrite-normalised values for the samples portray relatively high LREEs fractionation indicated by $(La/Sm)_{CN}$ ratio (3.27). The results indicate relatively higher LREEs fractionation in other granite {average $(La/Sm)_{CN}$ = 2.97, Haïmeur et al. 2004; $(La/Sm)_{CN}$ = 7.49, Frost et al. 2006; $(La/Sm)_{CN}$ = 5.78, Almeida et al. 2010; $(La/Sm)_{CN}$ = 6.13, Mikkola et al. 2014; $(La/Sm)_{CN}$ = 3.88, Moyen et al. 2003).

The La_{CN}/Yb_{CN} value (12.40) is relative higher to the $(Gd/Yb)_{CN}$ ratio (1.32), revealing depletion of the heavy HREEs over LREEs.

The studied sample show similar result when compared to granite rock {average $(La/Yb)_{CN}$ = 7.75, $(Gd/Yb)_{CN}$ = 1.53, Haïmeur et al. 2004; $(La/Yb)_{CN}$ = 42.1, $(Gd/Yb)_{CN}$ = 3.37, Frost et al. 2006; $(La/Yb)_{CN}$ = 49.3, $(Gd/Yb)_{CN}$ = 2.88, Almeida et al. 2010; $(La/Yb)_{CN}$ =57.9 , $(Gd/Yb)_{CN}$ = 5.12, Mikkola et al. 2014; $(La/Yb)_{CN}$ = 23.1, $(Gd/Yb)_{CN}$ = 2.40, Moyen et al. 2003}, which reveals depletion of the heavy HREEs relative to LREEs.

The analysed sample (MnO2) shows lower total REEs abundance (0.50), strong positive Eu anomalies (Eu/Eu* = 2.06) relative to the granitic values (average Eu/Eu* = 0.4, Haïmeur et al. 2004; Eu/Eu* = 0.48, Buriánek et al. 2012; Eu/Eu* = 1.12, Frost et al. 2006; Eu/Eu* = 0.89, Almeida et al. 2010; Eu/Eu* = 0.57, Mikkola et al. 2014; Eu/Eu* =1.55 Moyen et al. 2003).

The chondrite normalized rare earth elements (REEs) patterns for studied sample is displayed in figure 33A. It is sub-flat and show that the sample of the Nkout area reflect highly fractioned REEs compositions as revealed by the La_{CN}/Yb_{CN} ratio (Fig. 33A), with LREEs enrichment {$(La/Yb)_{CN}$ = 12.4} relative to HREEs {$(Gd/Yb)_{CN}$ = 1.31}, slightly strong positive Eu anomaly (Eu/Eu* = 2.06), suggesting plagioclase accumulation in the rock.

The multi-element normalized to Thompson, (1982) for the studied samples are shown in figure 33B. The patterns display negative Nb, Sr, Zr and Ti and Yb anomalies with Ta below detection limit (Fig 33B). These types of anomalies were interpreted by Thompson (1984) as the contribution of the continental crust to the genesis of the rock.

V.1.1.2 GRANODIORITE

The rock is represented in the plutonic group by the studied samples (NKR1 and DJO2). The geochemical composition of the rock is represented in table 4.

V.1.1.2.1. Major Element Oxides (MEO)

The variations in SiO_2 concentration for the studied rock samples range from 65.7 - 73.8 wt. % (average = 77 wt. %) similar to that of granodiorite rock (SiO_2 = 66.09) after Le Maître (1976), Sangmelima, Congo craton (SiO_2 = 67.08) after Shang et al. (2007), Gauldalen-Central Norway (SiO_2 = 73.96) after Pannemans et al. (2000), Rio Maria terrane-Brazil (SiO_2 = 72.34) after Almeida et al., (2010), Napier Complex of Enderby Land, Antarctica (SiO_2 = 69.83) Sheraton et al. (1985), and Kuhmo district, eastern Finland (SiO_2 = 66.6) after Käpyaho (2006).

The (total iron) $Fe_2O_3^*$ content range from 2.62 to 6.75 wt. % (average = 4.6) is closely similar to that of granodioritic rock (4.11, Le Maître 1976; 0.57, Pannemans et al., 2000; 2.4, Almeida et al., 2010; 1.01, Sheraton et al., 1985; and 3.6, Käpyaho, 2006).

The Al_2O_3 contents (13.7 - 14.9, average = 14.3, Tab. 4**)** are closely similar to granodioritic composition (15.73, Le Maître 1976; and 15.4, Shang et al. 2007 and 2010; 15.19, Pannemans et al. 2000, 14.5 Almeida et al. 2010; and 14.87, Sheraton et al. 1985; and 15.4 Käpyaho 2006).

Their alkali content K_2O (2.18 - 3.58 wt. %, average = 2.8) and Na_2O (3.8 - 3.87 wt. % average = 3.8) show similar content (2.73 and 3.75 respectively, Le Maître, 1976; and 2.8 and 3.67, Shang et al. 2007 and 2010; 3.2 and 4.5, Pannemans et al. 2000; 2.51 and 4.6, Almeida et al., 2010; 2.7 and 4.09, Sheraton et al., 1985; 3.6 and 4.7, Käpyaho 2006).

The K_2O/Na_2O ratios (0.5 - 0.94 wt. %, average = 0.7) are similar to the average granodiorite value (0.73, Le Maître, 1976; 0.76, Shang et al., 2007 and 2010; 0.76, Käpyaho 2006).

The total alkali ($Na_2O + K_2O$) contents (6.05 - 7.38 wt. %, average = 6.7) of the studied samples are similar to the average value of granodiorite rock (6.44, Le Maître, 1976; 6.34, Shang et al., 2007, 7.2 Almeida et al., 2010; 6.7, Sheraton et al. 1985; 8.3, Käpyaho 2006), indicating the association of more feldspars mineral in granodiorite.

The concentrations of MgO (0.59 - 1.12 wt. %, average = 0.85) and the CaO contents (2.62 - 3.15 wt. %, average = 2.8) are similar to the average values of granodioritic composition (1.74 and 3.83 respectively, Le Maître 1976; 0.18 and 1.59, Pannemans et al. 2000; 0.6and2.5 Almeida et al., 2010; 1.39 and 2.98, Sheraton et al. 1985; 1.87and 2.6, Käpyaho 2006).

TiO_2 (0.28 - 0.78 wt. %, average = 0.5) and MnO (0.04 - 0.08 wt. %, average = 0.06) concentrations in the studied samples are in minor amount, they vary and are similar to the average granodiorite values (0.54 and 0.08 respectively, Le Maître 1976; 2.8 and 0.05, Shang et al. 2007 and 2010; 0.05 and 0.03, Pannemans et al. 2000; 0.32 and 0.3, Almeida et al. 2010; 0.32, Sheraton et al. 1985).

The average Al_2O_3/TiO_2 ratio (34) of the studied samples are similar to that of the average value (31.4, Le Maître 1976).

Fe_2O_3/MgO ratio (5.23) is relative higher and similar compared to that of the granodioritic content (0.7, Le Maître 1976; 5.01, Shang et al. 2007 and 2010).

P_2O_5 contents (0.03 - 0.24wt. %, average = 0.15) are as well similar to the average values of granodiorite (0.8, Le Maître, 1976; and 0.04, Pannemans et al. 2000; 0.07 Almeida et al., 2010; 0.07, Sheraton et al. 1985; 0.43, Käpyaho 2006).

The major element contents of the studied rock samples are similar to that of the average contents of granodiorite according to Le Maître (1976), Shang et al. (2007 and 2010) and Pannemans et al. (2000), Almeida et al. (2010), Sheraton et al. (1985) and Käpyaho (2006).

On the Harker binary diagram, the sample plots are scattered with the other major elements (Fig. 30).

The samples display both peraluminous (DJO2) and metaluminous (NKR) characteristic on the A/NK vs. A/CNK diagram (Fig. 31A). The ratios of $Al_2O/CaO+Na_2O+K_2O$ is < 1.1, places the studied rock samples in a field of I-type igneous rock with calc-alkaline to high-K affinities on the K_2O vs SiO_2 diagram similar to granodiorite rock (Fig. 30B).

V.1.1.2.2. Trace Elements (TE)

The trace element contents of the studied samples are Ba (13.05 - 17.15ppm, average = 15.1), Zn (1.99 - 2.61 ppm, average = 2.3), Ni (0.330 - 0.45 ppm average = 0.39), Cr (5.99- 6.31 ppm; average = 6.51), Rb (0.492 - 2.59ppm; average = 1.50), V (1.14 - 1.37ppm; average = 1.25), Y (0.0372 - 0.269 ppm; average = 0.15), Th (0.338 - 1.06 ppm; average = 0.66), U (0.0104 - 0.0526 ppm; average = 0.035), Sr (1.68 - 1.9 ppm; average = 1.78), Zr (0.0003 - 0.045 ppm; average = 0.024), and Hf (0.002), while the concentrations of Te (below detection limit), Ta (below detection limit) are relatively similar to granodioritic rock.

The rock samples show significant low variations of average concentrations in the large ion lithophile elements (LILE), these include: Rb (average: 0.67 ppm), Th (average: 24.1 ppm), U (average: 4.25 ppm), Ba (average: 6.26 ppm), and Sr (average: 0.24 ppm) similar to average contents of the granodiorite rock (Shang et al., 2007; Pannemans et al., 2000; Sheraton et al., 1985; Almeida et al., 2010; Käpyaho, 2006).

The Rb/Ba (0.003 - 0.15) ratios are similar to the average contents of granodiorite (0.04, Shang 2007; 0.08, Pannemans et al. 2000; 0.04, Sheraton et al. 1985; 0.06, Almeida et al. 2010; 0.05, Käpyaho 2006), while Rb/Sr ratios (0.25 - 1.54) are relatively similar to the average value of granodioritic rock (0.12, Shang 2007; 0.3 Pannemans et al. 2000; 0.15, Sheraton et al. 1985; 1.40, Almeida et al. 2010; 0.05, Käpyaho 2006).

Th/U ratios (20.0 - 32.5) are relative higher than the rock values (0.3, Shang et al. 2007; 10, Sheraton et al. 1985; 3.66, Käpyaho 2006).

The concentrations of high field strength elements (HFSE) are also very low with uniform distribution (Zr = 0.011 ppm; V = 0.02 ppm; and Hf = 0.0008 - 0.001ppm) relatively similar to the granodioritic rock (Pannemans et al. 2000; Sheraton et al. 1985; Almeida et al. 2010; Käpyaho 2006).

The transition elements abundances of the studied samples vary widely whereas some are below detection limit. Y (0.02 - 0.17 ppm) and Nb (0.0041 - 0.0045 ppm) are very low and variable while Ta is below detection limit. Zr and Sr show a similar average abundance in the rock types.

Zr/Y (0.08 - 0.1610. average: 12 ppm) ratios are relatively low compared to the average contents of granodiorite rock (5.783, Pannemans et al., 2000; 34.65, Shang, 2007; 18 Sheraton et al., 1985; 1.04, Almeida et al., 2010; 16.5, Käpyaho, 2006) as well as Nb/Y (0.030-0.004l, average: 0.017 ppm) ratios are relatively similar to the average content of granodiorite and calco-alkaline series (0.75, Shang, 2007; 0.39, Pannemans et al., 2000; 0.57, Sheraton et al., 1985; 0.04, Almeida et al., 2010; 0.46, Käpyaho, 2006).

The SiO_2 content increases with decrease in the content of Co, Rb and Y while it is constant with the other trace elements, on the binary plots (Fig. 32).

V.1.1.2.3. Rare Earth Elements (REEs)

The rear earth elements (REEs) contents for the studied rock samples show lower concentrations light rear earth elements (LREEs) (La - Gd), La varies between 0.25 - 2.4 ppm (average = 1.3 ppm), and Gd varies between 0.0165 - 0.107ppm with average of 0.06 ppm.

The heavy rear earth elements (HREEs) (Tb - Lu) are variable. Tb varies between 0.0015 - 0.0127 ppm (average = 0.007 ppm), and Lu varies between 0.0006 - 0.0029 ppm with average of 0.001.

The REEs abundance of studied samples are low and varies form 0.9765 - 9.2092 ppm (average = 5.09 ppm) when compared to the granodiorite values (ΣREE 16.68 - 36.39 ppm, average = 29.5 ppm, Pannemans et al., 2000; ΣREEs=165.12 ppm Almeida et al., 2010; ΣREEs=190.47 ppm, Käpyaho, 2006).

The results were chondrite-normalised to the values of Evensen et al**.**, (1978). The fractionation is characterized by a significant enrichment in LREEs over HREEs as in the granite rock.

The $(Gd/Yb)_{CN}$ ranges from 3.03 - 4.18 (average = 3.60), which reveals depletion of heavy HREEs over LREEs, similar to that of the granodioritic rock {$(Gd/Yb)_{CN}$ = 2.3, Almeida et al., 2010; 5.3, Käpyaho, 2006}.

The $(La/Yb)_{CN}$ values range from 39.67 - 78.76 with an average value of 59.22, indicating high REEs fractionation similar to the granodiorite rock {$(La/Yb)_{CN}$ = 4.41 Pannemans et al., 2000; 30.02, Almeida et al., 2010; 48.6 Käpyaho, 2006}.

The studied rock samples also show both negative (Eu/Eu^*_{CN} = 0.36, sample NKR) and a slightly positive (Eu/Eu^* = 1.18, sample DJO2) Eu anomalies, with an overall average value of 0.77 similar to granodiorite rock which show negative Eu anomalies (Eu/Eu^*_{CN} =0.92, Almeida et al., 2010; 0.72, Käpyaho, 2006).

The plots are shown in figure 33A. On the chondrite-normalised pattern (Fig. 33A), the rock shows light REEs enrichment over HREEs similar to the granodiorite rock (Pannemans et al., 2000). The granodiorite displays gentle and parallel REEs patterns with slightly high and variable REEs abundance (ΣREE = 0.97 - 9.20 ppm, average = 5.09 ppm) when compared to the granodiorite rock.

The $(La/Yb)_{CN}$ values show high REEs fractionation which is 10 times higher than the chondrite values. The sample with the positive anomaly could probably be due to high plagioclase accumulation while the sample with the negative anomaly could roughly be correlated to the increase in SiO_2, hence to the magmatic differentiation process.

Multi-element normalized to the values suggested by Thompson (1982) for the studied samples are shown in figure 33B. On the diagram, the samples show similar pattern as in the

granodiorite rock (Fig. 33B). The rocks show negative Nb, Sr, Zr and Ti and Yb anomalies with Ta below detection limit as that of the granite rock.

V.1.1.3 TONALITE

The rock samples of the study area are represented in the plutonic rock group (DJO1, DJO3, MN01, and MN04). The geochemical composition of the rock is represented in table 3.

V.1.1.3.1. Major Element Oxides (MEO)

The studied rock samples are characterized by variation in SiO_2 contents (69 - 73.8 wt. % average = 71.7) which are slightly higher than the average values of the tonalitic rock (SiO_2 = 61.52 after Le Maître, (1976), Sangmelima, Congo craton (SiO_2 = 66.6) after Shang et al., (2007 and 2010), and Elder Creek, California (SiO_2 = 66.1) after Shervais (2008), Napier Complex of Enderby Land, Antarctica (SiO_2 =65.95) after Sheraton et al. (1985) and Kuhmo district, eastern Finland (SiO_2 = 67.8) after Käpyaho (2006).

The Fe_2O_3 contents (3- 4.09, average = 3.5 wt. %) are similar when compared to the average tonalite concentrations (1.83, Le Maître 1976; 3.78, Shang et al. 2007 and 2010; 5.15, Shervais 2008; 2.52, Sheraton et al., 1985; and 4.33, Käpyaho 2006).

The Al_2O_3 contents (14.4 - 15.5 wt. % average = 14.9) are similar to the average value of tonalitic rock (16.48, Le Maître, 1976; 16.54, Shang et al., 2007; 14.6, Shervais 2008; 14.50, Sheraton et al., 1985; 15.2, Käpyaho 2006).

The MgO contents rang from 0.64 - 0.88 wt. % (average = 0.7) are slightly depleted to that of the tonalit rock (2.80, Le Maître 1986; 1.6, Shang et al. 2007; 1.93, Shervais 2008; 1.87, Sheraton et al. 1985; 1.8, Käpyaho 2006).

CaO contents (3.02 - 3.4 wt. %, average = 3.3) are similarly lower to the average tonalite value (5.42, Le Maître 1976; 3.9, Shang et al. 2007; 5.66, Shervais 2008; 4.5, Sheraton et al. 1985; 4.26 Käpyaho 2006).

The Na_2O contents vary from 4.53 - to 4.8 wt. % (average = 4.7) while the K_2O contents range between 0.96 - 1.39 wt. % (average = 1.1). They are similar to the average value of tonalite rock (3.63 and 2.07 respectively, Le Maître, 1976; 4.1 and 0.22, Shervais, 2008; 3.9 and 1.3, Shang et al., 2007; 3.9 and 4.5, Sheraton et al., 1985; 4.33 and 1.62, Käpyaho, 2006). The average values of Na_2O are relative higher than the corresponding average K_2O.

The total alkali ($K_2O + Na_2O$) contents (5.67 - 6.1 wt. % average = 5.7) are similar to average value of tonalitic composition (5.7, Maître, 1976; 4.38, Shervais, 2008; 5.9, Shang et al., 2007; 8.3, Sheraton et al., 1985; and 5.9, Käpyaho, 2006).

K_2O/Na_2O ratios (0.2 - 0.3 wt. %, average = 0.25) in the studied samples are slightly lower when compared to the ratios of the tonalite rock (0.61, Le Maître 1976; 0.29, Shang et al. 2007).

TiO_2 contents (0.22 to 0.78 wt. % average = 0.5) are similar to the average value (0.73, Le Maître 1986; 0.39, Shang et al. 2007; 0.75, Shervais 2008; 1.57, Sheraton et al. 1985; 0.55, Käpyaho 2006).

The MnO contents vary from 0.03 to 0.13 wt. % with an average value of 0.08 are similar to the average concentrations (0.08, Le Maître 1986; 0.06, Shang et al. 2007and 2010; 0.11, Shervais 2008; 0.12, Sheraton et al. 1985; 0.07, Käpyaho 2006).

The concentrations of P_2O_5 in the studied samples are low and depleted ($\leq$ 0.09 wt. %) relative to the average concentrations (0.25, Le Maître 1976; 0.10, Shang et al. 2007and 2010; 0.17, Shervais 2008; 0.17, Sheraton et al. 1985, 0.10 Käpyaho 2006).

The major elements content of the studied rock is similar to the average contents of tonalitic rock (Le Maître, 1976; Shang et al., 2007 and 2010; Shervais, 2008; Sheraton et al., 1985 and Käpyaho, 2006).

On the binary plots for major element oxide, SiO_2 contents increase with decrease in the contents of the other elements. A negative correlation exists between SiO_2 and MgO ($r^2 = 0.62$), and SiO_2 and Na_2O ($r^2 = 0.89$) and SiO_2 and Al_2O_3 ($r^2 = 0.85$), SiO_2 and TiO_2 ($r^2 = 0.71$ Fig. 30). Negative correlation exist between SiO_2 and Fe_2O_3 ($r^2 = 0.24$), between SiO_2 and P_2O_5 ($r^2 = 0.51$) Fig. 30). A positive correlation is established between SiO_2 and MnO ($r^2 = 0.51$; Fig. 30).

The rock samples plot at the limit between peraluminous and metaluminous fields on the A/NK vs. A/CNK diagram with the ASI index (A/ CNK ~1) indicating I-type igneous rock, and a low-K composition (tholeiite series) as shown on the K_2O vs SiO_2 diagram (Fig. 31B).

V.1.1.3.2. Trace Elements (TE)

The concentrations of trace elements in studied rock are variable and low: Ba (5.29 - 24.3 ppm, average = 12.05), Zn (1.25 - 1.85 ppm, average = 1.58), Ni (0.42 - 0.61 ppm average = 0.51), Cr (6.68 - 7.57 ppm; average = 7.3), Rb (0.327 - 0.834 ppm; average = 1.58), V (1.33-1.56 ppm; average = 1.37), Y (0.0473 - 0.1415 ppm; average = 0.07), Th (0.138-1.005 ppm; average = 0.46), U (0.0054 - 0.0619 ppm; average = 0.025), Sr (1.115 - 2.45 ppm; average = 1.7 ppm), Zr (0.0002 - 0.007 ppm; average = 0.004), while the concentration of Hf (below detection limit), Te (below detection limit), Ta (bdl) are absolutely below detection limit similar to the average concentration of tonalite rock (Käpyaho, 2006; Sheraton et al., 1985)

The average value of the large ion lithophile elements (LILE) in the samples are significant low (average: Rb = 0.255 ppm, Th = 16.7 ppm, U = 3.04 ppm, Ba = 5.0 ppm, Sr = 2.3 ppm) similar to that of tonalite rock (Le Maitre, 1976).

The Rb/Ba (0.025 - 0.148) ratios in the studied samples are low and vary widely relative similar to tonalite rock (0.02, Shervais, 2008; 0.06, Shang, 2007; 0.02 Sheraton et al., 1985; 0.12, Käpyaho, 2006) as well as the average Rb/Sr ratios (0.25 - 0.74), relative similar when compared to

other tonalite rock (0.005, Shervais, 2008; 0.08, Shang, 2007; 0.03, Sheraton et al., 1985; 0.18, Käpyaho, 2006).

The Th/U ratios (4.2 - 89.7) are also closely similar to that of tonalitic (3.2, Shervais, 2008; 3.9, Käpyaho, 2006).

The average high field strength elements (HFSE) concentrations are also low (Zr = 0.001 ppm of uniform distribution; V = 0.024 ppm; and Hf is below detection limit). The concentrations of Zr range from 0.002 to 0.007 ppm are similar to the average value of the tonalitic rock.

The transition element abundances within the studied samples are low as well (Cr (average = 0.002ppm, and Ni average = 0.005ppm). Ta is below detection limit in all the granite, granodiorite and tonalite samples.

Zr/Y ratios (0.032 - 0.085 ppm; average: 0.057 ppm) are high than the Nb/Y ratios (0.006 - 0.048, average: 0.017 ppm). The Zr/Y (0.03 - 0.081) ratio is lower when compared to the average content in tonalite (5.44, Shervais, 2008; 15.2, Sheraton et al. 1985; 14.0 Käpyaho, 2006) as well as the Nb/Y (0.01 - 0.048) ratios, relatively similar to that of tonalite (0.16, Shervais, 2008; 0.62, Shang, 2007; 0.4 Sheraton et al., 1985; 0.43, Käpyaho, 2006).

SiO_2 content also increase with decrease in the content of Co, Rb, Pb, and Y as in the granodiorite. Cr and Ni show a positive correlation with SiO_2 while little or no correlation exists between Zr, Zn, Cr, Sr, and Ba with SiO_2 (Fig. 32).

V.1.1.3.3. Rare Earth Elements (REEs)

The rear earth elements (REEs) abundance of studied samples are low and vary form 0.95 - 6.11 ppm (average = 3.62 ppm) relative to the average abundance of tonalite rock (46.25 - 86.82 ppm, average = 72.9 Shervais, 2008; ΣREE = 91 ppm, Käpyaho, 2006).

The concentrations of light rear earth elements (LREEs = La - Gd) are variable. La ranges between 0.226 - 1.765 ppm (average = 0.96 ppm), while Gd varies between 0.02 - 0.05 ppm with average of 0.03 ppm. The concentrations of heavy rear earth elements (HREEs= Tb - Lu) vary. Tb varies between 0.0023 - 0.0068 ppm (average = 0.003ppm) and Lu varies between 0.0005 - 0.0019 ppm with average of 0.0009 ppm.

The REEs values show significant enrichment in LREEs over HREEs. The results were chondrite-normalised to the values of Evensen et al., (1978) with their fractionation similar to that of tonalitic rocks.

The $(La/Yb)_{CN}$ ratios are high, ranging between 34.11 and 307 (average = 153.53), while the $(Gd/Yb)_{CN}$ ratios are low (average = 6.07). This indicates depletion in HREEs relative to LREEs, similar to the average values of tonalitic rock {$(La/Yb)_{CN}$ = 2.7, $(Gd/Yb)_{CN}$ = 1.46, Shervais, 2008; $(La/Yb)_{CN}$ = 10.2, $(Gd/Yb)_{CN}$ = 1.95, Käpyaho, 2006}. The chondrite-normalized REEs patterns for

the samples are shown in figure 33C. On the diagram (Fig. 33C), they show LREEs enrichment rate of 1 to 10 times than the chondrite.

The REEs patterns show strong negative Eu anomalies (Eu/E^*_{CN} = 0.19 - 0.77; average = 0.41), similar values of tonalitic rock with slight positive Eu anomalies (0.84 > Eu/Eu* > 1.13, average = 0.90, Shervais, 2008; Eu/Eu* = 0.72, Käpyaho, 2006).

Multi-element of the studied samples are normalized to the values of Thompson, (1982). The pattern is shown in figure 33D. The rock shows similar multi-element behaviour with tonalitic rock when normalised to chondrite (Fig. 33B).

V.1.2. METAMORPHIC ROCKS

The metamorphic rocks of the Nkout study area consists of country rock and banded iron formation. Their whole rock major, trace and rare earth elements (REEs) data are presented in Table 4.

The protolith nature of country rock were determine by the construction of the discrimination diagram after De La Roche (1965), which is confirmed and established by the plot after Roser and Korsch, (1988).

The discrimination diagrams of De La Roche (1965) for the studied samples are shown in figure 34A and 34B. On the (Fe_2O_3 + TiO_2 + CaO)% vs (Al_2O_3)% and 100 MgO/(K_2O + MgO + Na_2O) vs 100 Na_2O/(K_2O + MgO + Na_2O) binary diagram (De La Roche, 1965), the studied samples plot in the field of igneous rocks, characterised with gabbroic to dioritic or basaltic composition (Figs. 34A and 34B). Therefore, the discrimination diagrams show igneous derive provenance.

The discrimination diagrams of Roser and Korsch (1988) for the studied samples are shown in figure 34. The F1 vs. F2 discrimination diagram of Roser and Korsch (1988) shows that the research samples plot on the area of mafic igneous rocks (where F1 = (-1.773 TiO_2 + 0.607 Al_2O_3 + 0.76 Fe_2O_3t -1.5 MgO + 0.616 CaO + 0.509 Na_2O - 1.224 K_2O) - 9.09) and F2 = (0.445 TiO_2 + 0.07 Al_2O_3 - 0.25 Fe_2O_3t - 1.142 MgO + 0.438 CaO + 1.475 Na_2O + 1.426 K_2O) - 6.861). This further confirms and establishes that the protolith of these samples could have resulted from mafic igneous rocks (Fig. 34).

We therefore infer that the studied metamorphic rock samples show mafic igneous rocks composition (Figs. 34A and 34B; Fig 35). The petrographic study of the rock samples provided that the mafic meta-igneous rocks provenance are made up of amphibole-biotite gneiss and garnet-magnetite gneiss. These rocks are usually underlined by magmatic rock.

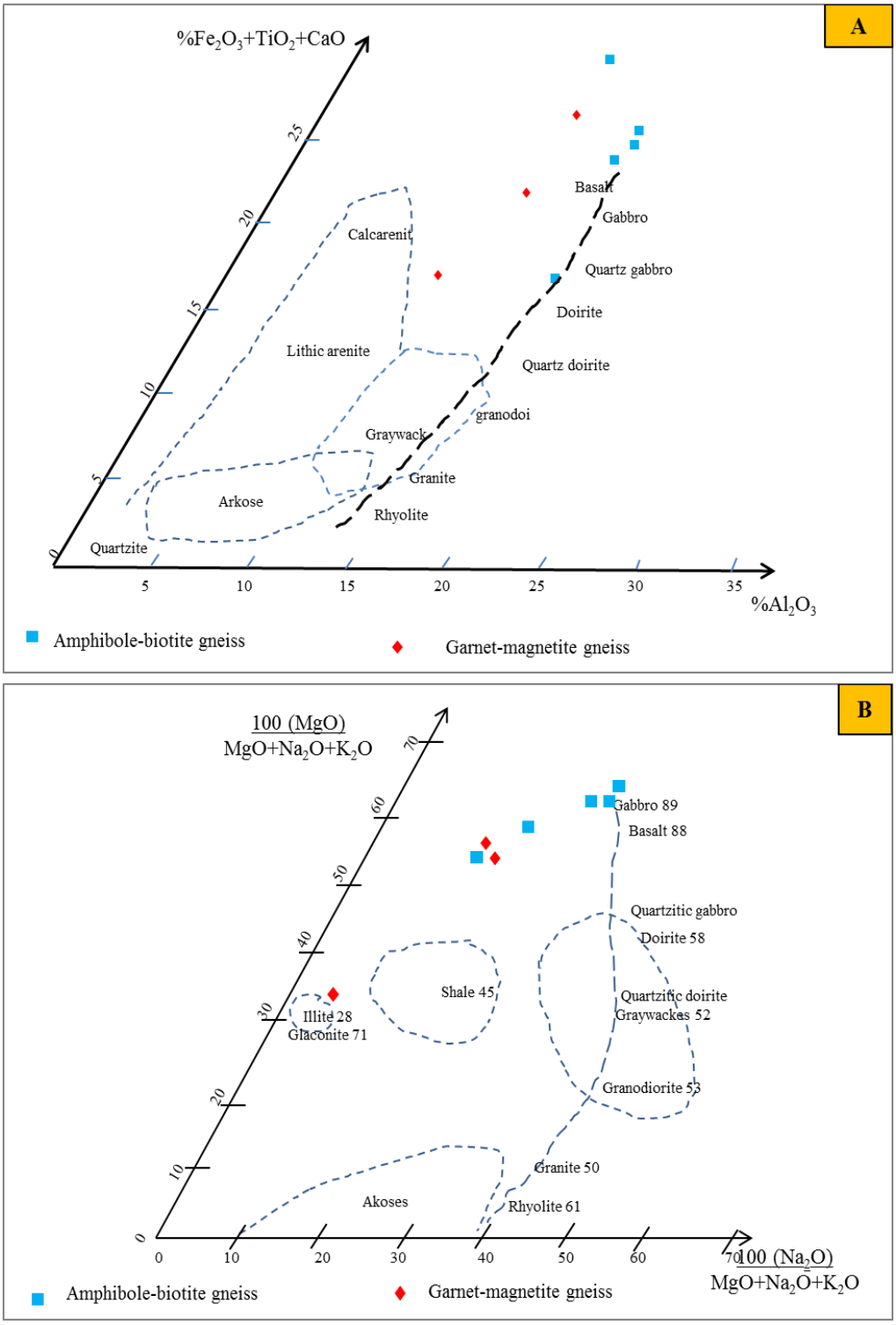

Figure 34: Protolith reconstruction and classification (after De La Roche, 1965) of gneiss at Nkout, (**A**) position of studied rock in the whole rock binary (Fe_2O_3 + TiO_2 + CaO)% vs. (Al_2O_3)% showing meta-igneous derive rock and (**B**) position of studied rocks in the silico-aluminate triangle 100 MgO/(K_2O + MgO + Na_2O) vs. 100 Na_2O/(K_2O + MgO + Na_2O) discrimination diagram confirming igneous derive rock.

Table 5: Major, trace and REEs elements geochemical composition (wt. %) of study Meta- igneous rock (gneiss)

	Garnet-magnetite gneiss			Amphibole-biotite gneiss				
Wt.%./Sample	WH4-11	WH3-8	CH7-6	EH2-3	MN03	DJO4	DJO5	MIE1
SiO_2	70.9	58.3	60.7	51.2	50.1	49.8	47.4	58.6
TiO_2	0.26	0.35	0.35	0.3	1.11	0.86	0.9	0.46
Al_2O_3	8.09	10.8	10.8	10.2	13.95	14	14.05	14.9
Fe_2O_3	15.3	23.9	20	25.6	13.85	13.05	15.3	8.77
MgO	2.57	3.3	1.49	4.72	6.61	6.17	6.6	6.15
MnO	0.07	0.09	0.09	0.13	0.23	0.18	0.18	0.13
CaO	0.85	2.03	0.85	2.97	10.1	9.78	8.16	7.46
Na_2O	0.74	1.18	0.19	1.34	2.9	2.69	2.22	2.79
K_2O	1.41	1.89	2.86	2.72	0.88	1.18	2.48	1.03
P_2O_5	0.06	0.25	0.05	0.09	0.09	0.06	0.06	0.08
LOI	0.26	-0.2	1.1	1.05	0.34	0.76	1.38	0.08
Total	100.57	101.99	98.72	100.39	100.21	98.59	98.83	100.55
Trace (Ppm)								
Ba	16.7	40.3	169	20.3	2.03	8.77	62.7	9.06
Co	0.349	0.488	0.425	0.241	0.253	0.319	0.862	0.352
Cr	11.5	12.55	4.67	6.45	6	5.25	7.38	7.25
Cu	0.2	<0.05	6.08	0.09	0.34	2.46	1.49	0.71
Fe	7080	9130	2270	3690	2420	1840	3250	2560
Ga	0.07	0.13	0.09	0.05	bdl	0.05	bdl	0.06
Ge	0.05	0.058	0.005	0.031	0.023	0.016	0.016	0.024
Hf	bdl	0.0008	bdl	0.001	bdl	bdl	bdl	bdl
Li	1.02	1.27	2.9	1.11	0.62	0.22	2.24	0.23
Mo	0.147	0.144	0.01	0.044	0.046	0.034	0.037	0.056
Nb	0.0007	0.0014	0.0013	0.0038	bdl	bdl	bdl	bdl
Ni	1.68	2.63	0.43	0.73	0.61	0.98	2.23	1.32
Pb	0.531	0.429	0.558	2.66	0.12	2.38	1.765	0.342
Rb	2.26	6.08	19.4	24	0.123	0.239	3.97	0.846
Sb	0.0054	0.0035	0.0329	0.0011	bdl	0.0008	bdl	0.0037
Se	0.12	0.07	0.09	0.1	0.02	0.03	0.04	bdl
Sr	0.939	2.35	1.21	1.22	1.435	1.235	3.62	1.3
Ta	bdl	bdl	bdl	0.001	bdl	bdl	bdl	bdl
Te	bdl	0.005	0.012	0.005	bdl	bdl	bdl	bdl
Th	0.225	0.423	0.319	0.136	0.0343	0.0335	0.0303	0.19
U	0.204	0.201	0.1905	0.328	0.0374	0.0025	0.008	0.0513
V	1.51	1.82	1.55	1.52	2.21	1.85	4.55	1.94
W	0.018	0.015	0.007	0.01	0.005	0.013	0.004	0.008
Zn	0.96	1.69	1.52	1.66	0.96	1.75	4.89	1.12
Zr	0.005	0.006	0.003	0.004	0.007	0.002	0.009	0.008
REE (Ppm)								
La	0.542	5.34	2.65	0.237	0.1145	0.349	0.1475	0.997
Ce	0.943	9.32	4.69	0.483	0.1815	0.523	0.298	1.685
Pr	0.1005	0.933	0.473	0.0556	0.0203	0.0676	0.0382	0.172
Nd	0.374	3.13	1.555	0.235	0.082	0.265	0.149	0.568
Sm	0.0532	0.286	0.187	0.0552	0.0244	0.0513	0.0375	0.0807
Eu	0.0091	0.0423	0.0437	0.0097	0.0069	0.0133	0.0059	0.0058
Gd	0.0283	0.0839	0.0561	0.0502	0.0232	0.0479	0.0375	0.0577
Tb	0.0026	0.0068	0.0031	0.0087	0.0039	0.0088	0.0061	0.0079
Dy	0.0138	0.0189	0.0094	0.0639	0.0257	0.0443	0.0357	0.0409
Y	0.0506	0.0654	0.0373	0.394	0.1485	0.222	0.202	0.23
Ho	0.0017	0.0028	0.0012	0.012	0.0054	0.0091	0.0075	0.009
Er	0.0042	0.0049	0.0032	0.0384	0.0174	0.0251	0.0232	0.0249
Tm	0.0006	0.0005	0.0006	0.0059	0.0024	0.0031	0.0028	0.003
Yb	0.0044	0.0054	0.0052	0.0574	0.0171	0.0244	0.0219	0.0244
Lu	0.0006	0.0004	0.0007	0.0073	0.0026	0.0032	0.003	0.0035
∑REE	2.1286	19.2403	9.7155	1.7133	0.6758	1.6571	1.0158	3.9098
$(La/Yb)_{CN}$	214.3182	1725.9259	901.9231	8.4146	10.6140	21.4344	13.6073	69.0574
$(Gd/Yb)_{CN}$	0.5909	1.2593	0.5962	0.1516	0.2281	0.3607	0.2785	0.3238
Eu/Eu*	5.8181	4.9469	4.8199	5.4646	4.4723	4.4276	6.2509	8.5241
$(Ce/Sm)_{CN}$	11.0440	22.0567	10.8238	5.7320	2.9420	5.0827	6.4746	29.6552

$Eu/Eu^* = Eu_{CN}/(Sm*Gd)_{CN}^{1/2}$, bdl: below dictection limit

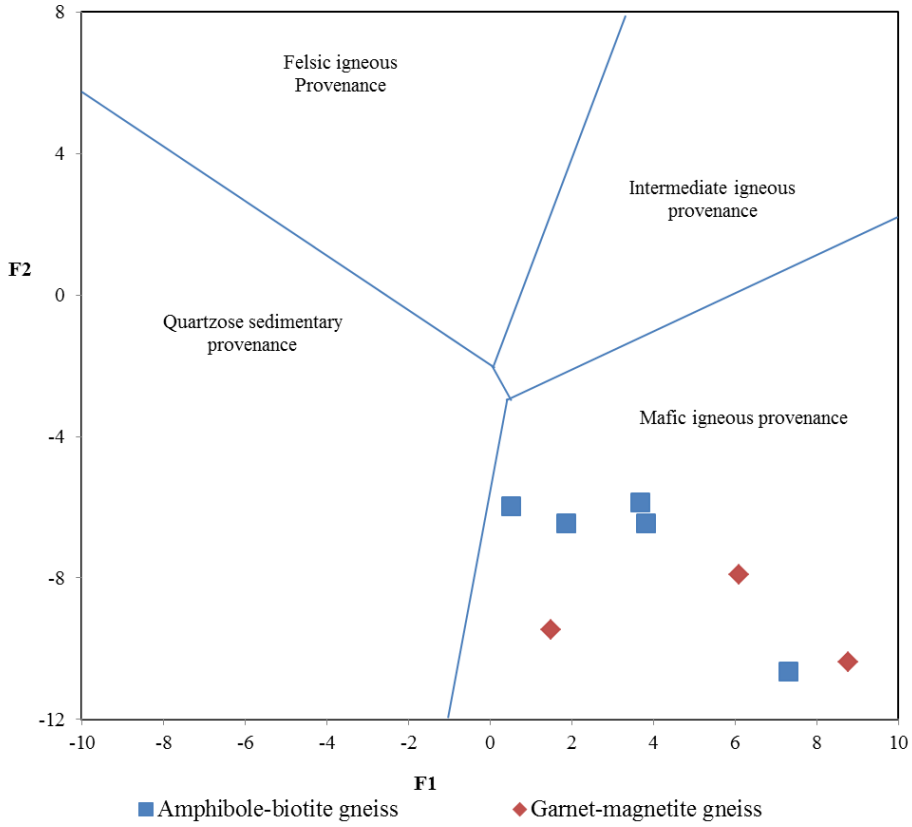

Figure 35: Protolith reconstruction and classification diagram for gneiss at Nkout. F1 vs. F2 discrimination diagram show mafic igneous provenance (after Roser and Korsch 1988). (F1 = (-1.773 TiO_2 + 0.607 Al_2O_3 + 0.76 Fe_2O_3t -1.5 MgO + 0.616 CaO + 0.509 Na_2O -1.224 K_2O) - 9.09) and (F2 = (0.445 TiO_2 + 0.07 Al_2O_3 - 0.25 Fe_2O_3t -1.142 MgO + 0.438 CaO + 1.475 Na_2O + 1.426 K_2O) - 6.861) for both garnet-magnetite gneiss and amphibole-biotite gneiss.

(A) META-IGNEOUS ROCK

The geochemical characteristic of the meta-igneous rock have permitted the classification of two rock groups. They are the garnet-magnetite gneiss and the amphibole-biotite gneissic rocks.

V.1.2.1. GARNET-MAGNETITE GNEISS

The meta-igneous rock is represented by garnet-magnetite gneiss rocks of the studied samples (WH4-11, WH3-8, and CH7-6). The geochemical composition is represented in table 5.

V.1.2 1.1 Major Element Oxides (MEO)

In the discrimination diagram of De la Roche (1965), the garnet-magnetite gneiss shows igneous rock characteristics of gabbroic to dioritic composition (Figs. 34A and 34B).

The SiO_2 contents (58.30 - 70.9 wt. %, average = 63.3) show relatively higher variable when compared the average content in gabbroic rock (50.14) after Le Maître (1976); California (SiO_2 = 55.9) after Shervais (2008); North Hatta Area, United Arab Emirates (SiO_2 = 50.52) after Tokhi et al. (2016); North Eastern Desert, Egypt (SiO_2 = 49.45) after Ibrahim et al. (2015); Gauldalen,

Central Norway (SiO_2 = 49) after Pannemans et al. (2000); SW Mongolia (SiO_2 = 50.0) Buriánek et al. (2012); and Channel Islands (SiO_2 = 49) after Key (1987).

The $Fe_2O_3^*$ contents range between 15 to 23 wt. % (average = 19.7 wt. %), relatively higher when compared to the gabbroic rock (3, Le Maître, 1976; 8.3, Shervais, 2008; 9.0, Tokhi et al., 2016; 4.03, Ibrahim et al., 2015; 9.7, Pannemans et al., 2000; and 9.4, Buriánek et al., 2012; 8.4, Key, 1987).

Al_2O_3 contents (8.09 - 10.8 wt. %, average = 9.8) vary and are relatively depleted compared to the average value after Le Maître (1986, Al_2O_3 = 16.6 wt. %) and Shervais, (2008, Al_2O_3 = 16.04 wt. %); Tokhi et al., (2016, Al_2O_3 = 14.18); Pannemans et al., (2000 Al_2O_3 = 17.8), Key (1987, Al_2O_3 = 16.4) and Buriánek et al., (2012, Al_2O_3 = 16.8).

The MgO contents (1.49 - 3.3wt. % average = 2.4) are similar to the average value (7.59, Le Maître 1976; 5.4, Pannemans et al. 2000; and 5.9, Buriánek et al. 2012; 8.7, Key 1987) while the CaO contents (0.85 - 2.03 wt. %) which does not exceed an average value of 1.2 wt. %, are slightly lower when compared to average value (9.5, Le Maître 1976; 5.2, Shervais 2008; 8.9, Pannemans et al. 2000; and 9.5, Buriánek et al. 2012; 11.0, Key 1987).

K_2O contents (1.41 - 2.89 wt. %, average = 2.2) are slightly higher than the average content (0.93, Le Maître, 1976; 0.31, Shervais, 2008; 0.05, Tokhi et al., 2016; 0.06, Ibrahim et al., 2015; 1.12, Pannemans et al., 2000; and, 1.7, Buriánek et al., 2012; 1.20, Key, 1987).

Na_2O contents vary from 0.10 - 1.18 wt. % (average = 0.7) and are relatively lower when compared to the average content of gabbroic rock (2.3, Le Maître 1986; 4.6, Shervais, 2008; 3.8 Pannemans et al., 2000; and 3.2, Buriánek et al., 2012; 2.1, Key 1987). The average concentration of Na_2O is lower than that of K_2O.

The total alkali contents (K_2O + Na_2O) of the studied samples are moderately high, ranging from 2.15 to 3.07 wt. % (average = 2.7) similar to the average value of gabbroic rock (3.3, Le Maître 1976; 4.9, Shervais, 2008; 0.78, Tokhi et al., 2016; and 3.4, Ibrahim et al., 2015; 3.3, Key, 1987) while the K_2O/Na_2O ratios range from 1.6 to 2.05 wt. % (average = 1.8) are relatively lower than that of gabbroic (0.3, Le Maître, 1976).

TiO_2 concentrations (0.26 - 0.35 wt. %) in the studied samples do not exceed an average value of 0.32 wt. %. They are slightly lower to the average value (1.12) when compared to the result of Le Maître (1976) but similar to the to the result (0.8) after Shervais (2008), 0.7 after Ibrahim et al., (2015); 1.4 after Pannemans et al., (2000) and 0.8 Key (1987)

The Cr_2O_3 content (0.01 - 0.02 wt. %, average = 0.1) are also low. The MnO concentrations in the studied samples are in trace amount and vary from 0.07 to 0.09 wt. % (average = 0.08 wt. %). They are relatively similar to the average concentration of gabbroic rock (0.12, Le Maître, 1976; 0.15, Shervais, 2008; 0.16 Tokhi et al., 2016; 0.16, Ibrahim et al., 2015; and 0.13, Buriánek et al., 2012).

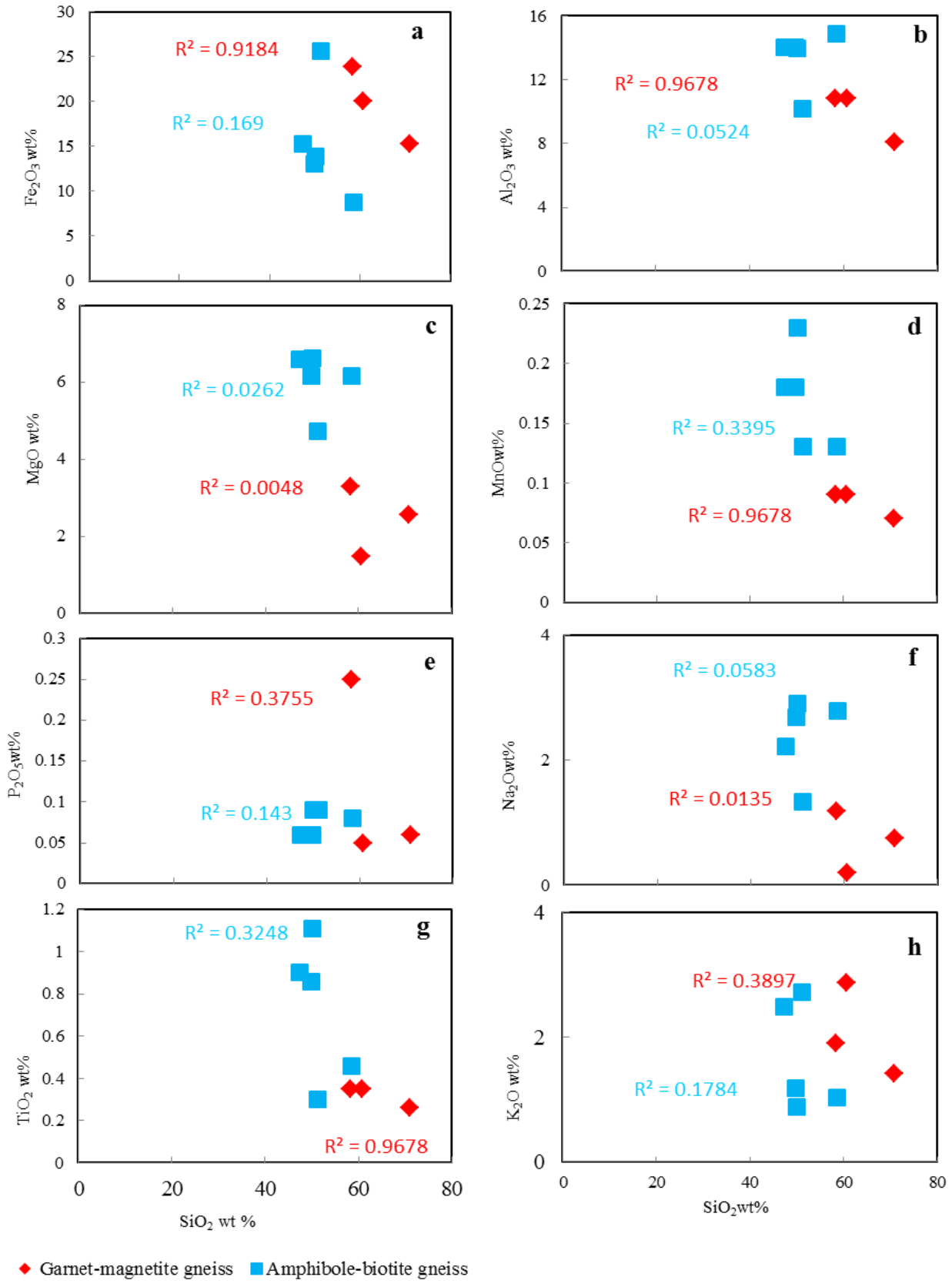

Figure 36: Binary plots for major element oxides variation with SiO_2 for Nkout gneissic country rock (garnet-magnetite gneiss and amphibole-biotite gneiss).

The P_2O_5 contents (0.05 - 0.25; average = 0.12 wt. %) vary relatively and are similar to the average content (0.29, Le Maître, 1976; 0.11, Shervais, 2008; and 0.17, Key, 1987).

The major element contents of the studied rock samples are similar to that of the average contents of gabbroic rock according to Le Maître, (1976), Tokhi et al., (2016), Ibrahim et al., (2015), Key (1987) and Buriánek et al., (2012).

In the binary plots for major element oxide, the samples show a strong negative correlations between SiO_2 and Fe_2O_3 ($r^2 = 0.91$), SiO_2 and Al_2O_3 ($r^2 = 0.95$ Fig. 36), SiO_2 and TiO_2 ($r^2 = 0.96$), and SiO_2 and MnO ($r^2 = 0.96$) contents and little or no correlation could be established between SiO_2 and MgO ($r^2 = 0.0048$), SiO_2 and Na_2O ($r^2 = 0.013$) and SiO_2 and P_2O_5 ($r^2 = 0.37$) contents, as the sample are scattered in the plots (Fig. 36). No positive correlation occurred.

On the F1 vs. F2 discrimination diagram, after Roser and Korsch (1988), the studied samples plot on the area of mafic-igneous rocks. These suggest that the protoliths of the samples could have resulted from mafic igneous rocks (Fig. 35).

V.1.2.1.2 Trace Elements (TE)

The large ion lithophile elements (LILE) average contents for studied rock (Rb = 9.24 ppm, Th = 0.33 ppm, U= 1.98 ppm), Ba = 75.33 ppm, and Sr = 1.49 ppm average) are low but similar to that of gabbroic rock (Le Maître, 1976; Shervais, 2008; Tokhi et al., 2016; Ibrahim et al., 2015; and Buriánek et al., 2012; Pannemans et al., 2000; and Key, 1987).

The average Rb/Ba (0.133) ratios of the studied samples are low and vary widely, relatively similar to the average content (0.04, Shervais, 2008; 0.07, Buriánek et al., 2012; 0.08, Pannemans et al., 2000; and 0.13, Ibrahim et al., 2015).

The average Rb/Sr ratios (7.00) are relative higher when compared to other gabbroic rock (0.001, Shervais, 2008; 0.02, Ibrahim et al., 2015; 0.19, Tokhi et al., 2016).

The averages Th/U ratios (1.62) are also relative lower than the average value but closely similar to that of the gabbroic content (2.9, Shervais 2008; and 1.0, Pannemans et al. 2000).

The concentration of HFSE are low (Zr = 0.003 - 0.006 ppm, V = 1.51 - 1.82 ppm, and Hf =0.0008 - 0.001 ppm).

The average transition elements abundances (Sc average: 0.09 ppm, Cr average: 9.5 ppm, and Ni average: 1.5 ppm, Cu average: 3.14 ppm, Zn average = 1.38 ppm, and Pb average: 0.50 ppm) are as well low whereas majority of the samples show that Ta is below detection limit.

The average Zr/Y ratios (average: 0.052 ppm) is higher than the Nb/Y ratios (average: 0.02ppm). The Zr/Y (0.08 - 0.098) ratio is lower when compared to the average value of the rock (3.91, Shervais 2008; 5.7, Pannemans et al., 2000; 2.4, Ibrahim et al., 2015; and 4.9, Tokhi et al., 2016; 3.1, Key, 1987) while the Nb/Y (0.01 - 0.038) ratios are relatively similar to the average value (0.096, Shervais, 2008; 0.35, Ibrahim et al., 2015; 0.39, Pannemans et al., 20000; and 36, Tokhi et al., 2016; 0.3, Key, 1987).

On the binary plots (Fig. 37), positive correlations are revealed between SiO_2 content and Cr, Y whereas the SiO_2 content increases with decrease in the content Ba, Co, Sr, Ni, Rb and Zn. Correlation is constant between SiO_2 with Pb, and Zr.

V.1.2.1.3 Rare Earth Elements (REEs)

The studied samples show relative low and variable rear earth elements (REEs) abundance ranging from 2.12 - 19.24 ppm (average = 10.36 ppm) when compared to gabbroic rock (31.1 > ΣREE > 35.8 ppm average = 33.8 ppm, Ibrahim et al. 2015; and average = 167 ppm, Buriánek et al., 2012; average = 71.8ppm, Key, 1987). The concentration REEs results vary from light rear earth elements (LREEs) to heavy rear earth elements (HREEs).

The LREEs contents (La - Gd) are very closely. La varies between 0.542 - 5.34 ppm (average = 2.84 ppm), while Gd varies between 0.0283 - 0.0839 ppm (average = 0.056 ppm).

The HREEs content (Tb - Lu) varies. Tb content (0.0015 - 0.0127 ppm average = 0.007 ppm), varies similar to Lu (0.0004 - 0.0007 ppm, average = 0.0005 ppm).

The results are chondrite-normalised to the values of Evensen et al**.** (1978). The results are as well fractionated, showing significant enrichment in LREEs over HREEs.

The chondrite-normalised values show Eu/Eu* values ranging between 0.71 - 1.30. Two samples (WH3-8 and WH4-11) display negative Eu anomalies while sample CH7-6 exhibits positive Eu anomaly (Eu/Eu* = 1.30).

The overall average value of the studied sample (Eu/Eu* = 1.005) is similar to the average value of gabbroic rock (0.49 > Eu/Eu* > 0.86, average = 0.63, Ibrahim et al., 2015; and 0.94, Buriánek et al., 20127; and 1.03, Shervais, 2008; average =1.14, Key, 1987).

The studied samples portray high LREEs fractionation {6.36 > $(La/Sm)_{CN}$ > 11.36} relative to the average content of gabbroic rock {0.79 > $(La/Sm)_{CN}$ > 1.13, Shervais 2008; 0.55 > $(La/Sm)_{CN}$ > 1.93, average = 0.96, Ibrahim et al., 2015; average = 3.27, Key, 1987}.

The $(Gd/Yb)_{CN}$ ranges from 5.20 - 12.57 (average = 8.80), while $(La/Yb)_{CN}$ ratios are relative high {83.68 > $(La/Yb)_{CN}$ > 671.77}, revealing depletion of the heavy HREEs over LREEs, similarly compared to the value of gabbroic rock {0.08 > $(Gd/Yb)_{CN}$ > 0.195 average = 0.10, and 0.08 > $(La/Yb)_{CN}$ > 0.198, average = 0.13, Shervais, 2008; average $(La/Yb)_{CN}$ = 0.17 and $(Gd/Yb)_{CN}$ = 0.081, Ibrahim et al., 2015; $(La/Yb)_{CN}$ = 7.03, $(Gd/Yb)_{CN}$ = 1.35, Key, 1987}.

The chondrite-normalised patterns (Fig. 38A) equally shows this important fractionation of the REEs with high $(La/Yb)_{CN}$ values ranging from 83.68 - 671.77, (average = 367.2), indicating LREEs enrichment.

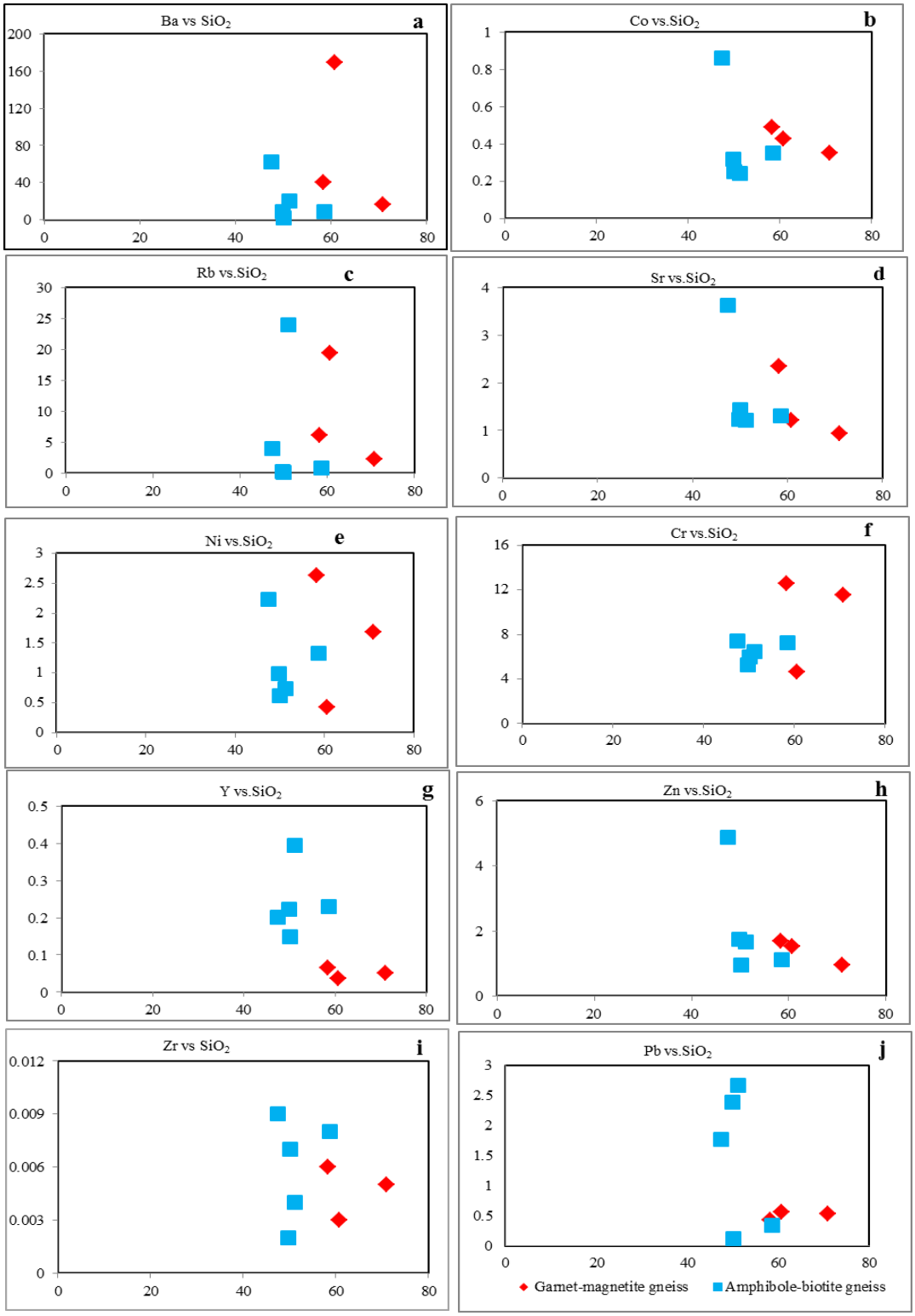

Figure 37: Binary diagram for some selected trace element variation with SiO_2 in gneissic rocks

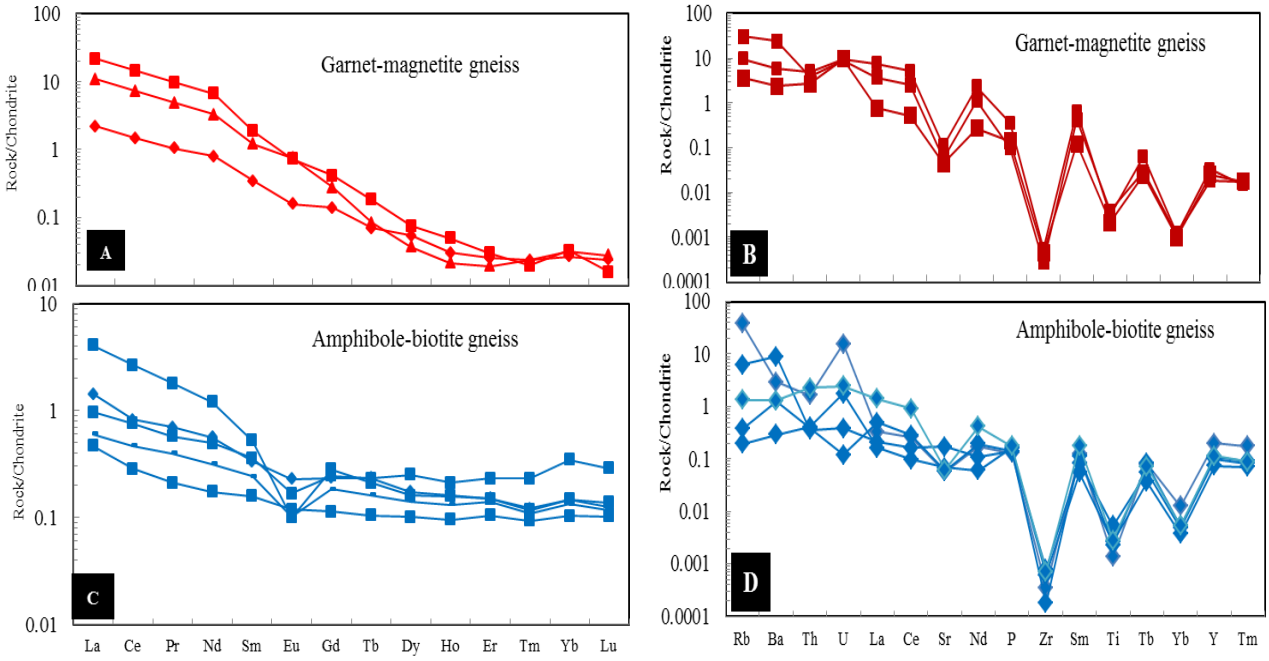

Figure 38: REEs and multi-element diagrams of Nkout gneissic rocks (A) Garnet-magnetite gneiss and (B) Amphibole-biotite gneiss. Values for normalisation are after Evensen et al. (1978) and Thompson et al. (1982) respectively.

The LREEs enrichment is 10 to 100 times higher than that of the chondritic values. The fractionation shown by $(Gd/Yb)_{CN}$ and $(Ce/Sm)_{CN}$ ratios are low ranging from 5.20 - 12.57 and 4.27 - 7.86 respectively, indicating HREEs depletion similar to the average value of gabbroic rock {$(Gd/Yb)_{CN} = 0.10$ relative to $(La/Yb)_{CN} = 0.13$, Shervais, 2008}.

Multi-elements are chondrite-normalized to the values suggested by Thompson, (1982) for the studied rocks. The patterns are shown in figure 38B. On the chondrite-normalized multi-element spider diagram, the studied samples show strong negative Ti, Yb and Zr anomalies and Ta is below detection limit similar to gabbroic rock (Fig. 38B), indicating that the continental crust and the mantle participated in the genesis of this rock (Thompson 1984).

V.1.2.2 AMPHIBOLE-BIOTITE GNEISS

The meta-igneous rock is represented by rocks sample of the studied area (EH2-3, DJO4, DJO5, MN03, and MIE1). The geochemical composition is represented in table 5.

V.1.2.2.1 Major Element Oxides (MEO)

On the discrimination diagram of De la Roche (1965), the studied samples show igneous rock characteristic of gabbroic to basaltic composition (Figs. 34A and B).

This rock show relative lower SiO_2 (47.4 - 58.6 wt. %; average: 49.62 wt. %.) variables similar to the average concentrations of gabbroic rock (50.14) after Le Maître (1986), North Hatta Area, United Arab Emirates (50.52) after Tokhi et al. (2016), Channel Islands (SiO_2 = 49) after Key (1987), and in North Eastern Desert, Egypt (49.45) after Ibrahim et al. (2015).

The Al_2O_3 contents are slightly lower and range between 10.2 - 14.05 wt. % (average = 13.4) when compared to the average content of gabbroic rock (15.48, Le Maître, 1986; 17.5, Ibrahim et al., 2015; and 14.1, Tokhi et al., 2016; 16.4, Key, 1987).

Fe_2O_3 contents (8.77 - 25.6 wt. %, average = 15.3) are relatively higher to the average value of gabbroic rock (3.01, Le Maître, 1986; 4.6, Ibrahim et al., 2015, and 9.14, Tokhi et al., 2016; 8.9, Key, 1987).

The MgO contents are relative lower ranging from 4.72 - 6.6 wt. % (average = 6.0) compared to the average content (7.59, Le Maître, 1976; 7.9, Ibrahim et al., 2015; and 8.5, Tokhi et al., 2016; 8.7, Key, 1987) as well as the CaO concentrations (2.97 - 10.10 wt. %, average = 7.6) which are relative higher to the average concentrations (9.58, Le Maître, 1976; 8.8, Ibrahim et al., 2015; and 14.2, Tokhi et al., 2016; 11.5, Key, 1987). This confirms the abundance of ferromagnesian silicate minerals (biotite) as revealed in the petrographic study.

The concentrations of Na_2O are similar to that of K_2O in the studied samples. The Na_2O contents range between 1.34 - 2.9 wt. % (average = 2.3 wt. %) similar to the average content of gabbroic rock (2.39, Le Maître, 1976; 2.80, Ibrahim et al., 2015; 2.1, Key, 1987) but higher to the average content of North Hatta Area (0.73, Tokhi et al., 2016).

The K_2O concentration (0.88 - 2.72 wt. % average = 1.65 wt. %) are slightly higher to the average values (0.93, Le Maître, 1976; 0.66, Ibrahim et al., 2015; and 0.05, Tokhi et al., 2016; 1.2, Key, 1987).

The total alkali content ($K_2O + Na_2O$) are moderately high, ranging from 3.82 to 4.06 wt. % (average = 3.9) to that of the average content (3.3, Le Maître, 1976; 3.4, Ibrahim et al., 2015; and 0.78, Tokhi et al., 2016, 3.3 Key, 1987).

The K_2O/Na_2O ratios (0.30 to 2.02 wt. %, average =1.6) are slightly higher to the average value (0.38, Le Maître, 1976; 0.23, Ibrahim et al., 2015; and 0.07, Tokhi et al., 2016).

The minor element concentrations such as TiO_2 show an average value of 0.79 wt. %, (0.3 - 1.11 wt. %) lower than the average value of gabbroic rock (1.12, Le Maître, 1976; 0.71, Ibrahim et al., 2015; and 0.32, Tokhi et al., 2016; 0.8 Key, 1987).

MnO concentrations in the rock samples are in trace amount and does not exceed an average value of 0.17 wt. %, lying between 0.13 - 0.23 wt. %. The average MnO content is relatively similar to the average content of the gabbroic rock (0.12, Le Maître, 1976; 0.16 Ibrahim et al., 2015; and 0.16, Tokhi et al., 2016; 0.17, Key, 1987).

The average P_2O_5 concentrations (0.07 wt. %) is lower in the studied samples relative to average concentration (0.24, Le Maître, 1986; 0.12 Ibrahim et al., 2015, and 0.03, Tokhi et al., 2016; 0.17, Key, 1987).

The major element contents of the studied rock samples show similar average composition of gabbroic rock according to Le Maître, (1976), Tokhi et al. (2016), Ibrahim et al. (2015), Key (1987) and Buriánek et al. (2012).

The binary plots for major element oxide shows a slight negative correlation that exists between SiO_2 and Fe_2O_3 ($r^2 = 0.16$), between SiO_2 and MnO ($r^2 = 0.33$), between SiO_2 and TiO_2 ($r^2 = 0.14$) and between SiO_2 and P_2O_5 ($r^2 = 0.14$ Fig. 36). No correlation could be established between SiO_2 and Al_2O_3 ($r^2 = 0.05$), SiO_2 and Na_2O ($r^2 = 0.056$), between SiO_2 and K_2O ($r^2 = 0.17$, Fig. 36) as the sample show scattered plot in the binary diagram.

On the F1-F2 diagram of Roser and Korsch (1988) for protolith reconstruction, the analysed amphibole-biotite gneiss samples established plot within the fields of mafic igneous rocks source pointing to a major contribution of igneous type derive rock, confirms the affinity with magmatism (Fig. 35B).

V.1.2.2.2 Trace Elements (TE)

The studied samples show very low large ion lithophile elements (LILE) composition. These include Rb (average: 7.08 ppm), Th (average: 00.58 ppm), U (average: 0.09 ppm), Ba (average: 23.45 ppm), and Sr (average: 1.8 ppm) similar to that of the average composition of gabbroic rock (Le Maître, 1986; Tokhi et al., 2016; Ibrahim et al., 2015; Key 1987).

The average Th/U ratios (0.4 - 13.4 average = 4.4) are also are relative lower than that of gabbroic rock (37.6, Ibrahim et al., 2015).

Rb/Ba (0.023 - 1.18ppm, average = 0.28) ratios are similar to the average contents (0.12, Tokhi et al., 2016; 0.14, Ibrahim et al., 2015).

The average Rb/Sr ratios (0.08 - 19.67 average = 4.3) are relatively similar to the average values (0.20, Tokhi et al., 2016; 0.027, Ibrahim et al., 2015).

The concentrations of high field strength elements (HFSE) composition are also low (Zr = 0.002 - 0.009 ppm with uniform distribution, V = 1.52 - 4.55 ppm and Hf = 0.001 ppm).

The transition elements abundances in the rock are equally low (Sc = 0.04 ppm, V = 2.53ppm, Cr = 6.27 ppm, and Ni = 1.13 ppm). Ta is relatively depleted, below detection limit.

The Zr/Y (0.009 - 0.047) ratios are lower to the average content (4.31, Tokhi et al., 2016; and 2.4, Ibrahim et al., 2015; 3.1, Key, 1987) but the average Nb/Y (0.01) ratios are relatively similar to that of gabbroic rock (4.31, Tokhi et al., 2016; and 0.35, Ibrahim et al., 2015; 0.32, Key, 1987).

The Zr/Y ratios (0.01 - 0.047 ppm; average: 0.029 ppm) are high than the Nb/Y ratios (0.009).

The SiO_2 contents increase with decrease in the content of Ba, Co, Ni, Rb, Pb, Sr, Y and Zn whereas a positive correlation is established with Zr, on the binary plots (Fig. 37).

V.1.2.2.3 Rare Earth Elements (REEs)

The studied samples show very low rear earth elements (REEs) contents (ΣREE = 0.52 - 3.92 ppm average = 1.79 ppm) relative to the gabbroic rock (31.1 > ΣREE > 35.8 ppm average = 33.8ppm, Ibrahim et al., 2015; average ΣREE=71.8, Key 1987).

The concentrations of light rear earth elements (LREEs = La - Gd) varies, La concentrations (0.1145 - 0.997 ppm, average = 0.36 ppm) varies similar to Gd (0.0232 - 0.0577 ppm average = 0.03).

The concentration of heavy rear earth elements (HREEs = Tb to Lu) varies relatively. Tb concentrations (0.0039 - 0.0088 ppm, average = 0.007 ppm) vary in similar manner to Lu (0.0026 - 0.0073 ppm, average = 0.0039 ppm).

The rock shows significant LREEs enrichment relative to HREEs when chondrite-normalised to values of Evensen et al., (1978). The chondrite-normalised values portrays high LREEs fractionation 2.9 > $(Ce/Sm)_{CN}$ > 29.6 relative to that of gabbroic rock {0.55 > $(La/Sm)_{CN}$ > 1.93, average = 0.96, Ibrahim et al. 2015; $(La/Sm)_{CN}$ =3.27, Key 1987}. The $(La/Yb)_{CN}$ ratio {2.80 > $(La/Yb)_{CN}$ > 27.7} indicates LREEs enrichment while the $(Gd/Yb)_{CN}$ ratio ranges from 0.70 – 1.91 (average = 1.34), indicates depletion of the heavy HREEs. This is similar to that of the gabbroic rock {average $(La/Yb)_{CN}$ = 0.17 and $(Gd/Yb)_{CN}$ = 0.081, Ibrahim et al. 2015; $(La/Yb)_{CN}$ = 7.03 and $(Gd/Yb)_{CN}$ =1.35, Key 1987}.

The rock is characterised by negative Eu anomaly (Eu/Eu* = 0.25 - 0.88, average = 0.66) probably linked to the crystallisation of amphibole and plagioclase similar to the average value of gabbroic rock (0.49 > Eu/Eu* > 0.86, average = 0.63, Ibrahim et al. 2015; Eu/Eu* =1.01, Key 1987).

The chondrite-normalised patterns of studied samples are highly fractionated, with strong LREEs enrichment {$(La/Yb)_{CN}$ = 2.80 - 27.75, average = 9.8}, middle REE {$(Ce/Sm)_{CN}$ = 1.79 - 5.041; average = 2.6} and HREEs {$(Gd/Yb)_{CN}$ = 0.70 - 1.91, average = 1.33; Fig 38C}. The LREEs enrichment is 10 times greater than the chondritic values.

The studied rocks values are normalized to the values of Thompson (1982). On the spider diagram, the rock display negative Ti, Yb and Zr anomalies (Fig. 38D**),** a characteristic of rock originated from the continental crust and mantle.

(B) META-SEDIMENTARY ROCK

The metamorphic unit of studied area consists of meta-sedimentary rock group. Their whole rock major, trace and rare earth elements (REEs) data of these rocks are presented in Table 6.

The nature of meta-sedimentary protolith rocks were determined by the construction of the discrimination diagram (Fig. 39) after Herron (1988). On the log (TFe_2O_3/K_2O) vs. log (SiO_2/Al_2O_3) protolith reconstruction diagram, the majority of the studied rock samples (12) plot on the field of Fe-derived sand composition and a minority (3) show quartz arenitic composition (Fig. 39), confirming their sedimentary source.

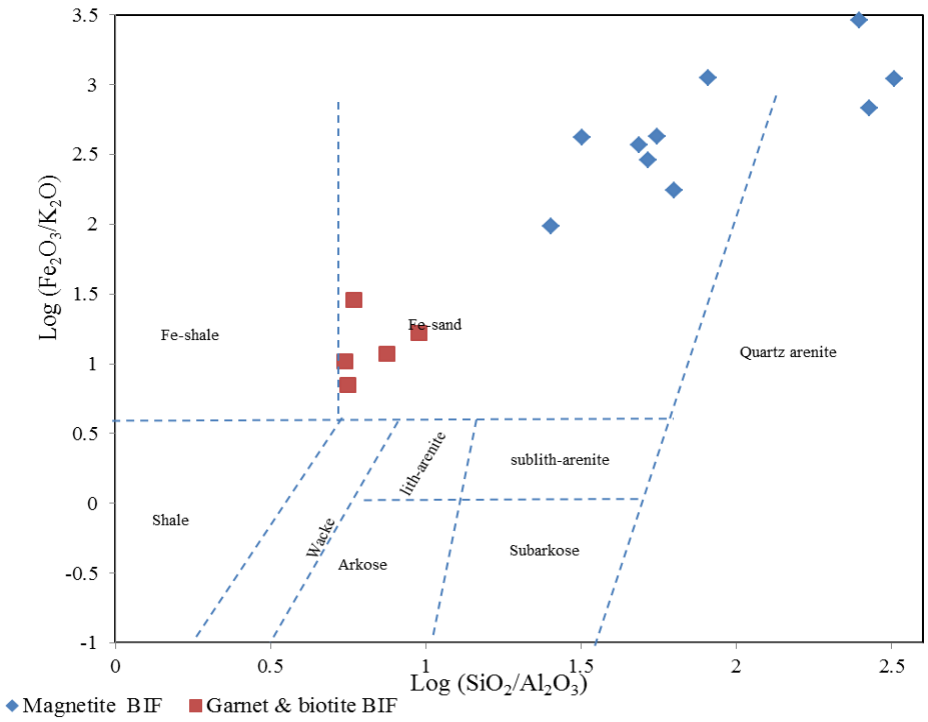

Figure 39: Protolith reconstruction diagrams of Nkout BIF: (a) log (TFe_2O_3/K_2O) vs. log (SiO_2/Al_2O_3) after Herron (1988).

The source of the sedimentary composition indicates that the protolith were enriched in iron and could probably represent metamorphosed iron formation of various grades. We therefore infer that the studied samples have Fe-sand composition derived protolith rock.

These meta-sedimentary rocks are represented by banded iron formation (BIF), and consist of two distinct petrographic types namely: magnetite BIF and garnet-biotite BIF.

We further compared these rocks with the average composition of Precambrian Fe-sand after Ramachandran et al. (2016), Elzien et al. (2014), Abu et al. (2017) and Mishra et al. (2012).

Table 6: Major, trace and rear earth elements (REEs) geochemical composition (wt. %) of representative metasedimentary rock (BIFs)

	Magnetite BIF									Garnet and biotite BIF				
Wt.%	WH4-5	WH4-8	WH4-10	WH4-2	CH7-1	CH7-2	CH24-1	CH24-2	CH24-3	CH7-3	CH7-6	WH3-6	WH3-9	WH4-3
SiO_2	45.5	40	42.5	38.8	43.1	38.6	40.3	41.9	38.1	51.8	60.7	52.5	54.5	50.8
TiO_2	0.03	0.03	0.01	0.02	0.01	0.02	0.06	0.01	0.02	0.33	0.35	0.26	0.21	0.17
Al_2O_3	0.72	0.82	0.17	0.7	0.16	0.74	1.59	0.13	0.47	8.85	10.8	9.54	7.25	5.33
Fe_2O_3	50.4	55.5	57.4	55.3	54.5	54.6	52.1	55.1	56	28.3	20	31.5	32.7	38.1
MgO	3.04	2.48	1.52	2.18	1.93	2.53	2.03	1.92	5.35	2.85	1.49	2.2	2.17	2.89
MnO	0.09	0.11	0.08	0.12	0.11	0.13	0.06	0.05	0.16	0.11	0.09	0.25	0.13	0.17
CaO	1.04	1.35	1.04	1.68	2.25	2.08	1.37	1.38	0.8	4.59	0.85	1.94	0.68	1.25
Na_2O	0.07	0.07	0.02	0.07	0.3	0.21	0.03	0.05	0.06	1.52	0.19	0.2	0.32	0.22
K_2O	0.29	0.15	0.02	0.13	0.08	0.19	0.54	0.05	0.05	0.99	2.86	3.05	2.79	2.3
P_2O_5	0.03	0.11	0.09	0.12	0.07	0.03	0.12	0.1	0.11	0.18	0.05	0.1	0.08	0.1
LOI	-1.1	-1.29	-1.39	-1.07	-1.15	-0.93	-0.23	-1.08	-0.43	0.47	1.1	-0.15	0.11	0.58
Total	100.12	99.34	101.47	98.06	101.37	98.21	97.98	99.62	100.7	100.02	98.49	101.41	100.96	101.92
Fe_2O_3/TiO_2	1680	1850	5740	2765	5450	2730	868	5510	1905	86	57	121	156	224
SiO_2/Fe_2O_3	0.903	0.721	0.74	0.702	0.791	0.707	0.774	0.76	1.47	1.83	3.035	1.667	1.667	1.333
Al_2O_3/TiO_2	24	27.333	17	35	16	37	26.5	13	23.5	26.81	30.85	36.69	34.52	31.35
SiO_2/Al_2O_3	63.19	48.78	250	55.42	269.37	52.16	25.34	322.30	119.14	5.85	5.62	5.50	7.517	9.53
Fe_2O_3/Al_2O_3	70	67.68	337.64	79	340.62	73.78	32.76	423.84	81.06	3.19	1.85	3.30	4.51	7.14
Na_2O+K_2O	0.36	0.22	0.04	0.2	0.38	0.4	0.57	0.1	0.11	2.51	3.05	3.25	3.11	2.52
K_2O/Na_2O	4.14	2.14	1.00	1.86	0.27	0.90	18.00	1.00	0.83	0.65	15.05	15.25	8.72	10.45
Trace (ppm)														
Ba	3.52	1.13	0.5	1.79	177.5	3.86	12.75	3.33	0.96	30.1	169	37.4	15.55	28.2
Co	0.245	0.17	0.13	0.07	0.06	0.07	0.30	0.08	0.13	0.95	0.42	0.32	0.28	0.27
Cr	13.6	7.61	8.17	3.67	6.16	5.61	4.71	5.76	5.68	4.95	4.67	8.56	7.19	4.09
Cu	0.38	0.6	0.37	bdl	1.04	0.59	1.54	0.24	0.47	5.89	6.08	0.06	0.11	0.53
Hf	bdl	bdl	bdl	bdl	0.001	0.001	0.001	0.001	0.001	0.001	0.001	bdl	0.001	bdl
Li	4.72	0.32	0.3	0.78	0.1	0.09	1.87	0.13	0.44	1.58	2.9	1.28	0.88	12.6
Mn	136	79.2	79.2	35.1	53.5	57.4	78.8	40	48.6	11.5	5.17	69.4	63.2	28.5
Mo	0.129	0.07	0.076	0.01	0.04	0.032	0.017	0.033	0.038	0.007	0.01	0.073	0.071	0.004
Nb	bdl	bdl	bdl	bdl	0.001	0.001	0.001	0.001	0.001	0.001	0.001	bdl	bdl	bdl
Ni	2.1	0.9	1.06	0.09	0.31	0.31	1.14	0.21	0.47	2.75	0.43	1.8	1.6	1.02
Pb	0.122	0.037	0.034	0.058	0.012	0.027	0.032	0.046	0.148	0.178	0.558	0.158	0.605	0.539
Rb	12.35	1.62	0.149	1.635	0.332	0.883	13.35	0.375	0.244	8.19	19.4	16.55	7.9	29.9
Sr	0.336	0.694	0.652	0.259	5.15	2.9	1.99	0.402	0.207	2.29	1.21	0.655	0.848	0.303
Th	0.067	0.024	0.011	0.031	0.024	0.043	0.073	0.021	0.023	0.225	0.319	0.296	0.276	0.068
U	0.015	0.03	0.01	0.156	0.005	0.015	0.046	0.129	0.035	0.132	0.191	0.112	0.058	0.078
V	1.08	0.98	0.97	0.8	0.93	0.94	1	0.99	0.92	1.4	1.55	1.66	1.12	1.07
W	0.013	0.011	0.026	0.018	0.008	0.011	0.009	0.006	0.006	0.006	0.007	0.033	0.013	0.01
Y	0.357	0.196	0.343	0.303	0.323	0.178	0.661	0.775	0.237	0.107	0.037	0.139	0.06	0.115
Zn	1.71	0.78	0.79	1.61	0.32	0.9	1.65	0.67	1.78	1.71	1.52	1.31	1.97	2.2
Zr	0.004	0.001	0.001	0.002	0.001	0.001	0.005	0.002	0.001	0.012	0.003	0.006	0.009	0.001
K/Rb	38.704	104.938	255.034	103.976	198.795	137.033	119.85	224	270.492	150.183	140.722	116.62	169.62	101.003
Th/U	2.331	0.797	1.078	0.197	2.7	2.841	1.591	0.16	0.652	1.705	1.675	2.643	2.726	0.871
Co/Zn	0.143	0.221	0.171	0.047	0.216	0.079	0.184	0.128	0.074	0.56	0.28	0.251	0.144	0.126
REE (ppm)														
La	0.558	0.175	0.076	0.108	0.179	0.109	0.344	0.199	0.14	1.87	2.65	0.897	1.555	0.565
Ce	0.857	0.321	0.16	0.215	0.297	0.157	0.6	0.377	0.302	2.99	4.69	1.82	3.1	1.06
Pr	0.086	0.036	0.021	0.026	0.032	0.016	0.068	0.05	0.039	0.274	0.473	0.197	0.334	0.11
Nd	0.34	0.143	0.149	0.122	0.127	0.076	0.287	0.229	0.185	0.789	1.555	0.65	1.14	0.369
Sm	0.045	0.029	0.022	0.028	0.024	0.01	0.072	0.065	0.037	0.07	0.187	0.104	0.145	0.048
Eu	0.022	0.012	0.017	0.01	0.014	0.006	0.033	0.027	0.008	0.016	0.044	0.021	0.038	0.013
Gd	0.046	0.029	0.041	0.038	0.033	0.018	0.093	0.082	0.037	0.041	0.056	0.058	0.067	0.031
Tb	bdl	bdl	bdl	bdl	bdl	bdl	0.013	0.012	bdl	bdl	bdl	bdl	bdl	bdl
Dy	0.04	0.025	0.039	0.037	0.034	0.016	0.083	0.078	0.037	0.021	0.009	0.042	0.021	0.021
Ho	0.009	0.006	0.009	0.009	0.009	0.004	0.02	0.019	0.007	0.004	0.001	0.006	0.002	0.004
Er	0.026	0.017	0.025	0.023	0.024	0.016	0.057	0.062	0.021	0.011	0.003	0.014	0.004	0.01
Tm	0.003	0.002	0.004	0.003	0.003	0.002	0.007	0.007	0.003	0.002	0.001	0.001	0.001	0.001
Yb	0.027	0.015	0.025	0.024	0.022	0.019	0.06	0.045	0.018	0.01	0.005	0.011	0.003	0.012
Lu	0.004	0.002	0.004	0.004	0.003	0.003	0.008	0.006	0.003	0.001	0.001	0.002	0	0.001
∑REE	2.07	0.818	0.596	0.654	1.126	0.632	2.405	2.033	1.078	6.21	9.716	3.83	6.416	2.249
Y/Ho	39.667	32.667	39.425	35.647	38	43.415	33.384	41.005	35.909	26.098	31.083	23.966	26.043	30.263
$(La/Yb)_{PAAS}$	1.534	0.843	0.223	0.334	0.609	0.421	0.425	0.325	0.564	14.353	37.551	5.955	33.7	3.469
$(Gd/Yb)_{PAAS}$	1.020	1.137	0.976	0.961	0.916	0.565	0.931	1.080	1.208	2.544	6.427	3.097	11.705	1.539
$(Tb/Yb)_{PAAS}$	0	0	0	0	0	0	0.811	0.962	0	0	0	0	0	0
Ce/Ce*	0.901	0.934	0.923	0.926	0.905	0.872	0.904	0.866	0.946	0.96	0.963	0.997	0.989	0.977
Pr/Pr*	0.903	0.947	0.768	0.927	0.936	0.82	0.927	0.975	0.927	1.014	0.996	1.027	1.01	1
Eu/Eu*	2.276	2.005	2.625	1.392	2.29	1.922	1.907	1.749	1.063	1.433	1.99	1.27	1.823	1.601
Y/Y*	1.467	1.24	1.454	1.322	1.472	1.713	1.271	1.566	1.186	0.9	0.863	0.671	0.638	0.999
$(Ce/Sm)_{PAAS}$	1.330	0.788	0.503	0.547	0.874	1.077	0.586	0.404	0.578	3.012	1.756	1.225	1.502	1.533
$(La/Sm)_{PAAS}$	1.823	0.905	0.504	0.579	1.105	1.575	0.707	0.447	0.564	3.965	2.088	1.271	1.586	1.720
$(La/Yb)_{CN}$	14.037	7.711	2.039	3.059	5.571	3.847	3.891	2.974	5.158	131.327	343.579	54.482	308.344	31.743
$(Gd/Yb)_{CN}$	1.382	1.540	1.321	1.302	1.240	0.765	1.261	1.463	1.636	3.446	8.706	4.195	15.854	2.085
Eu/Eu*	1.482	1.305	1.709	0.907	1.501	1.260	1.250	1.147	0.697	0.939	1.305	0.827	1.187	1.043
$(La/Sm)_{CN}$	7.783	3.862	2.151	2.470	4.718	6.722	3.018	1.909	2.406	16.925	8.914	5.425	6.769	7.343
$(Ce/Sm)_{CN}$	4.586	2.718	1.734	1.887	3.012	3.715	2.020	1.391	1.991	10.383	6.053	4.223	5.177	5.285

6

$Eu/Eu^* = Eu_{CN}/(Sm^*Gd)_{CN}^{1/2}$, bdl: below dictection limit, $(Ce/Ce^*)_{SN} = Ce_{SN}/(0.5La_{SN} + 0.5Pr_{SN})$;$(Pr/Pr^*)_{SN} = Pr_{SN}/(0.5Ce_{SN} + 0.5Nd_{SN})$;$(Eu/Eu^*)_{SN} = (Eu)_{SN}/(0.67Sm_{SN}+0.33Tb_{SN})$, $(Y/Y^*)_{SN} = 2Y_{SN}/(Dy_{SN}+Ho_{SN})$.

V.1.2.3 MAGNETITE BIF

The meta-sedimentary rocks are represented by the magnetite BIF (WH4-5, WH4-8, WH4-10, WH4-2, CH7-1, CH7-2, CH24-1, CH24-2, and CH24-3). Their geochemical compositions are represented in table 6.

V.1.2.3.1 Major Element Oxide (MEO)

The majority of the studied BIF samples (7) show Fe-sand composition while a minority (3) show quartz arenitic composition on the geochemical discrimination diagram of Herron (1988).

In the samples the contents of Fe_2O_3 and SiO_2 have values greater than 88.9 wt. % (Tab. 6; Fig. 40). The result shows that Fe_2O_3 and SiO_2 have been the two principal components of the studied samples (88.9 to 99.9 wt. %, average = 94.4; Tab. 6) similar to the average content of Fe-sand: Mesoproterozoic formation Kaimur-India (average = 92.87) after Mishra et al., (2012); Precambrian formation Merkhiyat-Sudan (average = 93.97) after Elzien et al. (2014); Proterozoic formation Kaladgi-Badami Indian (average = 96.6) after Ramachandran et al. (2016); and Neoproterozoic formation Anyaboni-Ghana (average = 94.3) after Abu et al. (2017).

The Al_2O_3 contents (0.13 - 0.82, average = 0.66) in the studied BIF samples (Tab. 6) except sample WH3-2 (1.65 wt. %) show lower value when compared to the average content of the Fe-sand (4.3, Mishra et al., 2012; 4.9, Elzien et al., 2014; 3.3, Abu et al., 2017; and 1.88, Ramachandran et al., 2016) and much more lower to the average PAAS value (18.98, McLennan 2001) and 15.20, Taylor et al., 1985).

The Fe_2O_3 contents (38.1 - 57.4, average = 51.2) are higher when compared to the average content (1.2, Mishra et al., 2012; 21.3, Elzien et al., 2014; McLennan 2001; and 4.5, Taylor et al., 1985).

The Fe_2O_3/Al_2O_3 ratio (67.6 - 423.8; average = 167.0) are relative higher compared to average value (0.2, Mishra et al., 2012; 5.91, Elzien et al., 2014; 0.34, McLennan, 2001; and 0.29 Taylor et al., 1985).

MgO contents (1.52 - 7.56 wt. %, average = 2.9) are as well high relative to the average content (0.05, Abu et al., 2017; and 0.1, Ramachandran et al., 2016). The studied samples are closely similar to the average PAAS (2.2, McLennan, 2001) and Upper Continental Crust values (2.2, Taylor et al., 1985).

CaO contents are similar, ranging from 0.33 - 1.7 wt. % with an average of 1.3 wt. % relative to the Fe-sand content (0.05, Mishra et al., 2012; 0.28, Elzien et al., 2014, 0.01, Ramachandran et al., 2016; average PAAS value 1.3, McLennan, 2001) but lower to the other fields (Upper Continental Crust 4.2, Taylor et al., 1985). Both lower and similar average values of MgO and CaO are relative to the average PAAS (McLennan, 2001) and Upper Continental Crust (UCC, Taylor et al., 1985) confirms the presence of ferromagnesian silicate minerals (biotite, chlorite) and suggesting the near absence of calcite and dolomite as revealed in the petrographic study.

The Na_2O (0.06 - 0.17 wt. %; average = 0.01) and K_2O (0.05 - 0.29 wt. %, average = 0.17) contents clearly indicate that the concentration of Na_2O is lower than that of K_2O. The average Na_2O concentration is similar to that of the Fe-sand (0.05, Abu et al., 2017; 0.06, Ramachandran et al., 2016; 0.07, Elzien et al., 2014; 0.04, Mishra et al., 2012), and that of average PAAS value (1.20, McLennan, 2001) but lower than the average Upper Continental Crust value (3.90, UCC, Taylor et al., 1985).

The average K_2O content is slightly similar to the average Fe-sand content (1.09, Mishra et al., 2012; and 0.05, Elzien et al., 2014) but relatively lower to the average PAAS (3.70, McLennan, 2001) and Upper Continental Crust value (3.4, UCC, Taylor et al., 1985). The K_2O/Na_2O ratios range from 1.29 to 3.38 in the studied BIF. Na_2O and K_2O contents are low and in most cases are less than the average detection limit.

The total alkali ($Na_2O + K_2O$) contents (0.04 to 0.57 wt. %) indicate the association of lesser feldspars mineral and a source of clastic component in the studied BIF, similar to the Fe-sand (1.1, Mishra et al., 2012; and 0.12, Elzien et al., 2014). The average alkali contents are relatively lower to the average PAAS (4.9, McLennan, 2001) and Upper Continental Crust value (7.3, Taylor et al., 1985).

The studied BIF samples show relatively variable minor element contents. TiO_2 contents (0.01 - 0.06 wt. %, average = 0.03) are relatively low and similar when compared to that of the Fe-sand (0.14, Abu et al., 2017; and 1.02, Ramachandran et al., 2016), average PAAS (1.0, McLennan, 2001) and Upper Continental Crust value (0.5, Taylor et al., 1985), probably related to the clay minerals.

The TiO_2/Al_2O_3 (0.02 - 0.07 wt. %; average = 0.04) are relatively low, indicating pure chemical precipitation closely similar to Fe-sand (0.05, Ramachandran et al., 2016; and 0.04, Abu et al., 2017). The average TiO_2/Al_2O_3 ration is similar to the average PAAS (0.05, McLennan, 2001) and Upper Continental Crust value (0.03, Taylor et al., 1985). MnO contents (0.06 - 0.16 wt. %, average = 0.1) are relatively low and varied as well, relative similar to the average PAAS (0.11, McLennan, 2001), Upper Continental Crust value (01, Taylor et al., 1985), and Fe-sand (0.01, Mishra et al., 2012; 0.5, Elzien et al., 2014).

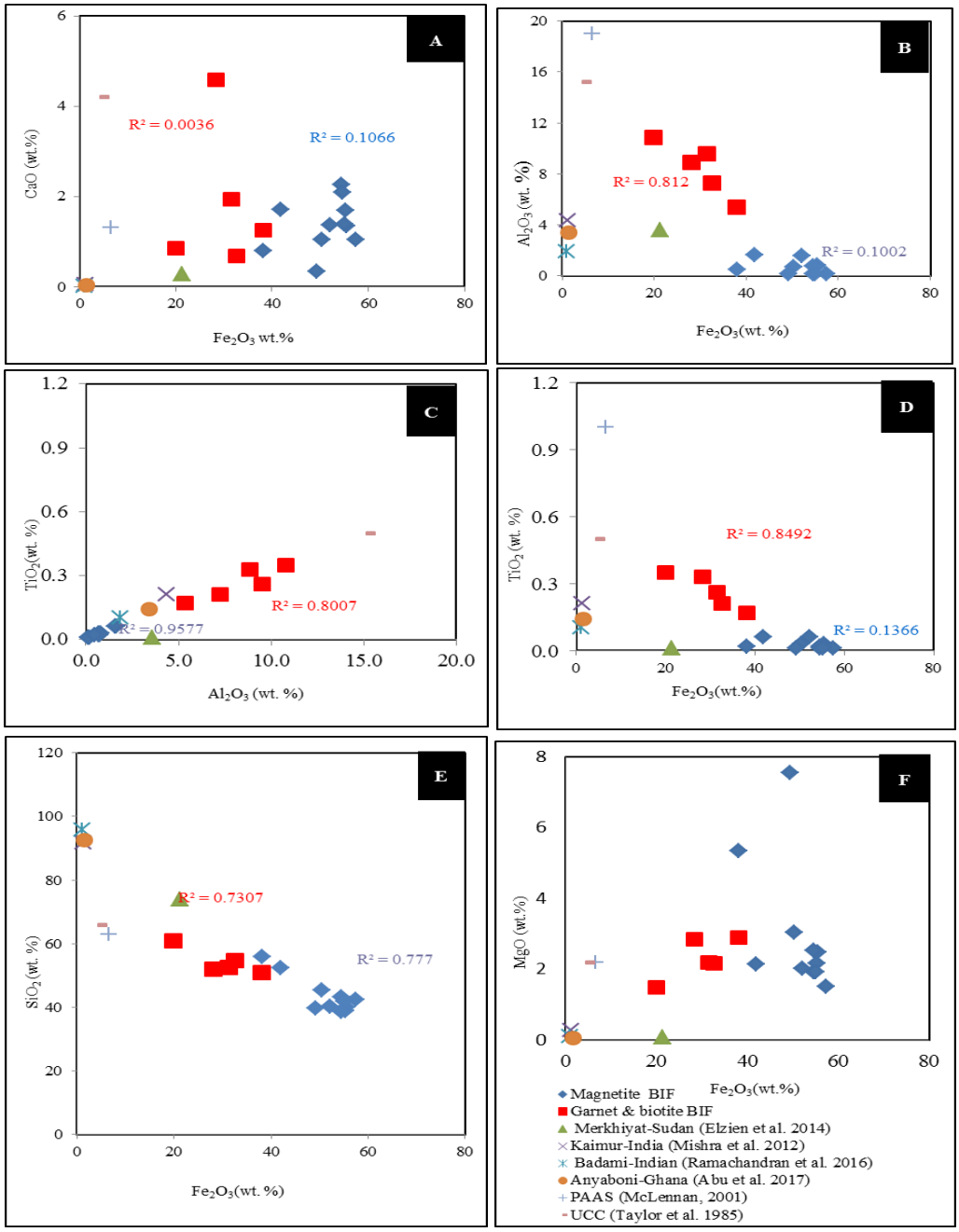

Figure 40: Binary variation diagram of Fe_2O_3 and SiO_2 (A), Fe_2O_3 and Al_2O_3 (B), TiO_2 and Al_2O_3 (C), Fe_2O_3 and TiO_2.(D), Oxides of Al, Si, and Ti portray a negative gradient with increasing Fe_2O_3 and CaO (E); Fe_2O_3 and MgO(F). {The average composition of UCC (Taylor et al., 1985) and PAAS (McLennan, 2001), and Fe sand (Merkhiyat-Sudan, Elzien et al. 2014; Kaimur-India, Mishra et al., 2012; Badami-Indian, Ramachandran et al., 2016; Anyaboni-Ghana, Abu et al., 2017), on the diagram is shown for comparison}.

The P_2O_5 concentrations (0.09 wt. %) are averagely low in all the magnetite BIF samples. The major element contents of the studied samples are similar to that of Fe-sand according to Mishra et al., (2012); Elzien et al., (2014); Ramachandran et al., (2016); and Abu et al., (2017).

On the binary variation diagram of Fe_2O_3 with some selected element oxide, a strong negative correlation exists between Fe_2O_3 and SiO_2 (r^2 = 0.77; Fig. 40A) and a slight negative correlation between Fe_2O_3 and MgO_2 (r^2 = 0.25; Fig. 40F); and a strong positive correlation exists between Al_2O_3 and TiO_2 (r^2 = 0.95; Fig. 40C) indicating slight input in this study. No correlation exists between Al_2O_3 and Fe_2O_3, Fe_2O_3 and TiO_2.

V.1.2.3.2 Trace Elements (TE)

The trace element compositions of the studied metamorphosed BIF samples show significant variations in the samples (Tab. 6).

The samples show low variable concentration of Ba (0.5 - 177.5 ppm, average = 177.5 ppm), Zn (0.32 - 1.78 ppm, average = 1.13 ppm), Ni (0.21 - 2.1 ppm, average = 0.73 ppm) are low. The concentration of Cr (3.67 - 13.6 ppm, average = 6.77 ppm), Rb (0.149 - 12.35 ppm, average = 3.43ppm), V (0.8 - 1.08ppm, average = 0.95 ppm), Y (0.171 - 0.775 ppm, average = 0.37 ppm), relatively similar when compared to average Fe-sand composition (Abu et al., 2017; Ramachandran et al. 2016; and Mishra et al., 2012), the average PAAS values (McLennan, 2001), and the Upper Continental Crust (UCC, Taylor et al., 1985).

The Th/U ratios (0.16 - 2.841) are relatively very low when compared to that of Fe-sand (Th/U average = 3.6 Mishra et al., 2012; and 5.2, Abu et al., 2017) and are equally lower when compared to the average PAAS (Th/U average = 4.7, McLennan, 2001) and Upper Continental Crust values UCC (Th/U average = 3.82, Taylor et al., 1985).

The Co/Zn ratio (0.04 - 0.22) are relative similar to average PAAS values (0.27, McLennan 2001) and average Upper Continental Crust values (0.23, UCC Taylor et al., 1985) and the Fe-sand (0.170, Ramachandran et al., 2016).

The Ni/Zn ratio (0.29 - 1.23) vary and are relative similar within the same range to average PAAS values (0.64, McLennan, 2001), Upper Continental Crust values (0.61 UCC Taylor et al., 1985), and the Fe-sand (0.60, Ramachandran et al., 2016).

The Rb/Ba (0.008 - 3.50ppm, average = 0.86) ratios are in similar range to the average content of Fe-sand rock (0.15, Ramachandran et al. 2016; 0.53, Mishra et al. 2012; 0.13, Abu et al. 2017), and average PAAS (0.24, Taylor et al., 1985) and UCC (0.203, McLennan 2001) values.

The average Rb/Sr ratios (0.002 - 0.71.67 average = 0.172) are relatively similar to that of Fe-sand composition (0.87, Ramachandran et al. 2016; 1.7, Abu et al., 2017) and average PAAS (0.8, Taylor et al., 1985) with UCC (0.32, McLennan, 2001).

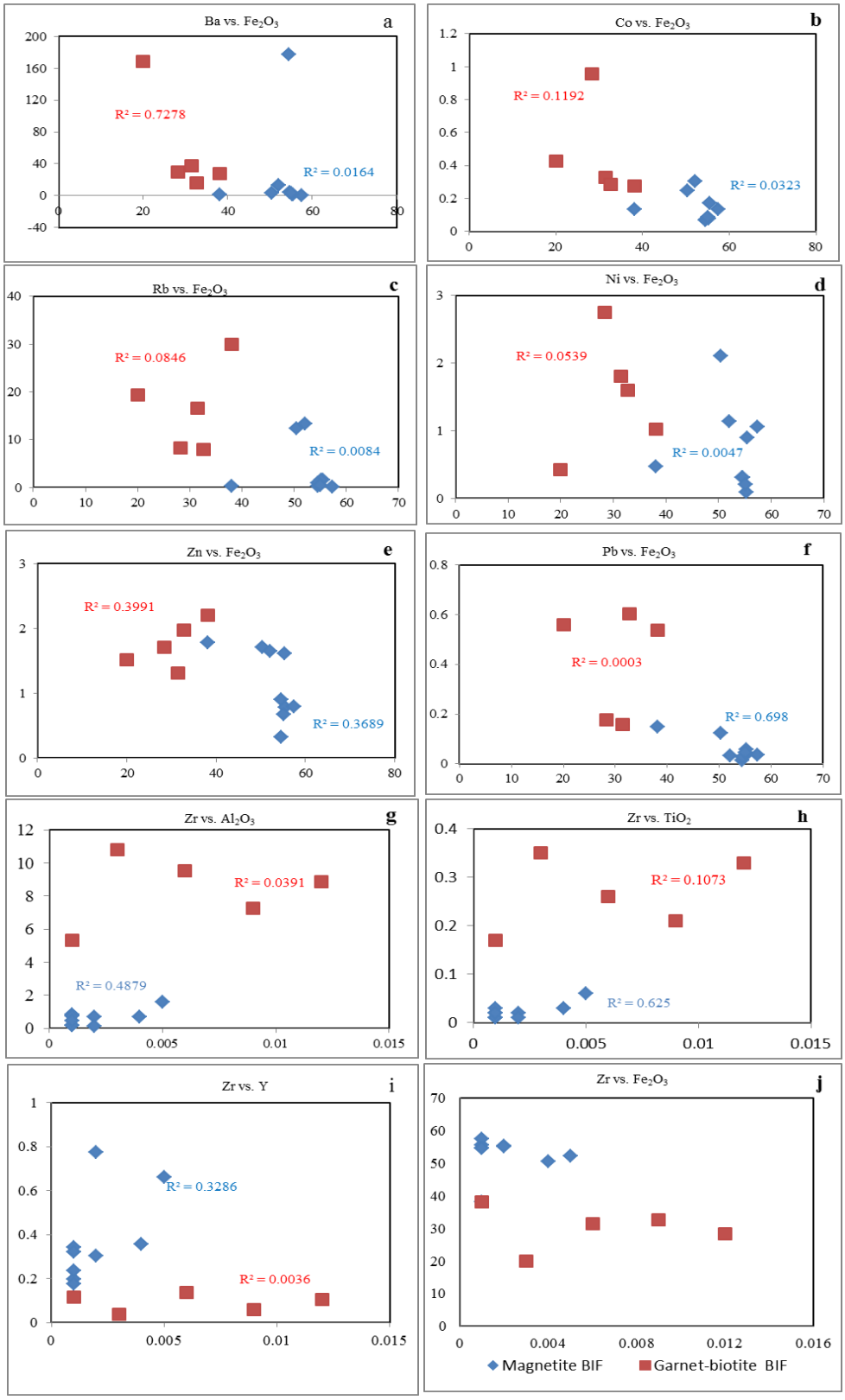

Figure 41: Binary diagram of some trace elements with Fe_2O_3 for banded iron formation in the Nkout area

The Zr concentrations (0.001 - 0.005 ppm), Co (0.069 - 0.245 ppm), Sr (0.402- 5.15 ppm) show moderately low contents and variable while Cu (0.24 - 1.54 ppm) Hf (0.001) content are very low when compared to the Fe-sand (Ramachandran et al., 2016; and Abu et al. 2017), the average PAAS values (McLennan, 2001) and Upper Continental Crust values (UCC Taylor et al., 1985). Zr content very and shows insignificant to null correlation that exists between Zr and Al_2O_3 and TiO_2 (Fig. 41), therefore, suggesting an insignificant input of a clastic material.

Moreover, detrital input is excluded for the low concentration of High Field Strength Elements (HFSE; Th (0.01 - 0.06 ppm), Zr (0.001 - 0.004 ppm), V (0.80 - 1.08 ppm), Sc (0.02 - 0.13ppm) and Hf (0.001 ppm)) which is relatively enriched in detrital material, similar to that average value of Fe-sand, PAAS and Upper Continental Crust values.

The average Zr/Y (0.002 - 0.011, average = 0.005) ratio is relative lower when compared to the average content (20.7, Ramachandran et al., 2016; and 7.0, Abu et al., 2017; 10.4, Mishra et al., 2012) but similar to the average Nb/Y (0.01) ratio relatively to Fe-sand rock (0.22, Ramachandran et al., 2016; 0.20, Abu et al., 2017; and 0.3, Mishra et al., 2012).

V.1.2.3.3. Rare Earth Elements (REEs)

The rear earth elements (REEs) contents of the studied BIF samples **(**Tab. 6, Fig. 42) are very low with ΣREE values ranging from 0.59 - 2.40 ppm when compared to the average Fe-sand (22.7, Ramachandran et al., 2016; 86.1, Mishra et al., 2012; 78.3, Abu et al., 2017). The studied values are also lower to the average PAAS values (184.7, McLennan, 2001), and Upper Continental Crust values (146.7, UCC Taylor et al., 1985).

The results of the studied BIF show significant enrichment of light rear earth elements (LREEs) over heavy rear earth elements (HREEs) concentrations, similar to average result of Fe-sand (72 ppm ΣLREE > 5.4 ppm ΣHREE, Abu et al. 2017; 20.7 ppm ΣLREE > 2.5 ppm ΣHREE, Ramachandran et al., 2016; and 78.8 ΣLREE > 9.24 ΣHREE, Mishra et al., 2012), average PAAS values (160.5 ppm ΣLREE > 12.18 ppm ΣHREE, McLennan, 2001), and average Upper Continental Crust values (132 ppm ΣLREE > 13.89 ppm ΣHREE, UCC Taylor et al., 1985).

The LREEs ranges from La - Gd. La varies between 0.24 - 1.8 ppm (average = 0.67 ppm), and Gd varies between 0.11 - 0.35 ppm (average = 0.17 ppm).

The HREEs range from Tb - Lu. Tb is low and variable (0.069 - 0.25 ppm, average =0.14 ppm), while Lu varies from 0.075 - 0.23 ppm (average = 0.013).

The results are both chondrite-normalised and PAAS-normalised to the values of Evensen et al. (1978) and Taylor and McLennan (1985) respectively.

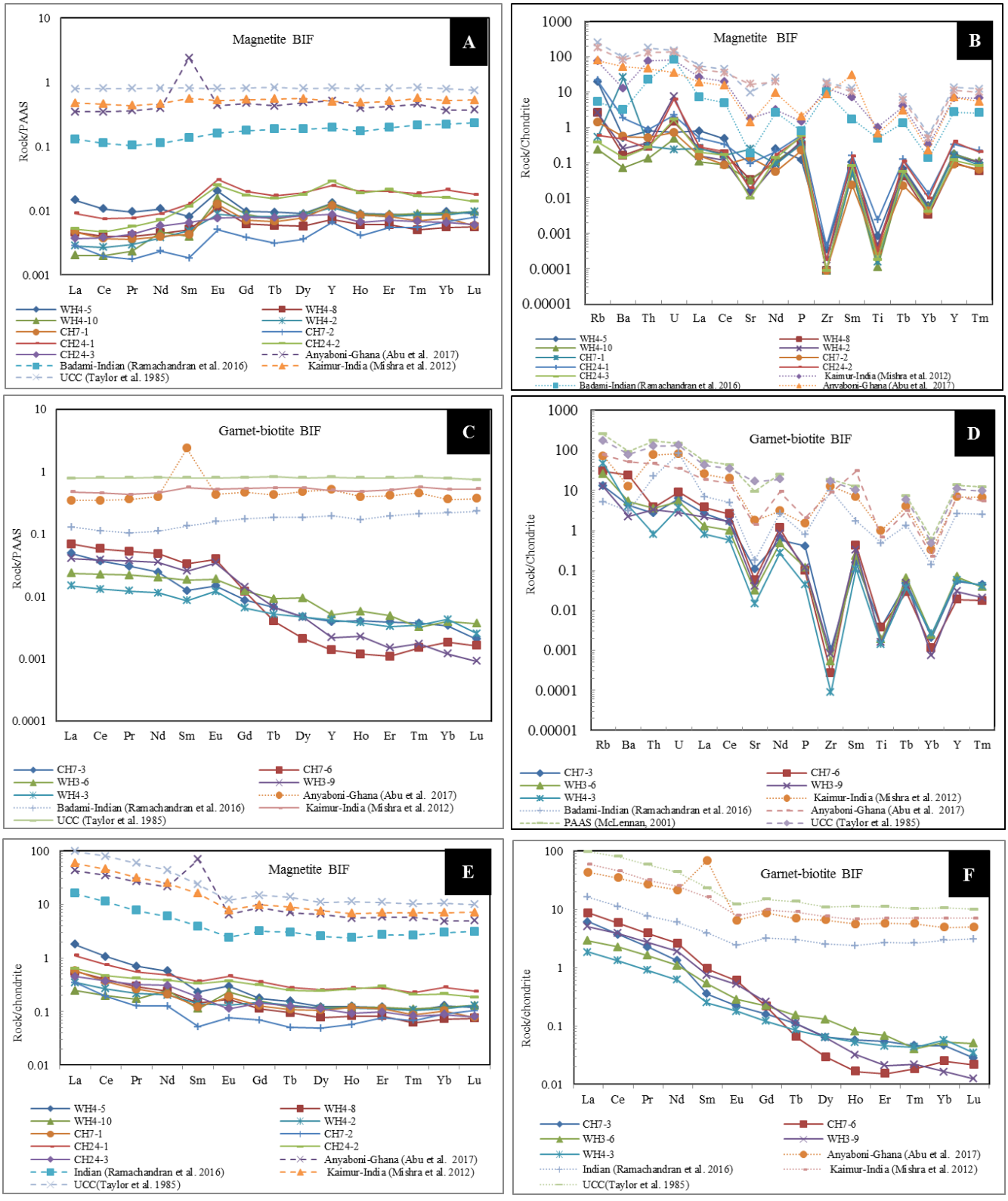

Figure 42: REEs and multi-elements diagram of Nkout BIF (A and C) magnetite BIF and garnet-biotite BIF, Values for Post-Archean Australian Shale (PAAS Taylor and MacLennan, 1985) and (BandD) magnetite BIF and garnet-biotite BIF chondrite-normalised (Thompson, 1982) multi element. (E and F) Magnetite BIF, and garnet-biotite BIF chondrite-normalised (Boynton, 1984) REEs diagram. The average composition of Fe-sand (Abu et al. 2017; Ramachandran et al., 2016; Mishra et al., 2012), UCC (Taylor et al., 1985) and PAAS (McLennan, 2001) are shown for comparison.

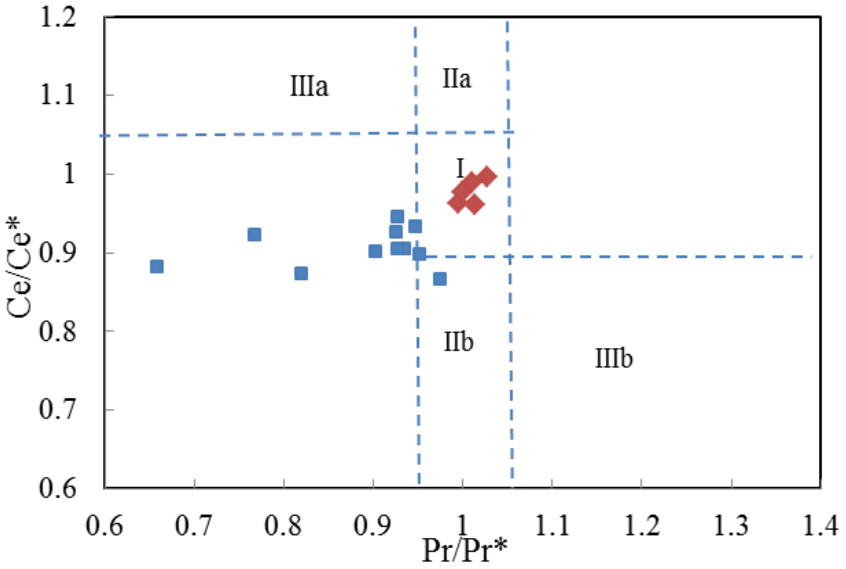

Figure 43: Ce/Ce* vs. Pr/Pr* diagram (after Bau and Dulski, 1996) for the Nkout BIFs Field I: neither Ce nor La anomaly, Field IIa. positive La anomaly, no Ce anomaly, Field IIb. negative La anomaly, no Ce anomaly, Field IIIa: positive Ce anomaly, Field IIIb. Symbols are as in Fig. 42. Note: $((Ce/Ce^*)_{SN} = Ce_{SN}/(0.5La_{SN} + 0.5Pr_{SN}; (Pr/Pr^*)_{SN} = Pr_{SN}/(0.5Ce_{SN} + 0.5Nd_{SN}; (Eu/Eu^*)_{SN} = (Eu)_{SN}/(0.67Sm_{SN} + 0.33Tb_{SN}))$

The Post-Archean Australian Shale (subscript PAAS) - normalized values show $(Gd/Yb)_{PAAS}$ ranges from 0.565 - 1.208 (average = 0.977). This reveals slight enrichment of the heavy HREEs relative to $(La/Yb)_{PAAS}$ and LREEs fractionation {0.22 > $(La/Yb)_{PAAS}$ > 1.534, average = 0.58}.

The samples show similar HREEs enrichment over LREEs when compared to the Fe-sand {average $(Gd/Yb)_{PAAS}$ = 1.29 and average $(La/Yb)_{PAAS}$, = 0.95, Abu et al., 2017}, the PAAS-normalized value {average $(Gd/Yb)_{PAAS}$ = 1.87 and La_{PAAS}/Yb_{PAAS}, average = 1.82} shows slight enrichment of the heavy HREEs relative to LREEs.

The rock samples show positive (1.063 > Eu/Eu* > 2.625, average = 1.91) Eu anomalies, and positive Y/Y*-anomaly (1.18 > Y/Y* > 1.71, average = 1.41) when compared to the average negative anomalies of Fe-sand (Eu/Eu* = 0.45, Abu et al. 2017; 0.95, Mishra et al., 2012).

The PAAS also shows negative Eu anomalies (Eu/Eu* = 0.6 McLennan, 2000), and the Upper Continental Crust shows negative anomalies (Eu/Eu* = 0.65 Taylor et al., 1985).

PAAS-normalised REEs pattern (Fig. 42A) shows LREEs depletion {$(La/Yb)_{PAAS}$ = 0.22 - 1.53, average = 0.58} relative to HREEs; positive Eu anomaly (Eu/Eu* = 1.06 - 2.625, average = 1.91) and negative Ce anomalies (Ce/Ce* = 0.86 - 0.94, average = 0.90).

However, Bau and Dulski (1996) have proposed the use of Ce/Ce* vs. Pr/Pr* diagram to discriminate the 'true' from 'false' Ce anomaly in BIF as a result of possibly anomalous abundance of La. In this diagram, the magnetite BIF plots in the field of La anomaly (Fig. 43).

The studied BIF samples show similar REEs pattern when compared to the PAAS-normalised Fe-sand (Abu et al., 2017; Mishra et al., 2012), and Upper Continental Crust values (Taylor et al., 1985).

The corresponding chondrite-normalized values show $(Gd/Yb)_{CN}$ ranges from 0.765 – 1.636 (average = 1.323), indicating HREEs depletion. The rock show both positive (1.250 > (Eu/Eu*) > 1.709, average value of 1.379) and negative {0.697 > $(Eu/Eu^*)_{CN}$ > 0.907, average = 0.82, samples WH4-2 and CH24-3} Eu anomalies.

The samples show high $(La/Sm)_{CN}$ value range from 1.909 - 7.78, indicating high LREEs fractionation while 2.039 > $(La/Yb)_{CN}$ > 14.037 (average = 5.365), indicating high HREEs fractionation.

The studied samples show LREEs enrichment {average $(La/Yb)_{CN}$ = 5.365} over HREEs {average $(Gd/Yb)_{CN}$ = 1.323}, similar to chondrite-normalized average value of Fe-sand {average $(La/Yb)_{CN}$ = 8.7 and $(Gd/Yb)_{CN}$ = 1.75, Abu et al. 2017; average $(La/Yb)_{CN}$ = 5.3 and $(Gd/Yb)_{CN}$ = 1.06, Ramachandran et al., 2016; and average $(La/Yb)_{CN}$ = 8.3 and $(Gd/Yb)_{CN}$ = 1.40, Mishra et al., 2012}.

The corresponding chondrite-normalized pattern shows LREEs enrichment and HREEs depletion and null to slightly positive Eu anomaly representing little fractionation of REE (Fig. 44B), while the Fe-sand show negative Eu anomalies {Eu/Eu* = 0.2, Abu et al., 2017; 0.68, Ramachandran et al., 2016; and 0.62, Mishra et al., 2012}.

Multi-element diagrams normalized to the values of Thompson (1982) for the magnetite BIF rocks are shown in figure 42E. The multi-element chondrite-normalized patterns display negative Ti, Yb, and Zr anomalies (Fig. 42E). Thompson (1984) interpreted the rock as coming or originated from the continental crust. Similar multi-element pattern is observed with the Fe-sand (Mishra et al., 2012; Ramachandran et al., 2016; Abu et al., 2017); Upper Continental Crust values (Taylor et al., 1985); and PAAS (McLennan, 2001).

V.1.2.4 Garnet-biotite BIF (CH7-3, CH7-6, WH3-6, WH3-9, and WH4-3)

The geochemical composition of the rock is represented in table 6 and corresponds to Fe-sand composition (Fig. 40).

The result shows that Fe_2O_3 and SiO_2 are the main components of the studied samples with contents ranging from 82.2 to 92.6 wt. % (Tab. 6).

V.1.2.4.1 Major Elements Oxide (MEO)

The studied samples show similarly high SiO_2 contents (50.80 - 60.50 wt. % average= 54.06) relative to Fe_2O_3 (31.50 - 38.10 wt. % average = 30.12) contents when compared to average content

of Fe-sand, Merkhiyat-Sudan (SiO_2=74.02, Fe_2O_3=21.3) after Elzien et al. (2014). The average SiO_2 content is relatively similar when compared to the average PAAS (62.80, McLennan, 2001) and Upper Continental Crust (66.0, UCC Taylor et al., 1985)

The Fe_2O_3 contents are largely enriched relative to the average PAAS values (6.50 wt. %, McLennan 2001) and Upper Continental Crust and (4.50, UCC Taylor et al., 1985).

The Al_2O_3 contents (5.33 - 9.54 wt. %, average = 8.3) are relatively high when compared to the average value of Fe-sand (3.6; Elzien et al., 2014; 4.36, Mishra et al., 2012: 1.88, Ramachandran et al., 2016) but lower to the average PAAS (18.98, McLennan, 2001) and Upper Continental Crust (15.20, UCC Taylor et al., 1985).

The Fe_2O_3/Al_2O_3 (1.8 - 7.1, average = 4.0) are relative lower to that of average PAAS value (0.34, McLennan, 2001) and Upper Continental Crust (0.29 Taylor et al., 1985) and similarly low compared to Fe-sand (0.28, Mishra et al., 2012; 5.9, Elzien et al., 2014).

The MgO contents (2.17 - 2.89, average = 2.3), as well as the CaO contents (2.17 - 2.89, average = 1.8) are low and very closely, compared to the Fe-sand {(0.08= MgO and 0.28= CaO), Elzien et al., 2014; (MgO = 0.27 and CaO = 0.05), Mishra et al., 2012}, indicating slight abundance of ferromagnesian silicate minerals (biotite). The average PAAS value are relative similar (2.20 and1.30 respectively, McLennan, 2001), with the Upper Continental Crust (2.02 and 4.20 respectively, UCC, Taylor et al., 1985).

The Na_2O and K_2O contents range between 0.19 - 1.52 wt. % (average = 0.49), and 2.30 - 3.05 wt. % (average = 2.37) respectively, clearly show that the concentrations of Na_2O are lower than that of K_2O.

When compared to the average Fe-sand value, the Na_2O contents are slightly similar (0.04, Mishra et al., 2012; 0.07, Elzien et al., 2014; and 0.05, Abu et al., 2017). The studied samples show average Na_2O values similar to the average PAAS (average =1.20 and, McLennan, 2001); but lower than the Upper Continental Crust (3.90, UCC Taylor et al., 1985).

The average K_2O contents (1.60, Abu et al., 2017; and 0.15, Ramachandran et al., 2016) are slightly lower in the Fe-sand, and much lower than the average PAAS (13.70, McLennan, 2001) but similar to the Upper Continental Crust (3.4, Taylor et al. 1985).

The total alkali contents (Na_2O + K_2O) are high and range from 2.5 to 03.2 wt. % (average=2.8).

The K_2O/Na_2O ratios (0.65 - 15.05) are relative high in the studied BIF samples, indicating the association of some feldspar minerals when compared to that of the magnetite BIF.

The minor element contents vary and are relatively low. TiO_2 (0.17 - 0.35 = average 0.26) contents are slightly lower compared to Fe-sand (0.12, Ramachandran et al., 2016; and 0.14, Abu et al., 2017). The average TiO_2 content is slightly lower when compared to the average PAAS value (1.00, McLennan, 2001) but similar to Upper Continental Crust (0.50, Taylor et al., 1985).

The TiO_2/Al_2O_3 ratios (0.027 - 0.033; average = 0.031) are relatively high to that of the average PAAS value (0.05, McLennan, 2001) and Upper Continental Crust (0.03, Taylor et al., 1985).

The Al_2O_3/TiO_2 ratios (31.35 - 36.69) indicate that the rock comes from a felsic source. Notably, Al_2O_3 resides in feldspars, while TiO_2 in mafic minerals.

The MnO contents (0.09 - 0.25 wt. %, average = 0.15) are similar relative to average PAAS value (0.11, McLennan, 2001) and Upper Continental Crust (0.10, Taylor et al., 1985).

The P_2O_5 contents (0.08 - 0.10 wt. %, average = 0.1) are similar relative to the average content (0.03, Mishra et al., 2012; 0.01, Ramachandran et al., 2016; 0.04, and Abu et al., 2017). The average PAAS value (0.16, McLennan, 2001) and Upper Continental Crust (0.17, Taylor et al., 1985) are similar to that of the average content of the studied samples.

The major element contents of the studied samples are similar to that of Fe-sand after Mishra et al., (2012); Elzien et al. (2014); Ramachandran et al. (2016); and Abu et al. (2017).

A binary variation diagram of Fe_2O_3 with some selected element oxide is shown in figure 40. A strong negative correlation exists between Fe_2O_3 and Al_2O_3 (r^2 = 0.81; Fig. 41B) and between Fe_2O_3 and TiO_2 (r^2 = 0.84; Fig. 41D); and a strong positive correlation exists between Al_2O_3 and TiO_2 (r^2 = 0.80; Fig. 41C). These suggest some detrital input in these studied samples.

V.1.2.4.2 Trace Elements (TE)

The studied BIF samples show relatively variable concentration of Ba (28.2 - 169ppm, average = 56.05 ppm), Zn (1.31 - 1.97ppm, average = 1.74 ppm), Ni (0.43 - 2.75ppm, average = 1.5 ppm), Cr (4.09 - 8.56ppm, average = 5.8 ppm), Rb (8.19 - 29.9ppm, average =16.38ppm), V (1.07 - 1.66ppm, average = 1.3 ppm), Y (0.06- 0.115ppm, average = 0.37 ppm), similar to that of Fe-sand (Abu et al., 2017; Ramachandran et al., 2016; and Mishra et al., 2012).

They are relative lower when compared to the average Upper Continental Crust values, (Taylor et al. 1985) and equally lower than the average PAAS values (McLennan, 2001).

The studied BIF samples are enriched in Large Ion Lithophile Elements (LILE) such as Ba (15.55 - 37.40 ppm) and Rb (7.90 - 16.55 ppm), and depleted in HFSE such as Zr, Hf, Th and U.

The average Th/U ratios (0.87 - 2.64, average = 2.3) are relatively lower when compared to that of Fe-sand (1.06, Ramachandran et al., 2016; 3.6, Mishra et al., 2012; and 5.2, Abu et al., 2017), the average PAAS values (4.7, McLennan, 2001), the average Upper Continental Crust values (3.82, Taylor et al., 1985).

The average PAAS values (0.27, McLennan, 2001) and Upper Continental Crust values (0.23) fall in the range of Co/Zn ratios (0.126 - 0.56) of the studied samples as well as the average Fe-sands value (0.17, Ramachandran et al., 2016).

The Ni/Zn ratios range from 0.28 - 1.6 (average = 0.9) are similar when compared to PAAS values (0.64, McLennan, 2001) and Upper Continental Crust values (0.61, Taylor et al., 1985). The average Fe-sand value (0.60, Ramachandran et al., 2016) falls in the same range value of the studied samples.

The average Rb/Ba ratios of the Fe-sand composition (0.15, Ramachandran et al. 2016; 0.13, Abu et al. 2017; 0.53, Mishra et al., 2012), and average PAAS (0.24, Taylor et al., 1985) and UCC (0.203 McLennan, 2001) values occur within the same range of the studied value (0.27 - 1.06 ppm, average = 0.47).

The average Rb/Sr ratios (0.07 - 1.77 average = 0.65) are relatively similar to the average value of Fe-sand composition (1.14, Mishra et al., 2012; 0.8, Ramachandran et al., 2016; 1.7, Abu et al. 2017), and average PAAS (0.8, Taylor et al. 1985) with UCC (0.32, McLennan 2001).

The Zr (0.001 - 0.006 ppm) contents, Co (0.277 - 0.958 ppm), Sr (0.303 - 2.29 ppm) Hf (0.001) and Cu (0.06 - 5.89 ppm) are moderately variable.

Their average values are very low when compared to the Fe-sandstone (Mishra et al. 2012; Ramachandran et al., 2016), the average PAAS values (McLennan, 2001) and Upper Continental Crust values (Taylor et al., 1985).

The average Zr/Y (0.008 - 0.011, average = 0.07) ratios are relative lower when compared to the average content in the Fe-sand composition (7.0, Abu et al., 2017; 20.7, Ramachandran et al., 2016; 10.4, Mishra et al., 2012).

The average Nb/Y (0.01) ratio is relatively similar to that of the Fe-sand rock (0.30 Ramachandran et al., 2016; 0.3, Mishra et al., 2012; 0.2, Abu et al., 2017).

A weak positive correlation exists between Zr and Al_2O_3 ($r^2 = 0.39$; Fig. 41) and between Zr and TiO_2 ($r^2 = 0.11$; Fig. 41), suggesting that there was a slight detrital input when compared with the magnetite BIF. Zr, Rb, Nb, Hf and Sr are commonly derived from the weathering of felsic rocks whereas Cr, Co, Sc and Ni are derived from the weathering of mafic sources.

V.1.2.4.3. Rare Earth Elements (REEs)

The sum of the rear earth elements (REEs) contents of studied BIF are relatively lower (2.24 - 9.17 ppm, average = 5.62) when compared to the average value of Fe-sand (ΣREE average = 78, Abu et al. 2017; 22 ppm, Ramachandran et al., 2016; 86ppm, Mishra et al., 2012), average PAAS values (ΣREE average = 184.7, McLennan, 2001), and average Upper Continental Crust values (ΣREE average = 146.7, UCC Taylor et al. 1985).

The concentrations of light rear earth elements (LREEs = La - Gd) are low and variable. La range between 1.82- 8.54 ppm (average = 4.87 ppm), and Gd range between 0.11 - 0.25 ppm (average of 0.19) respectively.

The concentrations of heavy rear earth elements (HREEs = Tb - Lu) are equally low and variable. Tb range from 0.065 to 0.15ppm (average = 0.0104 ppm), and Lu varies between 0.01 - 0.05 ppm (average of 0.02).

The REEs values are characterized by a significant enrichment in LREEs over HREEs, similar to the average value of Fe-sand (ΣLREE 72.9 > ΣHREE 5.4, Abu et al. 2017; ΣLREE 20.2 > ΣHREE 2.5, Ramachandran et al., 2016), PAAS (ΣLREE 160.5 > ΣHREE 12.18, McLennan, 2001), Upper Continental Crust (ΣLREE 132, > ΣHREE 13.89, Taylor et al., 1985).

The results are chondrite-normalised and PAAS-normalised to the values of Evensen et al**.**, (1978) and Taylor and McLennan (1985) respectively.

The PAAS-normalized values reveals depletion in HREEs as indicated by the $(Gd/Yb)_{PAAS}$ values {1.539 > $(Gd/Yb)_{PAAS}$ > 11.705, average = 5.060}.

The $(La/Sm)_{PAAS}$ value {1.27 > $(La/Sm)_{PAAS}$ > 3.965, average = 2.12} indicates high LREEs fractionation as also indicated by $(La/Yb)_{PAAS}$ value {3.469 > $(La/Yb)_{PAAS}$ > 14.35, average = 19.00} relative to the HREEs fractionation.

The studied samples show similar LREEs enrichment over HREEs when compared to the average PAAS value {$(La/Yb)_{PAAS}$ = 9.15 > $(Gd/Yb)_{PAAS}$ = 1.34, McLennan 2001} and Upper Continental Crust values {$(La/Yb)_{PAAS}$ = 9.21 > $(Gd/Yb)_{PAAS}$ = 1. 4, Taylor et al., 1985}, but indicating slight enrichment of the heavy HREEs relative to $(La/Yb)_{PAAS,}$ contrary to the Fe-sand {$(Gd/Yb)_{PAAS}$ = 1.29 > $(La/Yb)_{PAAS}$ = 0.95, Abu et al., 2017; $(Gd/Yb)_{PAAS}$ = 1.03 > $(La/Yb)_{PAAS}$ = 0.91, Mishra et al., 2012}.

The studied rocks show characteristically positive PAAS-normalised Eu-anomalies {1.27 > Eu/Eu* > 1.99} relative to negative average Fe-sand (Eu/Eu* = 0.4, Abu et al. 2017; 0.9, Mishra et al., 2012), PAAS (Eu/Eu* = 0.6, McLennan, 2001), and the Upper Continental Crust (Eu/Eu* = 0.65, Taylor et al., 1985).

The REEs pattern of studied BIF samples show strong LREEs enrichment {$(La/Yb)_{PAAS}$ = 3.46 - 37.55, average = 19.00} and HREEs depletion (Fig. 42C), and positive Eu anomaly (Eu/Eu* = 1.27 - 1.89, average = 1.62). It plots in the field of neither Ce nor La anomaly on the Ce/Ce* vs. Pr/Pr* diagram (Fig. 43).

The corresponding chondrite-normalized values show $(La/Yb)_{CN}$ values {31.74> $(La/Yb)_{CN}$ > 343.57 average = 173.98}, indicating LREEs enrichment relative to HREEs depletion {2.085 > $(Gd/Yb)_{CN}$ > 15.845, average = 6.83}, similar to the average value of Fe-sands {$(La/Yb)_{CN}$ = 8.7 > $(Gd/Yb)_{CN}$ =1.75, Abu et al. 2017; $(La/Yb)_{CN}$ = 8.3 > $(Gd/Yb)_{CN}$ = 1.4, Mishra et al. 2012}.

The studied samples show both positive and negative Eu- anomaly. The positive Eu-anomalies is in the range of 1.04 > (Eu/Eu*) > 1.305 while the negative Eu-anomalies range from

0.827 - 0.939 similar to average Fe-sand value (Eu/Eu*= 0.26, Abu et al. 2017; 0.62, Mishra et al. 2012), and UCC (Eu/Eu* = 0.65, Taylor et al., 1985).

The chondrite-normalized REEs diagram of sample BIF shows LREEs enrichment and HREEs depletion, positive Eu anomaly (1.04 - 1.31), indicating little REEs fractionation (Fig. 42D).

Both PAAS-normalised and chondrite-normalised REEs patterns for Fe-sand (Abu et al. 2017; Ramachandran et al. 2016; and Mishra et al. 2012), and Upper Continental Crust values (Taylor et al., 1985) are similar to the studied garnet-biotite BIF.

Multi-element chondrite-normalized (Thompson 1982) diagrams for the studied BIF samples are shown in figure 42F. On the diagram, the studied samples show similar pattern with that of Fe-sand (Mishra et al., 2012; Ramachandran et al., 2016; and Abu et al., 2017), Upper Continental Crust values (Taylor et al., 1985) and PAAS (McLennan, 2001). The BIF rock is depleted and show strong negative Ti, Yb, and Zr anomalies and a weak negative Sr anomalies, indicating characteristic of rock originating for the continental crust.

V.1.2.5 Correlation of BIFs

The relationship in magnetite-rich BIF between the SiO_2 and Fe_2O_3 reflects a strong negative correlation (-0.95; Tab. 7) between the two components. There exists an inverse distribution of quartz and iron minerals in the banded iron-formation.

Table 7: Pearson's correlation matrix for major element oxides of magnetite BIF

	Fe_2O_3	SiO_2	Al_2O_3	CaO	MgO	Na_2O	K_2O	TiO_2	MnO	P_2O_5	LOI
Fe_2O_3	1.00										
SiO_2	**-0.95**	1.00									
Al_2O_3	-0.05	-0.13	1.00								
CaO	-0.16	0.28	-0.27	1.00							
MgO	-0.45	0.27	-0.27	-0.14	1.00						
Na_2O	-0.30	0.31	0.21	0.60	-0.11	1.00					
K_2O	0.24	-0.39	0.89	-0.36	-0.26	0.09	1.00				
TiO_2	0.62	-0.76	0.49	-0.26	-0.27	-0.22	0.57	1.00			
MnO	0.14	-0.13	-0.14	0.33	-0.03	0.19	-0.09	0.19	1.00		
P_2O_5	-0.22	0.26	-0.09	0.06	-0.11	-0.33	-0.32	-0.07	-0.08	1.00	
LOI	-0.62	0.54	-0.07	0.07	0.60	0.03	-0.06	-0.38	-0.22	-0.25	1.00

There exists an inverse distribution of quartz and iron minerals in the garnet-biotite rich metamorphosed BIF. The relationship in between the SiO_2 and Fe_2O_3 reflects a strong negative correlation (-0.86; Tab. 8) between the two components.

Table 8: Pearson's correlation matrix for major element oxides of garnet-biotite BIF

	Fe_2O_3	SiO_2	Al_2O_3	CaO	MgO	Na_2O	K_2O	Cr_2O_3	TiO_2	MnO	P_2O_5	LOI
Fe_2O_3	1.00											
SiO_2	**-0.86**	1.00										
Al_2O_3	-0.92	0.73	1.00									
CaO	-0.07	-0.41	0.16	1.00								
MgO	0.30	-0.39	-0.21	0.48	1.00							
Na_2O	-0.27	-0.11	0.29	0.84	0.63	1.00						
K_2O	0.07	0.29	0.00	-0.86	-0.68	-0.93	1.00					
Cr_2O_3	-0.02	-0.18	0.14	0.58	0.30	0.43	-0.39	1.00				
TiO_2	-0.93	0.66	0.92	0.40	-0.04	0.53	-0.34	0.26	1.00			
MnO	0.46	-0.33	-0.25	-0.18	-0.10	-0.56	0.49	0.34	-0.40	1.00		
P_2O_5	-0.18	-0.06	0.29	0.60	0.82	0.87	-0.74	0.25	0.41	-0.45	1.00	
LOI	-0.24	0.17	-0.06	-0.05	-0.47	-0.09	-0.08	-0.56	0.10	-0.50	-0.36	1.00

V.1.3. IRON ORE TYPES

The BIF rock of studied area consists of iron ore group. Their whole rock major element oxide data are presented in Table 9.

Authors around the world have reported that iron ore bodies were resulted from BIF (Webb and Clout, 2008). It has been found that iron ore is as a result of sequential removal and replacement of gangue minerals in the host BIF structure (Alchin et al. 2008; Dalstra and Rosiere 2008). Beukes et al., (2008) reported that iron ores were formed by geochemical replacement and leaching of BIF protolith. The hypothesis indicates that BIF rock is a sure protolith of iron ore.

The nature of iron ore protolith rocks were determined by comparative study of major element oxide geochemical characteristics of BIF (Fig. 44). This study shows similar major element oxide geochemical pattern with the Precambrian BIF, indicating a generic protolith of the iron ore.

The ores are further compared with the average major element oxide composition of Precambrian BIF (Prasad et al., 2012; Adekoya et al., 2012; and Klien 2004) and average PAAS (McLennan, 2001) and Upper Continental Crust values (Taylor et al., 1985), Algoma-type (Gross et al., 1980), and Lake Superior-types (Gross et al., 1980).

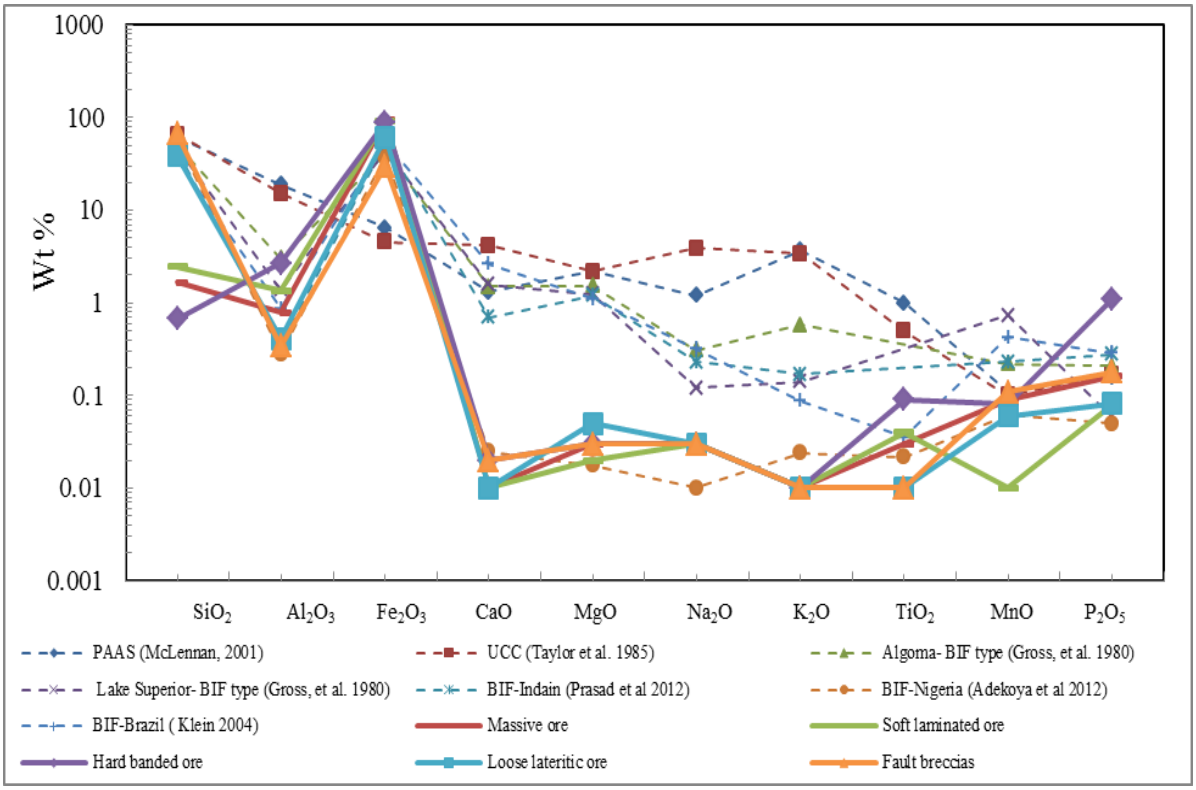

Figure 44: Major element oxide patterns of BIF and different ore types from Nkout deposits showing similar trend. The average major element oxide composition of Magnetite BIF and Garnet-biotite BIF (this study)**,** Lake Superior- BIF type (Gross et al., 1980); Algoma- BIF type (Gross et al., 1980); UCC (Taylor et al., 1985) and PAAS (McLennan 2001); BIF-Brazil (Klein 2004); BIF-Indian (Prasad et al., 2012); BIF-Nigeria (Adekoya et al., 2012) are shown on the diagram for comparison**.**

Table 9: Bulk major chemical composition (in wt. %) of Nkout iron ore types

Ore	Massive ore		Soft laminated ore		Hard banded ore		Loose lateritic ore		Fault breccias	
Type	1	1	II	II	III	III	IV	IV	V	V
Samples Wt.%	n1031	n1022	n1006	n1032	n1025	n1026	n1002	n1035	n1001	n1012
SiO_2	1.67	0.77	2.46	2.62	0.68	2.93	38.8	37.05	67.24	84.98
TiO_2	0.03	0.08	0.04	0.03	0.09	0.12	0.01	0.01	0.01	0.01
Al_2O_3	0.79	2.58	1.36	1.36	2.66	4.12	0.41	0.16	0.34	0.12
Fe_2O_3	94.29	92.83	91.74	85.48	88.84	88.26	61.26	61.24	29.92	14.68
MgO	0.03	0.02	0.02	0.05	0.03	0.04	0.05	0.02	0.03	0.03
MnO	0.09	0.03	0.01	0.26	0.08	0.09	0.06	0.31	0.11	0.01
CaO	0.01	0.01	0.01	0.01	0.02	0.02	0.01	0.02	0.02	0.02
Na_2O	0.03	0.03	0.03	0.03	0.03	0.03	0.03	0.03	0.03	0.03
K_2O	0.01	0.01	0.01	0.01	0.01	0.02	0.01	0.01	0.01	0.01
P_2O_5	0.162	0.355	0.079	0.13	1.092	0.103	0.081	0.134	0.178	0.064
Cr_2O_3	0.03	0.05	0.01	0.01	0.03	0.03	0.06	0.01	0.06	0.07
LOI	2.9	3.3	4.3	10.1	6.5	4.3	-0.7	1.1	2.1	0
Total	100.01	100.03	100.04	100.03	100.02	100.02	100.02	100.02	100.03	100.01
Fe	65.95	64.93	64.17	59.79	62.14	61.73	42.85	42.84	20.92	10.27
Fe_2O_3/Ti	3143	1160.38	2293.5	2849.3	987.11	735.5	6126	6124	2992	1468
SiO_2/ Fe_2O_3	0.018	0.008	0.027	0.031	0.008	0.033	0.633	0.605	2.247	5.789
Al_2O_3/ TiO_2	26.333	32.25	34	45.333	29.556	34.333	41	16	34	12
SiO_2/ Al_2O_3	2.114	0.298	1.809	1.926	0.256	0.711	94.634	231.56	197.765	708.167
Fe_2O_3/ Al_2O_3	119.35	35.981	67.456	62.853	33.398	21.422	149.42	382.75	88	122.333
Fe_2O_3+ SiO_2	95.96	93.6	94.2	88.1	89.52	91.19	100.06	98.29	97.16	99.66
Na_2O+K_2O	0.04	0.04	0.04	0.04	0.04	0.05	0.04	0.04	0.04	0.04
K_2O/Na_2O	0.04	0.33	0.33	0.33	0.33	0.67	0.33	0.33	0.33	0.33

The different types of iron ores are distinguished, consisting of five petrographic types namely; massive ore (I), hard laminated Ore (II), soft laminated Ore (III), loose lateritic ore (IV) and fault breccias (V) types.

V.1.3.1. Massive ore (I)

V.1.3.1.1 Major Elements Oxide (MEO)

The iron ore is represented by massive ore (I) samples (n1031 and n1022) which shows similar geochemical pattern to BIF composition (Fig. 44).

In the massive ore, the total Fe_2O_3 contents range from 92.83 to 94.29 wt.% with an average of 93.4 wt. % are relatively enriched when compare to the average value of Archean-Proterozoic BIF: Tamil Nadu, South India (Fe_2O_3 = 53.21), after Prasad et al. (2012); Muro, Central Nigeria (Fe_2O_3 = 38.02) after Adekoya et al. (2012); Mato Grosso Do Sul, Brazil (Fe_2O_3 = 54.7) after Klien, (2004); Upper Continental Crust (Fe_2O_3 = 4.5) after Taylor et al. (1985); Algoma-type (Fe_2O_3 = 41.33) after Gross et al., (1980); and average Lake Superior-type, (Fe_2O_3 = 44.51) after Gross et al., (1980).

The SiO_2 contents (1.67 to 0.77 wt. %) are very low and relative depleted compared to the average Upper Continental Crust value (66, Taylor et al., 1985), Algoma-type (50.5, Gross, et al. 1980), Lake Superior-type (47.2, Gross et al., 1980), and BIF (34.2, Klien, 2004; 54.3, Adekoya et al., 2012; and 44.6, Prasad et al., 2012).

The sum of Fe_2O_3 + SiO_2 values range from 93.6 - 95.9 wt. % (Tab. 9), as the two principal components of the studied ore samples.

Al_2O_3 contents (0.79 to 2.5 wt. %, average = 1.6 wt. %.) are depleted and vary relative to the average PAAS (18.98, McLennan 2001), Upper Continental Crust value (15.2, Taylor et al., 1985), but similar to the average value of Algoma-type (3.0, Gross, et al., 1980), Lake Superior-type (1.13, Gross et al., 1980) and BIF (0.35, Prasad et al., 2012; 0.28, Adekoya et al., 2012; 0.8 Klien 2004).

The Fe_2O_3/Al_2O_3 ratios range from 35.981 - 119.354 wt. % with an average of 77.0 wt. %. CaO contents (0.01 - 0.02 wt. %; average = 0.15) are low (Tab. 9), suggesting the absence of calcite and dolomite bearing minerals in the ore, similar to the average value of BIF (2.6 Klien, 2004; 0.7, Prasad et al., 2012; and 0.02, Adekoya et al., 2012). The Algoma-type (1.5, Gross et al., 1980) and Lake Superior-type (1.5, Gross et al., 1980) are equally depleted similar to the studied samples.

The MgO contents are low ranges from 0.02 to 0.03 wt. % similar to BIF (1.21 Prasad et al., 2012), Algoma-type (1.5, Gross et al., 1980), Lake Superior-type, (1.2, Gross et al., 1980), and average PAAS (2.2, McLennan 2001), Upper Continental Crust value (2.2, Taylor et al., 1985).

The K_2O contents are constant (0.01 wt. %) while the Na_2O contents (0.03 wt. % Tab. 9) indicate that the concentrations of Na_2O are slightly higher than that of K_2O. The K_2O contents are

depleted when compared to the average PAAS (3.7, McLennan 2001), Upper Continental Crust value (3.4, Taylor et al., 1985), but similar to the average value of Algoma-type (0.58, Gross et al., 1980), Lake Superior-type (0.14, Gross et al., 1980).

The total alkali ($Na_2O + K_2O$) contents are constantly on an average of 0.04 wt. %, indicating that the source of the clastic component was constant in composition.

The TiO_2 contents (0.03 to 0.08 wt. %, average = 0.05) are relatively similar and closed when compared to the average Upper Continental Crust value (0.5, Taylor et al., 1985), PAAS (1.0, McLennan 2001) and BIF (0.02, Adekoya et al., 2012; 0.08, Klien 2004).

The Al_2O_3/TiO_2 ratios varied considerably (26.3 - 32.2, average = 29.4), are probably related to the clay minerals.

The average BIF values (0.42, Klien 2004; 0.06, Adekoya et al., 2012; 0.23, Prasad et al. 2012), Algoma-type (0.22, Gross et al., 1980), and Lake Superior-type (0.73, Gross et al., 1980), show similar depleted MnO contents (0.03 to 0.09).

The Upper Continental Crust value (0.16, Taylor et al., 1985), PAAS (0.17, McLennan 2001), BIF (0.28, Klien 2004; 0.04, Adekoya et al., 2012; 0.28, Prasad et al., 2012), Algoma-type (0.21, Gross et al., 1980), and Lake Superior-type (0.06, Gross et al., 1980) are similar to the P_2O_5 contents and equally depleted, ranging from 0.162 to 0.355 wt. %.

The major element contents of the massive ore samples are similar to the average contents of BIF rock according to Prasad et al. (2012), Adekoya et al. (2012), Klien (2004), Taylor et al. (1985), Gross et al. (1980).

On the binary plots, the Fe_2O_3 contents of the massive ore (I) appear scattered with Al_2O_3, Cr_2O_3, K_2O, MgO, TiO_2, P_2O_5, while they appear closer to each other with CaO, Na_2O, SiO_2 and MnO oxide (Fig. 45).

V.1.3.2. Hard laminated Ore (II)

V.1.3.2.1 Major Elements Oxide (MEO)

The iron ore is also represented by hard laminated ore (II) samples (n1025 and n1026) which shows similar geochemical pattern to BIF composition (Fig. 44).

The ore show Fe_2O_3 contents (85.48 to 91.74) enriched relatively to the average BIF (53.21, Prasad et al. 2012; 54.7, Klien 2004) Upper Continental Crust value (4.5, Taylor et al. 1985), PAAS (6.5, McLennan 2001).

The ore show relative depletion in SiO_2 (2.46 - 2.62, average = 2.56) contents relative to the Upper Continental Crust value (66, Taylor et al., 1985), PAAS (62.8, McLennan, 2001), Algoma-type (50.5, Gross et al., 1980), Lake Superior-type (47.2, Gross et al., 1980) and BIF (34.2, Klien 2004; 57.3, Adekoya et al., 2012; 44.6, Prasad et al., 2012).

The two principal components of the studied samples, Fe_2O_3 + SiO_2 contents range from 88.1 to 94.2 wt. % (Tab. 9).

The average Al_2O_3 content (1.36) is depleted relative to the Algoma-type (3, Gross et al. 1980), but relatively similar to the average Upper Continental Crust value (0.35, Taylor et al. 1985), PAAS (0.7, McLennan 2001), Lake Superior-type (1.39, Gross et al., 1980) and other BIFs (0.35, Prasad et al., 2012; 0.28, Adekoya et al., 2012; and 0.87, Klein 2004).

MgO contents (0.02 - 0.05, average = 0.035) are relative low and does not exceed an average value when compared to the average BIF value (1.1, Klein 2004; 0.017, Adekoya et al., 2012; 1.21, Prasad et al., 2012).

The average CaO content (0.01) is constantly depleted and does not exceed an average value when compared to Algoma-type (1.51, Gross et al., 1980) and Lake Superior-type (1.24, Gross et al. 1980), and BIF (0.02, Adekoya et al., 2012; 2.63, Klein 2004; 0.7, Prasad et al., 2012).

The average Na_2O content (0.30) is depleted relative Upper Continental Crust value (3.9, Taylor et al., 1985), PAAS (1.2, McLennan 2001).

The K_2O contents (0.01) are lower, similar to BIF (0.17, Prasad et al., 2012; 0.03, Klein 2004), Algoma-type (0.31, Gross et al., 1980) and Lake Superior-type (0.12, Gross et al., 1980).

The average TiO_2 content (0.035) is relatively similar to BIF (0.08, Klein 2004; 0.02, Adekoya et al., 2012), Upper Continental Crust value (0.5, Taylor et al., 1985), PAAS (1, McLennan 2001).

The Al_2O_3/TiO_2 ratios varied considerably (34 - 45.3, average = 39.6), are slightly enriched.

The average Upper Continental Crust value (0.1, Taylor et al., 1985) and PAAS (0.1, McLennan 2001) are relatively depleted with uniform distribution similar to the studied MnO contents (0.01 - 0.26).

The Algoma-type (0.21, Gross et al., 1980), Lake Superior-type (0.06, Gross et al., 1980), and BIF (0.04, Adekoya et al., 2012; 0.28, Klein 2004; 0.28, Prasad et al., 2012) are relatively higher when compared to the average P_2O_5 content (0.1).

The major element contents of the hard laminated ore samples are similar to the average contents of BIF rock according to Prasad et al. (2012), Adekoya et al. (2012), Klien, (2004), Taylor et al., (1985), Gross et al., (1980).

The Fe_2O_3 contents appear scatter on the binary plot with K_2O, MgO, P_2O_5, Na_2O, and whereas they are closer with Al_2O_3, TiO_2, CaO, SiO_2, MnO, and Cr_2O_3 oxide (Fig. 45).

V.1.3.3 Soft laminated Ore (III)

V.1.3.3.1 Major Elements Oxide (MEO)

The studied ore samples are represented by soft laminated ore (III) samples (n1006 and n1032) which shows similar geochemical pattern with BIF composition.

The ore samples are relative enriched and variable in Fe_2O_3, (88.26 - 88.84, average = 88.5) contents relative to the average value of BIF (53.21, Prasad et al., 2012; 38.02, Adekoya et al., 2012; and 54.7, Klien 2004), Upper Continental Crust (4.5, UCC, Taylor et al., 1985), average Algoma-type (41.33, Gross et al., 1980), and average Lake Superior-type, (44.51, Gross et al. 1980).

The average SiO_2 content of the Upper Continental Crust (66.0, Taylor et al., 1985), PAAS (62.8, McLennan 2001), Algoma-type (50.5, Gross et al., 1980), and Lake Superior-type, (47.2, Gross et al., 1980) are relative enriched compared to the SiO_2 contents (0.68 - 2.93; average = 1.8).

The Fe_2O_3 + SiO_2 contents range from 89.52 to 91.19 wt. % with an average of 90.3 wt. %.

The Al_2O_3 contents (2.66 - 4.12, average = 3.9) are relatively depleted compared to the average Upper Continental Crust (15.2, Taylor et al., 1985), PAAS (18.98, McLennan 2001), but similar to the average Algoma-type (3, Gross et al., 1980), Lake Superior-type, (1.39, Gross et al., 1980) and BIF (0.35, Prasad et al., 201; 02.8, Adekoya et al., 2012; and 0.87, Klien 2004).

The MgO concentrations (0.03 - 0.04, average = 0.035) are low and are in trace amount while the CaO contents are depleted and does not exceed an average value (0.02) similar to the average value of Algoma-type (1.53and 1.51, Gross et al., 1980), Lake Superior-type (1.24and 1.58, Gross et al. 1980), PAAS (2.2 and 1.3, McLennan 2001) and Upper Continental Crust (2.2 and 4.2, Taylor et al., 1985).

The alkaline contents (Na_2O and K_2O) in most cases are (0.03 and 0.2) relatively low respectively. The concentrations of Na_2O are relative higher than that of K_2O. The average total alkali contents (Na_2O + K_2O = 0.045) are high similar to Algoma-type (0.89, Gross et al. 1980), Lake Superior-type (0.26, Gross et al., 1980), and BIF (0.40, Prasad et al., 2012; 003, Adekoya et al., 2012; and 0.33, Klien 2004).

The average TiO_2 concentrations of PAAS (1, McLennan 2001), BIF (0.02, Adekoya et al., 2012; 0.08, Klein 2004) and Upper Continental Crust (0.5, Taylor et al., 1985), are very similar in trace amount compared to the studied samples (0.09 to 0.12, average = 0.1).

MnO concentrations (0.08 - 0.09, average = 0.07) vary and depleted similar to BIF (0.42, Klein 2004; 0.06, Adekoya et al., 2012; 0.23, Prasad et al., 2012).

P_2O_5 contents (0.09 - 0.12) are also low and depleted similar to Algoma-type (0.21 Gross et al., 1980), Lake Superior-type, (0.06, Gross et al., 1980), Upper Continental Crust (0.17, Taylor et al., 1985), and PAAS (0.16, McLennan 2001).

The major element contents of the soft laminated ore samples are similar to the average contents of BIF rock after Prasad et al. (2012); Adekoya et al. (2012); Klien, (2004); Taylor et al. (1985); and Gross et al. (1980).

On the binary plot, the Fe_2O_3 content appear scatter with Al_2O_3, K_2O, P_2O_5,whereas TiO_2, CaO, SiO_2, MnO, Cr_2O_3, MgO, and Na_2O, appear closer (Fig. 45).

V.1.3.4 Loose lateritic ore (IV)

V.1.3.4.1 Major Elements Oxide (MEO)

On the major element geochemical comparative spider diagram, the loose lateritic ore (type IV, samples n1002 and n1035) shows similar geochemical pattern to BIF composition (Fig. 44).

The ore samples show relatively enriched Fe_2O_3 contents (61.24 to 61.26) similar to BIF (54.7, Klein 2004; 53.2, Prasad et al., 2012; and 38.0, Adekoya et al., 2012)

The variations in SiO_2 concentrations (38.8 - 37.05, average = 37.9) are slightly depleted when compared to average Upper Continental Crust (66.0, Taylor et al. 1985), and PAAS (62.8, McLennan 2001), Algoma-type (50.5, Gross et al. 1980), Lake Superior-type (47.2, Gross et al. 1980), and BIF (57.3, Adekoya et al. 2012; and 34.4, Klein 2004).

The average Al_2O_3 contents (0.02) vary much and show similarly depletion when compared to average value of BIF (0.87, Klein 2004; 0.28, Adekoya et al., 2012; 0.35, Prasad et al., 2012), Algoma-type (3, Gross et al., 1980) and Lake Superior-type (1.39, Gross et al., 1980) but are contrary low when compared to enriched average Upper Continental Crust (15.2, Taylor et al., 1985), and PAAS (18.98, McLennan 2001).

The average K_2O content (0.01) shows relatively depletion similar to Algoma-type (0.58, Gross et al. 1980) and Lake Superior-type (0.14, Gross et al. 1980), BIF (0.17, Prasad et al. 2012; 0.02, Adekoya et al. 2012; 0.03, Klein 2004).

The Na_2O contents (0.03) are uniformly distributed in the ore and are similar when compared to BIF (0.23, Prasad et al., 2012; 0.01, Adekoya et al., 2012), Algoma-type (0.31, Gross et al., 1980) and Lake Superior-type (0.12, Gross et al., 1980).

The CaO contents (01- 0.02) are depleted as well as MgO contents (0.02 - 0.05) similar to that of BIF (0.02 and 0.01, Adekoya et al., 2012; 0.7 and 1.21, Prasad et al., 2012),

The average TiO_2 content (0.01) is depleted the average Upper Continental Crust (0.5, Taylor et al. 1985), PAAS (1, McLennan 2001) and BIF (0.02, Adekoya et al., 2012; 0.08, Klein 2004).

The Al_2O_3/TiO_2 ratios varied considerably (16 - 41, average = 28.4), are probably related to the clay minerals similar to that of BIF (14.0, Adekoya et al., 2012; 10.87 Klein 2004), average Upper Continental Crust (30.4, Taylor et al., 1985), and PAAS (18.9, McLennan 2001).

The MnO contents (06 - 0.31) are depleted as well as P_2O_5 contents (0.03 - 0.05) are similar to the average Algoma-type value (0.22 and 0.21, Gross et al., 1980) and Lake Superior-type (0.73 and 0.06, Gross et al.,1980).

The major element contents of the soft loose lateritic samples show similar average contents of BIF rock after Prasad et al. (2012), Adekoya et al. (2012), Klien (2004), Taylor et al. (1985), Gross et al., (1980).

The Fe_2O_3 content of the loose lateritic ore (IV) appear scattered with MgO, MnO, CaO, Cr_2O_3, but closer with TiO_2, SiO_2, Na_2O, Al_2O_3, K_2O, and P_2O_5 on the Harker diagram (Fig 45).

V.1.3.5 Fault breccias (V)

V.1.3.5.1 Major Elements Oxide (MEO)

The geochemical comparative spider diagram shows similar geochemical pattern of Fault breccias with BIF (samples n1001, and n1012; Fig. 44).

The Fe_2O_3 contents of the studied ore samples (14.68 - 29.92, average = 22.3) are relative depleted and the least amongst the different ore types when compared to the average Algoma-type (41.33, Gross et al., 1980) and Lake Superior-type (44.51, Gross et al., 1980) but relatively enriched to that of the average Upper Continental Crust (4.5, Taylor et al., 1985), and PAAS (6.5, McLennan 2001).

The SiO_2 contents (67.24 - 84.98 wt. %) are relative enriched and highest between the different types relative to average Upper Continental Crust (66.0, Taylor et al., 1985), and PAAS (62.8, McLennan 2001), Algoma-type (50.5, Gross et al., 1980) and Lake Superior-type (47.2, Gross et al., 1980).

The Fe_2O_3 + SiO_2 contents (97.16 - 99.66) are the two principal components of the studied ore.

The Al_2O_3 contents (0.34 - 0.12, average = 0.23) are low and similar to that of BIF (0.87, Klein 2004; 0.28, Adekoya et al., 2012; 0.35, Prasad et al. 2012), Algoma-type (3, Gross et al., 1980) and Lake Superior-type (1.39, Gross et al., 1980) but are low contrary to average Upper Continental Crust (15.2, Taylor et al., 1985), and PAAS (18.98, McLennan 2001).

The average MgO contents (0.03) and CaO contents (0.02) are similarly depleted to the average BIF value (1.21and 0.7, Prasad et al., 2012; 0.1 and 0.2, Adekoya et al., 2012), Algoma-type (3, Gross et al., 1980) and Lake Superior-type (1.39, Gross et al. 1980), contrary to the slightly enriched average Upper Continental Crust (2.2 and 4.2, Taylor et al., 1985), and PAAS (2.2 and 1.3, McLennan, 2001).

The Na_2O contents (0.03) are equally depleted, as well as the average K_2O contents (0.01). The average total alkali contents (Na_2O + K_2O = 0.04) and the K_2O/Na_2O ratios (0.33) are similar to that of Algoma-type (Gross et al., 1980) and Lake Superior-type (Gross et al., 1980).

The TiO_2 contents are relatively depleted (0.12 - 0.34, average = 0.2). The Al_2O_3/TiO_2 ratios varied considerably (12 - 34, average = 23.4), are probably related to the clay minerals similar to that of BIF.

The MnO contents (0.01 - 0.11), and P_2O_5 contents (0.064 - 0.178) are equally low and relatively depleted similar to that of BIF (0.06 and 0.04, Adekoya et al., 2012; 0.4 and 0.2 Klein 2004).

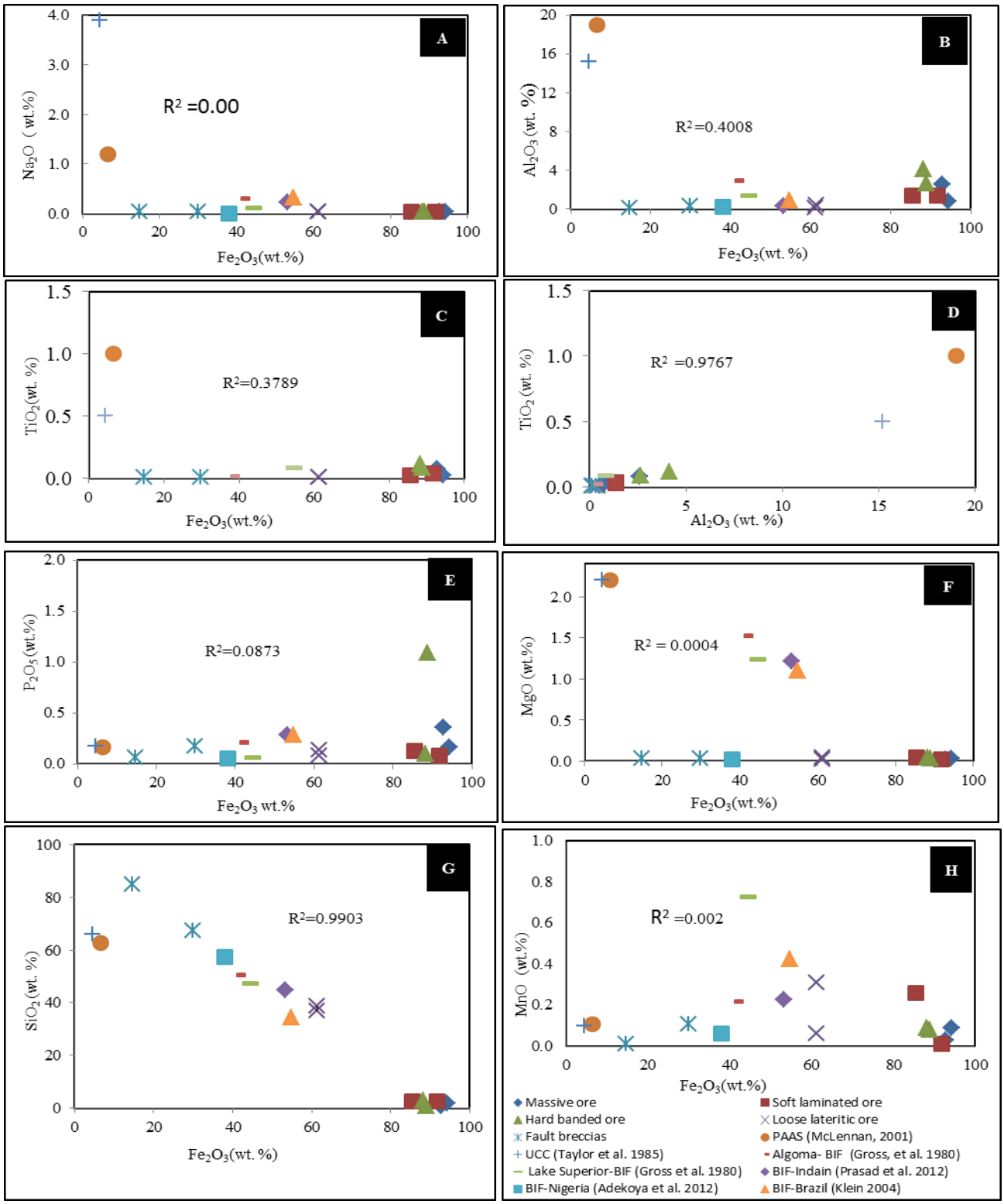

Figure 45: Binary plots for major element oxide variation with Fe_2O_3 in Nkout iron ore types.

The major element contents of the fault breccias samples show similar average contents of BIF rock after Prasad et al. (2012), Adekoya et al. (2012), Klien (2004), Taylor et al. (1985), Gross et al. (1980).

Fe_2O_3 content show negative correlation with SiO_2 on the binary plot and appears closer with TiO_2, Na_2O, Al_2O_3, K_2O, MgO, MnO, CaO, Cr_2O_3, and P_2O_5 (Fig 45).

The major element geochemical differences between the ore samples are evidently clear in the content of Fe_2O_3 that drops from massive ore (1) to fault breccias (V). The P_2O_5 content is approximately the same in all ore samples. SiO_2 content is enriched in lateritic ore, fault breccia, and depleted in massive ore (I), hard laminated Ore (II), soft laminated Ore (III) types. The result shows that Fe_2O_3 and SiO_2 are the main components of the study samples (88.1 to 100.06), suggesting that they belong to the oxide type metamorphosed BIF. The samples show contents of iron and silica, similar to BIF (Tab. 9).

The Al_2O_3 contents (0.13 - 4.12) in soft laminated Ores, lateritic and fault breccia are low, but higher in massive and hard laminated ores. These samples also show similar TiO_2 (0.01 - 0.12) contents, probably related to the clay minerals. CaO and MgO contents (0.01 - 0.02 and 0.02 - 0.05) respectively, confirming the presence of silicate minerals. K_2O and Na_2O contents (0.01 - 0.02) are reduced from massive to fault breccia ore.

LOI suggest in all the samples except for sample n1002, most probably reflects the presence of gibbsite and goethite as they contain water in their structure. Samples with Al_2O_3 contents (2.58 - 4.12) and LOI (3.3 - 10.1) indicate a strong positive correlation, which most probably reflects the existence of gibbsite. The Fe_2O_3 (88.26 - 94.26) and their corresponding LOI is certainly as the result of gibbsite and goethite as they contain H_2O in their structure.

The geochemical characteristics of Nkout banded iron formation (BIF), reveals three regrouped of ore categories identified from five structural types (Tab. 6): enriched (60 - 66 % Fe) consists of massive ore (I), soft laminated ore (II), hard laminated ore (III); intermediate ore (42 - 43 % Fe) represents, Loose lateritic ore (IV) BIF and the depleted iron ore (10 - 20 % Fe) represents fault breccia (V).

V.1.3.6 Correlation matrix of iron ore

The correlation matrix for all ore samples is presents in Table 10. It is necessary to note that the major element geochemical composition of ore reflects the mineral composition of metamorphosed BIF at Nkout.

A distinct negative correlation exists between Fe_2O_3 and SiO_2 content. High Fe_2O_3 content corresponds to low SiO_2 content and vice versa. It is obvious that Fe_2O_3 and SiO_2 show a very strong negatively correlated relationship (- 0.71). The negative correlation expresses a reciprocal effect of occurrence. This relationship is indicative of either a siliciferous contribution during the deposition of BIF or a desilicification in the upgrade of ore. The negative correlation coefficient for Fe_2O_3 and SiO_2 (- 0.71) is indicative with a negative slope, which decreases from the left to the right side of the graph (Fig. 45G). No distinct correlation pattern could be established between TiO_2

and Fe_2O_3 content but a strong positive correlation value (0.86) is evident (Fig. 45C). A very strong negative correlation relationship exists (-0.92) between Al_2O_3 and SiO_2. The negative slope in the graph indicates the depletion of Al_2O_3 content during silicification. Similar negative correlation occurrence is indicative in the graph of SiO_2 and TiO_2. A positive correlation that exists between Al_2O_3-TiO_2 (0.66) signifies that the augmentation of Al_2O_3 content is directly proportionate with TiO_2 content. Therefore, more TiO_2 content indicates more Al_2O_3 content for all BIF types; this most probably reflects the existence alumino-silicate minerals with Ti. A strong positive correlation value (0.82) between Fe_2O_3 and MgO is evident (Tab. 9). No distinct correlation pattern could be established between Fe_2O_3 - K_2O, and Fe_2O_3 - Na_2O contents. A strong positive correlation value (0.87) exists between Fe_2O_3 and CaO. A strong negative correlation exists between Fe_2O_3 and Cr_2O_3.

Table 10: Pearson's correlation matrix for major element oxides of Nkout iron ore types

	Al_2O_3	CaO	Cr_2O_3	Fe_2O_3	K_2O	MgO	MnO	Na_2O	P_2O_5	SiO_2	TiO_2
Al_2O_3	1										
CaO	0.01	1									
Cr_2O_3	-0.81	-0.5	1								
Fe_2O_3	0.45	0.87	-0.72	1							
K_2O	0.49	-0.8	0.01	-0.54	1						
MgO	-0.05	0.99	-0.38	0.82	-0.8	1					
MnO	0.67	0.22	-0.55	0.64	0	0.12	1				
Na_2O	0.73	0.64	-0.93	0.9	-0.2	0.55	0.75	1			
P_2O_5	0.76	0	-0.59	0.45	0.21	-0.1	0.95	0.68	1		
SiO_2	-0.92	-0.4	0.95	-0.71	-0.2	-0.3	-0.6	-0.9	-0.7	1	
TiO_2	0.66	0.54	-0.75	0.86	-0.3	0.44	0.93	0.93	0.83	-0.8	1

CONCLUSION

The plutonic rock consists of three rock types. These are granite, granodiorite and tonalite. The Nkout plutonic rocks show geochemical characteristics similar to those of Le Maître (1986); Moyen et al. (2003); Frost et al. 2006; Almeida et al. (2010); Mikkola et al. (2014); and Divakara-Rao et al. (1999); Shang et al. (2007); Pannemans et al. (2000); Almeida et al., (2010); Käpyaho (2006); and Sheraton et al. (1985), and Tonalitic composition (Le Maître 1986; Shang et al. 2007 and 2010; Shervais (2008); Sheraton et al. (1985), and Käpyaho (2006), which indicate that the rocks are of igneous origin (Debon and Le Fort 1983).

The granitic rock shows shoshonitic affinity, while the granodiorite rock show calc-alkaline to high-K affinities and the tonalite rock shows low-K one (tholeiite series). The granitic rock is

slightly peraluminous whereas the granodiorite rock show partly peraluminous and metaluminous characteristic and the tonalite rock characterizes the limit between peraluminous and metaluminous.

The SiO_2 contents in the rocks on the Harker binary diagram show increase with decrease in the content of the other elements, indicating a negative correlation that exists between them.

These rocks are poor in large ion lithophile elements (LILE) and high field strength elements (HFSE) compositions.

Their multi-element chondrite-normalized patterns (Thompson 1982) show a general negative Nb, Ti, Yb and Zr anomalies. However, their negative Nb, and Ti anomaly are indication for the tectonic setting suggesting subduction features which may be inherited from their TTG protolith.

These rocks show light REE enrichment relative to HREE depletion similar to igneous origin rock.

They show negative anomalies Eu anomalies indicating rough increase in SiO_2 and positive Eu anomaly (Pannemans et al., 2000, Shervais et al. 2008) suggesting plagioclase accumulation in the rock.

The discrimination diagrams of De La Roche (1965) for the studied metamorphic rock samples show igneous rocks characteristic similar to gabbroic and dioritic composition. The protolith nature of country rock is mafic-igneous rock protolith according to Roser and Korsch (1988) discrimination diagram.

The meta-igneous rock is represented by gneiss which consists of two distinct petrographic types, the garnet-magnetite gneiss and the amphibole-biotite gneissic rocks. The gneissic rocks show igneous rocks characterised similar to gabbroic to dioritic composition after Le Maître (1986), Shervais, et al. (2008), Tokhi et al. (2016), Ibrahim et al. (2015), Pannemans et al. (2000), Buriánek et al. (2012), and Key (1987).

These rocks show low large ion lithophile elements (LILE) composition and low concentration of high field strength elements (HFSE).

The chondrite-normalized spider diagram (Thompson 1982) for trace element compositions shows relative negative Ti, Yb, and Zr anomalies. Ta is below detection limit similar to gabbroic rock. Thompson (1984) interpreted the result indicating that the continental crust and the mantle participated in the genesis of this rock.

The gneissic rock show LREE enrichment relative to HREE depletion, slightly negative Eu anomaly similar to igneous rock (Ibrahim et al., 2015; Buriánek et al., 2012; Shervais, 2008).

The discrimination diagrams of Herron (1988) for the studied metamorphic rock samples show sedimentary characteristic similar to Fe-sand composition. The meta-sedimentary rock is

represented by banded iron formation (BIF) which consists of two distinct petrographic types, magnetite BIF and garnet-biotite BIF.

The BIF rocks show sedimentary rocks characteristic similar to Precambrian Fe-sand composition (Mishra et al., 2012; Elzien, et al., 2014; Abu et al., 2017; Ramachandran et al., 2016), average PAAS value (McLennan 2001) and average Upper Continental Crust (UCC, Taylor et al., 1985).

The magnetite BIF show low Al_2O_3 and low TiO_2 contents, which probably is related to the low clay minerals whereas the garnet-biotite BIF shows high Al_2O_3 contents and a strong negative correlation between Fe_2O_3 and Al_2O_3 suggesting some detrital input similar to Fe-sand.

The magnetite BIF shows low concentration of Large Ion Lithophile Elements (LILE) and high field strength elements (HFSE) relative to garnet-biotite BIF. Zr content shows insignificant to null correlation between Al_2O_3 and TiO_2 suggesting an insignificant input of a clastic material in Magnetite BIF whereas, the weak Zr - Al_2O_3 and Zr - TiO_2 positive correlation, suggest higher detrital input when compared with the magnetite BIF.

The multi-element chondrite-normalized pattern (Thompson 1982) for both BIFs displays negative Ti, Yb and Zr anomalies similar to Fe-sand (Mishra et al., 2012; Abu et al., 2017; Ramachandran et al., 2016).

The Post-Archean Australian Shale (subscript PAAS)-normalised REE pattern for magnetite BIF shows LREE depletion relative to HREE; positive Eu anomaly, negative Ce anomalies and La anomaly and a slight positive Y anomaly indicating hydrothermal and sea water with volcanic input similar to Fe-sand.

The garnet-biotite BIF shows strong PAAS-normalised LREE enrichment, HREE depletion, positive Eu anomaly and positive La anomaly indicating hydrogenous sea water with little fractionation similar to average PAAS value (McLennan 2001) and the Upper Continental Crust values (UCC, Taylor et al., 1985).

The corresponding chondrite-normalized REE pattern for magnetite BIF shows LREE enrichment relative to HREE depletion; both positive and negative Eu anomalies representing little fractionation of REE similar to the average chondrite-normalized REE value of Fe-sands (Mishra et al., 2012; Abu et al., 2017; Ramachandran et al., 2016).

The garnet-biotite BIF shows chondrite-normalized LREE enrichment relative to HREE depletion, positive Eu anomaly indicating little REE fractionation similar to the average chondrite-normalized REE value of Fe-sands (Mishra et al., 2012; Abu et al., 2017; Ramachandran et al., 2016).

The comparative major element oxide geochemical pattern for the studied ore samples show characteristics similar to Precambrian BIF composition, indicating a generic protolith of the iron

ore. The ore rock consists of five types; massive ore (I), hard laminated Ore (II), soft laminated Ore (III), loose lateritic ore (IV) and fault breccias (V) types.

They show similar average major element oxide composition when compared to BIF (Prasad et al. 2012; Adekoya et al. 2012; and Klien 2004) and average PAAS (McLennan, 2001) and average Upper Continental Crust values (Taylor et al., 1985), Algoma-type (Gross et al., 1980), and Lake Superior-types (Gross et al., 1980).

The enriched ores show high Fe grades (60 - 66 % Fe) relative to low abundances of SiO_2 indicating economic potential, whereas the depleted ores show low Fe grades (10 - 20 % Fe) relative to high abundances of SiO_2.

On the binary plot, the geochemical data revealed negative correlation of Fe_2O_3 with SiO_2 and Al_2O_3 thus, indicating that there are less iron silicate phases as well as aluminium contribution in iron oxide minerals.

LOI in all the ore samples most probably reflect the presence of gibbsite and goethite as they contain water in their structure.

V.2 GEOCHRONOLOGY

INTRODUCTION

The composition of lead (Pb) with their corresponding isotopes from rocks has been a widely used tool that provides important constraints on the genesis of deposits.

In order to determine geochronological characteristics of the rock, Pb-isotope compositions in magnetite BIF were investigated and were used for the following purpose: provide chronological information (absolute or relative) during the formation of BIF deposits, determine the source of Pb in BIF, and assess the tectono-metamorphic event.

To constraint the stated purposes, Pb isotope have been used effectively to obtain or yield a reliable age data.

Within this framework, the Pb-isotope database established by Stacey and Kramers (1975) is used to compare with the studied data. The average crustal growth curve of Stacey and Kramers (1975) is based on a two stage-evolution of continental crust, each stage being characterized by different U/Pb and Th/U ratios. The database covers the uranogenic Pb-isotopic ratios $^{206}Pb/^{204}Pb$, $^{207}Pb/^{204}Pb$ and the thorogenic Pb-isotopic $^{208}Pb/^{204}Pb$ ratios. Pb isotopic ratios show a certain characteristic that is age dependent and genesis, the age been restricted to the time that the lead was separated from the source rocks and was remobilised to it new host rock.

V.2.1 Pb-Pb ISOTOPE

Pb isotopic data obtained from magnetite BIF is presented in Table 11. Majority of the Pb concentration of the studied samples were intrinsically less than < 2 ppm average, though few (4

samples) were up to 6 ppm. The uranogenic Pb-isotopic ratio $^{206}Pb/^{204}Pb$ and $^{207}Pb/^{204}Pb$ ranges from 21.82 to 74.77, and from 16.4 to 26.01 respectively, while the thorogenic Pb-isotopic ratio ($^{208}Pb/^{204}Pb$) varies between 37.99 and 68.

V.2.2 Pb-Pb CHRONOLOGY

The two-stage model of Stacey and Kramers (1975) is compared with our Pb data in the Pb-isotopic composition plots. Figure 46 presents the initial uranogenic (Figs. 46 AandB) and thorogenic (Fig. 46C) diagrams with various Pb-isotope ratios in studied samples. The primary growth curve adopted is equivalent to the two-stage Pb evolution curve of Stacey and Kramers (1975) while the isochron line is considered as the secondary isochron (Fig. 46). The studied Pb isotopic data plots above the second-stage average crustal Pb-evolution curve (μ=9.74, Stacey and Kramer 1975, Fig. 46B). The data forms a linear array, and shows a systematic change in Pb-isotopic composition of the analysed magnetite BIF. The Pb-Pb data shows some limit of the isotopic composition and a relatively scattered characteristic at the less radiogenic end of the linear array.

Table 11: Pb-Pb data of Nkout Magnetite-rich BIF

Sample\Pb ratio	**206/204**	**207/204**	**208/204**	**208/206**	**208/207**	**206/207**	**Pb(ppm)**
WH4-F1	24.01	16.55	38.83	1.617	2.346	1.45	2
WH4-F3	21.82	16.4	38.34	1.758	2.338	1.327	2
WH4-F2	32.04	18.29	43.87	1.37	2.399	1.748	2
WH4-F4	22.86	16.83	39.28	1.718	2.334	1.36	2
WH4-F5	24.38	16.97	39.52	1.621	2.329	1.435	2
WH4-F6	32.28	18.11	43.59	1.351	2.408	1.779	6
WH4-F7	21.89	16.07	37.99	1.736	2.364	1.361	2
WH4-S1	28.04	17.22	44.64	1.592	2.592	1.63	5
WH4-S2	27.47	16.91	40.72	1.483	2.408	1.625	5
WH4-S3	42.46	20.27	46.72	1.1	2.303	2.101	3
WH4-S6	43.44	20.05	47.21	1.087	2.354	2.175	2
WH4-S7	74.77	26.01	68.12	0.911	2.619	2.871	2
WH4-S8	51.68	21.51	47.95	0.928	2.23	2.4	2

Faure (1977) proposed that the slope of the linear array of the $^{207}Pb/^{204}Pb$ versus $^{206}Pb/^{204}Pb$ diagram can be used to determine the age of the rock and to calculate the $^{238}U/^{204}Pb$ ratio (μ-value); it is equivalent to the difference between the measured ratio ($^{206}Pb/^{204}Pb$)m and the intercept ratio ($^{206}Pb/^{204}Pb$)ì divided by the slope of the isochron. The regression line fitting for the study yields a slope R = 0.519 ± 0.096 (at 95% confidence Level, 1σ precision input error calculation of 0.1%, is the same in both stages; Fig. 46C).

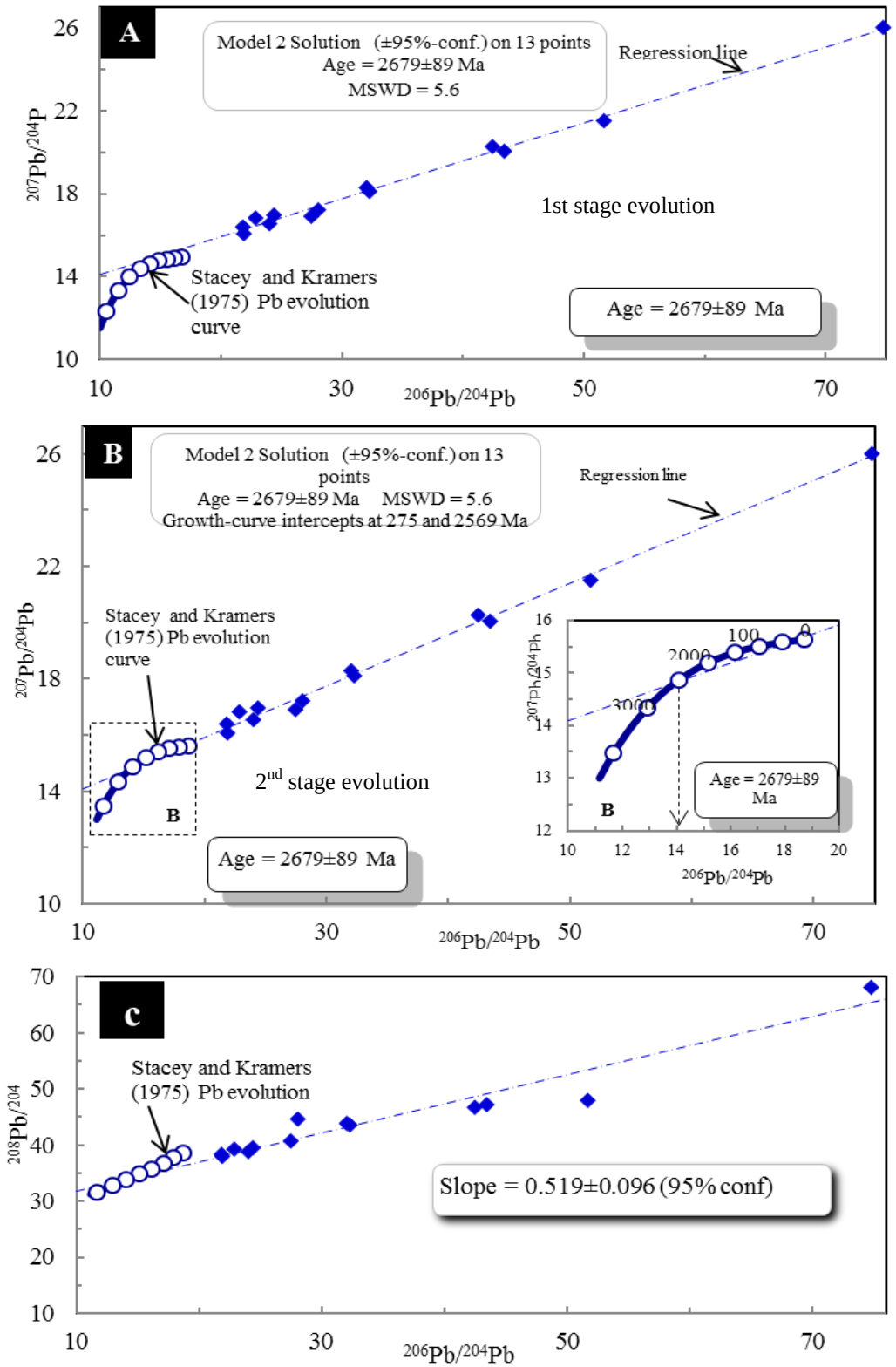

Figure 46: (A) $^{207}Pb/^{204}Pb$ versus $^{206}Pb/^{204}Pb$ for Nkout BIF. Isochron age is assumed at First stage evolution and Pb isotopic composition at 4.5Ga. (B) $^{207}Pb/^{204}Pb$ versus $^{206}Pb/^{204}Pb$ for Nkout BIF. Isochron age is assumed at second stage evolution and Pb isotopic composition at 3.7 Ga. (C) $^{208}Pb/^{204}Pb$ versus $^{206}Pb/^{204}Pb$ for Nkout BIF (calculation were done using isoplot 4.15 software of Ludwig (2011), with input error of 0.1% (1σ) for all isotopic ratios, with Stacey and Kramers (1975) model).

In the first stage (Fig. 46A), the Pb-Pb data plots below the Stacey and Kramers (1975) growth curve. The Pb-Pb data from metamorphosed banded iron formation from Nkout in the 1st stage shows a secondary isochron that defined an apparent age value of 2679 ± 89 Ma (MSWD = 5.6, Fig. 46A) as the regression line touches the curve tangentially.

In the second stage (Fig. 46B), they plot above the growth curve and lies on the less radiogenic end of the trend. The Pb-Pb data from metamorphosed banded iron formation from Nkout in the 2st stage shows a secondary isochron that defined an intercepted ages value of 275 and 2679 ± 89 Ma (MSWD = 5.6, Fig. 46B) as the regression line touches the growth curve at two distinct intercepts.

It is interesting to note that the determine age at the tangent of the regression line with the growth curve in the 1st stage coincide with the determine age at the upper intercept of the 2nd stage growth curve. The obtained μ-value for this study is 15.22.

CONCLUSION

Pb-isotopic data of magnetite BIF can be related to the general geological evolution and thus a useful tool for studying the metamorphic history of Archean events in Ntem complex.

The generally low Pb concentration in magnetite BIF has made the Pb-isotopic analysis difficult.

On the uranogenic Pb-isotopic diagram after Stacey and Kramers (1975), the first stage of the evolution of Pb starts with primordial isotope ratios (4.57 Ga ago) while the second stage starts with geochemical differentiation of the first reservoir (3.70 Ga ago). This growth curve is based upon that established by Ludwig (2011). In the Nkout area, the 1st stage is characterised by a secondary isochron that defined an age value of 2679 Ma as the regression line touches the curve tangentially, whereas the 2st stage shows a secondary isochron that defined an intercepted ages value of 275 and 2679 Ma (MSWD =5.6) as the regression line touches the growth curve at two distinct intercepts.

The results obtained in this study point to the existence of Neoarchean metamorphic event in the Ntem complex.

The whole-rock direct Pb–Pb data yielded an isochron age of ~2679 Ma (Neoarchean age) probably represents a metamorphic age after a prominent early to late tectono-metamorphic event.

CHAPTER VI. INTERPRETATION AND DISCUSSION

INTRODUCTION

In the chapter the principal results of the study area are interpreted and discussed. The discussion integrates the petrology, litho-stratigraphy, structural, geochemistry and geochronology aspects in order to determine the source, environment condition and the genesis of the rock, and to constrain the tectonic evolution based on the results of the previous chapter.

Litho-stratigraphically, we correlate the BIF of the studied area with that of the neighbouring deposits in terms of their geological structure and geochemistry in the Ntem complex. This correlation permits us to propose a model for the deposition and tectonic setting. The model of deposition of iron is assumed to have taken place continuously, and sources are assumed to be a chemical precipitation from ocean water (dominant) and/or detritus (minor).

Structurally, we determine the effect of structural emplacement and morphology of deposit as a potential tool for structural control mineralization.

Geochemically, the affinity, protolith, and provenance of the rocks resulting from the previous chapter were appropriate employed for their tectonic characteristic and setting.

Pb-isotopic data was related to the general geological evolution to establishing the metamorphic history of Archean events in Ntem complex.

VI.1 LITHO-STRATIGRAPHY

VI.1.1 STRATIGRAPHIC CORRELATION AND INTERPRETATION

The stratigraphic correlation between West, Centre and East deposits are in Figure 47. The correlation between rock units in the individual formation is used here to determine the depositional condition in the different parts of the Nkout basin. The litho-stratigraphic correlation was made possible by stratigraphic marker planes such as litho-unit and metamorphic grade. Lateral correlation between the deposits was based on the five metamorphosed BIF units interbedded with gneiss as a lithostratigraphic marker. The low metamorphic grade (greenschist facies) magnetite-rich units occurred at the upper part of the iron member in each of the three deposits. This unit compares well with respect to lithostratigraphy and geochemistry. The four mappable gneiss units (biotite-rich gneiss unit, garnet-magnetic gneiss unit, garnet-rich gneiss unit, and pyroxene-biotite unit) are correlated in the individual formation except for the pyroxene-biotite gneiss unit which correlated only in the East and Centre deposits. Also minor intercalations of pyroxene-biotite gneissic unit occur in the upper part of the East deposit and are not correlated with either West or Centre formations. The biotite-rich gneiss unit correlates in the upper West, Centre and East formations. The garnet-magnetic gneiss unit and garnet-rich gneiss units occurred in the middle of the East formation. The higher amphibolite metamorphic grade occurred in the litho-

stratigraphically equivalent middle of West and Centre formations, but here it also contains every thin intercalated biotite-rich gneiss unit.

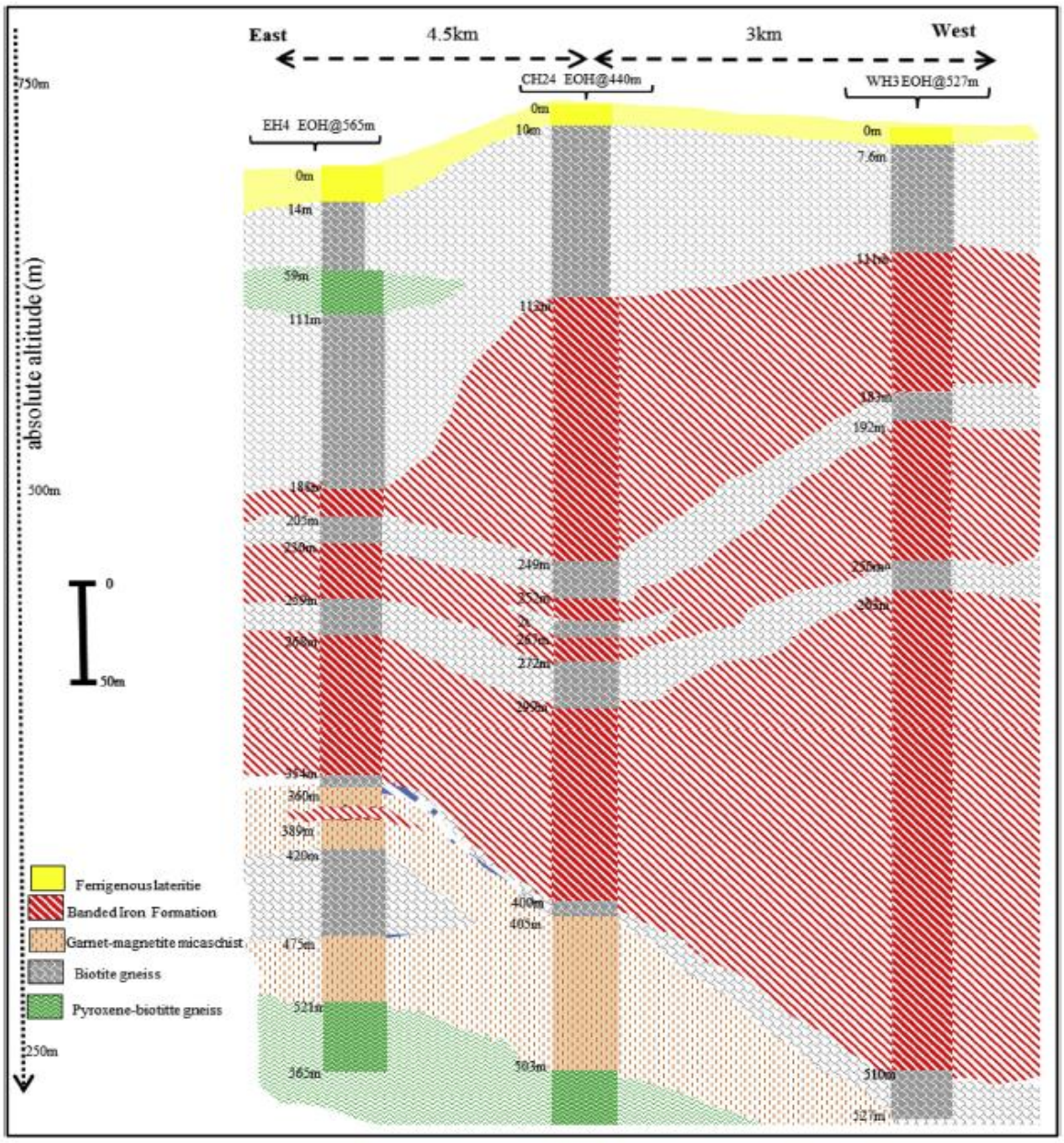

Figure 47: Stratigraphic division and correlation of Nkout formation units (boreholes lies along the same N-S line shown in **Fig. 13,** looking South).

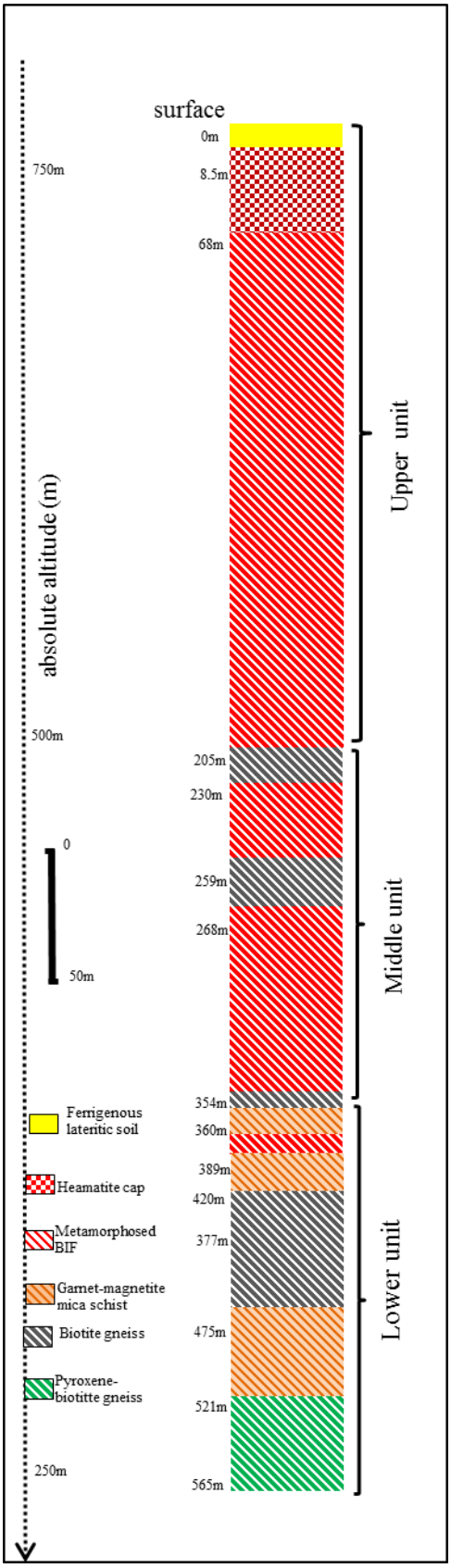

Figure 48: Synthetic stratigraphic relationship for the Nkout formations

The lower pyroxene-biotite unit in the West formation is not taken into account since stratigraphic evidence would suggest that it was not shallow enough and thus did not constitute part of the local depositional sitting.

Litho-stratigraphically, there is no marked difference between the garnet-biotite and garnet-amphibole metamorphosed BIF units. The correlation and comparison of the higher metamorphic grade (garnet-biotite BIF units and garnet-amphibole BIF units) of the lower part of the iron member was more meaningful as the individual iron formation units were not time-transgressive in the primary depositional environment. Our discussion and interpretation of data assumed that these units were deposited at the same time. The difference in metamorphic conditions and post depositional fluid flow were probably responsible for the difference in mineralogy between the two units (Nyame et al., 1998). Correlation across the three formations, however, was less uniform, in conjunction with a marked reduction in stratigraphic thickness from the West to the East succession (Fig. 47). The difference in thickness was probably due to the difference in basin morphology. Nevertheless, no part of the deposit had been strongly eroded as every unit remained intact.

The stratigraphic thickness of metamorphosed BIF in the East was less than that in the Centre and West deposits. Also, the depth variation in the Centre deposit is lower than that of the East and West. The combination of depth and thickness variations in the deposit from east to west indicates a folded synformal structure (Figs. 25 and 26). Also the thickness variation suggested that either the deposition took place for a longer period of time or that the sedimentary rate was rapid (Beukes 2004; Klein 2005).

Post-depositional processes have greatly affected the stratigraphic thickening of the deposit. The Nkout stratigraphic thickness is attributed to the later tight folding phase. The post depositional process of ductile to brittle deformation event at Nkout area has therefore affected the morphology of the stratigraphic sequences, but the primary thickness resulted from the primary sedimentary pile. The metamorphosed BIF is spatially associated with faults that produce offsets within the sequence.

The presence of only oxide facies (Tab. 5) iron unit in the entire deposit reflects the syn-sedimentary deposition or diagenetic redox conditions. The oxide thickness variation suggests the variable availability of the chemical constituents (Fe, O_2 and Si) in the different parts of the basin (Beukes and Cairncross 1991; Nelson et al., 1995). Thus the correlation of iron formations throughout the three deposits suggests that their deposition took place on a wide basin scale. We therefore propose that the individual formations were deposited contemporaneously in the same basin, which implied that the metamorphosed BIF deposition was a basin wide phenomenon.

The synthetic stratigraphy of Nkout basin is divided into three main units, an upper unit, middle unit and lower unit (Fig. 48). The upper unit is about 200m from surface and consists of oxidised and un-oxidised ore type. The oxidised ores consist of lateritic ore, and hematitic ore

(goethite-martite ore, magnetite/haematite ore, and haematite in breccias), while the un-oxidised ore type consists of metamorphosed BIF (magnetite-rich). The middle units are about 150 m thick and consist of quartz/magnetite metamorphosed BIF with minor intercalation of biotite gneiss. The lower unit (354 m to 565 m?) consists of gneissic country rock, which represents the footwall of the deposit. It is made up of biotite gneiss, garnet-magnetite micaschist and pyroxene gneiss with minor intercalation of quartz/magnetite metamorphosed BIF.

VI.1.2. DEPOSITIONAL ENVIRONMENT AND TENTATIVE MODEL

Banded iron formations are thinly banded iron-rich (Tfe >15%) marine metamorphosed sedimentary rocks, mainly composed of iron oxides and chert (James, 1954). Not all BIFs are pure chemical sediment. Some are commonly being contaminated by clastic component (Bau and Dulski, 1996; Basta et al., 2011). Al_2O_3 and TiO_2 contents have been considered to be generally immobile during hydrothermal, diagenetic and weathering processes and strong positive correlation occurrence between these elements is indicative of clastic contamination (Basta et al., 2011; Yang et al., 2015). In the Nkout area, the magnetite-rich BIF samples show high SiO_2 and Fe_2O_3 contents, similar to pure chemical sediment. The low Al_2O_3 and TiO_2 contents of the magnetite-rich BIF, together with positive correlation (r = 0.49; Tab. 6) between these elements are indicative of the low or even the absence of detrital components (Klein 2005, Ganno et al., 2017). However, the garnet-rich BIF has higher average contents of Al_2O_3 (8.73 wt. %), TiO_2 (0.27 wt.%), K_2O (2.37 wt. %) relative to metamorphosed magnetite-rich BIF, indicating clastic input (Lascelles, 2007; 2013; Basta et al., 2011). This is confirmed by the Pearson's inter-element correlations matrix (Tab. 7 and 8) in which strong positive correlations are observed between Al_2O_3 and TiO_2 (r =0.91) and K_2O (r = 0.52). From the above, we propose that Nkout magnetite-rich iron unit is detritus free, whereas garnet-bearing iron units have significant amounts of clastic material, and therefore, a depositional environment closer to the continent (Spier et al., 2007). Furthermore, the absence of carbonate facies BIF in the entire Nkout deposit suggests deep water, distal environment depositional setting, in areas of little or no organic carbon supplies (Klein and Beukes, 1993; Beukes 2004; Klein 2005).

The lithostratigraphic correlation of BIF units supports the fact that BIF's deposit took place on a basin-wide scale. Considering the extent of the Congo basin, it indicates that a huge amount of Fe^{2+} in ocean water was required (James, 1954). The BIF units were most probably deposited in an iron-rich environment of reduced Fe^{2+} rich hydrothermal fluid in a chemical stratified ocean. The Fe^{3+} was diagenetically converted to magnetite by same Fe^{2+} hydrothermal fluid. Similar depositional model was advocated in the Early Proterozoic Minas Supergroup of Quadrilátero Ferrífero, Brazil (Klein et al., 2000).

VI. 1.3. COMPARATIVE LITHO-GEOCHEMISTRY

The average major element compositions of the Nkout BIF (less metamorphosed magnetite-rich BIF) are compared with other BIFs of the Congo Craton (CC) and the Carajas Formation and Quadrilátero Ferrífero, in Brazil (Fig. 49). The average compositions of Superior-type BIF and Algoma-type BIF are also plotted in figure 49 in order to better constrain the Nkout BIF type. From this figure, the Nkout BIF show similar content of iron, silica and aluminium, with other Precambrian BIFs worldwide. Their average value of Na_2O, K_2O, TiO_2 and P_2O_5 have a close pattern with Mbarga BIF (Nforba et al., 2011), Elom BIF (Ganno et al., 2015) and Kouambo BIF (Ganno et al., 2017) in the Congo Craton (CC), Carajas and Quadrilatero Ferrifero BIFs (Spier et al. 2007) in Brazil, and Superior-type BIF; but different from Bikoula BIF (Teutsong et al., 2017) which has a close pattern with Algoma-type BIF (Fig. 49).

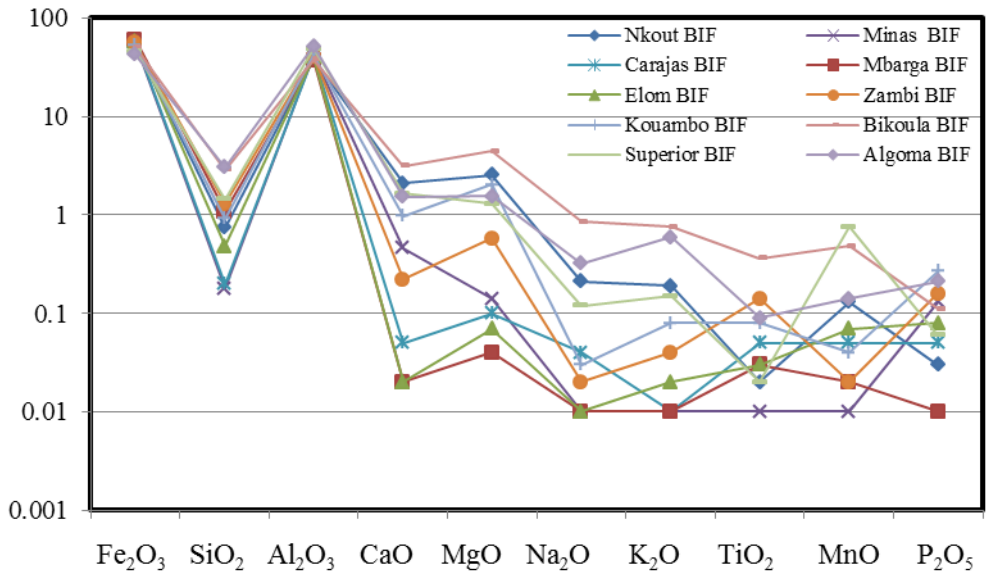

Figure 49. Major element Spider diagram comparing the composition of Nkout BIF with others (Congo craton, Carajas Formation and Quadrilátero Ferrífero (Brazil), Lake Superior-type and Algoma-type BIFs)

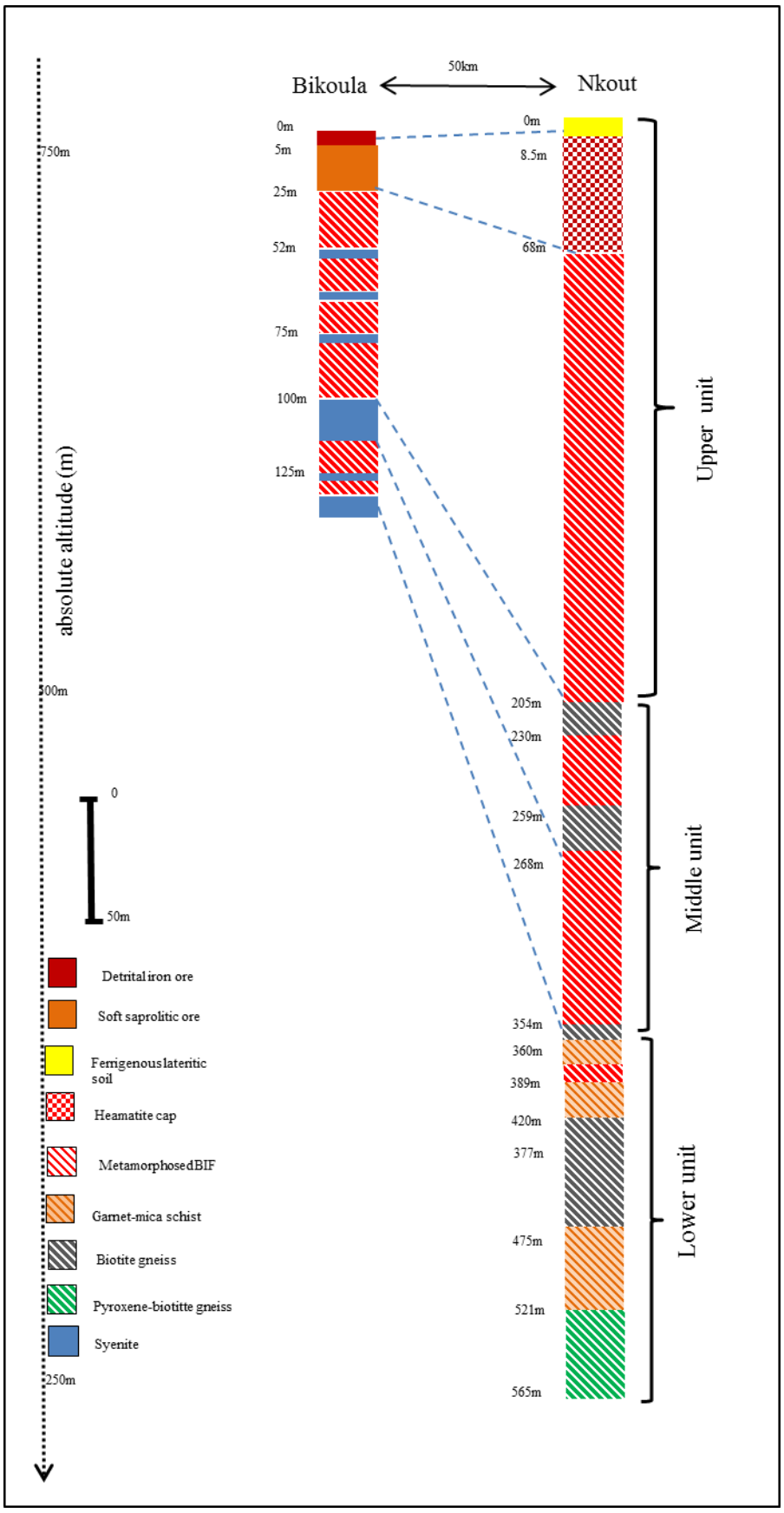

Figure 50. Correlation of the BIF unit of the Nkout and Bikoula on the lithostratigraphy

VI.2 STRUCTURAL ANALYSIS

VI.2.1 STRUCTURAL EMPLACEMENT AND MORPHOLOGY OF DEPOSIT

Structural or stratigraphic thickening during deformation is attributed to the multiple folding phases (D_2, D_3) and late stage faults (D_4) which played the role in defining the geometry of ore zone by segmenting into fault blocks (Angerer et al., 2009).

In the Nkout area, folding and refolding have brought about 3D 'dome, oval' shape and 2D lenses shape, whereas, the late stage faults N-S phase have mainly separated the deposit into three fault blocks namely, Nkout centre, west and east.

The Nkout east and west areas exhibit an isoclinal fold hinge structure that hosts mainly the enriched ore (haematite cap). The isoclinal fold hinges show active records of superimposed events during deformation which occur as rectilinear magnetic morphological outline providing substantial evidence of the strike extent of BIFs. The superimposed deformation events duplicated the E-W D_1 (primary bedding S_1 foliation) structures parallel to the isoclinal fold hinge. These have been the most favourable structure for characteristic supergene and hypogene enrichment processes which are responsible for the origin of the ore. The Nkout west breccia indicates that the deposit is spatially and temporally related to faulting, which lies immediately above a shallow-dipping thrust.

Within the Nkout centre area, the stratigraphic thicknesses are as a result of the later tight folding phase (D_2), with a northwest-plunging fold axis and a steeply-dipping axial plane. The enriched portions show triangular topographic morphological outlines reminiscent of fold interference structures. It is as a result of the refolding of early now sinuous E-W isoclinal folds by later N-S trending fold. This has affected numerous orientations of strike in the different phases of deformation. The interference of F_2 and F_3 folds equally brought about the development of dome-basin structures.

The Ngoa hill which is located approximately 4 km south-west of Nkout hill is attributed to the (D_2) folding phase. It exhibits an ellipsoidal morphology outline as a result of the fold interference structures; from the refolding of the NW-SE isoclinal folds by later NE-SW trending folds (Fig. 26and27). The 'oval' shaped fold hinge suggests that the Ngoa area rests on an unconformity or thrust fault emplacement. The brecciated quartzite beneath the BIF with extended mafic-like infilled vein (Fig. 22: CandF) provides evidence for thrust movement that arose from neighbouring plutonism.

VI.2.2 STRUCTURAL CONTROL

Authors from different background have recognized that geological structure had been the most important controlling factor in the location, shape, and mineralisation of BIF hosting high grade iron orebody (Dalstra and Rosière, 2008; Taylor et al., 2001; Martin and Morris, 2010).

Taylor et al. (2001) have demonstrated that most of the high grade iron mineralised sequence have reduced thickness relative to the less or un-mineralised iron formation. Moreover, Angerer and Hagmann (2009) indicated that the high grade ore zones are localized in areas where BIFs folding and faulting are intense. The high grade ore zones are often located at the fold hinges or at the hinge zones.

The presence of structural deformations in areas of deposit provide mechanisms where erosion and weathering processes were enhancers for the locating and preserving of mineralised ore deposits to be formed from their protore which was later upgraded (Taylor et al., 2001; Martin and Morris, 2010).

The Nkout area of deposit lines up with the steeply north-dipping fault with normal offset. The deposit was strongly tilted during the Pan African orogeny collision with Congo Craton (Nzenti et al., 1988). Here, the haematite-quartz prismatic banding was moderate to steep northerly dip within the upper, middle and lower domain throughout the study area. The consecutive deformation events, during the collision of the pan-African fold belt and Congo Craton (Toteu et al., 2004; Nedelec et al., 1986; Nzenti et al., 1988) together with the post granitic plutonic emplacement were reactivated. The previously developed structures were rotated and amplified into their current orientations.

The ductile to brittle deformation event in the Nkout area was likely controlled by dissolution-precipitation with significant silica redistribution. They laid down the primary bedding fabric (S_1) during diagenesis which has led to significant horizontal silica redistribution perpendicular to the vertical deposition of material. Primary thickness resulted from the primary sedimentary pile.

The Nkout structural control mineralisation on the banded iron formation (BIFs) brought about stratigraphic thickness or duplication, by faulting, folding and refolding, a phase which was mainly attributed to the main structural elements of strike and dip (Fig. 26 and 27).

The main orebody is structurally emplaced by a multiple folds interfering pattern (Fig. 26 and 27). The geometry of the area is dominated by fold interference of overturned F_{2a} folds superimposed by later, N-S trending upright F_{2b} folds. The folding is associated with ductile deformation followed by later brittle faults that laterally or vertically displaced the BIFs sequence.

The deposit is spatially associated with faults that produce offsets in the order of hundreds of meters. However, the steeply dipping normal faults with normal offset reflect the tectonic setting at the time of mineralisation (Fig. 26).

Folding controls

The study confirms the presence of multiple folding phases that affected the geometry of the BIFs. Major and minor folds, during deformation were involved for ore control and mineralisation. The Nkout strata (along strike) indicate that the sequence lies within an initial

synformal closure (Fig. 26). There are open to tight meso and minor antiform-synform pairs of fold closures across the structure which were characterised by the tight to isoclinal similar F_{2a} folds as a result of later refolding. Folding is as a result of progressive shortens during thrusting and magmatic emplacement leading to asymmetric or parasitic folds (Fig. 21 A-C). Open to tight micro- and meso-scale folds with fold hinges are common. Ore in the Nkout area is preserved as folded sheet within F_{2a} isoclinal and F_{2b} anti formal-syn formal closures which were of high consideration for ore control.

The main closure of the Nkout isocline trends approximately E-W in orientation and an axial plane that dips to the north. The overturned fold appears to be the earliest fold in the area. The F_{2a} Fold strikes N50-85°E and steeply dips towards the north indicating that the mineralised geometry was significantly modified. The early overturned F_{2a} folds with E-W axis have been refolded by an east-west compression to an upright N-S F_{2b}. The F_{2b} are upright folds that were associated with ductile and later brittle faults that displace the BIF sequence. The E-W trend F_{2a} fold axis has provided evidence for a generally N-S compressional regime during D_1, while the F_{2b} indicates a generally E-W compressional regime during D_2 (Dalstra, 1999).

Main mineralizations in the deposit scale are parallel to the trend of the folded zones, and most enrichment is confined in the fold hinges. The along-strike variation in BIF thickness is primarily attributed to early deformation isoclinal folding, whereas other thicknesses are attributed to the later open to tight folding phase (D_2). Fold hinges are the major structural features that put high-grade haematite ore of the Nkout area in close contact with BIFs (Fig. 26). The stratigraphic thickness is located at a double fold hinge zones (F_{2a}/F_{2b}), which is considered as the oldest generation of folds recognised on a micro- to macroscopic scale in the study area. The double hinges arose from superposed folding which are linked to well increases in the widths of magnetite and quartzo-feldspathic bands. Poor and thinly mineralisation bands have been on the fold limbs.

The Ngoa area (4 km south of Nkout hill, Fig. 26) is characterised by a cap of flat to moderately inclined BIF, with shallow to moderate dips of 15° to 35° to the southwest. Fold interference pattern indicates a near recumbent F_{2a} structures that have been refolded by later upright F_{2b} folds. The fold contains minor 'S'-symmetry fold which indicates antiformal closures to the northwest.

D_3 is associated with mega-scale close fold with a NE-striking fold axis and associated parasitic folds (F_3) which have caused substantial local thickening and enrichment.

Fault controls

Apart from the early folded structures, there exist localised faulting, shearing and thrusting which are restricted to the margins of the deposit and the country rocks. The development and evolution of shear bands enhance shear deformation which has contributed to the amplification of zones of weakness, resulting in the development of faults (Fig. 26).

On the structural map (Fig. 26), major and minor faults expressed a conjugate system that disrupts both BIFs and country rocks in the N-S and NW-SE direction. The N-S faults in BIF are deformed thrust faults that fit the refolding pattern with its very intense first phase of deformation. They are the most prominent type along the centre area, delineate between deposits, perpendicular to the strike direction to BIF lineament. The faults rapidly developed right lateral displacement towards the south in the following manner: (i) Strike-slip movement, (ii) Dip-slip movement along fault which offset the BIF sequence and (iii) opposite space displacements along faults.

Strike-slip movement are indicated by displacements while others are marked by infilled tectonic breccia, typically 1mm-3m wide and crosscut the BIFs banding at different angles (Fig. 22). Within the BIFs sequence, faulting did give little to no stratigraphic thickening but enhanced proximal wall rock enrichment with hydrothermal precipitation, suggesting a genetic relationship between D_4 phase and iron mineralisation. Two faults with normal throws (Figs. 22) are prominent in the deposit and appear to be deep sited but rapidly die out vertically to the surface. Within the deposit, the faults are locally close to widely spaced subparallel faults, with a normal offset as they occurred between hanging-wall and foot wall contact with BIFs. These faults strike east-west, with steep northerly dips, which produces displacement of up to 450 m.

Slickensides on the fault planes commonly indicate dip slip. Dip-slip movements are well-developed and occur near or along the contact between the ore body and the country rock, indicating considerable movement. These faults are actually steeply dipping and are typically rectilinear while a few are curved (Fig. 22). Displacement movement are accompanied by faults of open system. These faults are gently sloping with angular to sub-angular fault breccias at the base of the BIF, suggesting a thrust fault contact (Fig. 22).

Mineralisation upgrade in the Nkout area is spatially associated with largely concealed subhorizontal fault rather than major thrust fault which are thought to post-date mineralisation. The faults cut through the main F_2 folds in the orebody, suggesting that the mineralization pre-dated both prismatic layering and folding. The (F_{2b}) folds trend N-S with sub-vertical axial planes which are clearly anomalous to the regional fold trends of the Djoum area. The sub vertical orientations of the fold axial planes are as a result of late tilting, possibly associated with the Ntem thrust fault system. The deposit is spatially associated with east-west trending normal fault, which were active during a basin-wide extensional event at the end of the deposition.

Presumably, massive (haematite) ores were not yet formed, until the later thrust reactivation of the normal faults which have been essential to create fluid pathways for ore formation. Fluids that were channelled from the underlying magmatic and gneissic silica-under saturated rock source into the iron formation along the reactivated extensional faults was the most likely mechanism for silica removal and subsequent iron enrichment that formed the massive ores in the deposit.

Actually little or no dipping normal faults were active before or during deposition of the banded haematite and quartz.

Localised shearing

The strain-slip in banded iron formation (BIFs) though little and less intense indicates characteristic localised shearing. This occurs particularly at localities where the along-strike continuation of the banded iron formation is offset (Fig. 19D).

Localised shearing was restricted at the margins of the deposit, mainly external (within granitoids) and is hosted in the banded iron formation. The structural indices characterising localised shearing in BIF suggest a genetic link between the external structures within gneissic country rocks and the protracted multi-stage deformation history along pre-existing structures in BIF.

The NE to ENE and WNW shear domain show dominant control in the deposit (Fig. 26). The former shear domain appears in dominantly control the along-strike segmentation of the Nkout deposit. The later dip-slip shear movement affected the offset between the individual deposit (Central and Western part). Mineral stretching lineation in both BIF and gneissic country rock (garnet and quartz) indicates direction similar to that of the dominantly strike-slip sense movement.

A number of small-scale brittle faults were observed in drill core, which show little or no effect on deposit thickness but enhance influx of enriched fluid for mineralisation control. Shearing plays major important role in the formation iron ore as it facilitates the migration of ore forming fluids (Taylor et al., 2001; Dalstra and Guedes, 2004). Our proposed structural control model shows a genetic link from BIF diagenesis to iron ore formation in the deposit by the different deformation events.

VI.2.4 ORE MINERALISATION CONTROL

BIFs all over the world have been subjected to different degrees of deformation, such as folding, faulting and jointing to produce favourable environment for iron mineralisation.

Different authors have postulated different models for the origin of iron ore mineralisation (Beukes et al., 2003; Morris, 1985; Harmsworth et al., 1990; Subrata and Venkatesh, 2009), but previously accepted ore genesis models for high-grade deposits are now debatable (Taylor et al., 2001; Webb et al., 2003; Hagemann et al., 2008). Structural evolution plays an important control on the location and preservation of high grade ore. Intense folding to less deformed rocks has strong influence on high-grade ore genesis (Dalstra, 2006). Large scale mineralisation occurs during extensive deformation, which is in association with hydrothermal activity (Brown et al., 2004). Extensive structures that control deposition are important for the genesis of high-grade haematite ore (Taylor et al., 2001). The up grading of BIFs to high-grade (magnetite/haematite) ores involves shallow brines plus ascending or descending heated meteoric fluids by affecting primary un-

oxidised BIFs and simultaneously oxidizing magnetite to haematite and replacing quartz with hydrous iron oxides (Taylor et al., 2001; Webb et al., 2003; Dalstra and Guedes, 2004; Thorne et al., 2004; Lobato et al., 2008). In the process of time, deep burial upgrades the hydrous iron oxides to haematite. The late stage fault structures (D_4) have also provided additional pathways for downward percolation of supergene fluids (Angerer and Hagmann, 2009), such as waters and the subterranean solution which offers the necessary acidic environment for leaching of quartz from BIFs. The removal of silica has being the principal control factor of the enrichment of ore from BIF (Subrata et al., 2009; Cope et al., 2008). High-grade iron ore is as the result of sequential removal and replacement of gangue minerals by supergene/ hypogene-hydrothermal process (Alchin et al., 2008; Dalstra and Rosiere, 2008). Figueiredo and Silva (2008) indicate how hydrothermal altered BIFs are structurally related to yield high-grade ore at proximal alteration zone. Beukes et al. (2008) showed how supergene modifications during chemical weathering have hydrothermally upgraded iron ores to haematite/magnetite ore. According to other studies, main mineralization types are of supergene and hydrothermal origin (Alchin et al., 2008; Dalstra and Rosiere 2008; Hagemann et al., 1999; Webb et al., 2003; Dalstra and Guedes, 2004; Lobato et al., 2008). Many authors have demonstrated that different processes and not just a single one have been responsible for the formation of different types of iron ores (Subrata et al., 2009). There are differences of opinions regarding the origin of iron ore in the Congo Craton; more or less accepted that the parent rock is BIFs rich in magnetite/haematite and quartz. The studied deposits are more related to the structural control mineralisation in association mainly with favourable structural thickening during deformation (folding, faulting and subsequent weathering), where high-grade iron ores are mainly controlled by broadly E-W trending fold hinges, which is parallel to the S_1. The E-W orientation of S_1 structures plays an important key role in the interpretation and mineral control.

The Nkout banded iron-formation (BIF) comprises of the two major geological characteristics of supergene and hypogene controlled iron formation. BIF rich in haematite and quartz in the Nkout deposit were formed during early hydrothermal events (Suh et al., 2009). The high-grade iron ores are as the result of sequential removal and replacement of gangue minerals by supergene processes.

Supergene-modified hydrothermal model in the Nkout area involves warm basinal brines plus ascending or descending heated meteoric fluids for the up grading of iron formation to high-grade haematite ores (Taylor et al., 2001; Webb et al., 2003; Thorne et al., 2004). The studied iron mineralization is associated with syngenetic originated concentration of iron, which is located in an isoclinal fold structure, where its ore fabrics recorded superimposed events of deformation (D_1 and D_2) in favour of a hypogene origin of the massive haematite ore (Suh et al., 2009). Primary mineralisation controls have been in association with favourable Fe-rich stratigraphic horizons, metamorphic enhancement of grain size, structural thickening during deformation and folding,

subsequent weathering and enrichment of the oxide mineralisation. The processes of Fe-upgrade from BIF rock to haematite ore involved gangue dissolution which is a structurally controlled feature (Suh et al., 2009). Oxidation during weathering enhances the removal of gauge (quartz and carbonate), with the replacement of iron oxide (goethite, limonite, haematite) mineralization in voids are important for the upgrade of iron ore.

Geochemical data for the studied area indicates the existence of five structural ore types with specific geochemical characteristics: hard laminated ores, soft laminated, loose lateritic ore, massive iron ores, and fault breccia. Massive ore type, soft laminated ore and hard banded ore type show high Fe grades (up to 94.29-88.26wt. % total Fe_2O_3) with relatively low abundances of SiO_2 (0.68-2.93 wt. % total SiO_2), indicating high economic potential. Their macroscopic characteristics are in good correlation with their geochemical composition. Geochemical data revealed negative correlation between Fe_2O_3 with silica and alumina, thus indicating that there were less iron silicate phases as well as alumina contribution from iron oxide minerals.

The main structural ores types are directly or indirectly in association with banded magnetite/haematite and quartz. BIFs fabrics in the studied area is enhanced by the successive deformation events accompanying the leaching of gangues.

Hard banded ores (III) is directly in association with BIFs rich in magnetite/haematite and quartz. The ore fabrics were formed through leaching of silica by desilicification processes and gauge replacement and also precipitation of iron by hydrothermal fluids (Beukes et al., 2008). Small to large-scale faults and folds similar to those in BIFs are also common in the hard-banded ore body. Porosity enhanced the enrichment of ferric hydroxide as a precursor to magnetite and eventually haematite. Silica removals from BIF and successive precipitation of iron have resulted in the formation of haematite ore.

Soft laminated ore (II) was as results of the successive removal of silica or desilicification through the action of hydrothermal fluids in BIFs rich in magnetite/haematite and quartz, where precipitation of iron was partial or absent. The leached interstitial spaces generally were later filled with kaolinite and gibbsite that gave rise to a biscuity ore type which became very fragile in between the laminae.

Loose lateritic ore (IV) is enhanced by porosity or interstitial space of the already altered BIFs. This led to the development of protracted weathering with the enrichment of ferric hydroxide as a precursor of magnetite and eventually haematite.

Massive iron ores (I) is devoid of lamination. This suggests that there exists a syngenetic origin associated with banded magnetite/haematite quartz.

Fault breccia (V) is in association with BIFs rich in banded magnetite/haematite quartz as ferruginous siliceous BIF fragment embedded in a fine-grained groundmass resulting to a residual concentration.

The main orebody is located in the hinge zones of the refolded Nkout anticline. It is characterised by a strongly folded BIF that displays superposed structures related to two distinct fold phases and axial plane schistosity. Major mineralisation in the studied area includes magnetite (fresh Banded iron formation), haematite (weathered BIF), goethite (laterite material), sulphite, carbonate and silicates that occur in vein and fracture.

Magnetite ore is localized in areas where BIF is strongly folded (D_2) and faulted (D_4) at a meso-scale, laterally extensive along primary bedded fold limbs (Nkout centre and west) or "oval" shaped at fold hinges (Ngoa, Fig. 26). Massive magnetite ore enrichment was due to quartz removal or gangue leaching as a result of hydrothermal enrichment within the BIF. This has been considered being syn-D_2, which was enhanced by major fault zone.

Haematite ore is localised at major mineralised fold hinge and fault planes. These structures aid the Fe to be upgraded or enriched from protore BIF to haematite ore by the involvement of gangue dissolution. Haematite matrix in breccias BIF appears to be spatially and partially related to D_4-faulting. These faults have upgraded ore in the form of fault related hydrothermal breccias with irregularly oriented BIF fragments embedded in fine-grained haematite foliated matrix. The enrichment of fault zones and proximal wall-rocks alteration by hydrothermally concentrated haematite has indicated a genetic relationship between the D_4 tectonic and iron mineralisation. Massive haematite is structurally controlled and deposited along major fault zone as a result of hydrothermal enrichment within the BIFs, which are deformed and thickened by the later D_4, providing additional pathways for downwards percolating supergene fluids.

Goethite mineralization was important for the upgrade of iron ore, which took place during weathering at the latest stage of oxidation as a result of leaching, which involved the removal of quartz. It is enhanced especially along the highly permeable contacts between footwall mafic rocks and BIF hanging-wall.

Sulphite mineral in iron ore is more or less significant as trace amounts of galena and chalcopyrite, Pyrite and pyrrhotite are disseminated more within the magnetite band and within the same mineralisation stratum in BIF.

Carbonate mineral in ore is in trace amounts as the indication of calcite in the later occurrence as infills in fracture.

Silicates minerals contribute to high SiO_2, MgO, Al_2O_3 in the ore.

VI. 3 GEOCHEMISTRY

VI. 3.1 PLUTONIC ROCK

VI. 3.1.1 NATURE

The plutonic rocks are made of granite, granodiorite and tonalite. The geochemical characteristic shows that the granitic rock is rich silica content (71.9 % SiO_2), granodiorite rock (69.9 % SiO_2), as well as tonalite rock (71.77 % SiO_2; Tab. 4) indicating the felsic and siliceous composition of the rock.

The granite rock is slightly peraluminous while the granodiorite rock displays both peraluminous (DJO2) and metaluminous (NKR) characteristic. When compared to the Ntem complex high-k granitoids after Shang et al. (2010), the rock show similar geochemical characteristic (Fig. 51A).

The binary diagram of aluminium saturation index (ASI ≤1.1) versus SiO_2 after White and Chappell (1977), points to the I-type character for the granite, granodiorite and the tonalite rock similar to that of the Ntem complex granitoids after Shang et al. (2010),

On the Na_2O/K_2O versus SiO_2 plot, the Tonalite and granodiorite plot in the Na-granitoid field while granite members plot in the K-granite field (Fig. 51B). The granite of the study area plots in the K-granite field similar to that of the Ntem complex granitoids after Shang et al. (2010). The high sodium in tonalite and granodiorite with the high potassium contents in granite indicates slight mantle origination of magmatic contamination.

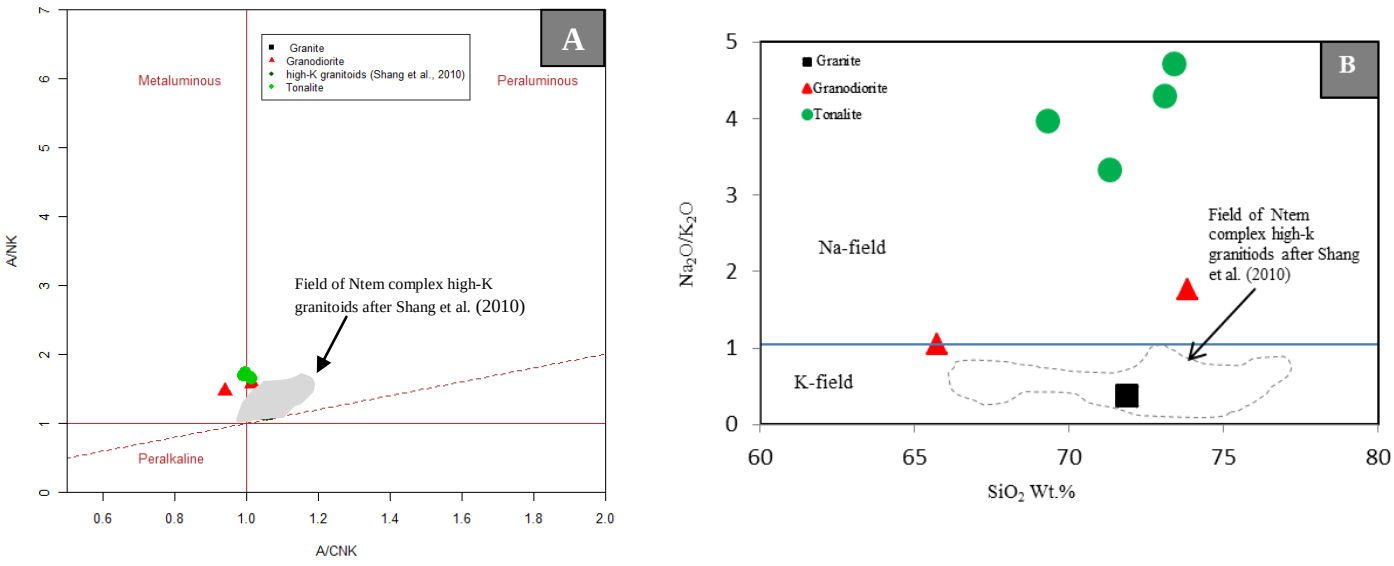

Figure 51. Geochemical characterization of Nkout plutonic rock (granite, granodiorite and tonalite): **(A)** Al_2O_3/ ($CaO+Na_2O+K_2O$) vs Al_2O_3/ (Na_2O+K_2O) diagram of Shand (1947), showing both metaluminous and peraluminous compositions **(B)** Na_2O/K_2O vs SiO_2 plot; showing Na-granitoid field and K-granite field.

The geochemical signatures in the plutonic rocks confirm the petrographic description of the rock which is characterized predominantly of biotite and quartz (silicate) K-feldspars, and plagioclase.

On the SiO_2 versus FeO* / (FeO* + MgO) diagram, the studied tonalite and granodiorite portray both magnesian and ferroan compositions similar to the chemistry of Archaean tonalitic gneisses, granodioritic TTG while the granite sample plot in the ferroan compositions field (Fig. 52A) similar to the field of peraluminous leucogranites. When compared to the Sangmelima charnockitic and tonalitic TTG and high-K granitoids of the Ntem complex after Shang et al. (2010), the studied tonalite granodiorite and granite rock samples show similar characteristic to that of Archaean tonalitic gneisses (Fig. 52A).

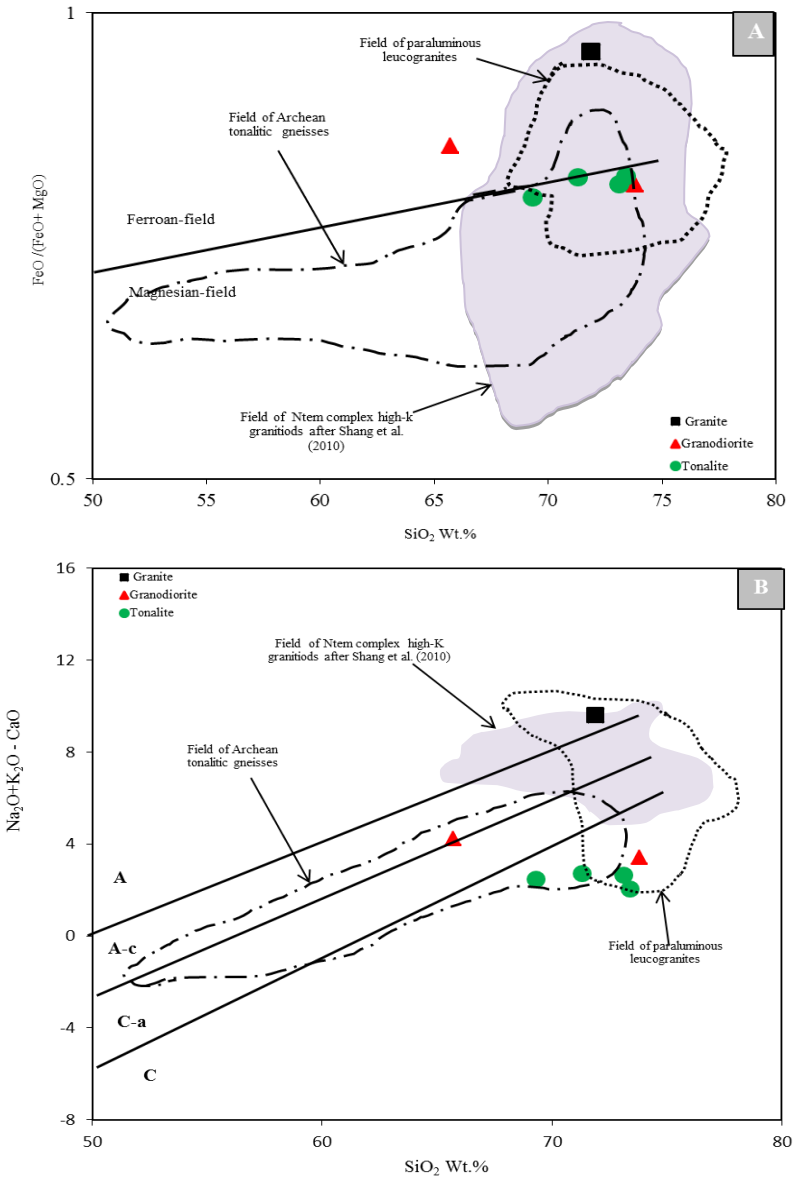

Figure 52. (A) SiO_2 versus FeO* / (FeO* + MgO), diagram showing both magnesian and ferroan compositions for the studied sample. **(B)** SiO_2 versus Na_2O+K_2O-CaO diagram after Frost et al. (2001), showing calcic and calc-alkalic and alkalic fields.

In the SiO_2 versus $Na_2O+K_2O–CaO$ diagram, the studied granodiorite and tonalite samples range from the calcic to the calc-alkalic fields (Fig. 52B), similar to the field of Archean tonalitic gneiss while the granite plots in the alkalic fields (Fig. 52) similar to peraluminous leucogranites (Frost et al., 2001).

The plutonic rocks show positive anomalies in incompatible trace elements notably large ion lithophile elements (Rb, Th, U, Ba, and Sr) and depletion in high field strength elements (Nb, Ta, Zr, V, and Hf), indicating a crustal source contribution in their genesis (Pearce et al., 1984). Nb and Ti are retained in rutile as a geochemical signature in subduction zones which is linked to the melting of subducted eclogite (Shang et al., 2007; 2004). Moreover, the subduction signatures (negative Nb Ti and Ta anomalies) are interpreted as source TTG and charnockite inherited features (Shang et al., 2007; 2010).

Moreover, the negative anomaly in Nb, Ti and Ta in the study area suggest a subduction process which is observed in thickened oceanic crust during or before the generation of the TTGs and granite. Therefore, we suggest that the negative Nb, and Ti anomaly (Figs. 33BandD) with Ta below detection limit in the plutonic rocks are indicative for the tectonic setting suggesting subduction features which are inherited from their TTG protolith. They are attributed to subduction signatures and could be interpreted as source TTG and charnockite inherited features.

When compared to high-K granite of the Ntem complex granitoid after Shang et al (2010), on the chondrite normalised pattern, the high-K granitoid show high contents of LREEs (1000-100 times higher than that of the chondrite values while the studied granitoids are 10 times higher than that of the chondrite values (Fig. 53).

The high contents of LREEs (10 times higher than that of the chondrite values) of the granite rock, on the chondrite normalised pattern could be related to either the enrichment of their source materials or to the presence of mineralization fluids (Fig. 53).

In the granite rock, the REEs characteristics display low REEs abundance, positive Eu anomalies (Eu/Eu*=2.04), enrichment in LREEs and strong depletion in HREEs certainly suggest igneous provenance source which probably could explained the presence of plagioclase or potassic feldspar content, hence could represent cumulative feldspar rich fractions. Their alkalic compositions are similar to peraluminous leucogranites.

The granodiorite rock portray high LREEs fractionation ($8.4 < La_{CN}/Sm_{CN} < 8.5$) low REEs abundances, positive and negative Eu anomaly, and depleted HREEs. The sample NKR show slight negative Eu anomaly (Eu/Eu* = 0.36) while DJO2 sample show positive anomalies (Eu/Eu* = 1.18 average). The sample with the positive Eu anomaly could probably be due to high plagioclase or potassic feldspar content while the sample with the negative Eu anomaly could roughly be correlated to the increase in SiO_2, hence attributed to the magmatic differentiation process.

In the tonalite rock, the REEs pattern shows LREEs enrichment relative to HREEs which indicates the incompatibility of LREEs during fractional crystallization of tonalitic melts. Its low REE abundances, negative Eu anomalies (Eu/Eu*= 0.45), depletion in HREEs (6.07) relative to enrichment in LREEs (153.53), can be attributed to the magmatic differentiation process and be correlated to the increase in SiO_2 as in granite and granodiorite.

Their negative Eu anomaly variation **(Fig. 53)** may also indicate melting under low and high water activity, respectively (Shang et al., 2010). These REE characteristics suggest that the TTG magmas could have been formed within the stability field from a subducted crust.

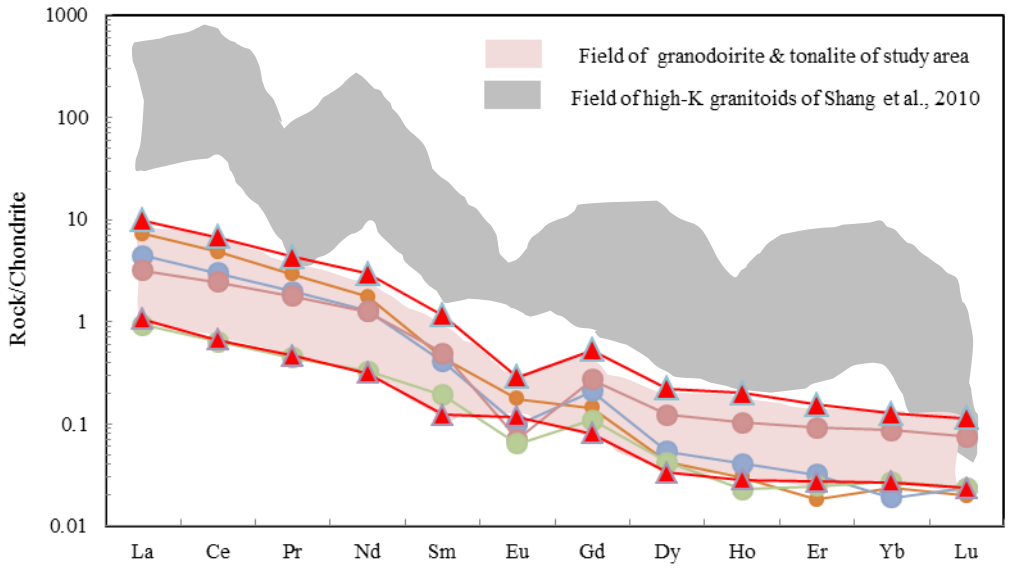

Figure 53. Chondrite normalized REE patterns showing four tonalite samples marked by negative Eu anomalies and two granodiorite samples marked by negative/positive Eu anomalies (note the field of high-K Ntem complex granitoid after Shang et al. (2010).

Moreover, many authors have showed that high-K granites of the Ntem complex were generated from the re-melting of TTGs and charnockites (Shang et al., 2007; 2010). The low total REE abundance (∑REE=0.5), low Zr abundance (0.002ppm, Tab. 4) and strong depletion in HREEs (Gd_{CN}/Yb_{CN} = 1.31) show typical Archaean TTG pattern, and probably inherited feature from the TTG protolith.

The Granodiorite rock show similar combination of low total REEs (5.09 ppm), low Zr abundance (0.045ppm, Tab. 4) and strong depletion in HREEs (3.60) certainly is corresponding to a typical Archean rock pattern as the granitic rock.

Moreover, tonalite rock show equivalently low total REEs abundance (3.67), low Zr abundance (0.004 ppm, Tab. 4) and depletion in HREEs strongly show typical Archaean rock pattern, suggesting inherited feature from the TTG protolith.

However, the granite, granodiorite and tonalite rocks are marked by similar recorded of TTG protolith; we conclude that these rocks are predominantly derived from partial melting of igneous TTG sources. Geochemical characteristics of the high-K granitic group are therefore inherited features from the TTG protolith and cannot be used for determining their tectonic setting.

VI. 3.2 GNEISSIC ROCK

VI. 3.2.1 NATURE OF PROTOLITH

The gneissic parent rock of the study area could be inferred using common geochemical methods. Several attempts have been made to use major and trace elements as provenance indicators.

The studied gneissic rocks are quartz-rich due to their high silicate content (Tab. 5), indicating their felsic composition.

All of the studied samples show relatively moderate K_2O abundance in the SiO_2-K_2O diagram (Peccerillo and Taylor, 1976; Fig. 54A); the amphibole gneiss show a wide range as was plotted in the shoshonite series and calc-alkaline series while the garnet gneiss samples plot on the high-K calc-alkaline series and calc-alkaline series. The bulk of the gneiss samples fall within the calc-alkaline series field. Even though the gneiss shows a relatively wide data dispersion, most of the samples plot in between shoshonite series and the calc-alkaline field.

On the Fe_2O_3*/ (Fe_2O_3* + MgO) versus SiO_2 diagram (Fig. 34B) the garnet-gneiss plot on the ferroan field while the amphibole plot on both ferroan (one sample) and the magnesian field (four samples) after Frost et al. (2001).

In the F1-F2 diagram of Roser and Korsch (1988), the analysed samples plot within the field of mafic igneous source rocks pointing to a major contribution of this type of igneous materials for the genesis (Figs. 35).

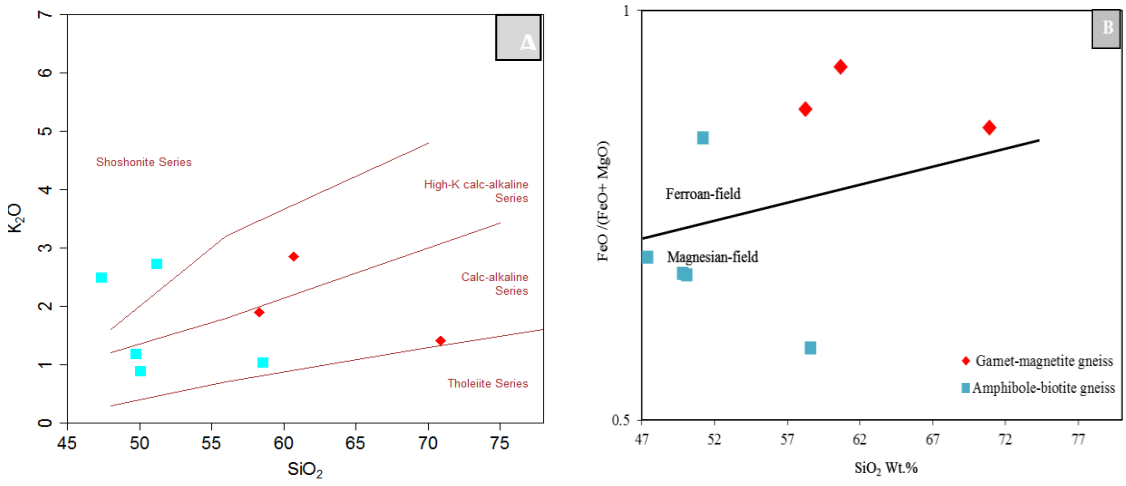

Figure 54: Geochemical characterization of study Gneiss (A) K_2O versus SiO_2 showing low-high K_2O (Peccerillo and Taylor, 1976). (B) FeO / (FeO+ MgO) versus SiO_2 after Frost et al., 2001.

The igneous providences is confirmed by the (Fe_2O_3+TiO_2+CaO)% vs. (Al_2O_3)% and 100 MgO/(K_2O+MgO+Na_2O) vs. 100 Na_2O/(K_2O+MgO+Na_2O) discrimination diagram of De La Roche (1965). The magmatic protolith is of composition close to that of diorite, and gabbro (Figs. 34A and 34B). The gneissic rocks show geochemical signature of ortho-derived rock of the calco-alkaline nature.

On the chondrite-normalized multi-element spider diagram, the rock display negative Nb, and Zr anomalies and positive Ba, Rb, Th, Tb, anomalies. Pearce et al. (1995) illustrates that subduction zone migmatization is characterized by pronounce depletion in Nb-Ta. The studied gneissic rocks show relative Nb and Ta depletion, with values below detection limit (Tab. 5), indicates inherent components of arc magma system source.

The chondrite normalized REEs pattern of the garnet-magnetite gneiss show evidence of LREE enrichment ($(La/Yb)_{CN}$=83.6-671.78; average=367.21) and HREEs-depletion and flat HREEs ($(Gd/Yb)_{CN}$ = 5.2-12.57; average= 8.8)) and relative slight negative Eu anomalies (Eu/Eu*=0.9) while the amphibole-biotite gneiss show similar slightly enrichment in LREEs ($(La/Yb)_{CN}$ = 9.88) relative to HREEs (Gd/Yb) =1.33), a negative Eu anomalies (average Eu/Eu*=0.66) indicate source rock that might be predominantly of felsic rock.

VI. 3.3 BANDED IRON FORMATION (BIF) ROCK

VI. 3.3.1 DETRITAL INPUT

The petrographic study of Nkout samples reveal that BIFs are well banded and display granoblastic texture (Fig. 10). Iron formation was defined for the first time as chemical sediments formed by precipitation of iron and silica component from solutions consisting of a mixture of seawater with hydrothermal fluids (James, 1954). The major composition of iron formation with mainly iron oxides and silica support this definition (Trendall, 2002). However, all BIFs are not pure chemical sediment but are commonly contaminated by clastic component (Bau and Dulski, 1996; Basta et al., 2011 and references therein). The Al_2O_3, NaO_2, K_2O and TiO_2 are mainly hosted in silicates, and usually used as contamination input tracers. Such impurities are terrigenous sediments carried by rivers or winds from weathered pre-existing rock or deposited by volcanic activity (Klein and Beukes, 1992) or pelagic sediments (Lascelles, 2007). Strong positive correlation between Al_2O_3 and TiO_2 have been reported for BIFs worldwide (Ewers and Morris 1981; Basta et al., 2011; Yang et al., 2015), and attributed to the clastic input. Moreover, detrital component in BIF could be gauged through elevated concentrations of HFSE (e.g., Zr, Hf, Ta, and Th) and ∑REE (McLennan et al., 1993; Bau, 1993; Bolhar et al., 2004).

In the Nkout area, the garnet-biotite BIF has higher average contents of Al_2O_3 (8.35wt.%), TiO_2 (0.26 wt.%), K_2O (2.39 wt.%) when compared to magnetite BIF, indicating clastic

contamination (Lascelles, 2007; Basta et al., 2011), whereas, the magnetite BIF showed high SiO_2 and Fe_2O_3 contents, similar to pure chemical sediment. Also, their low Al_2O_3, TiO_2 and ∑REE (average 1.44) contents are indicative of the absence of detrital component (Klein, 2005). From the above, we propose that Nkout West magnetite BIFs are detritus free whereas garnet-biotite BIF has significant amount of clastic material. Similar results were recently reported from Bikoula BIF located some 50 Km Northwest of Nkout deposit (Teutsong et al., 2017).

VI. 3.3.2 MINERAL PARAGENESIS AND EFFECT OF METAMORPHISM

VI. 3.3.2.1 Mineral paragenesis

Field investigations and petrographic study have revealed that Nkout West iron samples are well banded, with alternation of light and dark bands. The light band is mainly composed of recrystallised quartz whereas the dark band is mainly made up of iron and silicate minerals. Both quartz, iron and silicate minerals are coarse-grained and show granoblastic texture with intergranular triple junction, suggesting metamorphic recrystallization.

The mineral assemblages of magnetite BIF (Qtz + Mgt + Bt + Chl), together with the presence of garnet in garnet-biotite BIF indicate amphibolite facies metamorphism. Previous works have revealed that the Ntem Complex experienced multiple deformation events and regional metamorphism with the T-P peak conditions at 750°C, 5 - 6Kb (Tchameni, 1997, Lerouge et al. 2006). Teutsong et al. (2017) have recently reported granulite facies mineral assemblages in the Bikoula BIF whereas Ganno et al. (2016, 2017) showed that the Kouambo and Zambi BIF (Nyong series) have suffered greenschist to amphibolite-facies metamorphism. Thus Nkout West BIFs as other iron formations in the Ntem Complex were metamorphosed to various grades, ranging from amphibolite to granulite-facies conditions.

IV.3.3.2.2 Effect of metamorphism

The banded iron formation, especially those of Archean and Paleoproterozoic age have undergone various grades of metamorphism (Klein, 2005; Rosière et al., 2008). Trendall and Blockley (1970) argued that the metamorphism transformed the primary banded structures in BIF to metamorphic foliation. Also, because the mineralogy is controlled by the wall rock chemical composition, the metamorphism could be responsible for the partial re-distribution of chemical component in the rock. Therefore, chemical composition of metamorphosed BIFs is commonly used in literature to depict the effect of metamorphism.

LILE such as Ba, K, Rb, Th, and U were considered to be mobile during diagenetic and metamorphic processes, thus are good indicators to detect the effect of metamorphism in the BIFs (Lan et al., 2014; and references therein). K/Rb ratio is high in high- grade metamorphic rock (>500 for granulite) and very low in unmetamorphosed rock (230 for igneous rock and 200 for shale; Rudnick et al., 1985; Bauernhofer et al., 2009).

The average K/Rb ratios of the Nkout West BIFs are low, 169.07 and 135.62 for magnetite BIF and garnet-rich BIFs respectively, similar to un-metamorphosed rock (Rudnick et al., 1985). The stable behaviour of LILE in Nkout West BIFs suggests that these metamorphosed BIFs have kept original chemical composition during post-depositional processes. Based on this result, the geochemical composition of the studied BIF samples can be used to constrain the origin and depositional environment of Nkout West deposit.

VI. 3.3.3 ORIGIN OF NKOUT BIF

BIFs are well known to be chemical sediments mainly composed of iron and silica. Some authors have attributed the origin of Fe and Si in BIF to the weathering of continental rocks (Holland, 1984; Manikyamba et al., 1993; Kholodov and Butuzova, 2001) while others are in the opinion that it was derived from the leaching of basaltic rocks from ocean floor (Beukes and Klein 1990; Klein and Beukes, 1992; Bau and Möller, 1993). Huston and Logan (2004); Klein (2005) argued that Fe and Si were precipitated in solutions composed of hydrothermal fluids mingled with seawater, due to the fact that the REEs pattern of BIF have pronounced positive Eu anomalies. Proposed methods for distinguishing between seawater, hydrothermal, biogenic and detrital sources are based on the mineralogical and geochemical composition.

Hydrothermal fluid shows high Fe/Ti, Fe/Al and Si/Al ratios because Al^{3+} and Ti^{4+} are insoluble in sea water and resistant to hydrothermal alteration (Gurvich, 2006). The studied magnetite BIF samples display high average Fe/Ti (3102.42), Fe/Al (173.73) and Si/Al (140.19) ratios, similar to sediments with predominantly hydrothermal component. The average Fe/Ti, Fe/Al and Si/Al ratios of the garnet-biotite BIF are also high (128.78, 4.00 and 5.85 respectively) but are relatively low when compared to those of magnetite BIF. Bonatti (1975), Choi and Hariya (1992) have proposed the use of Si vs. Al binary diagram to discriminate hydrothermal metal rich deposit from hydrogenous deposit. The magnetite BIF samples plot mainly in the hydrothermal field confirming their high Si/Al ratio, whereas the garnet-biotite BIF plots in the hydrogenous field (Fig. 55A). Pure hydrothermal deposits contain little Al and high Al/Ti ratios (Marchig et al., 1982). The relative high content of Al (average = 8.35 wt. %) in garnet-biotite BIF justified their hydrogenous nature.

The predominantly hydrothermal origin of magnetite rich BIF is confirmed by the Fe/Ti vs. Al/(Al + Fe + Mn) diagram (Barrett, 1981) where they plot close to modern metalliferous hydrothermal sediments and far away from modern pelagic-terrigenous sediments (Fig. 55B). This diagram also shows that the garnet-biotite BIF has low hydrothermal component (< 70%).

Toth (1980) has proposed the use of Co/Zn ratio to detect the hydrothermal input of chemical sediment. According to this author, hydrothermal deposit display low Co/Zn ratio (0.15)

whereas hydrogenous deposit display high Co/Zn ratio (2.5). The average Co/Zn ratios of studied samples are 0.14 for magnetite BIF, 0.27 for garnet-biotite BIF.

These ratios are consistent with trace metal of predominantly hydrothermal sources (magnetite BIF), or with minor hydrogenous component (garnet-biotite BIF).

Hein et al. (1990); Usui and Someya (1997) argued that hydrogenous deposit show high ∑REE while the ∑REE of hydrothermal deposit are very low. In addition, the hydrothermal solution have a chondritic Y/Ho ratio (28), positive Eu anomaly, LREEs enrichment relative to HREEs while sea water is characterised by LREEs depletion and HREEs enrichment, positive Y anomaly and super-chondritic Y/Ho ratio (> 44) (Bau and Dulski, 1999).

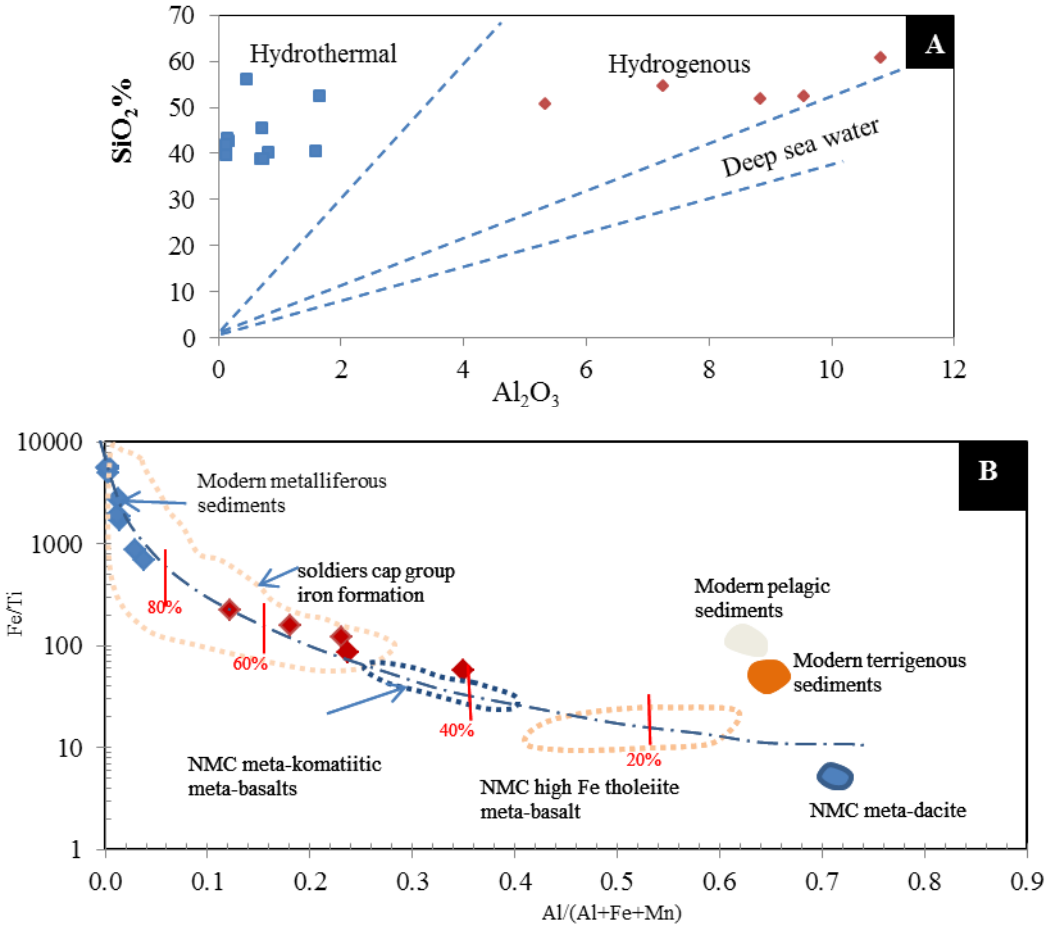

Figure 55: (A) Si vs. Al discrimination diagram of samples from Nkout areas plotted in the field of hydrothermal and hydrogeneous deposit. (B). Fe/Ti vs. Al/(Al + Fe + Mn) discrimination diagram showing the hydrothermal input and volcanic-clastic components in the hydrothermal sediment (after Hatton and Davidson, 2004). The curve represents mixing of East Pacific Rise deposits (EPR) with pelagic sediments (PC) the percentage indicate the approximate amount of EPR in the mixture (adopted from Barrett, 1981). The compositions for mean upper continental crust (UC, Taylor and McLennan, 1985), Red Sea hydrothermal deposits (RS, Marchig et al., 1982) and the Cyprus umber (CU).

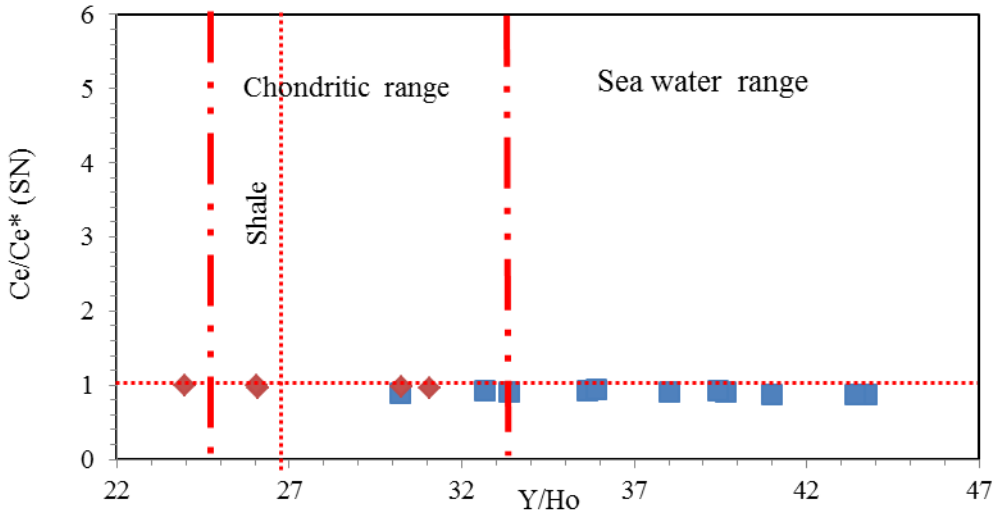

Figure 56: Ce/Ce* vs. Y/Ho diagram (Pecoits, 2009).

The PAAS-normalised REEs patterns of the Nkout West BIF show that the magnetite BIF display both positive Eu and Y anomalies (Eu/Eu* = 1.8; Y/Y* = 1.3) and depletion in LREEs, similar to un-metamorphosed Superior-type BIFs worldwide (Beukes and Klein, 1990; Bau and Dulski, 1996; Klein, 2005; Planavsky et al., 2010). These characteristics also suggest that the metamorphism that affected the Nkout BIFs did not alter the REEs-Y composition.

However, the magnetite BIF also exhibit positive Y anomaly, which is the signature, inherited from sea water. Their average Y/Ho ratio of 36.93 falls between hydrothermal (28) and seawater (>44, Fig. 56), therefore, suggests the mixture of hydrothermal solution and sea water.

The positive Y_{PAAS}-anomaly is typical in rapidly precipitated hydrothermal ferromanganese precipitation in Modern Ocean since the rapid precipitation does not allow for fractionation and the exchange between dissolved and adsorbed REEs - Y causing positive Y_{PAAS}-anomaly to develop (Bau and Dulski, 1996). The slight pronounce Y_{PAAS}-anomaly could be due to slower precipitation or dilution of precipitates REEs-Y pattern by siliciclastic detritus.

The garnet-biotite BIF samples show positive Eu anomaly and negative Y anomaly and chondritic Y/Ho ratio (27.49), also suggests crustal input material.

Both samples (magnetite BIF, garnet-biotite BIF) display no Ce anomalies due to the positive La anomaly (Fig. 43). Bau and Dulski (1996) have proposed that the absence of true Ce anomalies may be related to anoxic conditions that led Fe^{2+} to be oxidised to Fe^{3+} but not sufficient for Ce^{3+} to be oxidised to Ce^{4+}. Planavsky et al., (2010) reported the absence of true negative Ce anomaly in Archean and Paleoproterozoic iron formations and argued that microbially mediated Fe oxidation was the main process during their deposition. Therefore, we propose that the lack of true Ce anomalies in Nkout BIFs reflects the absence of free oxygen in the Ntem basin, leading to anaerobic microbial Fe^{2+} oxidation.

VI.4 GEOCHRONOLOGY

VI.4.1 METAMORPHIC RESETTING AGE

The whole rock Pb - Pb dating was applied on metamorphosed BIF samples. On the uranogenic diagram (Fig. 46A), the regression line does intercept the Stacey and Kramers (1975) growth curve. The secondary isochron Pb data yielded Pb-Pb isochron age of 2679 Ma. The whole rock Pb - Pb analyses present MSWD > 1; indicates a significant scatter plot sample data (Brooks et al., 1968, 1972; York, 1969). Actually, the scatter of the Pb data plots at the low-radiogenic end of the trend indicating that there was mobility and/or heterogeneity.

The heterogeneity of the radiogenic isotope signature within the same rock group may reflect the variable degree of crustal contamination at initial differences in U/Pb source ratio or post-depositional processes such as metamorphism or weathering (Rosholt et al., 1973, Barton et al. 1986). Not much is known on the effect of weathering on U/Pb systems in BIF. But many authors have suggested that U could be lost in oxidising ground water while Pb is retained in haematite and goethite (Rosholt et al., 1973). Armstrong (1986) demonstrated that U loss is strictly geological and does not affect Pb-Pb systematics. Many authors (Barton et al., 1986; Moorbath et al., 1973) have indicated that in low grade metamorphic rocks, whole-rock Pb-Pb isotope systems are stable but could be reset in high grade metamorphic rocks.

Therefore, the Pb-Pb age of 2679 Ma can either correspond to the depositional age or the age of complete isotope resetting metamorphism event which remobilised the Pb isotope of the Nkout West BIFs. Although there exists relative elevated measure Pb-Pb ratios in the studied BIF which could support the age of complete isotopic re-setting during metamorphism, similar elevated Pb-Pb ratios have been obtained in other BIF deposits worldwide (e.g Kraaipan BIF, South Africa (Anhaeusser et al., 1997); Minas deposit, Quadrilatero Ferrifero, Brazil (Babinski et al., 1995) and interpreted as the BIF depositional age. The Nkout West BIF is characterised by the preservation of primary sedimentary features and pure chemical composition. Thus, the 2679 Ma Pb-Pb date present the minimum depositional age of Nkout West formation, inferring a Neoarchean age.

The differences in the Pb composition of rock have been applied to understand the source of magma or hydrothermal interaction and subsequent crystallisation and deposition. Tosdal (1999) argued that the low Pb concentrations (1 - 2 ppm or less) characterise magmatic or hydrothermal system relative to crustal source rocks (10 - 30 ppm). Nkout Pb composition is roughly on average of <2.0 ppm possibly reflecting a hydrothermal Pb source. However, the heterogeneous nature in the isotopic composition may support a slight crust involvement (fluid-rock interaction) of Pb source.

In the Congo craton, metamorphosed BIF-hosted iron deposit are widespread. The first attempt for dating of BIF was made by Chombong and Suh (2013) who used SHRIMP U/Pb on zircon method to date metadacitic rocks intercalated with BIF at Njweng area (Mbalam iron

deposit). With this indirect method, they reported $^{207}Pb/^{206}Pb$ age of 2883 ± 20 Ma interpreted as either the age of crystallization of the dacite or the age of initial BIF deposition in the Ntem Complex, pointing to Mesoarchean age of the Ntem Complex BIF. Tchameni et al. (2000) have reported that Pb-Pb zircon evaporation age of 2666 ± 2 Ma and 2687 ± 3 Ma on high-K granitoid from the Ntem complex and attributed these ages to tectono-thermal events which follow the Archean accretion and differentiation of the North West Congo craton. Our result falls within the range of the ages reported in this high-K granitoids. More recently Chombong et al. (2017) have reported SHRIMP U/Pb on zircon age of 2699 ±7Ma in magnetite gneiss from the Nyong series. This suggest that the Nkout BIF is deposited during the Mesoarchean and later metamorphosed at 2679 Ma during the Neoarchean high-K granitoids emplacement in the Ntem complex.

VII. GENERAL CONCLUSIONS

INTRODUCTION

This chapter presents the general conclusion obtained in the results. The following conclusions were made from the petrographical, litho-stratigraphical, structural, geochemical, geochronological study of the Nkout area.

VII.1 PETROGRAPHY

The petrographical study reveals and confirms both field magmatic and metamorphic units.

The magmatic unit consists of granite, tonalie and granodiporite rocks as the most abundant plutonic rocks. The granite rock of the Nkout area consists of biotite granite and amphibole granite.

The metamorphic unit consists of gneissic country rocks, banded iron formation (BIF), and micaschist.

The gneiss country rock consists of biotite-rich gneiss, garnet-biotite gneiss and pyroxene-biotite gneiss. They were metamorphosed under medium amphibolite grade metamorphism.

Three types of BIF including magnetite BIF, garnet-biotite BIF, and garnet-amphibole BIF were petrographically distinguished on the mineralogical basis. They are strongly deformed and were metamorphosed under greenschist metamorphic facies to amphibolite metamorphic grade, resulting in crystallised magnetite and quartz. The rocks very little of the depositional to early diagenetic minerals were preserved, except in the magnetite-rich iron unit.

VII.2 LITHO-STRATIGRAPHY

Two stratigraphic members (iron-rich member and gneissic member), and several lithological units were distinguished.

Litho-stratigraphic correlation across the Nkout deposit is less uniform, with a marked reduction in stratigraphic thickness from West to East succession, inferring folded synformal and antiformal structure in the deposit. The correlation of BIF units supports the fact that BIF deposition took place on a basin-wide scale.

The synthetic stratigraphy of Nkout basin can be subdivided into three main units: an oxidized upper unit composed of high-grade haematite ore, a middle unit that is made up the fresh metamorphosed BIF and a lower unit made up of gneissic country rocks forming the footwall of the deposit. The footwall and the hanging walls are made up of gneiss intercalated with BIF.

Nkout magnetite-rich iron unit is detritus free whereas garnet-bearing iron units have significant amounts of clastic material, inferring a depositional environment closer to the continent. Furthermore, the absence of carbonate facies metamorphosed BIF in the entire Nkout deposit suggests deep water, distal environment depositional setting; in areas of little or no organic carbon supplies.

The BIF units were probably deposited in an iron rich environment of reduced Fe^{2+} rich hydrothermal fluids in a chemically stratified ocean.

VII.3 STRUCTURAL ANALYSIS

Four deformation phases were distinguished namely D_1, D_2 D_3 and D_4.

The D_1 deformation event is made up of S_1foliation and fold F_1. The S_1 foliation is characterised by layering and preferred orientation of minerals. The foliation strike NE-SW and dip to the NW. The minerals that underline the S_1 schistosity are haematite, magnetite, garnet, amphibole quartz, feldspars, and pyroxene in BIF and gneiss.

The D_2 deformation consists of S_2 schistosity, C_2 shearing and F_2 fold. The S_2 is axial plane schistosity on the F_2 fold. C_2 shearing planes show both dextral and sinistral shear movement. The synformal and antiformal fold strike NE-SW and NW-SE direction

The D_3 event is superimposed tectonism phase as a result of the transposition and reorientation of the D_2. It is essentially made up of S_3 foliation, C_3 shear planes and F_3 folds. The fold structures show N-S to SE-NW striking fold axis, with the development of parasitic folds. The S_3 fold axial plane schistosity is parallel and subparallel to the pre-existing NW-SE S_2 plane

The D_4 deformation phase is characterized by a brittle regime and shear zone, resulting in the fracturing of rocks (BIF and gneiss) marked by open and in-filled fractures, space cleavages, joints, cracks, veins and faults.

Structural evolution plays an important role in localising and preserving of high grade ore from banded iron formation. The most prospective structures often define the complex fault zones and multifold systems.

The BIF thicknesses are primarily attributed to:

The D_2 folds; (i) the early isoclinal E-W folding and (ii) the later tight N-S/NW-SE folding with a northwest-plunging fold axis.

The D_3 large-scale close fold with a NE-SW striking fold axis are associated parasitic folds.

The D_4 large to minor-scale faults marked by open to infill fault affected the orientation of the BIF units but did not cause any substantial thickening, rather enhanced influx of enriched fluids for mineralisation control. Early thrusts or late strike-slip movement have caused effective thicknesses (doubles between 200 m) as a result of major along-strike changes in thickness by sedimentary controls.

Localised shearing within the BIF units are restricted to the margins of the deposit control stratigraphic thickness along-strike and segmentation of the deposit. The strike-slip sense of movement and a dip-slip component at the evolution of shear zones ruptures and brought about the offset between individual deposit (East, Centre and West).

The successive four phases deformation events accompanied the leaching of gangues thereby enriching the deposit marked by supergene and hypogene enriched iron formation

Nkout iron mineralization is associated with syngenetic BIF which is located in an isoclinal fold structure where its ore fabrics record superimposed events of deformation (D_1 and D_2), occurring in favour of a hypogene origin for the massive haematite and magnetite ore.

The main orebody is located in the hinge zone of the refolded structure, characterised by a strongly folded core that displays superposed structures related to two distinct fold phases and axial plane schistosity. The E-W D_1 structure is the most favourable.

The processes of Fe-upgrade from BIF rock to haematite ore involved gangue dissolution which is structurally controlled.

VII.4 GEOCHEMISTRY

VII.4.1 -Plutonic rock

The granitic, granodiorite and tonalite roks are represented in the plutonic rocks of the studied area. The geochemical characteristic of these rocks show rich silica contents indicating the siliceous composition. The rocks are slightly peraluminous and metaluminous and are of I-type rocks.

The REEs characteristics of the granite rock display low REEs abundance, positive Eu anomalies (Eu/Eu*=2.04), suggesting plagioclase accumulation in the rock, enrichment in LREEs and strong depletion in HREEs suggest igneous provenance source.

The granodiorite rock show low REEs abundances, positive to negative Eu anomaly, and depleted HREEs, is attributed to the magmatic differentiation process, indicating melting under low and high water activity, respectively.

The tonalite low REEs abundances, negative Eu anomalies (Eu/Eu*= 0.45), depletion in HREEs relative to enrichment in LREEs, is equally attributed to the magmatic differentiation process and be correlated to the increase in SiO_2 as in granite and granodiorite.

These rocks show light REEs enrichment relative to HREEs depletion similar to igneous origin rock. They show negative anomalies Eu anomalies indicating rough increase in SiO_2.

The Nb, Zr, Ti Sr and Yb content show negative anomaly in all the rock types, interpreted as source TTG and charnockite inherited features

We therefore infer that the plutonic rocks are marked by similar recorded of TTG protolith, predominantly derived from partial melting of igneous TTG sources.

Their igneous TTG sources is similar with other TTG worldwide showing features similar to those of rocks derived from both subduction and crustal thickening environments in island spreading centres.

The negative Nb and Ta anomaly characterized rocks derived from convergent margins and is indicative of subduction as the principal tectonic setting, generated pluton by hydrous basaltic melt of thickened crust.

VII.4.2 -Gneissic rock

The metamorphic rocks consisted of garnet-magnetite gneiss and amphibole-biotite gneiss, both show meta-igneous rock nature characterised with gabbroic to dioritic composition.

Their magmatic protolith is of composition close to that of diorite, showing geochemical signature of ortho-derived rock of the calco-alkaline nature.

They show LREEs enrichment and HREEs-depletion and flat HREEs and relative slight positive/negative Eu anomalies, confirms source rock.

Their relative Nb and Ta depletion, with values below detection limit indicate inherent components of magmatic protolith, while the negative Ti, Yb and Zr anomalies characterised rocks originated from the continental crust and mantle.

VII.4.3 -BIF rock

The nature of meta-sedimentary rock which consisted of magnetite BIF and garnet-biotite BIF shows that they were gotten from Fe-derived sand and and quartz arenitic rock composition.

The Nkout BIF is made up of mainly oxide facies with Fe_2O_3 and SiO_2 being the two main components. The low Al_2O_3, TiO_2, Y, Nb, Zr and Th concentrations in the magnetite BIF suggests detritus-free chemical sediments; whereas their high corresponding concentrations in the garnet-biotite BIF indicates clay-rich contaminated input.

The Post-Archean Australian Shale (subscript PAAS)-normalised REEs pattern of the magnetite BIF typically shows LREEs depleted, HREEs enrichment, positive La and Y ($Y/Y^* = 1.3$) anomalies, and high Y/Ho ratios (36.93), a characteristic similar to that of modern seawater. Their positive Eu anomaly indicates the involvement of hydrothermal fluid. The garnet-biotite BIF shows positive Eu, and negative Y anomalies and chondritic Y/Ho ratio (27.49). The slight positive Y anomaly in the BIF therefore suggests a volcanic input.

The lack of true Ce anomaly in Nkout BIF reflects the absence of free oxygen in the Ntem basin, leading to anaerobic microbial Fe^{2+} oxidation.

The negative Ti, Yb, and Zr anomalies was interpreted as rock coming or originated from the continental crust.

Nkout BIF shows similar major element geochemical compositions as other Superior-type BIFs in the Congo craton and in Quadrilátero Ferrífero in Brazil.

VII.5 GEOCHRONOLOGY

The whole rock direct Pb-Pb data yielded an isochron age of 2679 Ma interpreted as the Neoarchean metamorphic resetting age.

REFERENCES

Abu M., and Zango M. S., 2017. Geochemical characteristics of the Neoproterozoic Anyaboni sandstone of the southeastern Voltaian Basin, Ghana. Scientific Research Journal, Volume V, Issue XI, 54, 2201-2796

Adekoya, J. A., Okonkwo C, T., Adepoju, M. O., 2012. Geochemistry of Muro Banded Iron-Formation, Central Nigeria International Journal of Geosciences, 3: 1074-1083

Alchin D., Lickford V., Mienie P. J., Nel D., Strydom M., 2008. An integrated exploration approach to the Sishen South Iron Ore Deposit, Northern Cape Province, South Africa, and its implication for developing a structural and/or resource model for these deposits; Economic Geology. 15, 317 – 338.

Almeida J .D. A. C., Dall'Agnol R., Dias S. B., Althoff F. J., 2010. Origin of the Archean leucogranodiorite–granite suites: Evidence from the Rio Maria terrane and implications for granite magmatism in the Archean, Lithos 120, 235–257.

Allmendinger, R. W., Cardozo, N. C., Fisher, D., 2013. Structural Geology Algorithms: Vectors and Tensors: Cambridge, England, Cambridge University Press, 289 pp.

Angerer T., Hagemann S., 2009. The Archean BIF Hosted Iron Ore at Koolyanobbing, Western Australia: a Structural Approach, "Smart Science for Exploration and Mining" 555-557.

Anhaeusser C. R., Walraven F., 1997. Polyphase crustal evolution of the Archean Kraaipan granite-greenstone terrane, Kraapvaal Craton, south Africa. Economic Geology Research Unit.

Armstrong R.A., 1986. Geochronological studies on Archaean and Proterozoic formations of the foreland of the Namaqua Front and possible correlates on the Kaapvaal Craton. Ph.D. Thesis, Univ. of the Witwatersrand, Johannesburg.

Babinski M., Van Schmus W. R. V., Chemale Jr. F., 1999. Pb–Pb dating and Pb isotope geochemistry of Neoproterozoic carbonate rocks from the Sao Francisco basin, Brazil: implications for the mobility of Pb isotopes during tectonism and metamorphism. Chemical Geology, 160: 175 - 199.

Babinski M., Chemale Jr. F., William R.V.S., 1995. The Pb/Pb age of the Minas Supergroup carbonate rocks, Quadrilátero Ferrífero, Brazil, Precambrian Research 72 : 235 - 245.

Bagnouls F., and Gaussen, 1957. Les climats biologiques et leur classification. Annales de Géographie, 66° année, N." 335: 193 - 220.

Barrett T. J., 1981. Chemistry and mineralogy of Jurassic bedded chert overlying ophiolites in the North Appenines, Italy. Chemical Geology 34: 289 - 317.

Barbey, P., Macaudière, J., and Nzenti, J.P., 1990, High-pressure dehydration melting of metapelites: Evidence from migmatites of Yaoundé (Cameroon): Journal of Petrology, v. 31, p. 401–428.

Barley M.E., Pickard A.L., Hagemann S.G., Folkert S.L., 1999. Hydrothermal origin for the 2 billion year old Mount Tom Price giant iron ore deposit, Hamersley Province, Western Australia. Mineralium Deposita 34: 784 - 789.

Barton E. S., Armstrong R.A., Cornell D.H., Welke H.J., 1986. Feasibility of total-rock Pb-Pb dating of metamorphosed banded iron formation; The Marydale Group, Southern Africa. Chemical Geology 59: 255 - 271.

Basta F. F., Maurice A. E., Fontbote L., Favarger P., 2011. Petrology and geochemistry of the banded iron formation (BIF) of Wadi Karim and Um Anab, Eastern Desert, Egypt: implications for the origin of Neoproterozoic BIF. Precambrian Research. 187: 277-292.

Bau M., Möller P., 1993. Rare earth element systematics of the chemically precipitated component in Early Precambrian iron-formations and the evolution of the terrestrial atmosphere-hydrosphere-lithosphere system. Geochim. Cosmochimemistry Acta, 57: 2239-2249.

Bau M., 1993. Effects of syn- and post-depositional processes on the rare-earth element distribution in Precambrian iron-formations. Europium Jounal of Mineral, 5: 257-267.

Bau M., and Dulski P., 1996. Distribution of yttrium and rare-earth elements in the Penge and Kuruman Iron Formation, Transval Supergroup, South Africa; Precambrian Research 79: 37 - 55.

Bauernhofer A. H., Hauzenberger C.A., Wallbrecher E., Muhongo S., Hoinkes G., Mogessie A., Opiyo-Akech N., Tenczer V., 2009. Geochemistry of basement rocks from SE Kenya and NE Tanzania: Indications for rifting and early Pan-African Subduction. International. Journal of Earth Science. 98: 1809 - 1834.

Bau M., Dulski P., 1999. Comparing yttrium and rare earths in hydrothermal fluids from the Mid-Atlantic Ridge: implications for Y and REE behaviour during near-vent mixing and for the Y/Ho ratio of Proterozoic seawater. Chemical Geology, 155: 77 - 90.

Bekker A., Slack J.F., Planavsky N., Krapez B., Hofmann A., Konhauser K. O., Rouxel O.J., 2010. Iron formation: the sedimentary product of a complex interplay among mantle, tectonic, oceanic and biospheric processes, Economic Geology, 105: 467-508.

Beukes N. J., 2004. Early option in photosynthesis, Nature, 431, 522-532

Beukes N.J., Klein C., 1990. Geochemistry and sedimentology of a facies transition from microbanded to granular iron-formation in the early Proterozoic Transvaal Supergroup, South Africa. Precambrian Research, 47: 99 - 139.

Beukes N. J., Carincross, B., 1991. A lithostratigraphic sedimentological reference profile for the late archean mozaan group, Pongola sequence: Application to the sequence stratigraphy and correlation with the Witwatersrand supper-group. South Africa Journal of geology, 94: 44 - 69.

Beukes N.J., Gutzmer J., Mukhopadhyay J., 2003. The geology and genesis of high-grade haematite iron ore deposits; Applied Earth Science, 112: 18 – 25.

Beukes N.J., Mukhopadhyay J., Gutzmer J., 2008. Genesis of high-grade iron ores of the Archean Iron Ore Group around Noamundi, India; Economic Geology, 103: 365 – 386.

Bolhar R., Kamber B. S., Moorbath S., Fedo C. M., Whitehouse M. J., 2004. Characterization of Early Archean chemical sediments by trace element signatures. Earth and Planetry Science, 222: 43 - 60.

Bonatti E., 1975. Metallogenesis at oceanic spreading centers, Earth and Planetry Science, 3: 401 - 433.

Boynton, W.V., 1984. Geochemistry of the rare earth elements: meteorite studies. In: Henderson, P. (Ed.), Rare Earth Element Geochemistry. Elsevier, pp. 63–114.

Brown, M.C., Oliver, N.H.S., Dickens, G.R., 2004. Veins and hydrothermal fluid flow in the Mt. Whaleback Iron Ore District, eastern Hamersley Province, Western Australia Precambrian Research, 128: 441 - 474.

Brooks, C., Wendt, I., Harre, W., 1968. A two-error regression and its application to Rb–Sr and initial Sr87/Sr86 ratios of younger Variscan granitic rocks from the Schwarzwald Massif, Southwest Germany, Journal of Geophysical Research, 73: 6071 - 6084.

Brooks C., Hart S.R., Wendt I., 1972. Realistic use of two error regression treatments as applied to rubidium- strontium data. Geophysical Space Physic 10: 551-77.

Buriánek D., Hanžl P., Budil P., Gerdes A., 2012. Evolution of the Early Permian volcanic-plutonic complex in the western part of the Permian Gobi-Altay Rift (Khar Argalant Mts., SW Mongolia) Journal of Geosciences, 57: 105 - 126.

Caen Vachette M., Vialette Y., Bassot J.P., Vidal P., .1988. Apport de la géochronologie à la connaissance de la géologie gabonaise. Chronique Recherche Miniére, 491: 35-54

Choi J H, Hariya Y, 1992. Geochemistry and depositional environment of Mn oxide deposits in the Tokoro Belt, northeastern Hokkaido Japan. Economic Geology, 87: 1265-1274.

Chombong N. N., Suh C.E., 2013. 2883 Ma commencement of BIF deposition at the northern edge of Congo craton, southern Cameroon: new zircon SHRIMP data constraint from metavolcanics. Episodes, 36: 47-57.

Chombong N. N., Suh C. E., Lehmann B., Vishiti A., Ilouga D. C., Shemang E. M., Tantoh B. S., Kedia A. C., 2017. Host rock geochemistry, texture and chemical composition of magnetite in iron ore in the Neoarchaean Nyong unit in southern Cameroon. Applied Earth Science. 1: 1-17, https://doi.org/10.1080/03717453.2017.1345507.

Cope I.L., Wilkinson J. J., Boyce A. J., Chapman J. B., Herrington R. J., Rarris C. J., 2008. Genesis of the Pic de Fon Iron Oxide Deposit, Simandou range, Republic of Guinea, West Africa; Economic Geology. 15**:** 339-360.

Dalstra H. J., Ridley J. R., Bloem E. J. M., Groves D. I., 1999. Metamorphic evolution of the central Southern Cross province, Yilgarn craton, Western Australia: Australian Journal of Earth Sciences, 46: 765 - 784.

Dalstra H. J., Guedes S., 2004. Giant hydrothermal haematite deposits with Mg-Fe metasomatism: A comparison of the Caraj´as, Hamersley, and other iron ores; Economic Geology. 99: 1793 - 1800.

Dalstra H. J., Rosière, C., 2008. Structural controls on high-grade iron ores hosted by banded iron formation: a global perspective. In: Hagemann, S., Rosiere, C., Gutzmer, J., Beukes, N.J. (Eds.), Banded Iron Formation-related High Grade Iron Ore. Reviews in Economic Geology. 15: 73 - 106.

Dalstra H. J., 2006. Structural controls of bedded iron ore in the Hamersley Province, Western Australia –an example from the Paraburdoo Ranges Applied Earth Science, 115(4): 139-145.

Debon, F. et Le Fort, P., 1983. A chemical mineralogical classification of common plutonic rocks and associations, Transactions of the Royal Society of Edinburgh, 73: 135 - 149.

De La Roche. H. 1965. Sur l'existence de plusieurs faciès géochimiques dans les schists paléozoïques des Pyrénées luchonnaises. Geologische Rundscha, 55, 274 - 301.

De Waele B., Lacorde M., Rivers J., 2015. Banded iron formations and associated detrital iron deposits of the Western Congo Craton. SEG Conference, September 2015.

Divakara R. V., Subba R. M. V., Murthy N. N., 1999. Granite forming events and their role in crust formation of the indian shield, Revista Brasileira de Geociências , 29 (1): 33 - 40.

Elzien, S. M., Farah, A. A., Alhaj, A. B., Mohamed, A. A., Al-Imam, O. A. O., Hussein, A. H., Khalid, M.K., Hamed, B.O., Alhaj, A.B., 2014. Geochemistry of Merkhiyat Sandstones, Omdurman Formation, Sudan: Implication of depositional environment, provenance and tectonic setting. International Journal of Geology, Agriculture and Environmental Sciences, 2: 3.

Evensen, N. M., Hamilton, P. J., O'Nions, R. K. 1978. Rare earth abundances in chondritic meteorites. Geochimica Cosmochimica and Acta 4: 1199 - 1212

Ewers W. E., Morris R. C., 1981. Studies of the Dales George member of the Brockman Iron Formation, Western Australia. Economic Geology, 76: 1929 - 1953.

Faure G., 1977. Principles of Isotope Geology, Wiley, New York, 464 p.

Feybesse J. L., Johan V., Triboulet C., Guerrot C., Mayaga-Mikolo F., Bouchot V., Eko N'dong J., 1998. The West Central African belt: a model of 2.5 – 2.0 Ga accretion and two-phase orogenic evolution. Precambrian Research, 87: 161 – 216.

Feybesse J.L., Johan V., Maurizot P., Abessolo A., 1986. "Mise en evidence d'une nappe syn métamorphe d'âge Eburnéen dans la partie Nord-Ouest du craton zaïrois, Sud-Ouest

Cameroun". In: Les formations birrimiennes en Afrique de l'Ouest, journée scientifique, compte rendu de conférences.Occasional Publications-CIFEG, pp. 105 – 111,

Figueiredo E., Silva R.C., Lobato L.M., Rosiere C.A., Hagemann S., Zucchetti M., Baars F. J., Morais R., and Andrade I., 2008. A hydrothermal origin for the jaspiitehosted, giant Serra Norte iron ore deposits in the Carajas mineral province, Para State, Brazil; Economic. Geology, 15: 255 - 290.

Fondo S., 2005. Macroeconomic Analysis of Bush meat Production and Trade in the Ngoyla-Mintom Forest Area, Southeast Cameroon, Southeast Forests Programme, Rapport final du Consultant à WWF, 120 p.

Frost, B, R., Barnes, C,G., Collins, W, J., Arculus, R. J., Ellis, D, J., and Frost C, D., 2001. A geochemistcal classification of granite rocks. Jounal of petrology. 42: 2033-2048

Forst C. D., Forst R. B., Kirkwood R., and Chamberline K.R., 2006. The tonalite – trondhjemite – granodiorite (TTG) to granodiorite- granite (GG) transition in the late Archean plutonic rock of the central wyoming province, Jounal Earth Science, 43: 1419 - 1444

Ganno S., Njiosseu T.E.L., Ngnotué T., Kouankap N.G.D., Nzenti J.P., 2017. A mixed seawater and hydrothermal origin of superior-type banded iron formation (BIF)-hosted Kouambo iron deposit, Palaeoproterozoic Nyong Series, Southwestern Cameroon: constraints from petrography and geochemistry. Ore Geology Reviews, 80: 860-875.

Ganno S., Ngnotue T., Nono G.K.D., Nzenti J.P, Notsa F.M., 2015. Petrology and geochemistry of the banded iron-formations from Ntem complex greenstones belt, Elom area, Southern Cameroon: Implications for the origin and depositional environment. Chemie der Erde 75: 375-387.

Ganno S., Moudioh C., Nzina N.A., Nono G.K.D., Nzenti J.P., 2016. Geochemical fingerprint and iron ore potential of the siliceous itabirite from Palaeoproterozoic Nyong Series, Zambi area, Southwestern Cameroon. Resource Geology, 66 (1): 71 - 80.

Ganno S., Tsozué D., Nono G. D. K., Tchouatcha M. S., Ngnotué T., Takam R. G., Nzenti J. P., 2018. Geochemical Constraints on the Origin of Banded Iron Formation-Hosted Iron Ore from the Archaean Ntem Complex (Congo Craton) in the Meyomessi Area, Southern Cameroon. Resource Geology, : 1 - 16. doi: 10.1111/rge.12172

Goodwin A.M., 1991. Precambrian Geology; The dynamic evolution of the continental crust, Academic Press, Harcourt Brace Jovanovich Publishers, New York, pp 1-666.

Gross G. A., McLeod C.R., 1980. A preliminary assessment of the chemical composition of iron-formation in Canada, Canadain Mineral, 18: 223-229.

Gross G. A., 1983. Iron-formation in fold belts marginal to the Ungava craton. In: Trendall, A.F., Morris, R.C., (Eds.), Iron Formation: Facts and Problems. Elsevier, Amsterdam, pp. 253 – 294.

Gross, G. A., 1996. Algoma-type Iron-formation. In: Lefebure, 801 D. V. and Hoy, T. (eds.), Selected British Columbia Mineral Deposit Profiles, Volume 2-Metallic Deposits. British Columbia Ministry of Employment and Investment, Open File, 13: 25 - 28.

Gurvich E. G., 2006. Metalliferous Sediments of the World Ocean: Fundamental Theory of Deep-Sea Hydrothermal Sedimentation. Springer Berlin, 416 p.

Hagemann S., Rosiere C., Gutzmer J., Beukes N. J., 2008. Introduction banded iron formation-related high grade iron ore, In: Hagemann, S., Rosiere, C., Gutzmer, J., Beukes, N.J. (Eds.), Banded Iron Formation-related High Grade Iron Ore. Reviews in Economic Geology, 15:1-4.

Hagemann S. G., Barley M.E., Folkert S.L., Yardley B.W., Banks D.A., 1999. A hydrothermal origin for the giant Tom Price iron ore deposit; In: Mineral Deposits, Processes to Processing (eds) Stanley C J et al (Rotterdam: A A Balkema) pp. 41- 44.

Haïmeur, J., Amrani el hassani I. E., E., Chabane A., 2004. Pétrologie et géochimie des granitoïdes calco-alcalins de Zaër (Maroc central): modèle pétrogénétique, Bulletin de l'Institut Scientifique, Rabat, section Sciences de la Terre, 26: 27 - 48.

Harmsworth R. A., Kneeshaw M., Morris R. C., Robinson C. J., Shrivastava P. K., 1990. BIF-derived iron ores of the Hamersley Province; In: Geology of the Mineral Deposits of Australia and Papua New Guinea (ed.) Hughes F E, Aus IMM. Mono, Melbourne 14 **:** 617 - 642.

Hatton O., Davidson G., 2004. Soldiers Cap Group iron-formations, Mt. Isa Inlier, Australia, as windows into the hydrothermal evolution of a base-metal-bearing Proterozoic rrift basin. Australian Jounal Earth Science, 51: 85 - 106.

Hein J. R., Schulz M. S., Kang J. K., 1990. Insular and submarine ferro-manganese mineralization of the Tongap-Lau region, Mar. Minerals. 9: 305 - 354.

Herron M. M., 1988. Geochemical Classification of Terrigenous Sands and Shales from Core and Log Data. Jounal of Sedimentary Petrology, 58: 820 - 829.

Holland H. D., 1984. The Chemical Evolution of the Atmosphere and Oceans, Princeton University Press, Princeton, pp. 582 - 589.

Huston D. L., Logan G.A., 2004. Barite, BIFs and bugs: evidence for the evolution of the Earth's early hydrosphere. Earth Planet Sciences and Letter, 220: 41 - 55.

Ibrahim A, E., Mahmoud H. B., Abdellah S. T., Ashraf F. M., Taher M. S., 2015. Geological, structural and petrotectonical aspectable features of neoproterozoic rocks, gabal el dob area,

north eastern desert, egypt international journal of scientific engineering and applied science (ijseas), 1: 2395 - 3470.

Ilouga C. D. I., Suh C. E., Ghogomu R. T., 2013. Textures and rare earth elements composition of banded iron formations (BIF) at Njweng prospect, Mbalam Iron Ore District, Southern Cameroon, International Journal GeoScience, 4: 146 – 165.

James H. L., 1954. Sedimentary facies of iron-formations, Economic Geology, 49: 235 – 293.

James H. L., 1992. Precambrian iron-formations: nature, origin, and mineralogic evolution from sedimentation to metamorphism. In: Wolf K H, Chilingarian G V. (Eds.), Diagensis III. Developments in Sedimentology 47: 543-589.

Kankeu, B., Greiling R. O., Nzenti, J. P., Ganno. S., Danguene, P, Y.E., Bassahak, J., Hell, J. V., 2017. Contrasting Pan-African structural styles at the NW margin of the Congo Shield in Cameroon, Journal of African Earth Sciences, 1-20.

Kamdem-Toham A. W., Adeleke, N.D., Burgess R., Carroll J., D'amico E., Dinerstein D., M., O, Some L., 2003. Forest Conservation in the Congo Basin, Science 299: 346.

Käpyaho A., 2006. Whole-rock geochemistry of some tonalite and high Mg/Fe gabbro, diorite, and granodiorite plutons (sanukitoid suites) in the Kuhmo district, eastern Finland Bulletin of the Geological Society of Finland, 78: 121–141.

Kato Y., Yamaguchi K.E., Ohmoto H., 2006. Rare earth elements in Precambrian banded Fe formations: secular changes of Ce and Eu anomalies and evolution of atmospheric oxygen. In: Kessler S E, Ohmoto H (Eds.), Evolution of the Atmosphere, Hydrosphere, and Biosphere on Early Earth: Constraints from Ore Deposits. Geological Society of America, Denver.

Kato Y., Kawakami T., Kano T., Kunugiza K., Swamy N.S., 1996. Rare-earth element geochemistry of banded iron formations and associated amphibolite from the Sargur belts, south India. J. SE Asian Earth Science. 14: 161 - 164.

Kelvin F. E. A., Frances W., Rollinson G.K., Charles J.M., 2014. Quantitative mineralogical and chemical assessment of the Nkout iron ore deposit, Southern Cameroon. Ore Geology Reviews 62: 25-39.

Klein C., Ladeira, E. A., 2000. Geochemistry and Petrology of Some Proterozoic Banded Iron-Formations of the Quadrilátero Ferrífero, Minas Gerais, Brazil, Economic Geology, 95: 405 - 428.

Klein C., 2005. Some Precambrian banded iron-formations (BIFs) from around the world: their age, geologic setting, mineralogy, metamorphism, geochemistry, and origin. American Mineralogist, 90: 1473 - 1499.

Klein C., Beukes N. J., 1992. Time distribution, stratigraphy, and sedimentologic setting, and geochemistry of Precambrian Iron-Formation, In the Proterozoic Biosphere: A

multidisciplinary study, (edited by Schopf J W, and Klein C) 139 - 46. New York, Cambridge University Press.

Klein C., Beukes N. J., 1993. Sedimentology and geochemistry of the glaciogenic late Proterozoic rapitan Iron-Formation in Canada, Economic Geology, 88: 542 - 565.

Klein, C., Ladeira E. A., 2004. Geochemistry and Mineralogy of Neoproterozoic Banded Iron-Formations and Some Selected, Siliceous Manganese Formations From The Urucum District, Mato Grosso Do Sul, Brazil, Economic Geology, 99:1233–1244.

Key C. H., 1987. Geochemistry of diorites and associated plutonic rocks of SE Jersey, Channel Islands, Mineralogical Magazine, 51: 217-229

Kholodov V. N., Butuzova G.Y., 2001. Problems of iron and phosphorus geochemistry in the Precambrian. Lithology and Mineral Resources, 36(4): 291 - 302.

Lan T. G., Fan H. R., Santosh M., Hu F. F., Yang, K. F., Liu Y. S., 2014, U-Pb zircon chronology, geochemistry and isotopes of the Changyi banded iron formation in the eastern Shandong Province: Constraints on BIF genesis and implications for Paleoproterozoic tectonic evolution of the North China Craton, Ore Geology Review, 56: 472 – 486.

Lascelles D. F., 2006. The Mount Gibson Banded Iron Formation-Hosted Magnetite Deposit: Two Distinct Processes for the Origin of High-Grade Iron Ore, Economic Geology, 101: 651-666.

Lasserre M., Soba D., 1976. Age Libérien des granodiorites et des gneiss à pyroxènes du Cameroun Méridional. Bulletin BRGM, 2 (4): 17-32.

Lascelles D. F., 2007. Black smokers and the Archean environment: uniformitarian model for the genesis of iron-formations. Ore Geology Review, 32: 381-411.

Lerouge C., Cocherie A., Toteu S. F., Milesi J. P., Penaye J., Tchameni R., Nsifa N. E., Fanning C. M., 2006. SHRIMP U-Pb zircon dating for the Nyong Series, South West Cameroon. Journal of African Earth Science 44: 413-427.

Le Maitre, R. W., 1976. The chemical variability of some common igneous rocks. Journal of Petrology, 17: 589 - 637.

Li X-H., Chen Y., Li J., Yang C., Ling X-X., Tchouankoue J.P., 2016. New isotopic constraints on age and origin of Mesoarchean charnockite, trondhjemite and amphibolite in the Ntem Complex of NW Congo Craton, southern Cameroon, Precambrian Research 276:14 – 23.

Lobato L. M., Figueiredo E Silva R. C., Hagemann S., Thorne W., and Zucchetti M., 2008. Hypogene alteration associated with high-grade banded iron formation-related iron ore; Economic Geology, 15: 107 - 128.

Ludwig K. R., 2011. Isoplot 3.00 - a Geochronological Toolkit for Excel. Berkely Geochronology Center, 67.

Manikyamba C., Balaram V., Naqvi S. M., 1993. Geochemical signatures of polygenetic origin of the banded iron formation (BIF) of Archean Sandur greenstone belt (schist belt), Karnataka nucleus, India. Precambrian Research, 61 :137 - 164.

Maurizot P., Abessolo A., Feybesse J. L., John L. P., 1986. Étude de prospection minière du Sud-Ouest Cameroun. Synthèse des travaux de 1978 à 1985, rapport BRGM 85 CMR 066, 274p.

Maurizot, P. 2000. Geological map of South- west Cameroon, edition Bureau de la Recherche Géologique et Minière. Orléan.

Maurizot, P., and Abessolo, A., 1985, A Digest of BRGM "South West Cameroon Mining Inventory" Final Report

Marchig V., Gundlach H., Möller P., Schley F., 1982. Some geochemical indicators for discrimination between diagenetic and hydrothermal metalliferous sediments. Mar. Geology, 50: 241 – 256.

Martin D. Mc. B., Morris P. A., 2010. Tectonic setting and regional implications of ca 2.2 Ga mafic magmatism in the southern Hamersley Province, Western Australia, Aust. Journal Earth Science, 57: 911 - 931.

McLennan S. M., Hemming S., McDaniel D. K., Hanson G. N., 1993. Geochemical approaches to sedimentation, provenance, and tectonics. In: Special Papers-Geological Society of America, 21 – 40.

McLennan, S.M., 2001. Relationships between the Trace Element Compositions of Sedimentary Rocks and Upper Continental Crust, Geochemistry Geophysics and Geo-systems, 2: 86 - 98.

Milesi, J. P., Toteu, S. F., Deschamps, Y., Feybesse, J. L., Lerouge, C., Cocherie, A., Penaye, J., Tchameni, R., Moloto-A-Kenguemba, G., Kampunzu, H. A. B., Nicol, N., Duguey, E., Leistel, J. M., Saint-Martin, M., Ralay, F., Heinry, C., Bouchot, V., Doumnang Mbaigane, J. C., Kanda Kula, V., Chene, F., Monthel, J., Boutin, P., and Cailteux, J., 2006, An overview of the geology and major ore deposits of Central Africa: Explanatory note for the 1:4,000,000 map ‘‘Geology and major ore deposits of Central Africa’’: Journal of African Earth Sciences, 44: 571-595.

Mikkola P., Heilimo E., Huhma H., 2014. Relationships between sanukitoids and crust-derived melts and their implications for the diversity ofNeoarchaean granitoids: a case study from Surmansuo and nearby areas, Eastern Finland, Bulletin of the Geological Society of Finland, 86: 23–40.

Mishra M. and Sen S., 2012. Provenance, tectonic setting and source-area weathering of Mesoproterozoic Kaimur Group, Vindhyan Supergroup, Central India, Geologica Acta, 10(3) 283 - 293,

Moorbath S., O'Nions R, K., Pankhurst R, J., 1973. Early Archaean age for the Isua Iron Formation West Greenland, Nature, 245:138 - 139.

Morris R. C., 1985. Genesis of iron ore in banded iron-formation by supergene and supergene-metamorphic processes-a conceptual model, In: Wolff, K.H. (Ed.), Handbook of Strata-bound and Stratiform Ore Deposits. Elsevier, Amsterdam, 13: 73 - 235.

Moyen J. F., Martin H., Jayananda M., Auvray B., 2003. Late Archaean granites: a typology based on the Dharwar Craton (India), Precambrian Research, 127: 103 – 123.

Mvondo H., Den Brok S. W. J., Mvondo O. J., 2003. Evidence for symmetric extension and exhumation of the Yaoundé Nappe (Pan-African fold Belt, Cameroon), Journal of African Earth Sciences, 36: 215 - 231.

Ndema, M.J.L., Ngnotue, T., Ngo Nlend, C.D., Nzenti, J.P., Suh, C.E., 2014. Origin and evolution of the formation of the Cameroon Nyong Series in the western border of the Congo Craton. Journal of Geosciences and Geomatics, 2: 62 – 75.

Ndime E. N., Ganno S., Soh L. T., Nzenti J. P., 2018. Petrography, lithostratigraphy and major element geochemistry of Mesoarchean metamorphosed banded iron formation-hosted Nkout iron ore deposit, north western Congo craton, Central West Africa, Journal of African Earth Sciences, 148: 80 – 98.

Ndime E. N., Ganno S., Nzenti J.P., 2019. Geochemistry and Pb–Pb geochronology of the Neoarchean Nkout West metamorphosed banded iron formation, southern Cameroon, International Journal of Earth Sciences, 108: 1551 – 1570.

Nedelec A., Macaudiere J., Nzenti J. P., Barbey P., 1986. Évolution structurale et metamorphique des schistes de Mbalmayo (Cameroun), Implications pour la structure de la zone mobile panafricaine d'Afrique Centrale, au contact du craton du Congo. Comptes Rendus Academie Sciences Paris, 303: 75-80.

Nédélec A., Nsifa E. N., Martin H., 1990. Major and trace element geochemistry of the Archaean Ntem plutonic complex (South Cameroon): Petrogenesis and crustal evolution provenance of detritus for the Nyong Group. Precambrian Research, 47: 35 – 50.

Nelson J. P., Beukes N. J., Carincross B., 1995. Tectonic-stratigraphic setting of the 2.9Ga Mozaan group of the pongla supper group and correlation with the witwaterand supper-group. Extented abstracts of the south African geocongress, 838 - 840.

Nforba M. T., Suh C. E., Kabeyene K. V. K., 2012. Mbalam iron ore project, northern edge of the Congo craton, southeast Cameroon. In: Goldfarb R.J., Marsh, E.E., Monecke E. (Eds.), Proceedings of the Society of Economic Geologists on the Challenge of Finding New Mineral Resources: Global Metallogeny, Innovative Exploration and New Discoveries, SEG Extended Abstracts. Colorado, G-22.

Ngako V., Affaton P., Njonfang E., 2008. Pan-African tectonics in northwestern Cameroon: implication for the history of western Gondwana. Gondwana Research, 14: 509 – 522.

Ngnotué T., Ganno, S., Nzenti J. P., Schulz B., Tchaptchet T. D., Suh C. E. 2012. Geochemistry and geochronology of Peraluminous High-K granitic leucosomes of Yaoundé series (Cameroon): evidence for a unique Pan-African magmatism and melting. Event in North Equatorial Fold Belt. International Journal of Geosciences, 3: 525-548

Nsoh F. E., Agbor T. A., Etame J., Suh E. C., 2014. Ore-textures and geochemistry of the Nkout iron deposit South East Cameroon. Sciences, Technologies et Développement, 15: 43 – 52.

Nsifa E. N., Tchameni R., Belinga S. M. E., 1993. De l'existence des formations dans le complexe cratonique du Ntem (Sud-Cameroun), Projet 273, Archaean cratonic rocks Africa, 23 p.

Nsifa, N.E., Tchameni, R., Nedelec, A., Siqueira, R., Pouclet, A., 2013. Structure and petrology of Pan-African nepheline syenites from the South West Cameroon; Implications for their emplacement mode, petrogenesis and geodynamic significance. Jounal of African Earth Sciences, 87: 44-58.

Nyame F. K., Kase K., Yamato M., 1998. Spessartine garnet in a manganiferous carbonate formation from Nsuta, Ghana, Resource Geology, 48 (1): 13 - 22.

Nzenti J. P., Barbey P., Macaudière J., Soba D., 1988. Origin and evolution of the late Precambrian high-grade Yaounde gneisses (Cameroon), Precambrian Research. 38: 91 - 109.

Nzenti J. P., Barbey P., Jegouzo, P., Moreau C., 1984. Un nouvel exemple de ceinture granulitique dans une chaîne protérozoïque de transition: les migmatites de Yaoundé Cameroun, Comptes Rendus de l'Academic Science of Paris, 299: 1197 - 1199.

Nzenti, J. P., Barbey, P., Tchoua, F.M. 1999. Evolution crustale au Cameroun: éléments pour un modèle géodynamique de l'orogenèse néoproterozoïque. In Géologie et environnements au Cameroun, GEOCAM Cameroun 2: 397- 407.

Nzenti, J. P., Abaga, B., Suh, C. E., Nzolang, C. 2010. Petrogenesis of peraluminous magmas from the Akum-Bamenda Massif, Pan-African Fold Belt, Cameroon, International Geology Review, 1-29, DOI: 10.1080/00206810903442402.

Nzooh, Z. L., 2003. Statut des grands et moyens mammifères et activités humaines dans le massif forestier de Ngoila - Mintom, Fund Rapport World Wildlife (WWF) p.75.

Pannemans B., Roberts D., 2000. Geochemistry and petrogenesis of trondhjemites and granodiorite from Gauldalen, Central, Norwegian Caledonides. Norgesgeo/ogiskeundersekelse Bulletin, 437: 43 - 56.

Peccerillo, A., Taylor, S.R., 1976. Geochemistry of Eocene calc-alkaline volcanic rocks from the Kastamonu area, Northern Turkey. Contributions to Mineralogy and Petrology 58, 63–81.

Pearce J. A., Harris N. W., and Tindle A. G., 1984. Trace element discrimination diagrams for the tectonic interpretation of granitic rocks, Journal of Petrology, 25: 956 - 983.

Peccerillo A., Taylor S. R., 1976. Geochemistry of Eocene calcalkaline volcanic rocks from the Kastamonu area, Northern Turkey. Contribution of Mineral and Petrology, 58: 63-81.

Pecoits E, Gingras M, Barley M, Kappler A, Posth N, Konhauser K., 2009. Petrography and geochemistry of the Dales Gorge banded iron formation: paragenetic sequence, source and implications for palaeo-ocean chemistry. Precambrian Research, 172:163–187.

Penaye J, Toteu S. F., Tchameni R., Van Schmus W. R., Tchakounte J., Ganwa A., Miyem D., Nsifa E. N., 2004. The 2.1 Ga West Central African Belt in Cameroon: extension and evolution, Journal of African Earth Sciences, 3:159 - 164.

Planavsky N., Bekker A., Rouxel O. J., Kamber B., Hofmann A., Knudsen A., Lyons W. T., 2010. Rare Earth Element and yttrium compositions of Archaean and Paleoproterozoic Fe formations revisited: new perspectives on the significance and mechanisms of deposition, Geochemistry Cosmochemistry Acta, 74: 6387 - 6405.

Pouclet A., Tchameni R., Mezger K., Vidal M., Nsifa E. N., Shang C. K., Penaye J., 2007. Archaean crustal accretion at the northern border of the Congo Craton (South Cameroon), the charnockite-TTG link, Bulletin of the Geological Society of France, 178: 331 - 342.

Poulton S. W., Fralick P. W., Canfield D. E., 2010. Spatial variability in oceanic redox structure 1.8 billion years ago. Natural Geoscience, 3: 486 - 490.

Prasad K. S. S., Sankar D. B., Reddy Y.V., 2012. Geochemistry and Origin of Banded Iron-Formation from the Granulitic Terrain of North Arcot District, Tamil Nadu, South India Chemical Science Transactions, 1(3): 482 – 493.

Pufahl P. K., 2010. Bio-elemental sediments. In: James N. P., Dalrymple R.W. (Eds.), Facies Models 4. Fourth ed. Geological Association of Canada, St. John's, NL, Canada, 477 - 504.

Ramsay, J.G., Huber, M.I., 1987. The Techniques of Modern Structural Geology, In: Folds and Fractures, Academic Press, London, 2: 700 pp.

Ramsay, J.G., 1967. Folding and Fracturing of Rocks. McGraw-Hill Book Co., New York, 568 pp.

Ramachandran, A., Madhavaraju J., Ramasamy S., LEE Y. I., RAO S., Chawngthu D, L., Velmurugan K., 2016. Geochemistry of Proterozoic clastic rocks of the Kerur Formation of Kaladgi-Badami Basin, North Karnataka, South India: implications for paleo-weathering and provenance, Turkish Journal Earth Science, 25: 126 - 144.

Rolin P., 1992. Pre´sence d'un chevauchement ductile majeur d'age panafricain dans la partie centrale de la Re´publique Centrafricaine: re´sultats pre´liminaires. Comptes Rendus de l'Acade´mie des Sciences, 315 : 467 - 470.

Roser B. P., Korsch R. J., 1988. Provenance Signatures of Sandstone-Mudstone suites determined using discriminant function analysis of major-element data. Chemical Geology, 67: 119–139.

Rosholt J. N., Zartman R. E., Nkomo L. T., 1973. Lead isotope systematics and uranium depletion in the Granite Mountains, Wyoming. Bull Geology Society of Amsterdam, 84: 989 - 1002.

Rosière C. A., Spier C. A., Rios F. J., Suckau V. E., 2008. The itabirites of the Quadrilátero Ferrífero and related high-grade iron ore deposits: an overview. In: Hagemann SG et al. (eds) Banded Iron Formation–Related High-Grade Iron Ore. Reviews in Economic Geology, 15: 223 – 254.

Rudnick R. L., McLennan S. M., Taylor S. R., 1985. Large ion lithophile elements in rocks from high-pressure granulite facies terrains, Geochimica et Cosmochimica Acta, 49: 1645 - 1655.

Shand, S.J., 1947. Eruptive rocks, Their Genesis, Composition, Classification, and their Relation to Ore Deposits, Wiley, New York, p. 488.

Shang C. K., Liégeois J. P., Satir M., Frisch W., Nsifa E. N., 2010. Late Archaean high-K granite geochronology of the northern metacratonic margin of the Archaean Congo Craton, Southern Cameroon: Evidence for Pb-loss due to non-metamorphic causes. Gondwana Research, 475: 1 -19.

Shang C. K., Satir M., Nsifa E. N., Liegeois J. P., Siebel W., Taubald H., 2007. Archaean high-K granitoids produced by remelting of the earlier Tonalite–Trondhjemite– Granodiorite (TTG) in the Sangmelima region of the Ntem complex of the Congo craton, southern Cameroon, International Journal of Earth Sciences, 96: 817–842.

Shang C. K., Satir M., Siebel W., Taubald H., Nsifa E. N., Westphal M., Reitter E., 2001. Genesis of K-rich granitoids in the Sangmelima region, Ntem complex (Congo craton), Cameroon. Terra Nostra, 5: 60 - 63.

Shang C. K., Satir M., Siebel W., Nsifa N. E., Taubald H., Liegeois J. P., and Tchoua F. M., 2004a. Major and trace element geochemistry, Rb-Sr and Sm - Nd systematics of the TTG magmatism in the Congo Craton: case of the Sangmelima region, Ntem complex, southern Cameroon, Journal Sciences African Earth Science, 40: 61 - 79

Shang C. K., Siebel W., Satir M., Chen F., Mvondo J. O., 2004b. Zircon Pb-Pb and U - Pb systematics of TTG rocks in the Congo Craton: constraints of crustal formation, crystallization and Pan-African lead loss, Bulletin of Geosciences, 79: 205 - 219.

Sheraton W., Ellis D., Kuehner S. M., 1985. Rare-earth element geochemistry of Archaean orthogneisses and evolution of the East Antarctic shield, Journal of Australian Geology and Geophysics, 9: 207 - 218

Shervais J. W., 2008. Tonalites, trondhjemites, and diorites of the Elder Creek ophiolite, California: Low-pressure slab melting and reaction with the mantle wedge, Geological Society of America, 438: 113 - 132,

Soh T. L., Nzepang T., M., Chongtao W., Ganno S., Ngnotue T., Kouankap N. G. D., Simon S. J., Zhang J., Nzenti J. P., 2018. Geology and geochemical constrains on the origin and

depositional setting of the Kpwa-Atog Boga banded iron formations (BIFs), northwestern Congo craton, southern Cameroon. Ore Geology Reviews, 95: 620 - 638.

Somarin A. K., 2011. Petrography, Geochemistry and Petrogenesis of Late-Stage Granites: An Example from the Glen Eden Area, New South Wales, Australia, Earth and Environmental Sciences, (Ed.), ISBN: 978-953-307- 468-9.

Spier C. A., De Oliveira S. B., Rosiere C. A., 2003. Geology and geochemistry of the Aguas Claras and Pico Iron Mines, Quadrilatero Ferrifero, Minas Gerais, Brazil. Miner. Deposita, 38 : 751 - 774.

Spier C. A., de Oliveira S. M. B., Sial A. N., Rios F. J., 2007. Geochemistry and genesis of the banded iron formations of the Caue Formation, Quadrilatero Ferrıfero, Minas Gerais, Brazil. Precambrian Research, 152: 170 - 206.

Stacey J. S., Kramers J. D., 1975. Approximation of terrestrial lead isotope evolution by two-stage model: Earth and Planetary Science Letters, 26: 207 - 221.

Subrata R., Venkatesh A. S., 2009. Mineralogy and geochemistry of banded iron formation and iron ores from eastern India with implications on their genesis, Jounal of Earth System and Science, 118(6): 619 – 641.

Suchel J. B., 1987. Les climats du Cameroun, Thèse présentée à l'Université de Bordeaux II, p199.

Suh C. E., Cabral A., Shemang E. M., Mbinkar L., Mboudou G. G. M., 2008. Two contrasting iron-ore deposits in the Precambrian mineral belt of Cameroon, West Africa, Explore Mineral Geology, 17: 197 - 207.

Suh C. E, Cabral A. R., Ndime E. N., 2009. Geology and ore fabrics of the Nkout high-grade haematite deposit, southern Cameroon. Smart Science for Exploration and Mining, 1: 558 - 560.

Taylor D., Dalstra H. J., Harding A. E., Broadbent G., Barley M. E., 2001. Genesis of high-grade haematite orebodies of the Hamersley Province, Western Australia, Economic Geology, 96: 837 - 873.

Taylor S. R., McLennan S. M., 1985. The Continental Crust: Its Composition and Evolution. Blackwell, London. Oxford, 1 - 328.

Taylor, C. D., Schulz, K. J., Doebrich, J. L., Orris, G. J., Denning, P. D., and Kirschbaum, M. J., 2009, Geology and nonfuel mineral deposits of Africa and the Middle East:, U.S. Geological Survey Open-File Report 2005-1294-E, p. 246.

Tchameni R., 1997. Géochimie et géochronologie des formations de l'Archéen et du Paléoproterozoïque du Sud-Cameroun (Groupe du Ntem, Craton du Congo), Thèse de l'Univérsité d'Orléans, France, p.395.

Tchameni R., Mezger K., Nsifa N. E., Pouclet A., 2001. Crustal origin of Early Proterozoic syenites in the Congo Craton (Ntem Complex), South Cameroon, Lithos, 57 (1): 23 - 42.

Tchameni R., Mezger K., Nsifa N. E., Pouclet A., 2000. Neoarchaean evolution in the Congo craton: evidence from K rich granitoids of the Ntem complex, Southern Cameroon, Jounal of African Earth Science, 30: 133 - 147.

Tchameni R., Pouclet A., Mezger K., Nsifa E. N., Vicat J. P., 2004. Monozircon and Sm-Nd whole rock ages from the Ebolowa greenstone belts: evidence for the terranes older than 2.9 Ga in the Ntem complex (Congo craton, South Cameroon), Jounal of Camroon Acadmi of Science, 4 (3): 213 - 224.

Tchameni R., Lerouge C., Penaye J., Cocherie A., Milesi J. P., Toteu S. F., Nsifa E. N., 2010. Mineralogical constraint for metamorphic conditions in a shear zone affecting the Archean Ngoulemakong tonalite, Congo craton (southern Cameroon) and retentivity of U-Pb SHRIMP zircon dates, Journal of Africa Earth Science, 58: 67 - 80.

Teutsong T., Bontognali T. R. R., Ndjigui P. D., Vrijmoed J. C., Teagle D., Cooper M., Vance D., 2017. Petrography and geochemistry of the Mesoarchean Bikoula banded iron formation in the Ntem complex (Congo craton), Southern Cameroon: Implications for its origin. Ore Geology Reviews, 80: 267 - 288.

Thorne W. S., Hagemann S. G., Barley M., 2004. Petrographic and geochemical evidence for the hydrothermal evolution of the North Deposit, Mt. Tom Price, Western Australia; Mineralum Deposita, 39: 766 - 783.

Thompson A. B., 1982. Dehydratation melting of pelitic rocks and the generation of H_2O-undersaturated granitic liquids, Amerian Jounal of Sciences, 282: 1567-1595.

Thompson, R. N., Morrisson, M. A., Hendry, G. L. Parry, S. J. 1984. An assessment of the relative role of crust and mantle in magma genesis, An element approach, Philosophical Transactions of the Royal Society London, 310: 549-590.

Thurston P. C., Kamber B. S., Whitehouse M., 2012. Archean cherts in banded iron formation: insight into Neoarchean ocean chemistry and depositional processes. Precambrian Research, 214: 227 – 257.

Tokhi M. El., Mahmoud B. E. D. A., Arman H., 2016. Geochemical Characters of the Gabbroic Rocks in Ophiolite Sequences of North Hatta Area, United Arab Emirates Acta Physica Polonica, p.130.

Tosdal R. M., Wooden J. L., Bouse R. M., 1999. Pb isotopes, ore deposits, and Metallogenic Terranes, Application of radiogenic isotopes to ore deposit research and exploration. Reviews in Economic Geology, 12: 1 - 28.

Toteu S. F., Van Schmus W. R., Penaye J., Nyobe J. B., 1994. U - Pb and Sm - Nd evidence for Eburnean and Pan-African high-grade metamorphism in cratonic rocks of southern Cameroon. Precambrian Research, 67: 321 -347.

Toteu S. F., Penaye J., Poudjom Djomani Y. H., 2004. Geodynamic evolution of the Pan-African belt in Central Africa with special reference to Cameroon, Canadian Journal of Earth Sciences, 41: 73 - 85.

Toteu, S. F., Van Schmus, W. R., Penaye, J., Michard, A. 2001- New U-Pb and Sm-Nd data from North-Central Cameroon and its bearing on the pre-pan African history of Central Africa. Precambrian Research.108: 45 - 73

Toteu S. F., Penaye J., Deloule E., Van Schmus W. R., Tchameni R., 2006. Diachronous evolution of volcano-sedimentary basins, North of the Congo Craton: Insights from U–Pb ion microprobe dating of zircons from the Poli, Lom and Yaounde´ Groups (Cameroon), Journal of African Earth Sciences, 44: 428 - 442.

Toth J. R., 1980. Deposition of submarine crusts rich in manganese and iron. GSA Bull, 91(1): 44 - 54.

Trendall A. F., 2002. The significance of iron-formation in the Precambrian stratigraphic record. International Association of Sedimentology, 33: 33 - 66.

Trendall A.F., Blockley J.G., 1970. The iron formations of the Precambrian Hamersley Group Western Australia with special reference to the crocidolite. Geological Survey of Western Australia Bulletin, p.365.

Usui A., Someya M., 1997. Distribution and composition of marine hydrogenetic and hydrothermal manganese deposits in the northwest Pacific. In: Nicholson, K., Hein, J.R., Buhn, B., Dasgupta, S. (Eds.), Manganese Mineralization: Geochemistry and Mineralogy of Terrestrial and Marine Deposits, 119: 177 - 198.

Vicat, J.P., Nsifa, E., Tchameni, R., Pouclet, A., 1998. La ceinture de roches vertes de Lolodorf-Ngomezap (Sud-Cameroun): pétrologie, géochimie et cadre géodynamique. Geocam 1: 325–337.

Walraven F., 1993. Geochronological investigation in lithologies of the Archean craton of the Kasai region, southwestern Zaire. Abstract conference IGCP project 273, Bujumburra, Burundi.

Webb A., and Clout J., 2008. Banded Iron Formation-Related Iron Ore Deposits of the Hamersley Province, Western Australia; Econonic Geology, 15 197–221.

Webb A. D., Dickens G. R., Oliver N. H. S., 2003. From banded iron formation to iron ore: geochemical and mineralogical constraints from across the Hamersley Province, Western Australian Chemistry and Geology, 197: 215 - 251.

White A. J. R. Chappell B. W., 1977. Ultrametamorphism and granitoids genesis, Tectonophysics, 43, 7 - 22.

Yang X, Q., Zhang Z, H., Duan S, G., Zhao X, M., 2015. Petrological and geochemical features of the Jingtieshan banded iron formation (BIF): a unique type of BIF from the Northern Qilian Orogenic Belt, NW China, Ore Geology Review, 63: 418 - 443.

York D., 1969. Least-squares fitting of a straight line with correlated errors, Earth Planet Science Letter, 5: 320 - 334.

Young G. M., 2013. Precambrian supercontinents, glaciations, atmospheric oxygenation, metazoan evolution and an impact that may have changed the second half of Earth history, Geoscience Front, 4: 247 - 261.

Zhai M., Santosh M., 2011. The early Precambrian odyssey of the North China Craton: a synoptic overview. Gondwana Research, 20: 6 - 25.

Zhai M. G., Santosh M., 2013. Metallogeny of the North China Craton: link with secular changes in the evolving Earth. Gondwana Research, 24: 275 - 297.

Zhang, X. J., Zhang, L. C., Xiang, P., Wan, B., Pirajno, F., 2011. Zircon U–Pb age, Hf isotopes and geochemistry of Shuichang Algoma-type banded iron-formation, North China craton: Constraints on the ore-forming age and tectonic setting. Gondwana Research, 20: 137 – 148.

APPENDIX

Journal of African Earth Sciences 148 (2018) 80–98

Contents lists available at ScienceDirect

Journal of African Earth Sciences

journal homepage: www.elsevier.com/locate/jafrearsci

Petrography, lithostratigraphy and major element geochemistry of Mesoarchean metamorphosed banded iron formation-hosted Nkout iron ore deposit, north western Congo craton, Central West Africa

Ekah Nzume Ndime[a], Sylvestre Ganno[a,*], Landry Soh Tamehe[a,b], Jean Paul Nzenti[a]

[a] Department of Earth Sciences, University of Yaoundé I, P.O. Box. 812, Yaoundé, Cameroon
[b] Key Laboratory of CBM Resource & Reservoir Formation Process, Chinese Ministry of Education, School of Resource and Geoscience, China University of Mining and Technology, Xuzhou, Jiangsu, 221116, China

ARTICLE INFO

Keywords:
Lithostratigraphy
Oxide facies
Nkout metamorphosed BIF
Ntem basin
Congo craton

ABSTRACT

The Nkout banded iron formation (BIF) or iron deposit is located in the northwestern margin of the Congo Craton (CC) and is hosted within high-grade metamorphic Ntem complex. It is mainly made up of metamorphosed banded iron formations with resource estimation of 1.8 Bt @ 32.6% Fe indicated, and 0.9 Bt @ 30.3% Fe inferred. Nkout iron deposit is subdivided into three prospects namely East, Centre and West deposits. Results from lithostratigraphic studies allow detailed correlations between units in the Nkout succession. The litho-package from the top to the base stratigraphy comprises iron-rich member and the gneissic member. The first member forms the upper and middle units while the second member forms the lower unit and represents the footwall of the deposit. The upper unit is ~200 m deep and consists of oxidized (hematite) and un-oxidized (fresh metamorphosed BIF) ore types. The middle unit is approximately 150 m thick and consists of fresh metamorphosed BIF with minor intercalation of biotite gneiss. The lower unit is made up of garnet-magnetite micaschist, biotite gneiss and pyroxene-biotite gneiss.

The Nkout banded iron formation belongs to oxide facies magnetite-rich type which has suffered greenschist to amphibolite facies metamorphism, leading to recrystallization of chlorite, amphibole and garnet minerals. Its overall major oxide bulk chemistry is very similar to that of most Archaean iron-formations worldwide, with high SiO_2 and Fe_2O_3 contents. However, the garnet-rich BIF has higher contents of Al_2O_3 (8.73 wt%), TiO_2 (0.27 wt%), K_2O (2.37 wt%) relative to magnetite-rich BIF, suggesting clastic contamination, thus a depositional environment closer to the continent. Furthermore, the absence of carbonate facies BIF in the entire Nkout deposit suggests deep water distal depositional setting, in an area of little or no organic carbon supplies.

The lithostratigraphic correlation of metamorphosed BIF unit reveals both thicknesses and depth variations from West to the East, inferring a folded structure for the Nkout deposit. However the occurrence of BIF units in the entire deposit supports the fact that BIF deposition took place on a basin-wide scale. Considering the extent of the Ntem basin, it is suggested that a huge amount of Fe^{2+} in sea water was required. Thus, the deposition of Nkout BIF probably involved an iron rich environment of reduced Fe^{2+} rich hydrothermal fluid in chemically stratified sea water, similar to the depositional model proposed for the Minas BIF Supergroup of Quadrilátero Ferrífero in Brazil.

1. Introduction

In central-west Africa, the most important iron deposits are hosted in metamorphosed banded iron formations (BIFs) and located in the northern portion of the Congo craton (CC) with huge deposits in Congo (Avima, Nabeba, Badondo Zanaga, Mayoko), Gabon (Belinga, Baniaka), and southern Cameroon (Mbalam, Nkout, Bikoula, Kouambo, Meyomessi, Kpwa-Atog Boga, Mamelles) (Caen Vachette et al., 1988; Suh et al., 2009; Anderson et al., 2014; De Waele et al., 2015; Ganno et al., 2017, 2018; Teutsong et al., 2017; Soh Tamehe et al., 2018). Most of these deposits have not yet been studied and very little is known on the stratigraphy of the Congo basin; the depositional environment of BIF and the ore-forming processes. In this study, we take the advantage of the intense drilling activity of Nkout iron ore deposit to improve the understanding of the lithostratigraphy which is established on the basis of borehole data generated from boreholes drilled with deeper

* Corresponding author.
E-mail addresses: sganno2000@gmail.com, sganno@uy1.uninet.cm (S. Ganno).

https://doi.org/10.1016/j.jafrearsci.2018.06.007
Received 28 June 2017; Received in revised form 6 June 2018; Accepted 8 June 2018
Available online 11 June 2018
1464-343X/

stratigraphic targets, and the interest in the overlying Archaean metamorphosed BIF succession. The Nkout mining project undertaken by Caminex SA is part of the emerging iron ore province in central Africa, situated some 240 km SE of Yaoundé in Cameroon. It is made up of a vast quantity of iron ore deposit, evolving to be a larger iron ore producer with metal value of 1.8 Bt at 32.6% Fe indicated, 0.9 Bt at 30.3% Fe inferred (http://www.imicplc.com/Nkout.aspx). Previous studies on Nkout metamorphosed BIF were focused on mineralogy and ore-textures of high-grade ore, (Suh et al., 2009; Anderson et al., 2014; Nsoh et al., 2014). More recently, Ndime et al. (personal communication) performed whole-rock geochemistry and reported first direct whole rock Pb-Pb date of 2679 ± 89 Ma interpreted as the Neoarchean metamorphic event attributed to high-K granitoid emplacement in the Ntem complex. In this contribution, after detailed logging of diamond drilled cores from nine representative boreholes, we provide the petrography, major element geochemistry and lithostratigraphic data. The goal of the study is the construction of the synthetic stratigraphic column of the Nkout basin with the aim of constraining the structure and the depositional setting of the deposit.

2. Geological setting

2.1. Regional geological setting

The north western Congo craton (NWCC) crops in Gabon, Congo, and Cameroon and comprises Archaean rocks which are mainly composed of Tonalite-Trondjemite-Granodiorite (TTG) gneisses and greenstone belt assigned to the Archaean Ntem Complex in Cameroon (Maurizot et al., 1986; Feybesse et al., 1998, Fig. 1A). The greenstone belt in the Ntem Complex is comprised of metavolcanics with mafic-ultramafic compositions (amphibolites and pyroxenites) and banded iron formation (BIF) (Shang et al., 2010; Ganno et al., 2015). Polycyclic metamorphism and magmatism affected the Ntem complex. The Archean tectonothermal event of the Congo craton (CC) showed oldest rocks of the Ntem complex to be of the metamorphic rocks greater than 3000 Ma (Toteu et al., 1994; Tchameni et al., 2001). The granitoid plutonism (granodiorite, granite, syenite and charnockite intrusions) and charnockitisation (charnockitic gneiss) were reported at 2900-2500Ma (Toteu et al., 1994; Shang et al., 2004a,b). During these events the rocks were subjected to a series of low to high grade metamorphism responsible for granulation which includes gneissification, charnockitisation and up-lifting responsible for rock deformation (Caen-Vachette et al., 1988; Toteu et al., 1994). During the Pan-African orogeny (~600 Ma), the central African fold belt (CAFB) - a mobile belt - thrusted southward onto the northern edge of the Congo craton and collided with the Ntem complex (Nzenti et al., 1988; Toteu et al., 2004). The effect of the collision extends from Cameroon to Central African Republic and continues into the Borborema Province in NE Brazil (Rolin, 1992).

Four Archean deformation stages affected the NWCC. The earlier D_1were identified within the metamorphic rock unit in the E-W trending (S_1) foliation that steep dip to the north. The D_2 is dominantly dome and basin related to diapiric movement in the mid-to lower crust (Tchameni et al., 2000). It is responsible for the intrusions emplaced along the NE-SW trending (S_2) foliation as a result of the local early deformed S_1 into low amplitude isoclinal folds. The S_2 is a regional, vertical and steeply dipping foliation, mainly within the greenstone units in the Ntem complex (Shang et al., 2004a,b), with variable orientation (N-E to N-S) associated with mainly the N-S trending sinistral and dextral strike-slip faults (Shang et al., 2001, 2004a,b). The D_3 is mainly the mylonitic (S_3) foliation and shear zone (C_3) observed near the contact zones. D_4 is brittle phase deformation.

Recent reviews of the geochronologic data from the Ntem complex reveals that the charnockites crystallized at ~2.92 Ga; the trondhjemites and associated amphibolite protoliths, crystallized synchronously at 2.87–2.86 Ga (Li et al., 2016).

2.2. Geology and stratigraphy of the Nkout deposit

The Nkout deposit is an iron ore body occurring roughly in an E-W direction with steep dips (50–65°) toward the N and NW (Suh et al., 2009; Anderson et al., 2014). It extends for approximately 9 km long and a lateral width of about 0.8 km, subdivided into West, Centre and South deposits (Fig. 1B). Nkout deposit is made up of metamorphosed oxide-facies magnetite-rich BIF (itabirite), which is deposited along the contact of biotite-magnetite gneiss, garnet-pyroxene gneiss in the south. Biotite gneiss and pyroxene granite (charnockite) assemblages occur in the north of the study area. A series of N-S and NE-SW strike-slip faults

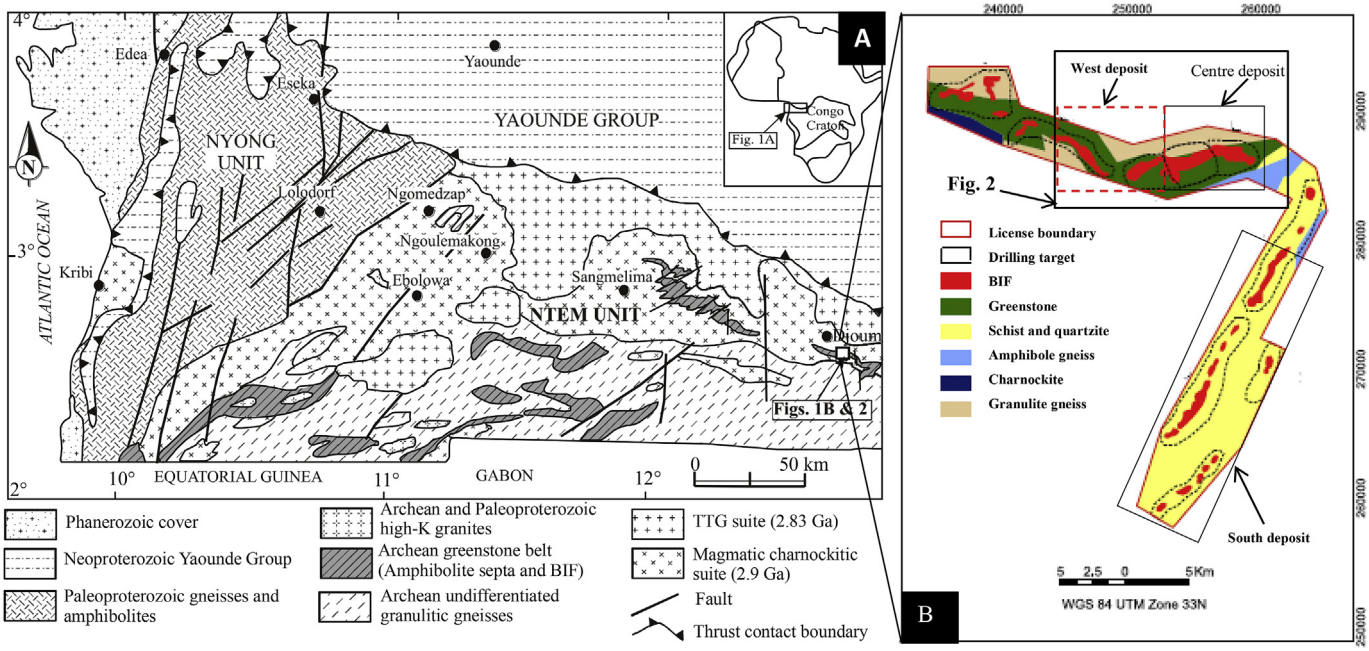

Fig. 1. A) Simplified geologic map of SW Cameroon (Maurizot et al., 1986); the square indicates the relative position of the studied metamorphosed BIF; B) Geological map of Nkout metamorphosed iron deposit (after Anderson et al., 2014).

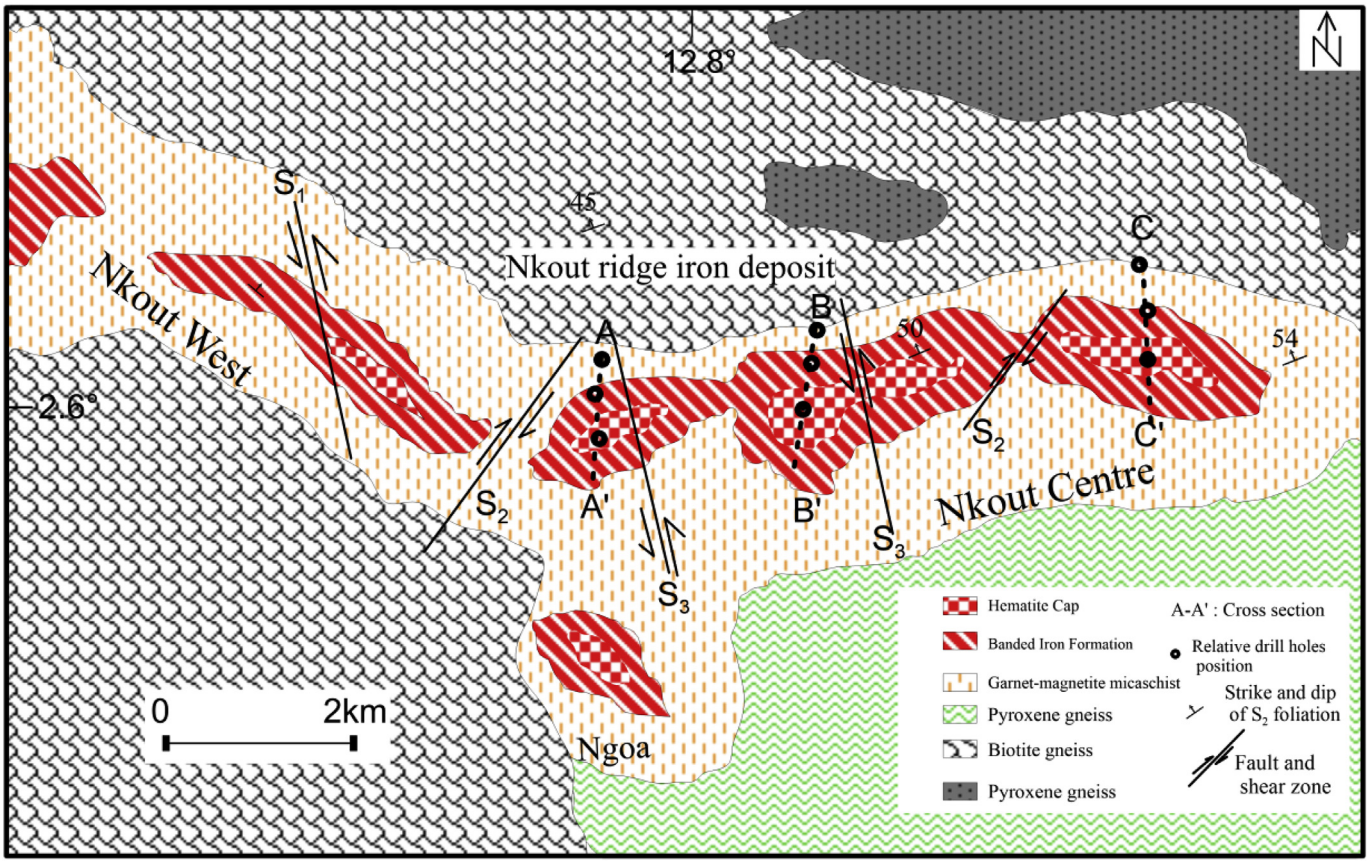

Fig. 2. Local geological map of Nkout prospect.

delimit the individual deposits (Fig. 2). The banded iron formation grades upwards from an un-oxidized to a partly oxidized BIF. The uppermost part of the metamorphosed BIF has been affected by weathering and oxidation processes resulting in high grade ore, which consists of a lateritic cap and saprolite material (Anderson et al., 2014). They are earthy, firm to clayey, friable, and crumbly or biscuity and many are moderate to well-banded. The fresh unweathered part of the metamorphosed BIF deposit shows an isoclinal fold structure (Suh et al., 2009). Recently, Ndime et al. (personal communication) reported a Pb/Pb age of 2689 ± 87 Ma for the Nkout metamorphosed BIF, interpreted as the metamorphic age, which was probably contemporaneous with the high-K granitoids emplacement within the Ntem complex.

3. Methods

Nine (09) diamond drill holes spatially distributed in three sections of Nkout area were chosen. Nkout mineral exploration property is owned by Caminex S.A (a subsidiary of International Mining & Infrastructure Corporation (IMIC) PLC, a British-London based company).

The cores were logged lithologically at their respective depth intervals. Core samples were collected from representative drill holes. Care was taken during sample preparation and study of the different lithologies on the field by observing surface outcrops and core material.

Thirty one (31) thin sections were prepared in Geotech Lab Vancouver (Canada) out of 32 diamond drill cores sampled. The thin sections were studied in a standard optical microscope in transmitted and reflected light to constrain mineral assemblages, textures and abundance in the different mappable units at the University of Yaoundé I. Photomicrographs of samples were taken under plane polarized light (PPL), cross polarized light (XPL) and reflected light (RL).

Whole-rock analyses were done using the pulp by Inductively Coupled Plasma-Atomic Emission (ICP-AES) for major elements at ALS Minerals Global Group Vancouver (Canada). The samples were pulverized and 50–60 g were obtained for the analyses. Carbon and sulphur by combustion in furnace was used for whole rock geochemistry to quantify the major elements. The majority of these analytes have a lower detection limit of 0.01%, with the exception of Na_2O (0.05%) and P_2O_5 (0.005%). Loss on ignition ("LOI") was determined by 0.5 g, ignited for 2 h at 1000 °C and then weighed again. Most of the whole rock samples correspond to the same sample points where the thin sections were sampled, for correlation between geochemistry and mineralogy.

4. Results

4.1. Petrography

Nkout deposit is mainly made up of banded Iron formation (metamorphosed BIF), associated with country rocks made up of gneiss and micaschist.

4.1.1. Country rocks

4.1.1.1. Biotite-rich gneiss. Biotite-rich gneiss samples were collected from the upper contact between gneiss and metamorphosed BIF. Biotite-rich gneiss sample shows gneissic structure with alternating millimetric quartzo-feldspathic and ferromagnesian layers in hand specimen (Fig. 3A), and displays heterogranular and granoblastic microstructure on thin sections (Fig. 3B and C). It consists mainly of quartz (25–30%), plagioclase (20–25%), K-feldspars (20–25%), biotite (10–15%) and magnetite (2–5%).

Quartz crystals are the most abundant minerals in the gneiss assemblages with equigranular coarse-grain sizes, and are dominantly granoblastic in texture. Quartz crystals (0.06–0.20 mm) are anhedral to subhedral, exhibit polycrystalline ribbons or single crystals with

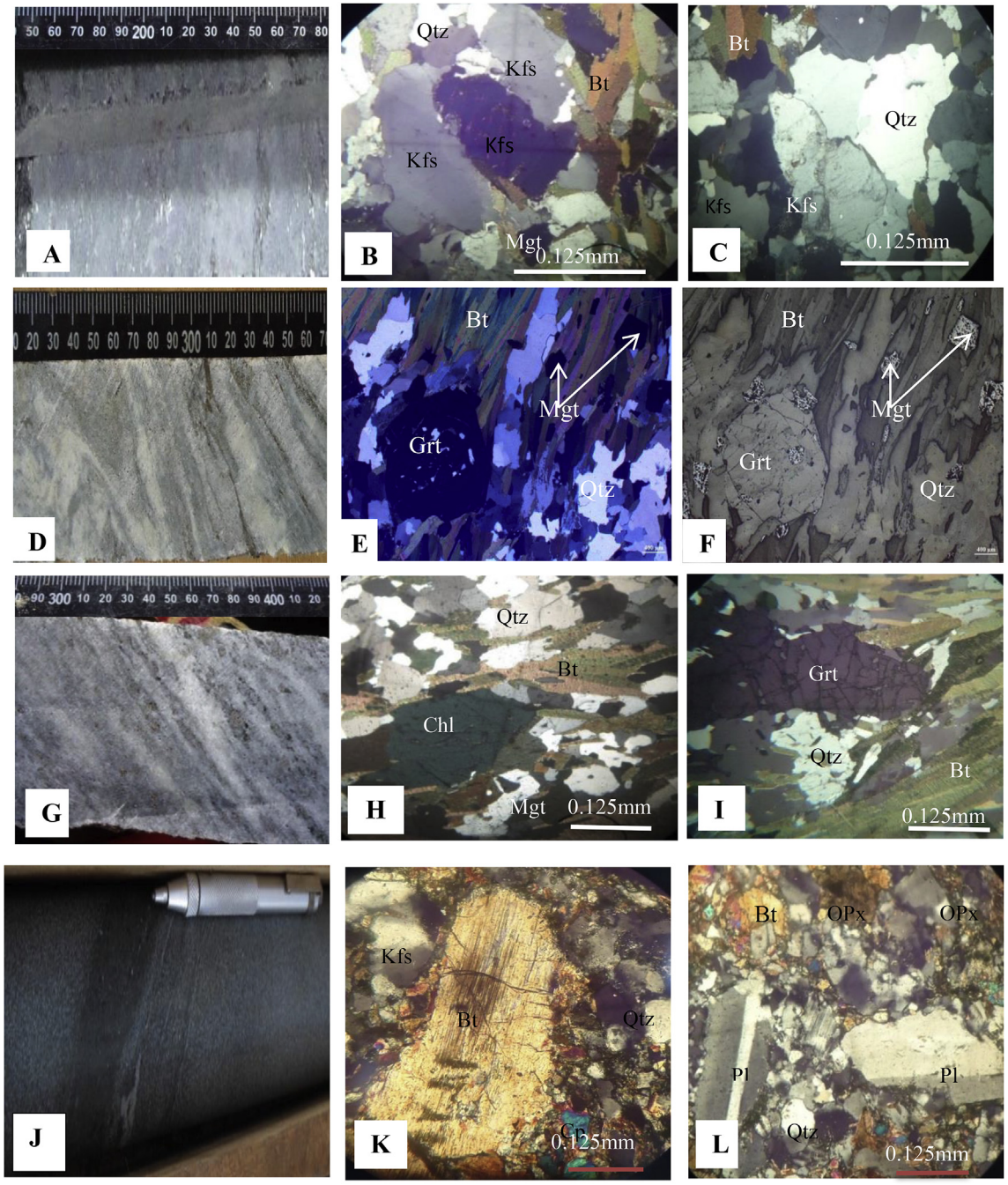

Fig. 3. Hand specimen and photomicrographs of country rock: core photos of biotite gneiss (A); garnet-rich gneiss (D); garnet-magnetite micaschist (G); pyroxene gneiss (J), Photomicrographs showing granoblastic microstructure and mineral assemblage of biotite gneiss (B & C); garnet-magnetite micaschist (E: transmitted light & F: Reflected light); and garnet-rich gneiss (H & I) and pyroxene gneiss (K & L).

undulatory extinction and the coarse-grained domains occur as mega-crystals. The deformational features are indicative of dynamic re-crystallization. The interlocking grain boundaries shared with the other minerals are smoothly curved (Fig. 3C). Quartz crystals are in association with K-feldspar and biotite.

K-feldspar crystals are anhedral to subhedral in shape and measures up to 0.15–0.24 mm in sizes, indicating granoblastic texture (Fig. 3B). Some crystals show interlocking grain boundaries with quartz. They are often associated with biotite, quartz and biotite crystals.

Magnetite occurs as large subhedral to anhedral crystals which measures up to 0.21 mm, showing granoblastic texture (Fig. 3C). The magnetite crystals are dark-grey in colour, and commonly surrounded by other coarse-grained minerals (K-feldspar and quartz). They exhibit interlocking grain boundaries with quartz, in association with biotite, quartz and K-feldspars.

Biotite crystals occur as anhedral to subhedral flakes (0.16 mm), commonly altered to secondary greenish-blue chlorite minerals. They share grain boundaries that are straight or smoothly curved with the other minerals. The biotite crystals are commonly porphyroblastic. The biotite porphyroblasts are of various sizes, and mainly shows a granoblastic texture (Fig. 3B). Biotite is often associated with magnetite, quartz and K-feldspars.

Plagioclase is commonly medium-to coarse-grained (0.01–0.2 mm) and euhedral to subhedral with polysynthetic twins.

4.1.1.2. Garnet-biotite gneiss. Garnet-biotite gneiss samples were

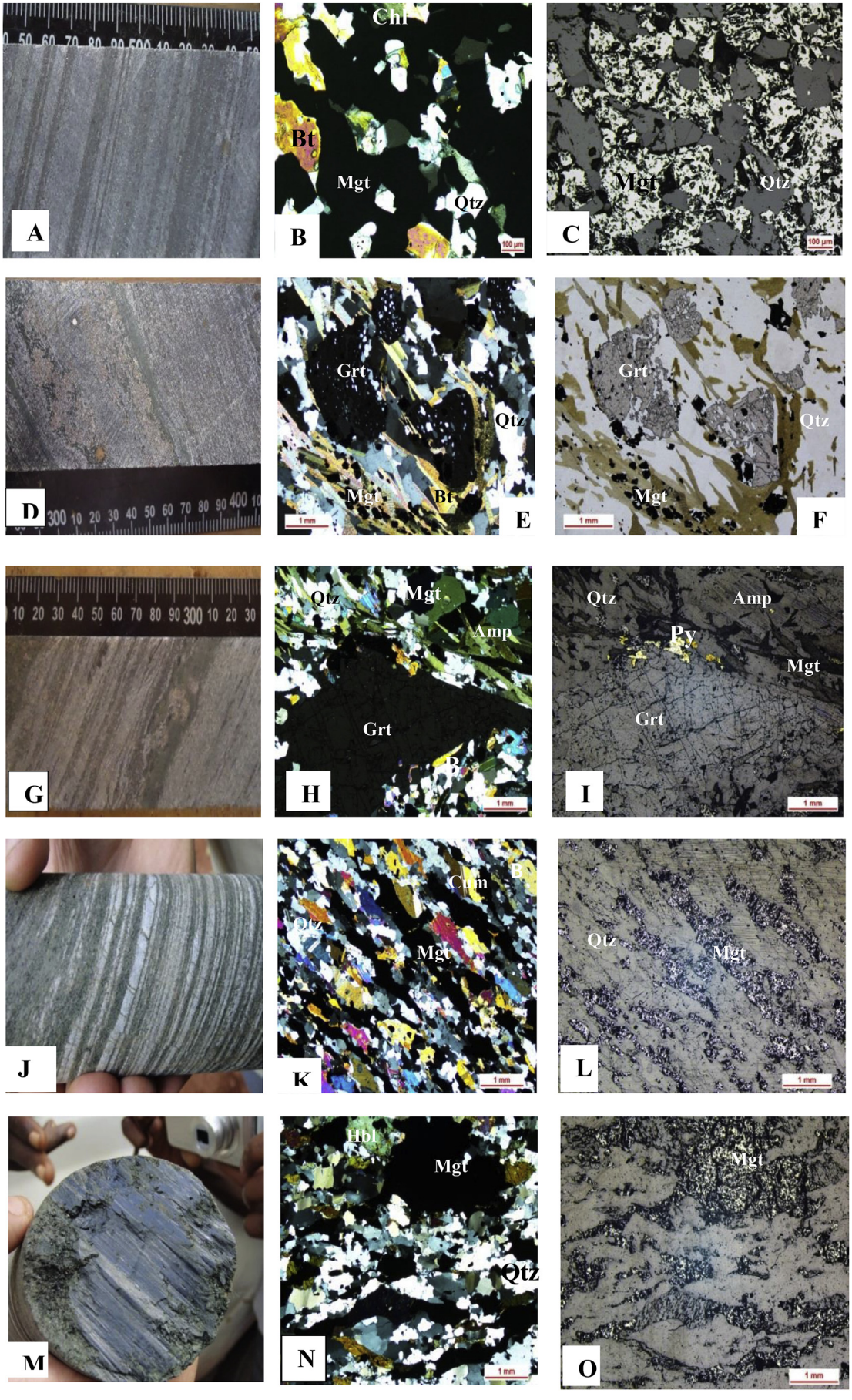

(caption on next page)

Fig. 4. Hand specimen (A,D,G, J, M) and photomicrographs (B, E, H, K, N: transmitted light and C, F, I, L, O: reflected light) of metamorphosed BIFs: core photos of magnetite-rich BIF (A); garnet-biotite BIF (D); garnet-amphibolite BIF (G); amphibole BIF (J & M); Photomicrograph showing granoblastic microstructure and mineral assemblage of magnetite - BIF (B & C), garnet-biotite BIF (E & F), garnet-amphibolite BIF (H & I); cummingtonite BIF(K, L) and hornblende BIF (N, O).

collected from an interlayer of gneiss (Fig. 4D). The rock is dark-grey in colour and medium-to coarse-grained. The garnet-biotite gneiss samples are rich in garnet, and show gneissic structure in hand specimen with alternating millimetric quartzo-feldspathic and mafic minerals layers (Fig. 3D). Under a microscope, garnet-biotite gneiss display heterogranular and granoblastic microstructure, composed of quartz (30–35%), garnet (25–30%), biotite (20–25%), K-feldspar (5–10%) and magnetite (2–5%).

Large euhedral to subhedral crystals of garnet porphyroblasts with average size of 0.20 mm are rich in fine-grained quartz, and biotite inclusions (Fig. 3E and F). The garnet is surrounded by a foliated matrix of secondary chlorite, biotite and quartz (Fig. 3F). It exhibits smooth curved interlocking grain boundaries with quartz and biotite. Garnet porphyroblasts are associated with quartz, K-feldspars and biotite crystals.

Quartz is the most abundant minerals and displays variable grain sizes. It occurs as coarse to fine-grained subhedral to anhedral crystals and also exhibits granoblastic texture. Some quartz grains are ribbon with undulose extinction, a deformational feature indicative of re-crystallization, while others are undeformed. Quartz also exhibits interlocking curved grain boundaries at contact with other neighbouring crystals.

Anhedral to subhedral biotite crystals occur as flakes of various dimensions (0.05–0.08 mm) and orientations, some of which are partially altered to light greenish blue chlorite (Fig. 3F). Biotite crystals are commonly medium-to coarse-grained and occur as individual grain in a foliated matrix. It exhibits interlocking grain boundaries with quartz grains, some of which are straight while others are smoothly curved.

K-feldspar porphyroblasts are about 0.125 mm in size, and are often in association with quartz, biotite and garnet.

Magnetite crystals are euhedral to subhedral, coarse to medium (0.025 mm) grained. Magnetite is the main Fe-oxide mineral component of garnet-biotite gneiss and is associated with quartz, biotite and garnet.

4.1.1.3. Garnet-magnetite micaschist. This rock is medium to coarse-grained with schistose structure in hand specimens (Fig. 3G). It consists mainly of biotite (20–25%), garnet (15–20%), magnetite (20–25%), quartz (10–15%), and secondary chlorite (01–03%). The garnet-magnetite micashist displays heterogranular and granoblastic microstructure under the microscope (Fig. 3E and F).

Garnet porphyroblasts show micro-fractures due to deformation and display disseminated fine-grained (0.20 mm) quartz inclusions that developed in microcracks (Fig. 3I). Euhedral to subhedral garnet porphyroblasts exhibit interlocking grain boundaries with quartz and biotite as neighbouring crystals. The garnet porphyroblasts are often surrounded by a schistose matrix that mainly consists of chlorite, biotite and quartz minerals. Garnet crystals are associated with biotite, magnetite and quartz.

Anhedral to subhedral biotite crystals (0.60 mm) are partially to completely alter to light-green chlorite minerals. Individual biotite crystals are commonly medium-to coarse-grained in sizes with the long axis of biotite flakes defined a direction parallel to schistosity. Biotite is associated with quartz, magnetite and garnet, and shows interlocking grain boundaries with quartz and garnet.

Quartz grains are subhedral to anhedral and mostly medium to coarse-grained (0.1–0.8 mm) with wavy extinction. They are often associated with biotite, magnetite, and garnet. Granoblastic texture of quartz mainly occurs as recrystallized mineral aggregates with equiangular triple points. They exhibit interlocking curved grain boundaries at contacts between neighbouring minerals. Quartz is associated with biotite, magnetite and garnet.

Magnetite crystals occur as subhedral to anhedral, coarse-to medium-grained (0.025 mm) dominantly showing granoblastic texture. They are mainly surrounded with other coarse-grained minerals and often occur in the interstice of biotite and quartz, showing interlocking grain boundaries. The mineral assemblage of garnet-magnetite micaschist is quartz-garnet-magnetite-biotite, which is consistent with amphibolite grade metamorphism.

4.1.1.4. Pyroxene-biotite gneiss. This rock is medium to coarse-grained with gneissic structure in hand specimen (Fig. 3J). It consists mainly of quartz (25–30%), plagioclase (25–30%), K-feldspars (20–25%), biotite (10–15%), and pyroxene (3–5%). Pyroxene-biotite gneiss displays heterogranular and granoblastic microstructure (Fig. 3K and L).

Quartz grains are subhedral to anhedral and mostly medium to coarse-grained (0.20 mm), dominantly showing granoblastic texture with wavy extinction. Quartz is one of the most abundant minerals in the pyroxene-biotite gneiss assemblages (Fig. 3L), some of which occur as both reduced aggregates and individual grains. These grains exhibit interlocking grain boundaries at contacts between neighbouring minerals, such as biotite, pyroxene, and plagioclase.

Biotite crystals (0.23 mm) occur as flakes with infilled cleavages parallel to their long axes. Equigranular fine-grained biotite, quartz and pyroxene disseminatedly surround the rims of biotite porphyroblasts with intergrowth (Fig. 3K). Biotite is associated with quartz, plagioclase and pyroxene crystals.

Plagioclase occurs as large to small subhedral to anhedral grains, commonly showing granoblastic texture (Fig. 3L). Pyroxene (Clino- and orthopyroxene) crystals are subhedral to anhedral in form and consist of grain size that measures up to 0.14 mm. Large subhedral pyroxene crystals present inclusions of quartz. The pyroxene crystals are commonly altered into amphibole/chlorite (Fig. 3K).

K-feldspars porphyroblasts display subhedral to euhedral grain forms with average grain-size of 0.19 mm. They are in association with biotite, quartz and pyroxene.

4.1.2. Banded iron formations (BIFs)

BIF commonly displays alternating micro (1–5 mm) - to meso (1–1.5 cm)-bands of Fe- and Si-rich layers. The iron-rich bands are mainly composed of iron oxides (magnetite with minor hematite) and silicate minerals (chlorite, garnet and biotite), whereas the Si-rich bands are mainly composed of quartz. Based on the mineral content and composition, metamorphosed BIF at Nkout area have been subdivided into four types, namely magnetite BIF, amphibole BIF, garnet-biotite BIF and garnet-amphibole BIF.

4.1.2.1. Magnetite BIF. The medium to coarse-grained magnetite BIF samples show schistose structure (Fig. 4A) and are composed primarily of quartz (30–35%), magnetite (20–30%), and secondary chlorite (15–20%) and biotite (5%). Heterogranular and granoblastic microstructures prevail in the rock type (Fig. 4B and C).

Quartz is one of the most abundant mineral in the magnetite-bearing BIF assemblage with variable grain sizes. It is medium to coarse grained (average 0.25 mm) which locally exhibits undulose or wavy extinction and recrystallization. Quartz grains occur as large to small subhedral to anhedral crystals dominantly showing granoblastic texture and exhibits curved interlocking grain boundaries. Fine magnetite grains (0.02 mm) occur as inclusions in quartz porphyroblasts.

Magnetite is the main iron mineral of the Nkout metamorphosed magnetite BIF and occurs in both magnetite-rich bands and silica-rich bands (Fig. 4C). Magnetite occurs as large subhedral to anhedral grains

dominantly showing granoblastic texture. Magnetite exhibits an interlocking grain texture with curved grain boundaries. These grains are distributed uniformly and are interconnected to form aggregates of different sizes. It occurs around quartz and other mafic minerals (Fig. 4C).

Chlorite minerals are anhedral to subhedral crystals (average grain size 0.13 mm) which are light-green with schistose structure (Fig. 4B). They are commonly surrounded by magnetite coarse-grained minerals and often occur in the interstices of minerals. Most of the secondary chlorite grains are derived from the alteration of biotite minerals. These grains exhibit interlocking grain boundaries at contacts between neighbouring mineral and are in association with magnetite, biotite and quartz.

The mineral assemblages of magnetite BIF are quartz, magnetite, chlorite and biotite, consistent with amphibolite facies metamorphism.

4.1.2.2. Garnet-biotite BIF. The garnet-biotite BIF are medium to coarse-grained foliated rocks (Fig. 4D), composed of quartz (30–35%), magnetite (20–30%), garnet (15–20%), biotite (10–15%), and chlorite (0–5%). They display heterogranular and granoblastic microstructure (Fig. 4E and F).

Biotite occurs as flakes of various dimensions and also forms euhedral inclusions in garnet (Fig. 4E). Subhedral to anhedral biotite crystals (0.16 mm) display magnetite and quartz inclusions (Fig. 4F). Fine-grained magnetite (0.04 mm) inclusions occur in biotite porphyroblasts. Biotite aggregates surround and occur at the rims of garnet porphyroblasts. Biotite grains show interlocking grain boundaries at contacts between garnet and quartz, some of which are smoothly curved surfaces whereas others are straight.

The garnet crystals occur as euhedral to subhedral porphyroblastic grains that measure up to 0.23 mm in size, and are surrounded by a foliation matrix made up of magnetite, biotite and quartz minerals (Fig. 4E and F). Garnet porphyroblasts (0.23 mm) contain mineral inclusions of magnetite and quartz some of which are within developed microfractures. Garnet exhibits interlocking curved grain boundaries.

Quartz is one of the main components in the biotite-garnet BIF, as occurs as euhedral or subhedral, fine grained (0.2 mm) crystals. Most of the quartz grains show wavy extinction (Fig. 4E and F) which is indicative of micro-deformation and recrystallization. Quartz in biotite-garnet BIF occurs as both aggregates with equiangular triple points and individual grains, exhibiting curved grain boundaries commonly showing granoblastic texture.

Magnetite is the main Fe-oxide mineral component of garnet-biotite BIF. It is subhedral to anhedral, exhibiting both individual grains and aggregates which are disseminated with the rims of garnet, and as inclusions within the biotite porphyroblasts (Fig. 4F). Magnetite grains (0.24 mm) exhibit curved rough to smoothly interlocking grain boundaries, and dominantly exhibit granoblastic texture. Some magnetite crystals occur as interstitial aggregates in coarse-grained quartz and garnet.

Secondary chlorite flakes (0.16 mm) result from alteration of biotite. The mineral assemblages of garnet-biotite BIF is quartz, magnetite, garnet and biotite.

4.1.2.3. Garnet-amphibole BIF. Garnet-amphibole BIF samples were collected from the contact between gneiss and BIF. The garnet-amphibole rich BIF is medium to coarse-grained foliated rock (Fig. 4G). It is composed of quartz (30–55%), magnetite (20–25%), garnet (10–15%), amphibole (10–15%), and biotite (5–10%). It is heterogranular and granoblastic in microstructure (Fig. 4H and I).

Garnet is one of the main mineral components at the low unit of Nkout metamorphosed BIF. It shows dominantly granoblastic texture. Garnet porphyroblasts (0.42 mm) are anhedral to subhedral in shape, rich in quartz inclusions, embedded in biotite, quartz and amphibole foliated matrix. Garnet crystals show typical microstructures produced through brittle deformation, with two phases of micro-cleavages that are typical on garnet porphyroblast crystals. These microcracks are at right angle to each other. The first generation of micro-cleavages is parallel to the foliation matrix (biotite and quartz) which is parallel to the direction of maximum elongation. The second phase of micro-cleavages is characteristically shorter, and is at right angle to the former. The micro-cleavages are generally restricted to the garnet crystals only, and propagation into the surrounding foliated matrix is not evident. The majority (50–60%) of the garnet crystals show intense fragmentation, although a few crystals remained intact which are the late stage crystallization.

Quartz is the most ubiquitous minerals in all the occurrences, although the proportions and grain sizes are highly variable. Quartz crystals are euhedral or subhedral (0.24 mm), dominantly showing a granoblastic texture. Quartz occurs as disseminated inclusions within the garnet porphyroblasts (Fig. 4H and I). Some quartz grains show wavy extinction and recrystallization.

Biotite occurs as fine to coarse subhedral to anhedral grains, dominantly showing an inequigranular granoblastic texture (Fig. 4H and I). Some of the biotite grains are partially altered to chlorite. Subhedral biotite crystals (0.21 mm) are associated with biotite, magnetite, garnet and quartz. Biotite grains exhibit textural interlocking curved grain boundaries.

Magnetite is the main Fe-oxide mineral components of garnet-amphibole-rich BIF. It occurs as subhedral to anhedral aggregate disseminated with the rim of garnet and interstitial aggregates in coarse-grained garnet (Fig. 4I). Magnetite grains (0.22 mm) exhibit curved interlocking grain boundaries which dominantly show granoblastic texture.

Sulfides in the Nkout metamorphosed BIF are composed of pyrite. Pyrite is light-yellow and is commonly surrounded by coarse-grained garnet, amphibole and quartz minerals and often occurs in the interstitial spaces. Pyrite occurs as subhedral to euhedral and displays smoothly curved contacts with the other minerals (Fig. 4I).

The garnet-amphibole BIF shows amphibolite facies mineral assemblages composed of quartz, garnet, amphibole and biotite.

4.1.2.4. Amphibole BIF. The amphibole-rich BIF consist of two types namely; cummingtonite-rich BIF and hornblende-rich BIF.

Cummingtonite-rich BIF shows foliated structure and is medium to coarse-grained with alternating millimetric to centimetric iron and siliceous layers (Fig. 4J). It is composed of magnetite (30–35%), cummingtonite (30–35%), quartz (20–30%), and biotite (0–5%).

Quartz occurs as large subhedral to anhedral grains (0.24 mm), dominantly showing granoblastic texture (Fig. 4K and L). Most quartz grains are recrystallized, displaying wavy extinctions and exhibiting inequigranular texture (Fig. 4L). It occurs mainly as both aggregates and individual grain and exhibits interlocking grain boundaries. Quartz grain occurs as interstitial aggregates in coarse-grained cummingtonite parallel to the long axes of mineral foliation. Their pronounced deformational features are indicative of dynamic recrystallization.

Biotite crystals are partially altered to chlorite with an average grain size of 0.16 mm and are associated with quartz, cummingtonite and magnetite.

Cummingtonite crystals occur as large to small subhedral to anhedral grains, dominantly showing granoblastic texture. Cummingtonite is one of the main components that occurs mainly as individual grains, associated with biotite, magnetite and quartz. It exhibits smooth curved grain boundaries showing elongated coarse to medium grains. The long axes of recrystallized cummingtonite aggregates defined a stretching lineation which is parallel to the direction of foliation.

Magnetite occurs in both Fe-rich bands and quartz-rich bands as grains and aggregates (Fig. 4K and L) with subhedral to anhedral shape ranging from 0.21 mm to 0.30 mm in size exhibiting granoblastic texture. Their grain boundaries with other minerals are straight to smoothly curved. Magnetite grains also occur as interstitial aggregates in coarse-grained quartz and cummingtonite bands. Magnetite is often

associated with quartz, cummingtonite and biotite. Cummingtonite BIF shows amphibolite grade mineral assemblage consisting of quartz, cummingtonite, magnetite and biotite.

Hornblende-rich BIF is a medium to coarse-grained foliated rock (Fig. 4M) composed of quartz (20–30%), magnetite (25–30%), hornblende (20–25%) and biotite (10–15%). This rock displays heterogranular and granoblastic microstructure (Fig. 4N and O).

Biotite flakes occur in various dimensions and are anhedral to subhedral commonly showing granoblastic texture. Grain boundaries are straight to smoothly curved with other minerals (Fig. 4N). Biotite is associated with quartz, magnetite and hornblende.

Magnetite occurs in both magnetite-rich bands and quartz-rich bands as either individual grains or as aggregates. It occurs around quartz and other mafic minerals, and exhibits interlocking grain boundaries with other minerals that are smoothly curved (Fig. 4O). Magnetite grains (0.1 mm) occur as inclusions in quartz and biotite porphyroblasts.

Quartz is the main component in the hornblende-rich BIF, and shows both aggregates with equiangular triple points. Quartz grains display undulose extinction and curved to smooth interlocking grain boundaries.

With average grain size of 0.13 mm, hornblende crystals are subhedral. They exhibit interlocking grain boundaries at contacts between neighbouring minerals such as quartz and magnetite.

Hornblende-rich BIF shows amphibolite facies mineral assemblage which consists of quartz, hornblende, magnetite and biotite.

4.1.3. Ore types

Nkout iron ore can be broadly divided in to five field categories namely; lateritic (indurated) ore type, goethite-martite (soft) ore type, hematite in breccias (brecciated) ore type, Magnetite/heamatite (massive) ore type and quartz-martite/magnetite (hard laminated) metamorphosed BIF.

4.1.3.1. Laterite ore type. Laterite ore type is found mostly at the surface of the study area. It blankets the iron ore deposit and occur in 5–15 m thickness from surface. It is the weathering and erosion products of earlier formed laminated and massive ores which contained hard to friable material in nature. Laterite ore is reddish brown to brownish iron oxides composed mainly of goethite (Fig. 5A).

4.1.3.2. Goethite-martite ore type. The most important ore in Nkout is the laminated (vuggy) ore in the weathering zone and which is formed by the removal of gangue minerals. This ore type is soft laminated ore. Individual lamellae measures from a few millimeters to centimeters in thickness and is highly porous and fragile (Fig. 5B).

4.1.3.3. Hematite in breccias type. The Nkout deposit hosts fault breccias and fault related hydrothermal breccias that are characterised by fine hematite and medium to coarse-grained structure (Fig. 5C). This ore type is moderately porous and permeable. The possibilities for the origin could either be (i) Lump breccia of un-oxidized hematite BIF that underwent mechanical fracture and transportation into the zone of high oxidation with a “powdery” iron oxide that consolidated them; (ii) The metamorphosed BIF might have occurred at fault zone thus representing a fault breccia (Fig. 5C).

4.1.3.4. Magnetite/heamatite ore type. Magnetite/heamatite ore is massive, compact and dense with packed hematite minerals and appear to be the precursor of martite ore. The ore is generally dark grey iron (Fig. 5D and E). In this type of ore, hematite crystals are fine grained and tightly packed forming a compact mass (Fig. 5E).

4.1.3.5. Quartz-martite/magnetite ore type. The high-grade iron ore in Nkout is hosted in quartz-martite (i.e. hematite pseudomorphs after magnetite) metamorphosed BIF. The un-oxidized metamorphosed BIF is observed below the weathering front, characterised by alternating bands/laminations with quartz. The thickness of an individual band, however, varies between few millimeters and 10 cm and does not extend more than 30 m before they pinch and merge with other bands (Fig. 5F, G, 5H, 5I, 5J).

4.2. Lithostratigraphy

This section presents the lithostratigraphy of Nkout iron ore deposit. It is subdivided into three main prospects namely; Nkout East, Nkout Centre, and Nkout West. The detailed logging of 9 representative boreholes enabled us to identify all the mappable members and units of the entire Nkout deposit. The members are (i) metamorphosed banded iron formation (BIF) or iron-rich member and (ii) gneissic country rock or gneissic member. These units are distinguished by the mineral abundance and metamorphic grade. The iron formation dips approximately 50–65° to the north while gneiss formations display a sharp transition to gradational contact with the iron-rich member, and form both footwall and hanging wall of the deposit. The gneissic member is typically foliated and directly in association with the iron-rich member in the stratigraphy.

4.2.1. Nkout west prospect

This section is based on the results of three representative drill holes (WH3, WH4, WH8) selected from 52 completed diamond drill holes at Nkout West prospect. The depths of the different holes are 459 m, 527 m, 80 m respectively for WH3, WH4, and WH8.

4.2.1.1. Iron formation member. The iron formation member has different thicknesses that vary from one hole to another. The first interception of iron formation is located at depth of 85 m below surface. The total thicknesses along section vary between 85-467 m and 111–510 m (WH3, WH4), with the largest thickness being ~ 400 m (Fig. 6A). It is composed of three lithological units on the mineral abundance basis. These units include magnetite-bearing iron unit, garnet and biotite-bearing iron unit, and garnet and amphibole-bearing iron unit.

The magnetite-bearing iron unit is distinguished from the other units by the magnetite abundance. It is found at sharp hanging wall contact with biotite-bearing gneiss unit and has an overall thickness of 236 m. The magnetite-bearing iron unit is coarse to medium-grained, with less or limited lateral extension and composed mainly of quartz, iron oxide (magnetite, hematite) and chlorite.

The garnet and biotite-bearing iron unit is rich in biotite and garnet. It is medium to coarse-grained rock unit, (dark grey in colour rock, and located at various depths of the deposit stratigraphy), which lies between the magnetite-bearing unit and garnet and amphibole-bearing BIF unit at various intervals. This unit is found at the footwall contact which is made up of garnet and biotite-bearing gneiss of the gneissic member and is in sharp contact with the biotite-bearing gneiss at the bottom of the iron-member.

Garnet-amphibole-bearing iron unit and amphibole-bearing iron unit are found at the footwall contact of the footwall of gneissic members. They are medium to coarse-grained rocks, dark grey in colour. They show foliation similar to that of garnet and biotite iron unit. These units are overlaid by the garnet and biotite-bearing unit with a sharp contact.

4.2.1.2. Gneissic formation member. Gneiss at the hanging wall was intercepted just below the lateritic surface (at varying depth of 5–16 m) while the footwall contacts were intercepted at 412 m and 510 m respectively at different holes (WH3, WH4). Minor intercalations (1–5 m) were intercepted at various depths, 250 m and 390 m. The total gneissic formation thicknesses along section vary between 85 m and 111 m (WH3, WH4), with the largest thickness being ~120 m

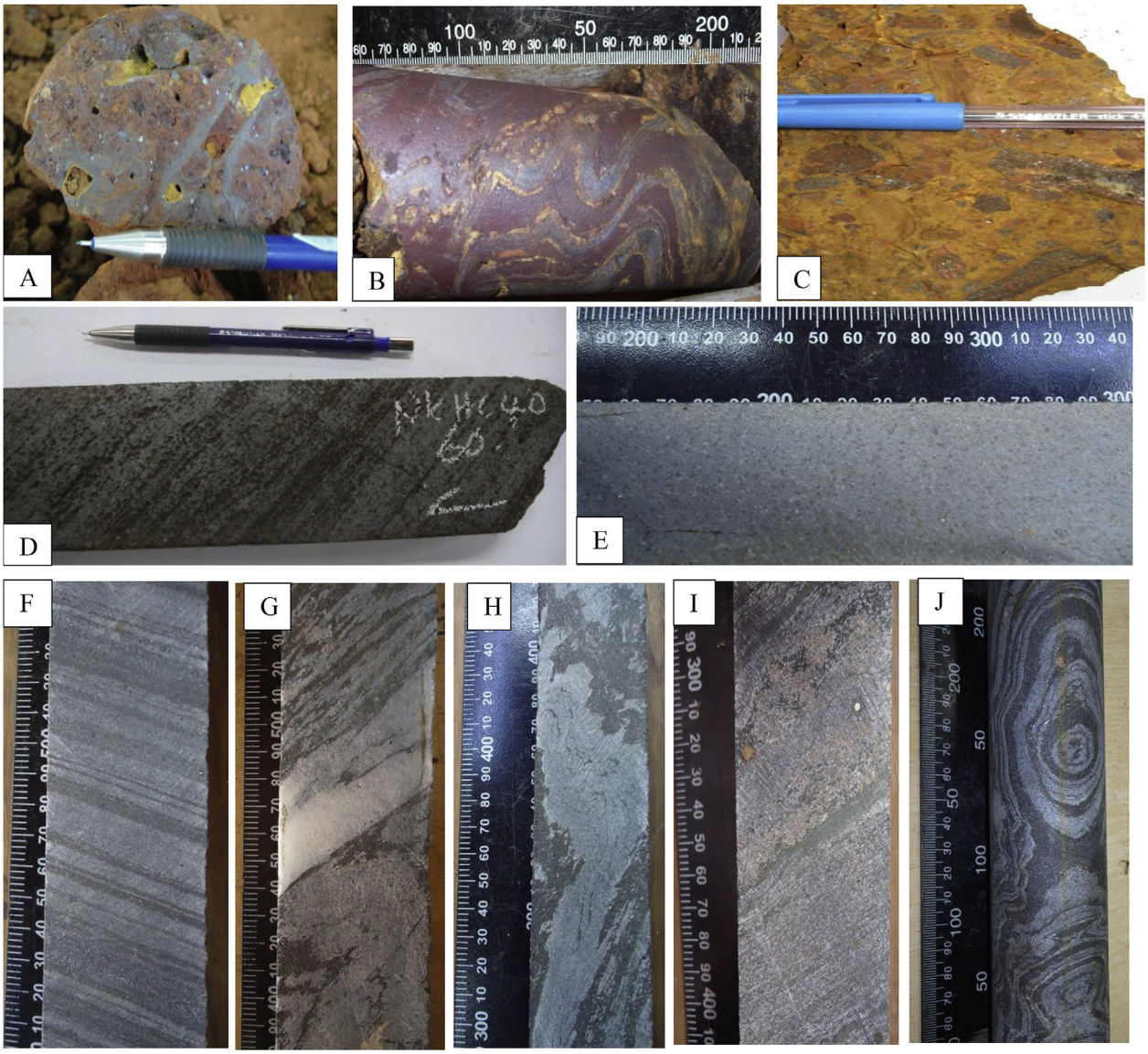

Fig. 5. Field photographs of Nkout drill core showing: (A) ferrigenous lateritic ore (indurated); (B) Heamatite-quartz with preserved banding (friable soft); (C) Quartz-hematite breccia (fault breccias); (D) magnetite-quartz ore (biscuity); (E) Hematite ore (massive); (F) Compositional laminated metamorphosed BIF; (G) Distorted band quartzite intercalation; (H) Irregular banded BIF bearing amphibole; (I) diffused banding bearing garnet; (J) Folded magnetite BIF.

(Fig. 6A). The gneissic formation member is composed of three main units (biotite-bearing gneiss unit, garnet-magnetite-bearing micaschist unit and garnet-bearing gneiss unit).

The biotite-bearing gneiss unit is a medium to coarse-grained foliated rock unit, generally leucocratic, which forms sharp contact between the iron-rich members, occupying both footwall and hanging wall contact. It is overlain by lateritic layer and is underlain by the magnetite-rich iron unit of the lower layer in the stratigraphy. This unit occupies a total depth of 110 m in the stratigraphy and is intercepted at the interval depths ranging from 7.6 m to 111 m, 192 m–200 m, and 510 m to 527 m. The mineral assemblage is mainly made up of biotite, quartz and feldspars, which is consistent with amphibolite facies metamorphism.

Garnet-magnetite-bearing micaschist unit is medium to coarse-grained rock unit, characterising a transitional boundary between the iron-rich member and the biotite-rich gneiss unit on the footwall sharp contact. It is intercepted at depth of 379 m–412 m, occupying a total interval of 32 m in the stratigraphic column and is sandwiched between garnet-biotite iron unit and the biotite-rich gneissic unit.

The garnet-bearing gneiss is in sharp contact between the iron-rich members and occupies the footwall of the deposit. This unit is medium to coarse-grained, with gneissic foliation characterised with alternation of grey and dark bands.

The stratigraphic relationship between the iron-rich member and the country rock (gneiss) lithologies is shown on the lithostratigraphic section (Fig. 6A) of the entire Nkout-West prospect and on the AA cross section (Fig. 6B).

4.2.2. Nkout centre prospect

This section is based on the result of three representative drill holes (CH4, CH7 and CH24) selected from 110 completed diamond drill holes at Nkout Centre. The depths of the different holes are 440 m, 540 m, 80 m respectively (Fig. 7A). Fig. 7B presents the Nkout Centre lithological section (BB' cross-section in Fig. 2).

4.2.2.1. Iron formation member. The iron member of the Nkout Centre prospect shows different thicknesses. It was initially intercepted at the depths of 76 m below surface on CH7 and 112 m on CH24. The total iron formation thicknesses across the section vary between 85 - 390 m and 112–400 m respectively, with the largest thickness being ~400 m

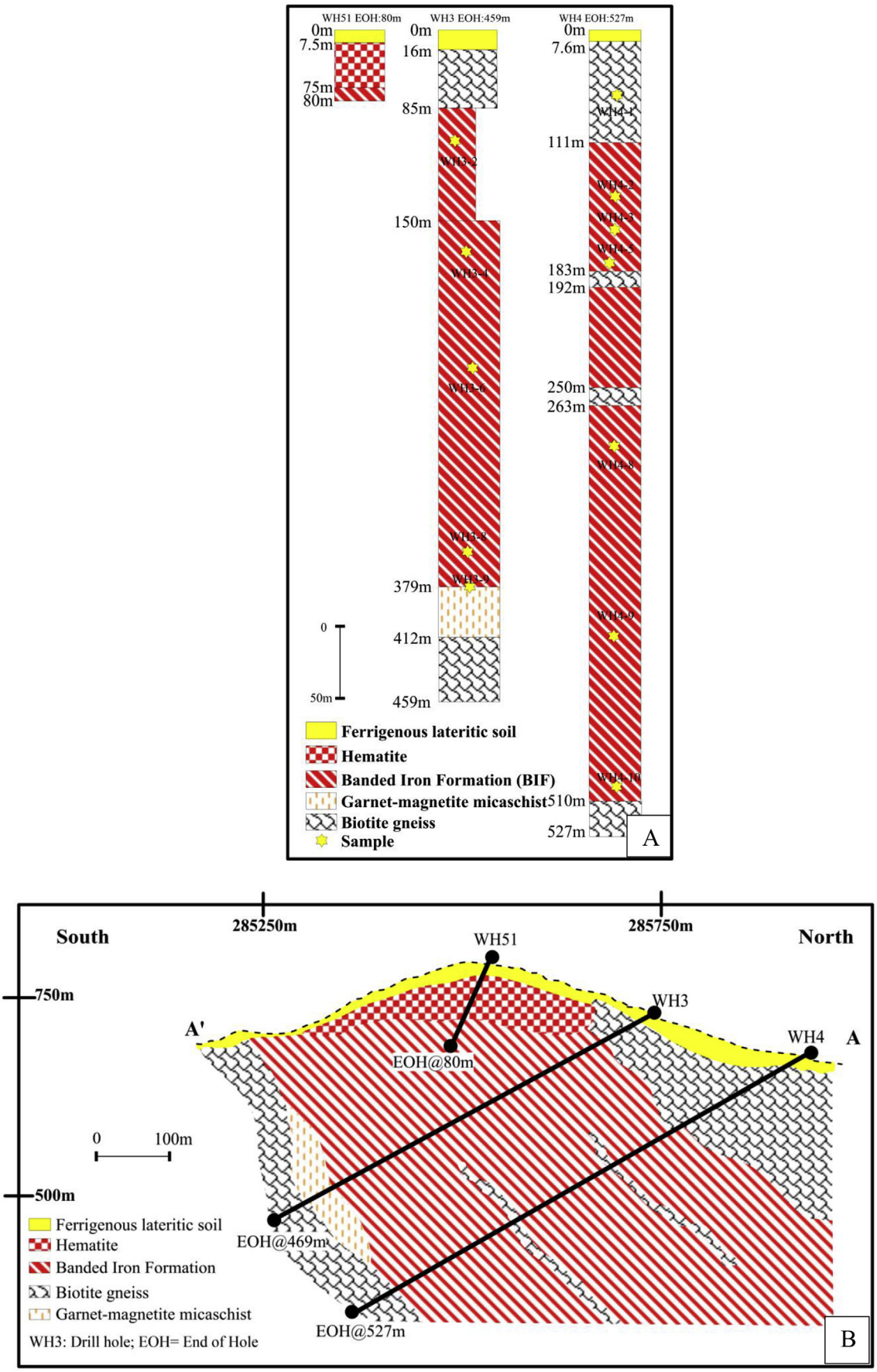

Fig. 6. A) Stratigraphy log of Nkout-West deposit (A-A′ in Fig. 2) with sample location; B) Geological S-N (dip) cross-section (A-A′ in Fig. 2) of Nkout-west deposit (looking west).

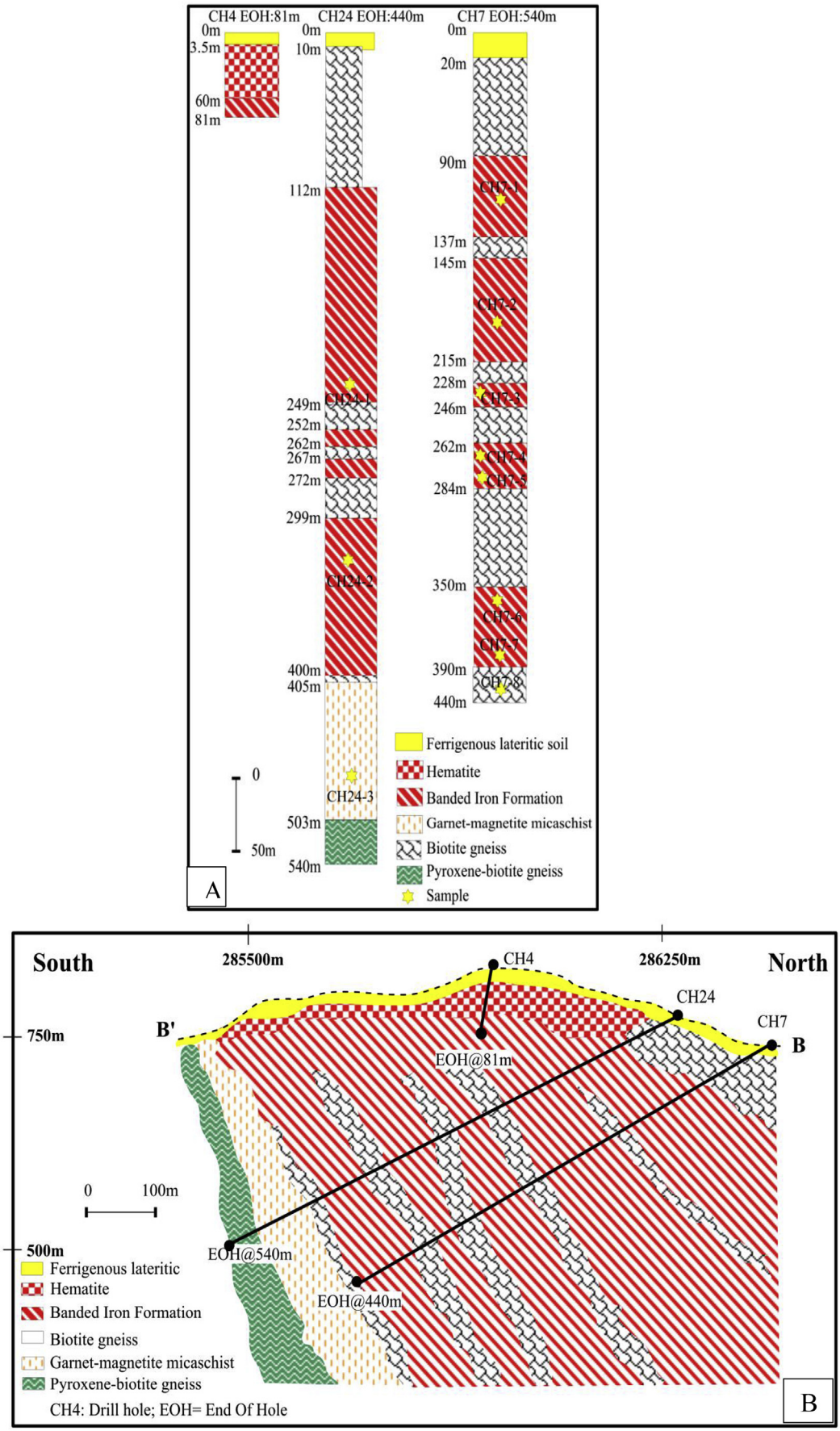

Fig. 7. A) Stratigraphy log of Nkout-Centre deposit (Centre B-B′ in Fig. 2) with sample location; B) Geological S-N (dip) cross-section (B-B′ in Fig. 2) of Nkout-Centre deposit (looking west).

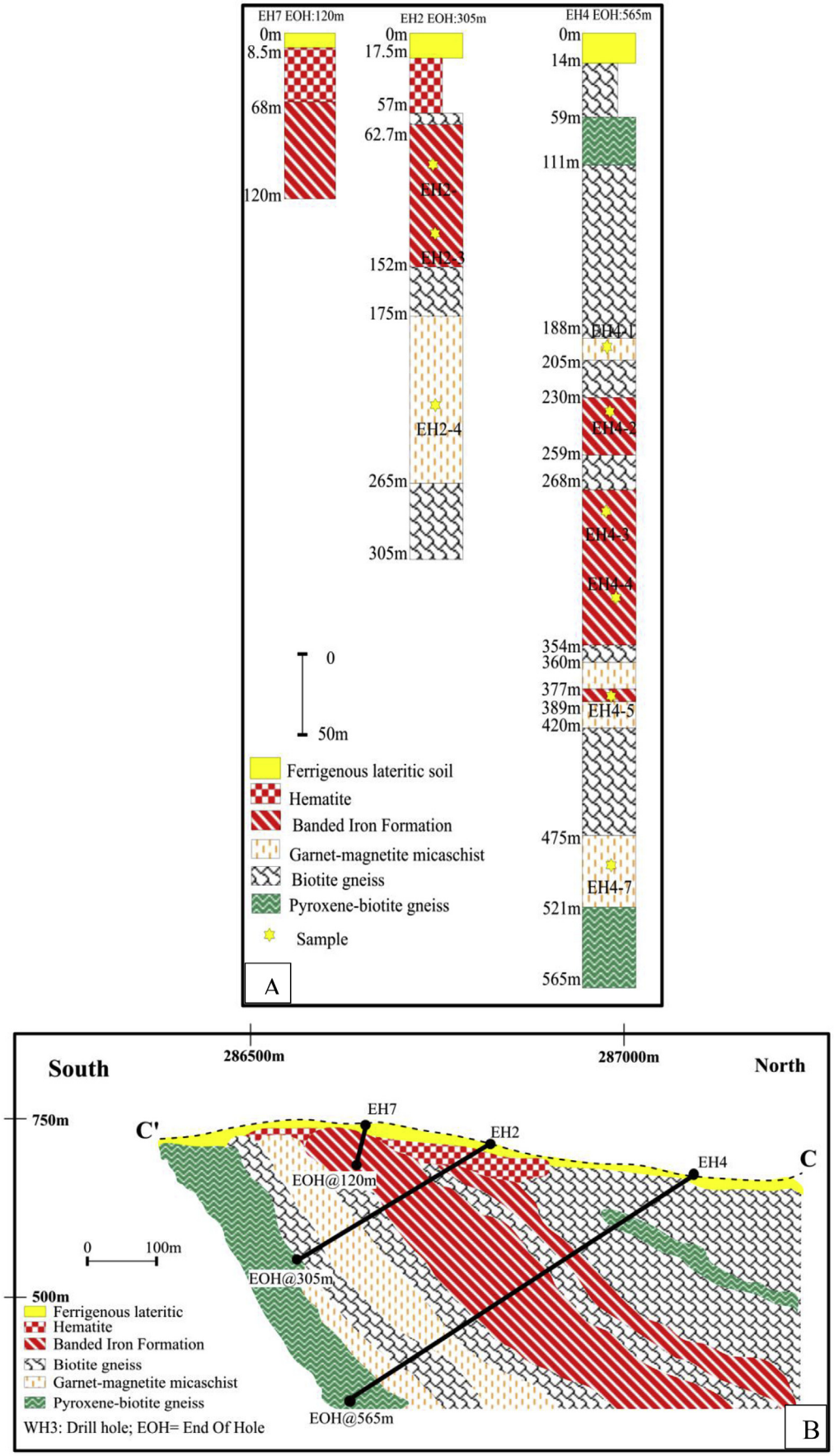

Fig. 8. A) Stratigraphy log of Nkout-East deposit (C-C′ in Fig. 2) with sample location; B) Geological S-N (dip) cross-section (C-C′ in Fig. 2) of Nkout-East deposit (looking west).

Table 1
Major elements geochemical composition (%) and elemental ratio of Nkout West BIFs.

Major element	Nkout -West										
	Garnet-amphibole BIF		Garnet-biotite BIF			Magnetite BIF					
	WH3-8	WH3-4	WH3-6	WH3-9	WH4-3	WH4-5	WH4-8	WH4-9	WH4-10	WH3-2	WH4-2
Fe_2O_3	23.9	29.2	31.5	32.7	38.1	50.4	55.5	49.3	57.4	41.9	55.3
SiO_2	58.3	56.4	52.5	54.5	50.8	45.5	40	39.6	42.5	52.5	38.8
Al_2O_3	10.8	8.6	9.54	7.25	5.33	0.72	0.82	0.13	0.17	1.65	0.7
CaO	2.03	1.27	1.94	0.68	1.25	1.04	1.35	0.33	1.04	1.7	1.68
MgO	3.3	2.41	2.2	2.17	2.89	3.04	2.48	7.56	1.52	2.14	2.18
Na_2O	1.18	0.1	0.2	0.32	0.22	0.07	0.07	0.02	0.02	0.17	0.07
K_2O	1.89	2.77	3.05	2.79	2.3	0.29	0.15	0.03	0.02	0.1	0.13
Cr_2O_3	0.02	0.03	0.02	0.02	0.01	< 0.01	< 0.01	< 0.01	< 0.01	< 0.01	< 0.01
TiO_2	0.35	0.28	0.26	0.21	0.17	0.03	0.03	< 0.01	< 0.01	0.06	0.02
MnO	0.09	0.28	0.25	0.13	0.17	0.09	0.11	0.03	0.08	0.07	0.12
P_2O_5	0.25	0.06	0.1	0.08	0.1	0.03	0.11	0.07	0.09	0.12	0.12
LOI	−0.2	−0.11	−0.15	0.11	0.58	−1.1	−1.29	0.17	−1.39	−0.83	−1.07
Fe/Ti	68.3	104.3	121.2	155.7	224.1	1680	1850	4930	5740	698.3	2765
Si/Fe	2.44	1.93	1.67	1.67	1.33	0.9	0.72	0.8	0.74	1.25	0.7
Al/Ti	30.86	30.71	36.69	34.52	31.35	24	27.33	13	17	27.5	35
Fe/Al	2.21	3.40	3.30	4.51	7.15	70.00	67.68	379.23	337.65	25.39	79.00
Si/Al	5.4	6.56	5.5	7.52	9.53	63.19	48.78	304.62	250	31.82	55.43
K/Na	1.6	27.7	15.25	8.72	10.45	4.14	2.14	1.5	1	0.59	1.86
Na/K	0.62	0.04	0.07	0.11	0.1	0.24	0.47	0.67	1	1.7	0.54
Ca + Mg	5.33	3.68	4.14	2.85	4.14	4.08	3.83	7.89	2.56	3.84	3.86
K + Na	3.07	2.87	3.25	3.11	2.52	0.36	0.22	0.05	0.04	0.27	0.2
Al + Ca	3.22	3.53	1.61	1.38	15.95	14.7	4.45	0.6	2.61	0.59	17.23	3.42

Major element	Nkout-Centre							Nkout-East					
	Magnetite BIF					Garnet-biotite BIF		Magnetite BIF			Amphibole BIF		
	CH7-1	CH7-2	CH24-1	CH24-2	CH24-3	CH7-3	CH7-6	EH4-1	EH4-2	EH4-6	EH2-1	EH2-3	EH2-4
Fe_2O_3	54.5	54.6	52.1	55.1	38.1	28.3	20	43.4	55	79.7	45.2	25.6	47.5
SiO_2	43.1	38.6	40.3	41.9	56	51.8	60.7	49	43	3.26	51.1	51.2	44.7
Al_2O_3	0.16	0.74	1.59	0.13	0.47	8.85	10.8	3.06	0.39	1.76	0.31	10.2	1.43
CaO	2.25	2.08	1.37	1.38	0.8	4.59	0.85	0.29	0.19	0.13	0.25	2.97	1.54
MgO	1.93	2.53	2.03	1.92	5.35	2.85	1.49	1.96	0.33	1.05	2.56	4.72	3.5
Na_2O	0.3	0.21	0.03	0.05	0.06	1.52	0.19	0.2	< 0.01	< 0.01	0.02	1.34	0.07
K_2O	0.08	0.19	0.54	0.05	0.05	0.99	2.86	0.9	< 0.01	0.71	< 0.01	2.72	0.38
Cr_2O_3	< 0.01	< 0.01	< 0.01	< 0.01	< 0.01	0.03	< 0.01	< 0.01	< 0.01	< 0.01	< 0.01	< 0.01	< 0.01
TiO_2	< 0.01	0.02	0.06	< 0.01	0.02	0.33	0.35	0.02	< 0.01	0.15	0.01	0.3	0.04
MnO	0.11	0.13	0.06	0.05	0.16	0.11	0.09	0.05	0.06	0.12	0.19	0.13	0.07
P_2O_5	0.07	0.03	0.12	0.1	0.11	0.18	0.05	0.06	0.11	0.06	0.12	0.09	0.12
LOI	−1.15	−0.93	−0.23	−1.08	−0.43	0.47	1.1	−0.71	−1.6	−2.4	−1.11	1.05	−0.6
Fe/Ti	5450	2730	868.3	5510	1905	85.8	57.1	2170	5500	531.3	4520	85.33	1188
Si/Fe	0.79	0.71	0.77	0.76	1.47	1.83	3.04	1.13	0.78	0.04	1.13	2	0.94
Al/Ti	16	37	26.5	13	23.5	26.82	30.86	153	39	11.73	31	34	35.75

(*continued on next page*)

Table 1 (*continued*)

Major element	Nkout-Centre						Nkout-East					
	Magnetite BIF				Garnet-biotite BIF		Magnetite BIF			Amphibole BIF		
	CH7-1	CH7-2	CH24-1	CH24-2	CH24-3	CH7-3	CH7-6	EH4-1	EH4-2	EH4-6	EH2-1	EH2-3	EH2-4
Fe/Al	340.6	73.78	32.77	423.9	81.06	3.2	1.85	14.18	141	45.28	145.8	2.51	33.22
Si/Al	269.4	52.16	25.35	322.3	119.2	5.85	5.62	16.01	110.3	1.85	164.8	5.02	31.26
K/Na	0.27	0.9	18	1	0.83	0.65	15.05	4.5	1	71	0.5	2.03	5.43
Na/K	3.75	1.11	0.06	1	1.2	1.54	0.07	0.22	1	0.01	2	0.49	0.18
Ca +- 5.04	3.86	4.18	4.61	3.4	3.3	6.15	7.44	2.34	2.25	0.52	1.18	2.81	7.69
K +- 0.45	0.2	0.38	0.4	0.57	0.1	0.11	2.51	3.05	1.1	0.02	0.72	0.03	4.06
Al +- 3.42	2.58	2.79	3.22	3.53	1.61	1.38	15.95	14.7	4.45	0.6	2.61	0.59	17.23

(Fig. 7A). Three litho-assemblage units namely magnetite-bearing iron unit, garnet-biotite-bearing iron unit, garnet-amphibole-bearing iron unit were observed.

The magnetite-bearing iron unit has similar lithological characteristics to that of the West prospect. It is found at sharp hanging wall contact with biotite-bearing gneiss unit and has an overall thickness of 227 m. The garnet-amphibole-bearing iron unit is the least extended of all of the iron-rich units of the Nkout Centre prospect. It displays a fairly consistent pattern of an increased metamorphic grade and is found at depths of 228 m in drill hole CH7 and 252 m in drill hole CH24. The garnet-amphibole-bearing iron unit lies between biotite-bearing gneiss of the gneissic member. It is found at the contact of the footwall of gneissic members in drill hole CH7. It is a medium to coarse-grained foliated rock, dark grey in colour. This unit is intercalated between biotite-bearing gneissic units with a sharp contact in drill hole CH24.

4.2.2.2. Gneissic formation member. Hanging wall gneissic formation member displays sharp contacts with the iron-rich member, which was intercepted below the lateritic surface (at varying depths of 10 m–20 m) while the footwall contacts are intercepted at 390 m and 400 m respectively. Minor intercalations (1 m–10 m) were intercepted at various depths. The total thicknesses along section vary between 220 m and 265 m, with the largest thickness of ~265 m (Fig. 7A). This member is composed of the biotite-bearing gneiss unit, garnet and magnetite-bearing micaschist unit and pyroxene and biotite-bearing gneiss unit.

The biotite-bearing gneiss unit is characterised by the hanging wall in sharp contact between the iron-rich members. This unit is overlain by a lateritic layer which in turn is underlain by magnetite-bearing iron unit. It occupies a total depth of 70 m–100 m respectively and was intercepted at varying depth interval in the drill hole.

The garnet and magnetite-bearing micaschist unit characterised transitional and gradational boundaries between the magnetite-bearing iron unit and the pyroxene and biotite-bearing gneiss unit at the footwall. This unit shows compositional banding marked by magnetite and garnet layer and quartz-rich layer. It is intercepted at depths of 405 m–503 m, occupying a total interval of 98 m in the stratigraphic column.

The pyroxene-biotite-bearing gneiss unit is in sharp contact between the garnet and magnetic unit and characterised the footwall of the deposit. It is a medium to coarse-grained rock unit, with gneissic foliation characterised by the alternation of grey and dark bands. It was intercepted at depths of 503 m–540 m, making a total thickness of 37 m.

The stratigraphic relationship between the hanging and footwalls country rock (gneiss) and the iron-rich member lithologies is shown on the litho-stratigraphic section (Fig. 6A) and on the BB' cross section (Figs. 6B and 2).

4.2.3. Nkout east prospect

Three representative drill holes (EH2, EH4, and EH7) with depths of 305 m, 565 m and 120 m respectively, were selected from about 200 completed diamond drill holes at Nkout East prospect. Detailed logs of these drill holes revealed that the Nkout East prospect has two iron-rich units (magnetite-bearing iron unit and amphibole-bearing iron unit) and three gneissic units.

4.2.3.1. Iron formation member. The first interception of iron formation is located at depth of 62 m below surface (EH2). The total iron formation thicknesses across-section vary between 62 to 152 m and 234–389 m (EH2, EH4), with the largest thickness being ~150 m (Fig. 8A).

The magnetite-bearing iron unit is found at sharp hanging wall contact with biotite-bearing gneiss unit and has an overall thickness of ~80 m. The amphibole-bearing iron unit is found at the contact of the footwall of biotite-bearing gneiss units. This unit is overlaid by biotite-bearing gneiss unit with a sharp contact.

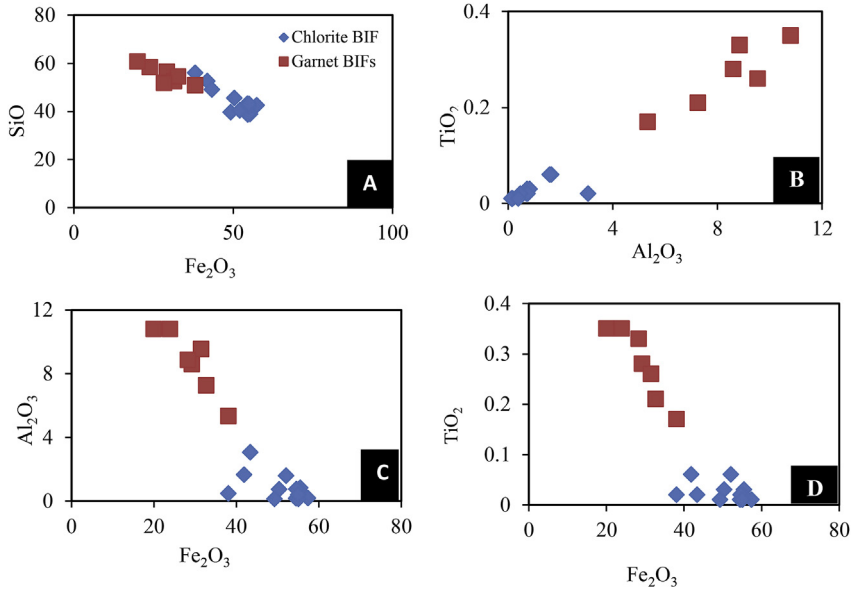

Fig. 9. Variation diagram of Fe_2O_3 and SiO_2 (A), Fe_2O_3 and Al_2O_3 (B), TiO_2 and Al_2O_3 (C), Fe_2O_3 and TiO_2 (D).

Table 2
Pearson's correlation matrix for major element oxides of magnetite-rich BIF.

	Fe_2O_3	SiO_2	Al_2O_3	CaO	MgO	Na_2O	K_2O	TiO_2	MnO	P_2O_5	LOI
Fe_2O_3	1.0000										
SiO_2	**−0.9479**	1.0000									
Al_2O_3	−0.0459	−0.1260	1.0000								
CaO	−0.1576	0.2750	−0.2702	1.0000							
MgO	−0.4507	0.2724	−0.2736	−0.1362	1.0000						
Na_2O	−0.2992	0.3050	0.2129	0.5997	−0.1121	1.0000					
K_2O	0.2356	−0.3947	**0.8874**	−0.3627	−0.2615	0.0940	1.0000				
TiO_2	0.6166	−0.7595	**0.4917**	−0.2615	−0.2657	−0.2224	0.5687	1.0000			
MnO	0.1358	−0.1327	−0.1359	0.3251	−0.0286	0.1871	−0.0945	0.1941	1.0000		
P_2O_5	−0.2183	0.2647	−0.0886	0.0639	−0.1139	−0.3305	−0.3176	−0.0650	−0.0756	1.0000	
LOI	−0.6205	0.5423	−0.0695	0.0700	0.5975	0.0287	−0.0647	−0.3750	−0.2224	−0.2543	1.0000

4.2.3.2. Gneissic formation member. The interception of gneiss formation at the hanging wall is located just below the lateritic surface (at varying depths of 14 m–57 m). The footwall contacts are intercepted at 152 m and 420 m respectively (EH4 and EH2). Minor intercalations (1 m–10 m) were intercepted at various depths, 90 m, and 259 m. The total gneissic formation thicknesses along section vary between 68 m and 270 m, with the largest thickness being ~270 m (Fig. 8A). The Nkout East lithological section is shown on Fig. 8B (CC' cross-section on Fig. 2).

4.3. Major elements geochemistry

The whole rock major element data of Nkout West, Centre and East deposits are presented in Table 1. These results show that Fe_2O_3 and SiO_2 are the main components with contents ranging from 82.2 to 99.9 wt% in the West deposit, 80.1 to 97.6 wt% (Centre deposit) and 76.8 to 98.0 wt% (East deposit), suggesting that they belong to the oxide type BIF (James, 1954). Oxides of Al, Si, and Ti portray a negative gradient with increasing Fe_2O_3 (Fig. 9).

4.3.1. Magnetite BIF

The samples with high content of iron and silica are metamorphosed magnetite-rich BIF in which the two components have values greater than 88.9% (Nkout West), 92.4% (Nkout Centre), and 82.96% (Nkout East). Their Al_2O_3 and TiO_2 contents are relatively low, ranging from 0.13 wt% to 3.06 wt% and from < 0.01 wt% to 0.15 wt% respectively. Four samples (WH3-2, CH24-1, EH1 and EH3) show slightly high Al_2O_3 contents (1.65 wt%, 1.59 wt%, 3.06 wt% and 1.76 wt% respectively) indicating detrital contamination, but their low TiO_2 contents suggest that this contamination was trivial. CaO and MgO contents are slightly high in the three prospects (Nkout West: CaO = 0.33–1.7 wt% and MgO = 1.52–7.56 wt%; Nkout Centre: CaO = 0.8–2.25 wt% and MgO = 1.92–5.35 wt%; Nkout East: CaO = 0.13–0.29 wt% and MgO = 0.33–1.96 wt%), confirming the presence of silicate minerals (chlorite) as also revealed by petrography. The contents of K_2O and Na_2O are strongly depleted in all the three deposits (average = 0.13 wt % and 1.10 wt%, respectively), and below detection limit (0.01) in some samples (EH4-1, EH4-6) The P_2O_5 concentration is low (average 0.085 wt %) in all the magnetite-rich BIF samples.

The relationship between the SiO_2 and Fe_2O_3, reflects a strong negative correlation (r = -0.94; Table 2) between the two components and in an inverse distribution of quartz and iron minerals in the iron-formation.

4.3.2. Garnet-biotite BIF

The SiO_2 content in garnet-biotite BIF samples is high (SiO_2: 50.8–60.7 wt%) while Fe_2O_3 content is relatively low (Fe_2O_3: 20.0–38.1 wt%). The Al_2O_3 contents in garnet-biotite BIF are high, ranging from 5.33 wt% to 10.80 wt%). Similarly, the contents of K_2O and MgO are relatively high (mean = 2.32 wt% and 1.86 wt%, respectively), while low contents are observed in TiO_2 (0.17–0.35 wt%) and P_2O_5 (0.05–0.18 wt%).

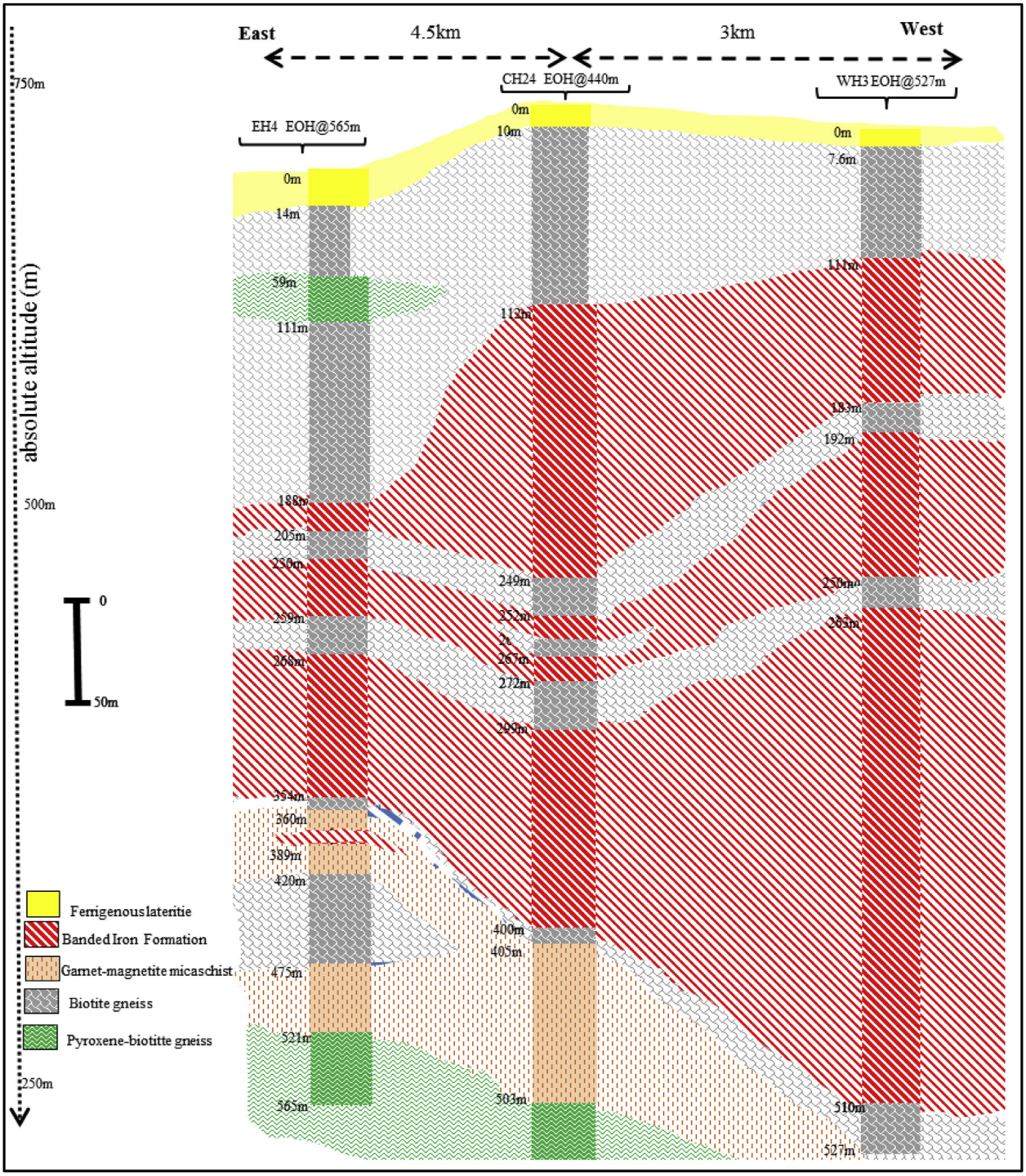

Fig. 10. Stratigraphic correlation of Nkout formation units (boreholes lie along the same N-S line as shown in Fig. 2) showing stratigraphic relationship for the Nkout formations, depositional-dip-oriented subsurface correlation of deposit (boreholes lie along the line shown in Fig. 2).

4.3.3. Garnet-amphibole BIF

The Fe_2O_3 concentration in the garnet-amphibole rich BIF is low (23.90–29.20 wt%) while their SiO_2 and Al_2O_3 contents are high (SiO_2 = 56.40 to 58.30 wt% and Al_2O_3 = 8.60 to 10.80 wt%). CaO (1.27–2.03%), MgO (2.41–3.30%), K_2O (1.89–2.77%) and Na_2O (0.10–1.18%) contents are also high (Table 1). As revealed in the petrographic studies, MgO and CaO contents are probably associated to Mg-Ca-rich amphibole or garnet minerals whereas K_2O and Na_2O are related to feldspar mineral phase.

4.3.4. Amphibole-rich (cummingtonite/hornblende) BIF

The amphibole-rich BIF samples display low Fe_2O_3 concentration, ranging between 25.6- and 47.5 wt%), while their SiO_2 and Al_2O_3 contents are high (SiO_2 = 44.7 to 51.1 wt% and Al_2O_3 = 0.31 to 10.20 wt %). The K_2O and MgO contents are also high (K_2O = 0.01–2.72 wt%, and MgO = 2.56–4.72 wt%) whereas the TiO_2 (0.01–0.3%) and P_2O_5 (0.09–0.12%) contents are low. CaO (0.25–2.97%) and Na_2O (0.02–1.34%) contents are high (Table 1).

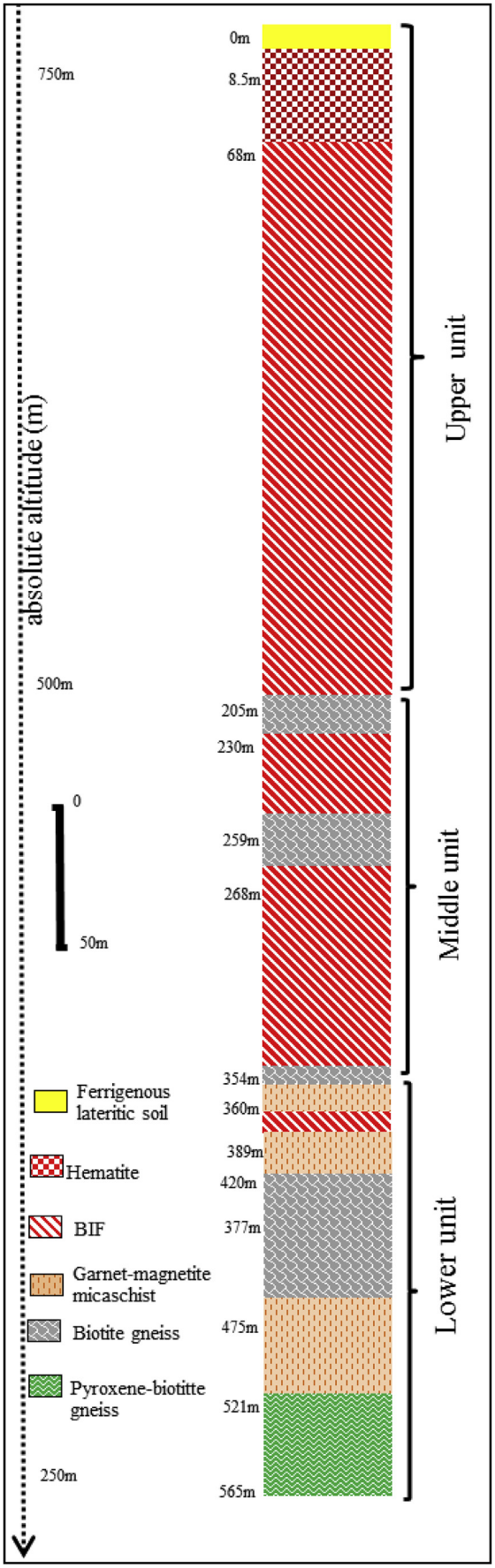

Fig. 11. Synthetic stratigraphy of Nkout iron deposit showing the main lithological units.

5. Discussion

5.1. Stratigraphic correlation and interpretation

Fig. 10 presents the stratigraphic correlation between West, Centre and East deposits. The correlation between rock units in the individual formation is used here to determine the depositional condition in the different parts of the Nkout basin. The litho-stratigraphic correlation was made possible by stratigraphic marker plans such as litho-unit and metamorphic grade. Lateral correlation between the deposits was based on the five BIF units interbedded with gneiss as a lithostratigraphic marker. The low metamorphic grade (greenschist facies) magnetite-rich units occurred at the upper part of the iron member in each of the three deposits. This unit compares well with respect to lithostratigraphy and geochemistry (Table 1). The four mappable gneiss units (biotite-rich gneiss unit, garnet-magnetic gneiss unit and garnet-rich gneiss unit, and pyroxene-biotite unit) are correlated in the individual formation except for the pyroxene-biotite gneiss unit which correlated only in the East and Centre deposits. Also minor intercalations of pyroxene-biotite gneissic unit occurred in the upper part of the East deposit and are not correlated with either West or Centre formations. The biotite-rich gneiss unit correlates in the upper West, Centre and East formations. The garnet-magnetic gneiss unit and garnet-rich gneiss units occurred in the middle of the East formation. The higher amphibolite metamorphic grade occurred in the lithostratigraphically equivalent middle of West and Centre formations, but here it also contains every thin intercalated biotite-rich gneiss unit. The lower pyroxene-biotite unit in the West formation is not taken into account since stratigraphic evidence would suggest that it was not shallow enough and thus did not constitute part of the local depositional sitting.

Lithostratigraphically, there is no marked difference between the garnet-biotite and garnet-amphibole BIF units. The correlation and comparison of the higher metamorphic grade (garnet-biotite BIF units and garnet-amphibole BIF units) of the lower part of the iron member was more meaningful as the individual iron formation units were not time-transgressive in the primary depositional environment. Our discussion and interpretation of data assumed that these units were deposited at the same time. The difference in metamorphic conditions and post depositional fluid flow were probably responsible for the difference in mineralogy between the two units (Nyame et al., 1998). Correlation across the three formations, however, was less uniform, in conjunction with a marked reduction in stratigraphic thickness from the West to the East succession (Fig. 10). The difference in thickness was probably due to the difference in basin morphology. Nevertheless, no part of the deposit had been strongly eroded as every unit remained intact.

The stratigraphic thickness of metamorphosed BIF in the east was less than that in the centre and west deposits. Also, the depth variation in the centre deposit is lower than that of the east and west. The combination of depth and thickness variations in the deposit from east to west indicated a folded synform structure (Fig. 10). Also the thickness variation suggested that either the deposition took place for a longer period of time or that the sedimentary rate was rapid (Beukes, 2004; Klein, 2005). Post-depositional processes have greatly affected the stratigraphic thickening of the deposit. The Nkout stratigraphic thickness is attributed to the later tight folding phase. The post depositional process of ductile to brittle deformation event at Nkout area has therefore affected the morphology of the stratigraphic sequences but the primary thickness resulted from the primary sedimentary pile. The metamorphosed BIF is spatially associated with faults that produce offsets within the sequence.

The presence of only oxide facies (Table 1) iron unit in the entire deposit reflects the syn-sedimentary deposition or diagenetic redox conditions. The oxide thickness variation suggested the variable availability of the chemical constituents (Fe, O_2 and Si) in the different parts of the basin (Klein and Ladeira, 2000; Nelson et al., 1995). Thus the

Table 3
Pearson's correlation matrix for major element oxides of garnet-rich BIF.

	Fe_2O_3	SiO_2	Al_2O_3	CaO	MgO	Na_2O	K_2O	Cr_2O_3	TiO_2	MnO	P_2O_5	LOI
Fe_2O_3	1.0000											
SiO_2	**−0.8646**	1.0000										
Al_2O_3	**−0.9159**	0.7252	1.0000									
CaO	−0.0738	−0.4062	0.1636	1.0000								
MgO	0.2993	−0.3897	−0.2082	0.4794	1.0000							
Na_2O	−0.2695	−0.1067	0.2856	0.8403	0.6349	1.0000						
K_2O	0.0656	0.2870	−0.0035	−0.8573	−0.6778	−0.9266	1.0000					
Cr_2O_3	−0.0207	−0.1848	0.1376	0.5775	0.3010	0.4330	−0.3927	1.0000				
TiO_2	**−0.9331**	0.6611	**0.9163**	0.4015	−0.0448	0.5260	−0.3370	0.2612	1.0000			
MnO	0.4560	−0.3279	−0.2513	−0.1818	−0.0969	−0.5648	0.4868	0.3435	−0.4018	1.0000		
P_2O_5	−0.1812	−0.0582	0.2948	0.6049	**0.8191**	0.8682	−0.7361	0.2542	0.4121	−0.4538	1.0000	
LOI	−0.2398	0.1743	−0.0597	−0.0487	−0.4715	−0.0910	−0.0806	−0.5596	0.1012	−0.4960	−0.3642	1.0000

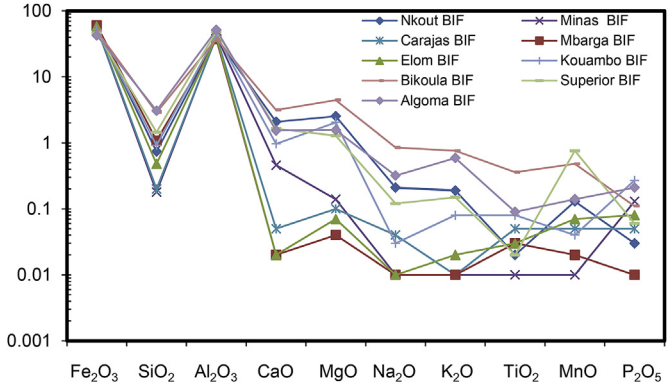

Fig. 12. Spider diagram comparing the major element composition of Nkout metamorphosed BIF with those of Congo craton, Carajas Formation and Quadrilátero Ferrífero (Brazil), Lake Superior-type and Algoma-type BIFs.

correlation of iron formations throughout the three deposits suggests that their deposition took place on a wide basin scale. We therefore propose that the individual formations were deposited contemporaneously in the same basin which implied that the BIF deposition was a basin wide phenomenon.

The synthetic stratigraphy of Nkout basin is divided into three main units, an upper unit, middle unit and lower unit (Fig. 11). The upper unit is about 200 m from surface and consists of oxidized and un-oxidized ore types. The oxidized ores consist of lateritic ore, and hematitic ore (goethite-martite ore, magnetite/heamatite ore, and hematite in breccias), while the un-oxidized ore type consists of metamorphosed BIF (magnetite-rich). The middle units are about 150 m thick and consisted of quartz/magnetite metamorphosed BIF with minor intercalations of biotite gneiss. The lower unit (354 m–565 m?) consist of gneissic country rock and represents the footwall of the deposit. It is made up of biotite gneiss, garnet-magnetite micaschist and pyroxene gneiss with minor intercalation of quartz/magnetite metamorphosed BIF.

5.2. Depositional environment and tentative model

Banded iron formations are thinly banded iron-rich (TFe > 15%) marine sedimentary rocks, mainly composed of iron oxides and chert (James, 1954). Not all BIFs are pure chemical sediments. Some are commonly being contaminated by clastic components (Bau and Dulski, 1996; Basta et al., 2011). Al_2O_3 and TiO_2 contents have been considered to be generally immobile during hydrothermal, diagenetic and weathering processes and strong positive correlation occurrence between these elements is indicative of clastic contamination (Basta et al., 2011; Yang et al., 2015). In the Nkout area, the magnetite BIF samples show high SiO_2 and Fe_2O_3 contents, similar to pure chemical sediment. The low Al_2O_3 and TiO_2 contents of the magnetite-rich BIF, together with weak positive correlation (r = 0.49; Table 2) between these elements are indicative of the low or even the absence of detrital components (Klein, 2005; Ganno et al., 2017). However, the garnet-rich BIF has higher average contents of Al_2O_3 (8.73 wt%), TiO_2 (0.27 wt%), K_2O (2.37 wt%) relative to magnetite-rich BIF, indicating clastic input (Lascelles, 2007; Basta et al., 2011). This is confirmed by the Pearson's inter-element correlations matrix (Table 3) in which strong positive correlations are observed between Al_2O_3 and TiO_2 (r = 0.91) and K_2O (r = 0.52). From the above, we propose that Nkout magnetite-rich iron unit is detritus free, whereas garnet-bearing iron units have significant amounts of clastic material, and therefore, a depositional environment closer to the continent (Spier et al., 2007). Furthermore, the absence of carbonate facies BIF in the entire Nkout deposit suggests deep water, distal depositional setting, in areas of little or no organic carbon supplies (Klein and Beukes, 1993; Beukes, 2004; Klein, 2005).

The lithostratigraphic correlation of BIF units support the fact that BIF's deposition took place on a basin-wide scale. Considering the extent of the Congo basin, it appears that a huge amount of Fe^{2+} in ocean water was required (James, 1954). The BIF units were most probably deposited in an iron rich environment of reduced Fe^{2+} rich hydrothermal fluid in a chemically stratified ocean. The Fe^{3+} was diagenetically converted to magnetite by same Fe^{2+} hydrothermal fluid. A similar depositional model was advocated in the Minas Supergroup of Quadrilátero Ferrífero, Brazil (Klein and Ladeira et al., 2000).

5.3. Comparative geochemistry

The average major element compositions of the Nkout BIF (magnetite BIF) are compared with other BIFs of the CC and the Carajas Formation and Quadrilátero Ferrífero, in Brazil (Fig. 12). Average compositions of Superior-type BIF and Algoma-type BIF are also plotted in Fig. 12 in order to better constrain the Nkout BIF type. From Fig. 12, the Nkout BIF has similar content of iron, silica and aluminium, as other Precambrian BIFs worldwide. Their average value of Na_2O, K_2O, TiO_2 and P_2O_5 have a close pattern with Mbarga BIF (Nforba et al., 2011), Elom BIF (Ganno et al., 2015) and Kouambo BIF (Ganno et al., 2017), KAB BIF (Soh Tamehe et al., 2018) in the CC, Carajas and Quadrilatero Ferrifero BIFs (Spier et al., 2007) in Brazil, and Superior-type BIF; but different from Bikoula BIF (Teutsong et al., 2017) which has a close pattern with Algoma-type BIF.

6. Conclusion

The petrography, major element geochemistry and lithostratigraphy of Nkout iron deposit revealed important information about the geology and depositional setting:

1. Two stratigraphic members (iron-rich member and gneissic member), and seven lithological units were distinguished.
2. All the succession has been metamorphosed to amphibolite and

granulite facies and very little of the depositional to early diagenetic minerals were preserved, except in magnetite-rich iron unit.

3. Lithostratigraphic correlation across the Nkout deposit is less uniform, with a marked reduction in stratigraphic thickness from West to the East succession, inferring folded synformal structure in the Nkout deposit. The correlation of BIF units supports the fact that BIF deposition took place on a basin-wide scale.
4. The synthetic stratigraphy of Nkout basin can be subdivided into three main units: an oxidized upper unit composed of high-grade hematite ore, a middle unit composed of fresh metamorphosed BIF and a lower unit made up of gneissic country rocks forming the footwall of the deposit.
5. Nkout magnetite-rich iron unit is detritus free whereas garnet-bearing iron units have significant amounts of clastic material, inferring a depositional environment closer to the continent. Furthermore, the absence of carbonate facies BIF in the entire Nkout deposit suggests deep water, distal environment depositional setting; in areas of little or no organic carbon supplies.
6. The BIF units were probably deposited in an iron rich environment of reduced Fe^{2+} rich hydrothermal fluids in a chemically stratified ocean.
7. Nkout metamorphosed BIF shows similar major element geochemical compositions as other Superior-type BIFs in the Congo craton and in Quadrilátero Ferrífero in Brazil.

Acknowledgement

This study is a part of the senior authors PhD thesis research work at the University of Yaoundé I. The authors would like to express their gratitude to the management staff of 'IMIC/CAMINEX SA' for the permission to collect diamond drill core samples from Nkout deposit and logistic facilities during field work. We gratefully acknowledge H. A. Wanas and three anonymous reviewers for their critical and constructive comments of the manuscript. This is the contribution of ICGP-Y 646 project.

References

Anderson, K.F.E., Frances, W., Rollinson, G.K., Charles, J.M., 2014. Quantitative mineralogical and chemical assessment of the Nkout iron ore deposit, Southern Cameroon. Ore Geol. Rev. 62, 25–39.

Basta, F.F., Maurice, A.E., Fontbote, L., Favarger, P., 2011. Petrology and geochemistry of the banded Iron formation (BIF) of wadi karim and um anab, eastern desert, Egypt: implications for the origin of neoproterozoic BIF. Precambrian Res. 187, 277–292.

Bau, M., Dulski, P., 1996. Distribution of yttrium and rare-earth elements in the penge and kuruman iron-formations, transvaal Supergroup, South Africa. Precambrian Res. 79, 37–55.

Beukes, N.J., 2004. Early option in photosynthesis. Nature 431, 522–532.

Caen Vachette, M., Vialette, Y., Bassot, J.-P., Vidal, P., 1988. Apport de la géochronologie à la connaissance de la géologie gabonaise. Chron. Rech. Min. 491, 35–54.

De Waele, B., Lacorde, M., Rivers, J., 2015. Banded iron formations and associated detrital iron deposits of the Western Congo Craton. In: SEG Conference, September 2015.

Feybesse, J.L., Johan, V., Triboulet, C., Guerrot, C., Mayaga-Mikolo, F., Bouchot, V., Eko N'dong, J., 1998. The West Central African belt: a model of 2.5–2.0 Ga accretion and two-phase orogenic evolution. Precambrian Res. 87, 161–216.

Ganno, S., Njiosseu, T.E.L., Ngnotué, T., Kouankap, N.G.D., Nzenti, J.P., 2017. A mixed seawater and hydrothermal origin of superior-type banded iron formation (BIF)-hosted Kouambo iron deposit, Palaeoproterozoic Nyong Series, Southwestern Cameroon: constraints from petrography and geochemistry. Ore Geol. Rev. 80, 860–875.

Ganno, S., Ngnotue, T., Kouankap Nono, G.K.D., Nzenti, J.P., Notsa, F.M., 2015. Petrology and geochemistry of the banded iron-formations from Ntem complex greenstones belt, Elom area, Southern Cameroon: implications for the origin and depositional environment. Chem. Erde 75, 375–387.

Ganno, S., Tsozué, D., Kouankap Nono, G.D., Tchouatcha, M.S., Ngnotué, T., Gamgne Takam, R., J.P Nzenti, 2018. Geochemical constraints on the origin of mineralized banded iron formation from the Meyomessi area, Archaean Ntem Complex (Congo Craton), southern Cameroon. Resour. Geol. http://dx.doi.org/10.1111/rge.12172.

James, H.L., 1954. Sedimentary facies of iron-formations. Econ. Geol. 49, 235–293.

Klein, C., Ladeira, E.A., 2000. Geochemistry and petrology of some proterozoic banded iron-formations of the Quadrilátero Ferrífero, Minas gerais, Brazil. Econ. Geol. 95, 405–428.

Klein, C., 2005. Some Precambrian banded iron-formations (BIFs) from around the world: their age, geologic setting, mineralogy, metamorphism, geochemistry, and origin. Am. Mineral. 90, 1473–1499.

Klein, C., Beukes, N.J., 1993. Sedimentology and geochemistry of the glaciogenic late proterozoic rapitan iron-formation in Canada. Econ. Geol. 88, 542–565.

Lascelles, D.F., 2007. Black smokers and density currents: an uniformitarian model for the genesis of banded iron-formations. Ore Geol. Rev. 32, 381–411.

Li, X.-H., Chen, Y., Li, J., Yang, C., Ling, X.-X., Tchouankoue, J.P., 2016. New isotopic constraints on age and origin of Mesoarchean charnockite, trondhjemite and amphibolite in the Ntem Complex of NW Congo Craton, southern Cameroon. Precambrian Res. 276, 14–23.

Maurizot, P., Abessolo, A., Feybesse, J.L., John et Lecomte, P., 1986. Étude de prospection minière du Sud-Ouest Cameroun. Synthèse des travaux de 1978 à 1985, rapport BRGM 85 CMR 066. pp. 274.

Ndime, E. N., Ganno, S., Nzenti J-P., Petrology and Depositional Age of the Neoarchean Banded Iron Formation-hosted Nkout West Iron Deposit (Southern Cameroon): Evidence from Geochemistry and Direct, Pb-pb Geochronology, (Personal Communication).

Nelson, J.P., Beukes, N.J., Carincross, B., 1995. Tectonic-stratigraphic setting of the 2.9Ga Mozaan group of the pongla supper group and correlation with the witwaterand supper-group. In: Extented Abstracts of the South African Geocongress, pp. 838–840.

Nforba, M.T., Suh, C.E., Kabeyene, K.V.K., 2011. Mbalam iron ore project, northern edge of the Congo craton, southeast Cameroon. In: Goldfarb, R.J., Marsh, E.E., Monecke, E. (Eds.), Proceedings of the Society of Economic Geologists on TheChallenge of Finding New Mineral Resources: Global Metallogeny, Innovative Exploration and New Discoveries, SEG Extended Abstracts. Colorado, G-22.

Nsoh, F.E., Agbor, T.A., Etame, J., Suh, E.C., 2014. Ore-textures and geochemistry of the Nkout iron deposit South east Cameroon. Sci. Technol. Dev. 15, 43–52.

Nyame, F.K., Kase, K., Yamato, M., 1998. Spessartine garnet in a manganiferous carbonate formation from Nsuta, Ghana. Resour. Geol. 48 (1), 13–22.

Nzenti, J.P., Barbey, P., Macaudière, J., Soba, D., 1988. Origin and evolution of the late Precambrian high-grade Yaounde gneisses (Cameroon). Precambrian Res. 38, 91–109.

Rolin, P., 1992. Présence d'un chevauchement ductile majeur d'âge panafricain dans la partie centrale de la République Centrafricaine: résultats préliminaires. In: Comptes Rendus de l'Académie des Sciences, Paris, vol. 315. pp. 467–470.

Shang, C.K., Liégeois, J.P., Satir, M., Frisch, W., Nsifa, E.N., 2010. Late Archaean high-K granite geochronology of the northern metacratonic margin of the Archaean Congo Craton, Southern Cameroon: evidence for Pb-loss due to non-metamorphic causes. Gondwana Res. 475, 1–19.

Shang, C.K., Satir, M., Siebel, W., Taubald, H., Nsifa, E.N., Westphal, M., Reitter, E., 2001. Genesis of K-rich granitoids in the Sangmelima region, Ntem complex (Congo craton). Cameroon. Terra Nostra 5, 60–63.

Shang, C.K., Satir, M., Siebel, W., Nsifa, N.E., Taubald, H., Liegeois, J.P., Tchoua, F.M., 2004a. Major and trace element geochemistry, Rb-Sr and Sm-Nd systematics of the TTG magmatism in the Congo Craton: case of the Sangmelima region, Ntem complex, southern Cameroon. J. Afr. Earth Sci. 40, 61–79.

Shang, C.K., Siebel, W., Satir, M., Chen, F., Mvondo, J.O., 2004b. Zircon Pb-Pb and U-Pb systematics of TTG rocks in the Congo Craton: constraints of crustal formation, crystallization and Pan-African lead loss. Bull. Geosci. 79, 205–219.

Soh Tamehe, L., Nzepang, T.M., Chongtao, W., Ganno, S., Ngnotue, T., Kouankap, N.G.D., Simon, S.J., Zhang, J., Nzenti, J.P., 2018. Geology and geochemical constrains on the origin and depositional setting of the Kpwa–Atog Boga banded iron formations (BIFs), northwestern Congo craton, southern Cameroon. Ore Geol. Rev. 95, 620–638.

Spier, C.A., Oliveira, S.M.B., Sial, A.N., Rios, F.J., 2007. Geochemistry and genesis of the banded iron formations of the cauê formation, Quadrilátero Ferrífero, Minas gerais. Brazil. Precambrian Res. 152, 170–206.

Suh, C.E., Cabral, A.R., Ndime, E., 2009. Geology and ore fabrics of the Nkout high-grade haematite deposit, southern Cameroon. Smart Science for Exploration and Mining1 558–560.

Tchameni, R., Mezger, K., Nsifa, N.E., Pouclet, A., 2000. Neoarchaean evolution in the Congo craton: evidence from K rich granitoids of the Ntem complex, Southern Cameroon. J. Afr. Earth Sci. 30, 133–147.

Tchameni, R., Mezger, K., Nsifa, N.E., Pouclet, A., 2001. Crustal origin of early proterozoic syenites in the Congo craton (Ntem complex), South Cameroon. Lithos 57 (1), 23–42.

Teutsong, T., Bontognali, T.R.R., Ndjigui, P.D., Vrijmoed, J.C., Teagle, D., Cooper, M., Vance, D., 2017. Petrography and geochemistry of the Mesoarchean Bikoula banded iron formation in the Ntem complex (Congo craton), Southern Cameroon: implications for its origin. Ore Geol. Rev. 80, 267–288.

Toteu, S.F., Penaye, J., Djomani, Y.P., 2004. Geodynamic evolution of the Pan-African belt in central Africa with special reference to Cameroon. Can. J. Earth Sci. 41, 73–78.

Toteu, S.F., Van Schmus, W.R., Penaye, J., Nyobe, J.B., 1994. U-Pb and Sm-Ndevidence for Eburnean and Pan-African high-grade metamorphism in cratonic rocks of southern Cameroon. Precambrian Res. 67, 321–347.

Yang, X.Q., Zhang, Z.H., Duan, S.G., Zhao, X.M., 2015. Petrological and geochemical features of the Jingtieshan banded iron formation (BIF): a unique type of BIF from the Northern Qilian Orogenic Belt, NW China. J. Asian Earth Sci. 113, 1218–1234.

Geochemistry and Pb–Pb geochronology of the Neoarchean Nkout West metamorphosed banded iron formation, southern Cameroon

Ekah Nzume Ndime, Sylvestre Ganno & Jean Paul Nzenti

International Journal of Earth Sciences
GR Geologische Rundschau

ISSN 1437-3254
Volume 108
Number 5

Int J Earth Sci (Geol Rundsch) (2019)
108:1551-1570
DOI 10.1007/s00531-019-01719-5

Springer

International Journal of Earth Sciences (2019) 108:1551–1570
https://doi.org/10.1007/s00531-019-01719-5

ORIGINAL PAPER

Geochemistry and Pb–Pb geochronology of the Neoarchean Nkout West metamorphosed banded iron formation, southern Cameroon

Ekah Nzume Ndime[1] · Sylvestre Ganno[1] · Jean Paul Nzenti[1]

Received: 7 February 2018 / Accepted: 16 April 2019 / Published online: 7 May 2019

Abstract
The Nkout West iron deposit of the northern edge of the Congo craton in southern Cameroon forms part of the northwest plunging isoclinal mega fold composed of metamorphosed banded iron formations (BIFs), which have been deformed and metamorphosed, resulting in recrystallized magnetite, quartz and silicates. Here, we present whole-rock geochemistry together with Pb–Pb isotopic compositions and dating of metamorphosed BIF, with the aim to constrain the genesis and elucidate the metamorphic resetting age. Based on the mineral composition, two types of BIF (magnetite BIF, garnet BIF) have been distinguished. The magnetite BIF shows high SiO_2 and Fe_2O_3 and low Al_2O_3, TiO_2, HFSE and $\sum$REE contents similar to detritus-free chemical sediments. In contrast, their high concentrations in garnet BIF indicate clay-rich-contaminated input. The Co/Zn ratios are consistent with trace metals of hydrothermal sources (0.14 for magnetite BIF) or with minor hydrogenous component (0.27 for garnet BIF). The PAAS-normalized REE-Y patterns of the studied metamorphosed BIFs show LREE depletion relative to HREE and positive Eu anomalies. The magnetite BIF exhibits positive Y anomaly ($Y/Y^*_{PAAS} = 1.3$), which is the signature inherited from sea water, but its Y/Ho (39.93) ratio suggests a mixture of hydrothermal solution with sea water. The garnet BIF shows positive Eu, negative Y anomalies and chondritic Y/Ho ratio (27.49), which is consistent with hydrothermal solution with significant clastic contamination. Whole-rock Pb concentration is roughly on average of 2.0–6.0 ppm, suggesting a hydrothermal Pb source. The Pb–Pb dating yielded an age of 2679 Ma, interpreted as the Neoarchean metamorphic event in the Ntem complex.

Keywords Metamorphosed BIF · Hydrothermal solution · Sea water · Pb isotope · Nkout West deposit · Southern Cameroon

Introduction

Precambrian banded iron formations (BIFs) are thinly banded or laminated iron-rich (TFe > 15%) sedimentary rocks of marine origin, commonly composed of iron oxides (magnetite and hematite) and gangue (quartz) minerals (James 1954). Four main facies of metamorphosed BIFs have been distinguished based on their iron mineralogy. They include oxide, carbonate, silicate and sulfide facies, among which the oxide facies is the most important (James 1954). Banded iron formations are distributed throughout the geologic record around the world, with depositional peak at ca. 2.7–2.5 Ga, and then abruptly disappeared after ca. 1.85, with an exception of a few Neoproterozoic iron formations between 0.8 and 0.6 Ga (Klein 2005; Bekker et al. 2010). They are commonly associated with greenstone belts and other Precambrian supracrustal sequences (James 1992; Zhai and Santosh 2011, 2013). Banded iron formations can be divided into Algoma type, Superior type, and Rapitan type based on depositional environment and geotectonic setting (Gross and McLeod 1980). Algoma type BIF is associated with arcs setting (Gross 1983; Klein and Beukes 1992) and is typically found in Archean greenstone belts. In the Congo craton, the Algoma type is located within the Ntem complex in the Bikoula area (Teutsong et al. 2017) and in the Meyomessi area (Ganno et al. 2018). Superior-type BIF or continental margin BIF is located on stable continental platforms and was mainly deposited in Paleoproterozoic times, while Rapitan-type BIF is exclusively Neoproterozoic in age and is associated with a glacially influenced depositional environment (Gross 1983; Klein and Beukes 1992). Superior-type

✉ Sylvestre Ganno
sganno2000@yahoo.fr; sganno@uy1.uninet.cm

[1] Department of Earth Sciences, University of Yaoundé I, P.O. Box 812, Yaoundé, Cameroon

BIF is laterally very extensive and constitute a major iron ore resource worldwide, with major deposits being located in the Hamersley basin in Australia (Barley et al. 1999; Lascelles 2006), the Superior Province (Abitibi belt) in North America (Trendall 2002; Pufahl 2010), the Amazon craton of Brazil (Spier et al. 2003, 2007), the Kaapvaal craton of South Africa (Beukes and Klein 1990); and the Congo craton (Ganno et al. 2017). BIFs are not only an important source of iron ore for industry, but due to the fact that their deposition has been linked to significant compositional changes in the earth's atmosphere, these BIFs play an important role in understanding the evolution of life, oceans, and the atmosphere in the Archean and Proterozoic times (Poulton et al. 2010; Bekker et al. 2010; Young 2013; Ganno et al. 2015).

The Nkout metamorphosed BIF deposit is located in the northern margin of the Congo Craton (CC) within the Ntem Complex. This complex hosts many iron ore deposits such as Mbalam (Suh et al. 2008; Chombong and Suh 2013; Ilouga et al. 2013), Elom (Ganno et al. 2015), Zambi (Ganno et al. 2016), Bikoula (Teutsong et al. 2017), Kouambo (Ganno et al. 2017), Meyomessi (Ganno et al. 2018), and Gouap (Soh Tamehe et al. 2018, 2019) deposited in an active continental margin tectonic setting (Soh Tamehe et al. 2018). The Nkout BIF deposit is divided into three prospects, namely, Nkout East, Nkout Centre and Nkout West (Fig. 1). The latter (2 km long) forms part of the west limb of the northwest plunging isoclinal fold, composed of iron ore of economic importance which occurs in close association with metamorphosed BIFs. Previous studies on Nkout deposit were focused on mineralogy and ore-textures of high-grade ore (Suh et al. 2009; Anderson et al. 2014; Nsoh et al. 2014) but little is known on the origin, the tectono metamorphic event and the stratigraphy of the deposit. In this study, after both field mapping and a detailed logging of three representative diamond drilled holes of the Nkout West deposit, whole-rock geochemical analyses and Pb–Pb isotopic compositions and dating were performed, with the aim to constrain the stratigraphy of the Nkout West deposit and to investigate the genetic model and elucidate the metamorphic age.

Geological setting

General geological setting

The north-western margin of the Archaean CC in Cameroon is represented by the Ntem Complex (Fig. 1a) (Maurizot et al. 1986; Nédélec et al. 1990; Goodwin 1991). The Ntem Complex is divided into two main structural units: the Ntem unit (where Nkout is located) and the Nyong unit in the western area (Toteu et al. 1994; Tchameni et al. 2001; Penaye et al. 2004; Lerouge et al. 2006, Fig. 1a). A thrust contact boundary of Pan-African age separated the Ntem Complex and the Yaoundé Group of the Pan-African orogenic belt in Central Africa (Nzenti et al. 1988; Toteu et al. 2004, 2006). The Ntem complex constitutes the immediate margin of the CC with the Pan-African orogenic belt (Shang et al. 2004). The Ntem complex comprises Palaeoarchaean to Mesoarchaean and late Archaean charnockites, Mesoarchaean greenstone formation, late Archaean TTG

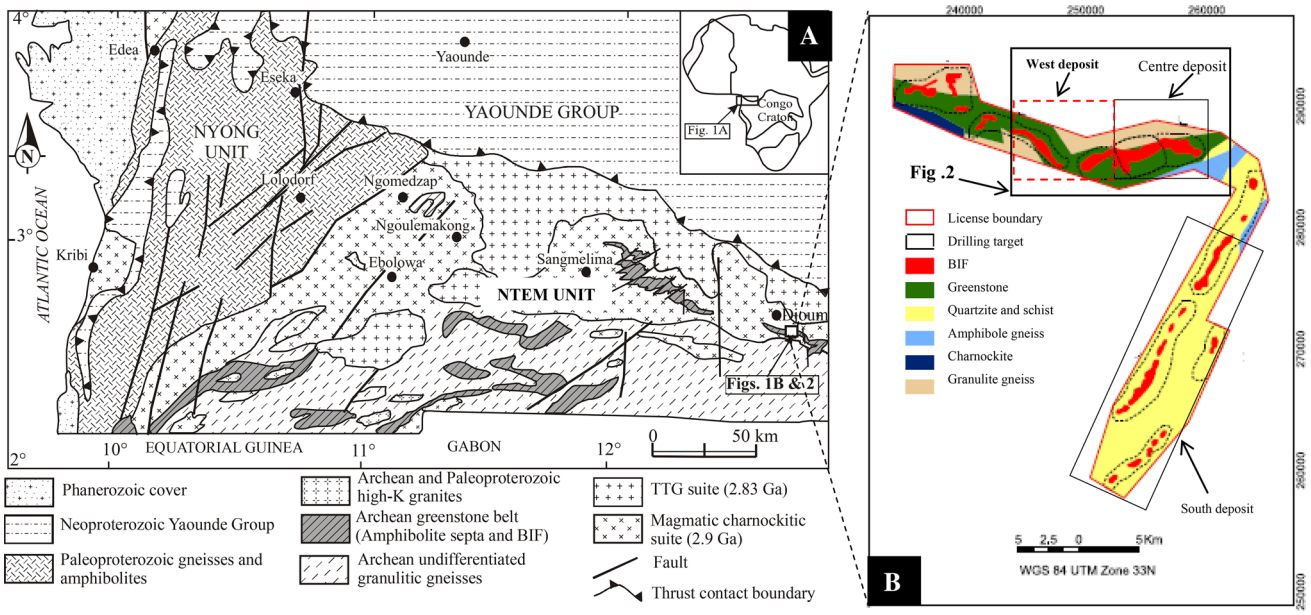

Fig. 1 (**a**) Simplified geologic map of SW Cameroon (Maurizot et al. 1986); (**b**) geological map of Nkout iron deposit (after Anderson et al. 2014)

(tonalite, trondjhemite, granodiorite) basement, and high-K granites (Nédélec et al. 1990; Tchameni et al. 2000; Shang et al. 2001, 2004, 2010; Pouclet et al. 2007). The TTG suite is made up of tonalites and granodiorites including high-K granites, some of which are charnockitic (Pouclet et al. 2007). The greenstone belt in the Ntem unit comprises metavolcanics with mafic–ultramafic compositions, namely, amphibolite, gneisses and metamorphosed banded iron formation (Shang et al. 2010; Ganno et al. 2015, 2018; Soh Tamehe et al. 2019). Most of the BIF deposits within the Ntem complex are of Superior type due to their association with sedimentary rocks, their geochemical characteristics with Eu anomaly < 1.8 and their continental margin tectonic setting (Ganno et al. 2017; Soh Tamehe et al. 2018), except the Bikoula BIF which belongs to Algoma type (Teutsong et al. 2017). The metasedimentary rock of the greenstone belt was dated to be ca. 3.1 Ga (Tchameni et al. 2004, 2010). New SIMS zircon U–Pb result reveals that the charnockites crystallized at ca. 2.92 Ga; the trondhjemites and associated amphibolite protoliths crystallized synchronously at 2.87–2.86 Ga (Li et al. 2016). Two important reactivation episodes related to syntectonic plutonism and coeval metamorphism affected the Ntem Complex in Eburnean and Pan-African times (Toteu et al. 1994; Lerouge et al. 2006). The Eburnean-tectono metamorphic event (~2100 Ma) brought about the amphibolite facies metamorphism, while during the Pan-African orogeny (~600 Ma), the Yaoundé series, drifted southward and collided with the Ntem Complex forming a major nappe structure with peak granulite facies metamorphism (Nzenti et al. 1984, 1988). The main structural features of the Ntem Complex are the E–W trending, steeply dipping foliation, vertical stretching lineation, and isoclinal folds (Suh et al. 2009; Ganno et al. 2015).

Geology of the Nkout iron deposit

The Nkout-banded iron formation is located on the Ntem Complex, an emerging iron ore province in West and Central Africa. Previous work indicates that the Nkout area comprises TTG granite, charnockitic gneiss, schist, amphibolite, and metamorphosed banded iron formation (BIF) (Suh et al. 2009; Shang et al. 2010; Ganno et al. 2016; Ndime Ekah et al. 2018). The BIF comprises beds of magnetite-bearing quartzite that are concordant with the country rocks. The country rock comprises granite–charnockite assemblage in the north, whereas greenstone and gneissic rocks are located in the south (Suh et al. 2009). Caen Vachette et al. (1988) attributed the BIF rock in the Ntem Complex to be Archaean in age similar to their host country rocks. The Nkout deposit exhibits an ENE–WSW (N70°E) trending (9 km long) ridge that defines the northwest plunging isoclinal fold structure. It is subdivided into West, Centre and South deposits (Fig. 1b; Anderson et al. 2014, Ndime Ekah et al. 2018).

The Nkout West deposit which is the focus of this paper is approximately 2 km long and 400–500 m wide (Fig. 2), bounded by N–S and NE–SW striking faults (Suh et al.

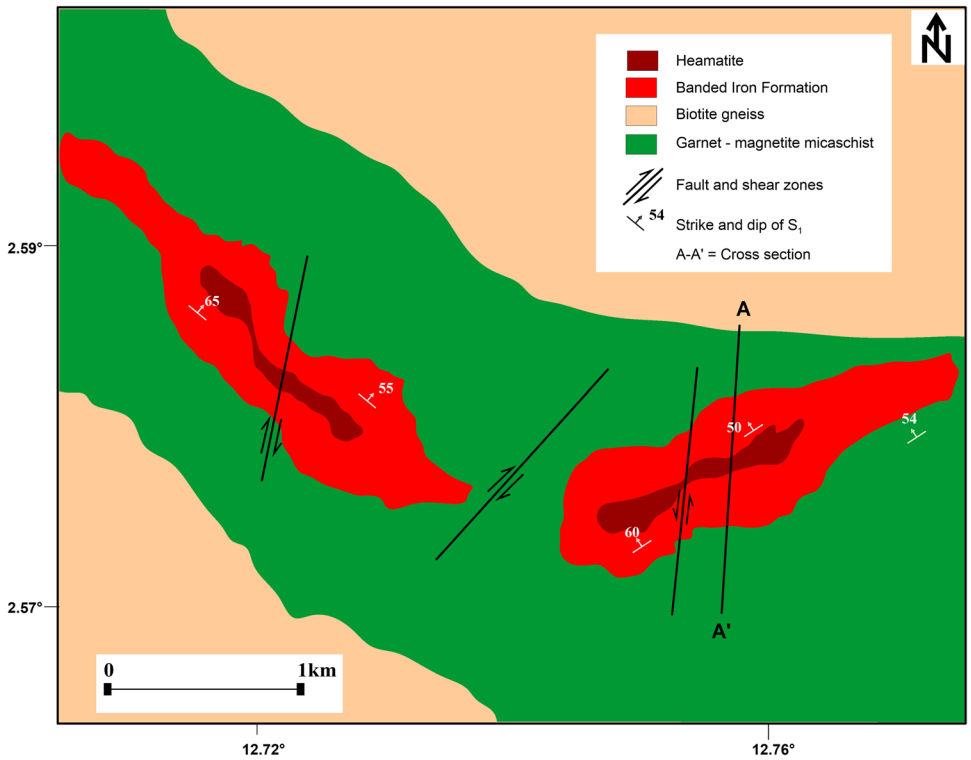

Fig. 2 Local geological surface map of Nkout West iron prospect

2009). The bulk BIF deposit is made up of metamorphosed magnetite-rich BIF. The hanging and foot walls comprise the country rock which is made up of biotite gneiss, biotite–garnet gneiss and garnet magnetite micaschist (Fig. 3).

Sampling and analytical methods

Core samples were collected from three representative drill holes of the Nkout West prospect, a mineral exploration property owned by Caminex S.A. Care was taken during sample preparation and transportation from site to the laboratory to avoid cross contamination and confusion. Twelve (12) polished thin sections were prepared from representative samples at Geotech Lab (Vancouver, Canada) using conventional technics. Petrographic study was done under both transmitted and reflected light petrographic microscope. Fifteen representative metamorphosed BIF samples were investigated in terms of their whole-rock geochemistry and thirteen for total whole-rock Pb–Pb isotope geochronology.

Whole-rock geochemical methods

Whole-rock analyses were done using the pulp by inductively coupled plasma-atomic emission (ICP-AES), for major elements geochemistry and inductively coupled plasma mass spectrometry (ICP-MS), for trace elements geochemistry and REE at ALS Minerals Global Group Vancouver (Canada). The samples were pulverized and 50–60 g were obtained for the analyses, 0.2 g of rock powder was fused with $LiBO_2$ and dissolved in 100 mm^3, 5% HNO_3. 63 elements were obtained by various ionic leach technique and ICP-MS. The majority of these analyses have a lower detection limit of 0.01%. Loss on ignition ("LOI") was determined using 0.5 g of pulverized rock sample, ignited for 2 h at 1000 °C and then weighed again. Trace element and REE digestions were done with lithium borate ($LiBO_2$) and fusion. Four acid digestions were done for the base metals and an aqua regia digestion for the volatile gold-related trace elements. The analytical precisions for trace elements show detection limit between 0.01 and 10 ppm while those for REE were detected from 0.01 to 5 ppm. The precisions were done using certified high-grade reference material.

Pb-composition method

The Pb composition method was done as an add-on to the trace level for acid digestion methods at ALS Minerals Global Group Vancouver (Canada). In the default method, a prepared 0.5 g of sample was digested with four acids ($HClO_4$, HF, HNO_3 and HCl) to dryness followed by leaching with HCl. After cooling, the resulting solution is diluted to volume (25 ml) with 10% HCl, mixed and analysed with HR ICP-MS Isotope analysis method. The ICP-MS instrument was carefully tuned to rapidly scan the isotopes of interest and provided a level of precision that is fit for the purpose of age determination. Six Pb isotope ratios ($^{206}Pb/^{204}Pb$, $^{207}Pb/^{204}Pb$, $^{208}Pb/^{204}Pb$, $^{208}Pb/^{207}Pb$, $^{208}Pb/^{206}Pb$, and $^{206}Pb/^{207}Pb$) are reported. Precision and accuracy were monitored using certified Pb isotope and internal rock standards. The standards were used and data quality assurance was verified by running these standards between samples as unknown. The age determination was calculated and plots were prepared using Isoplot 4.15 program (Ludwig 2011) according to the Pb evolution model of Stacey and Kramers (1975).

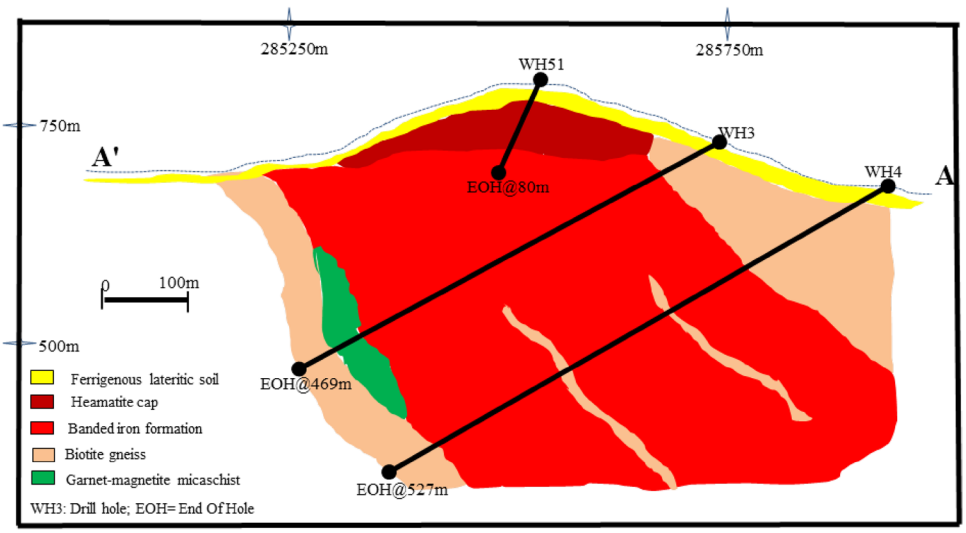

Fig. 3 Geological N–S cross section (A–A′ in Fig. 2) of Nkout west iron deposit

Results

Lithostratigraphy

This section consists of results of three representative drill holes (WH3, WH4, WH51) selected from 52 completed diamond drill holes in the Nkout West area. The depths of the different holes are 459 m, 527 m, and 80 m, respectively, for WH3, WH4, and WH51. The detailed loggings of these holes have enabled us to identify all the mappable lithostratigraphic units of the Nkout West BIF deposit (Fig. 3), namely, (1) banded iron formation (BIF) and (2) gneissic country rock. The Nkout West litho-assemblages within the deposit are illustrated in the cross section (AA′) (Figs. 3, 4).

Banded iron formation unit

The banded iron formation unit has different thicknesses and varies from one hole to another, dipping approximately 50°–65° to the north. The BIF is intercepted at a located depth of 85 m below surface. The total BIF thicknesses across section vary between 85–467 and 111–510 m, with the largest thickness being approximately ~400 m (Fig. 3). It consists of two lithotypes, namely, magnetite-rich BIF, and garnet-BIF (Fig. 1B).

Gneissic formation unit

The gneissic formation unit constitutes the country rocks and exhibits varying thicknesses at different depths for the different holes. This formation displays sharp, transition to gradational contact with the BIF unit, and makes up both footwall and hanging walls of the deposit (Fig. 3). The gneiss formation is intercepted at the hanging wall located just below the lateritic surface (at varying depths between 5 and 16 m). The footwall contacts are intercepted at 412 m and 510 m, respectively, at different holes. Minor intercalations (1–5 m) are intercepted at various depths (183 m, and 250 m). The total gneissic unit thicknesses on the cross section vary between 85 and 111 m, with the largest thickness being about ~120 m (Figs. 3, 4). The Nkout West gneissic formation unit consists of three rock types, namely, biotite-rich gneiss, garnet and magnetic-rich micaschist, and garnet-rich gneiss. These rock units are typically foliated and are directly in association with the banded iron formation unit in the stratigraphy.

Petrography

The Nkout West iron deposit is mainly made up of banded iron formation (metamorphosed BIF) associated with gneissic country rocks.

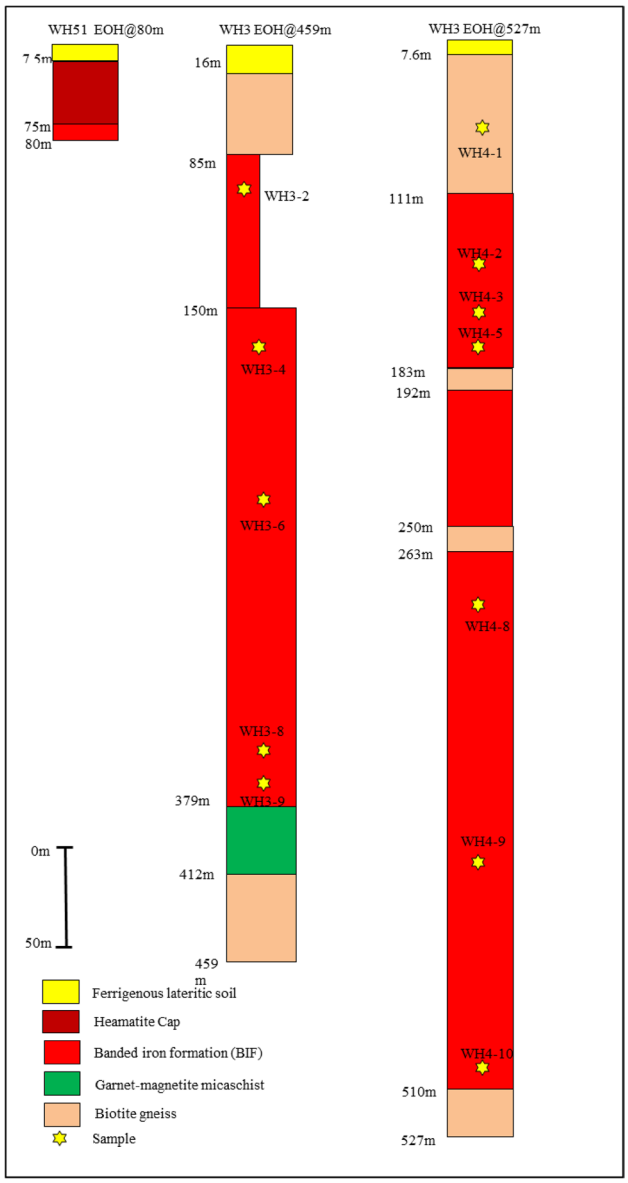

Fig. 4 Stratigraphy of the Nkout West iron deposit with sample locations

Banded iron formations (BIF)

Nkout West BIF commonly displays alternating micro (1–5 mm)- to meso (1–1.5 cm)-Fe- and Si-rich bands. The iron-rich band is composed of iron oxides (magnetite with minor hematite) and silicate minerals (chlorite, garnet and biotite in some cases), whereas the Si-rich bands are mainly composed of quartz. Two types of BIF have been distinguished based on the mineral occurrences, namely, magnetite BIF and garnet BIF.

Magnetite BIF

The medium- to coarse-grained magnetite BIF shows schistose structure (Fig. 5a) and bands are composed primarily of quartz (30–40%), magnetite (25–35%), biotite (10–15%) and secondary chlorite (2–5%). Heterogranular and granoblastic microstructure prevail in the rock type (Fig. 5b). Quartz crystals are medium to coarse-grained (average: 0.25 mm), locally exhibiting undulose or wavy extinction, and are subhedral to anhedral in shape. Magnetite crystals are the main iron mineral of the Nkout metamorphosed magnetite BIF and occur in magnetite-rich bands (Fig. 5b). Magnetite crystals occur as large subhedral to anhedral grains dominantly showing granoblastic texture (Fig. 5b). They exhibit interlocking grain texture with curved grain boundaries. These grains are distributed uniformly and are interconnected to form aggregates of different sizes. The chlorite crystals are anhedral to subhedral in form (average grain size: 0.01 mm), light green with schistose structure, and commonly surround iron oxide minerals (Fig. 5b). Biotite crystals are subhedral to anhedral. They are flakes of various dimensions, some of which are commonly altered to chlorite (Fig. 5b). The mineral assemblage of magnetite BIF is made up of quartz, magnetite, biotite and chlorite.

Garnet BIF

The garnet-rich BIF is medium to coarse-grained foliated rock (Fig. 5c, e); bands are made mainly of quartz (20–30%), biotite (20–15%), magnetite (15–10%), amphibole (5–10%),

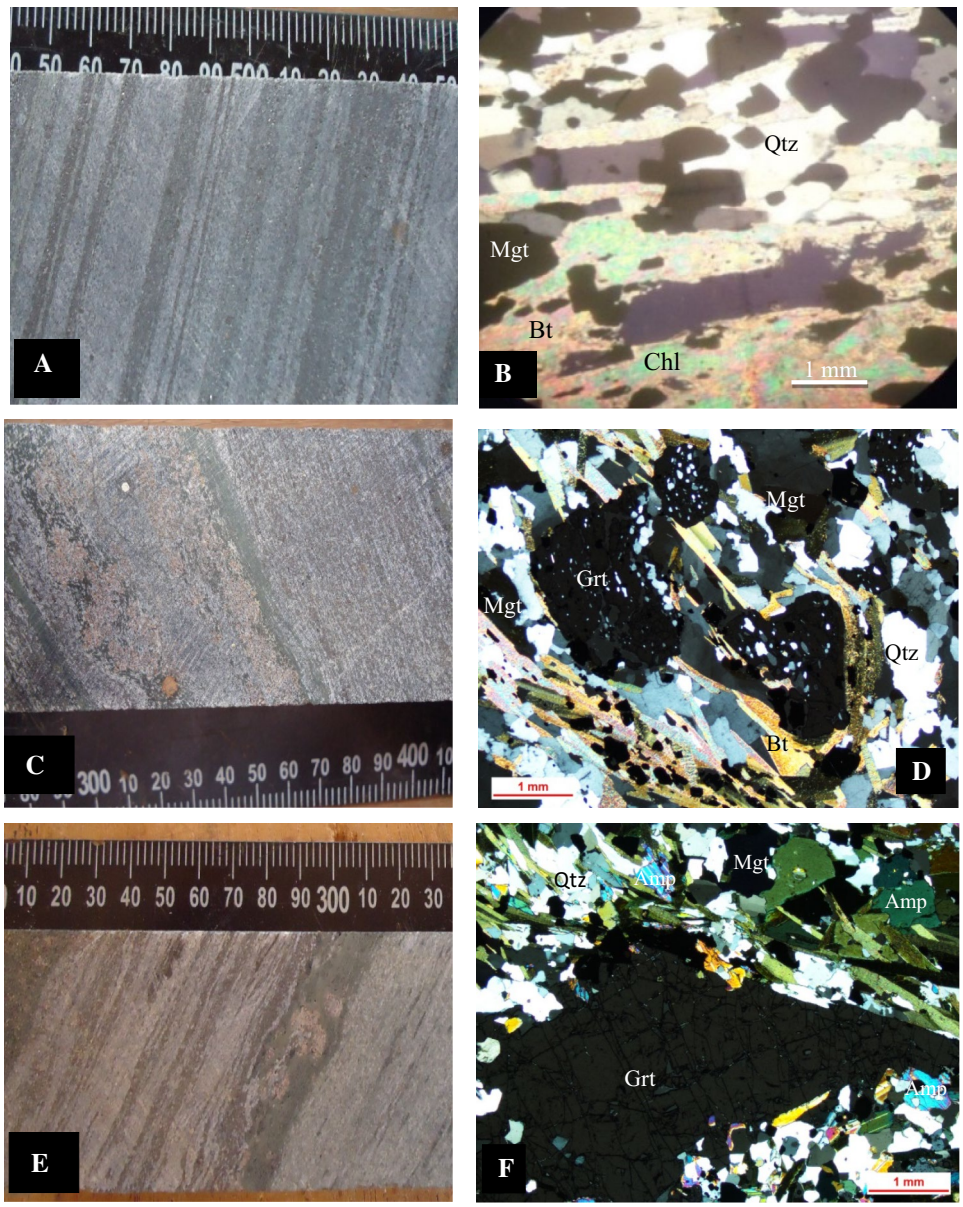

Fig. 5 Hand specimen and photomicrographs of BIF: core photos of magnetite BIF (**a**); garnet BIF (**c**, **e**); photomicrograph showing granoblastic microstructure and mineral assemblage of magnetite BIF (**b**), garnet BIF (**d**, **f**)

garnet (5–10%), and chlorite (< 5%). The rock displays heterogranular and granoblastic microstructure (Fig. 5d, f). Quartz in the garnet BIF is one of the main components; they are euhedral or subhedral, fine-grained crystals. They show wavy extinction (Fig. 5c) and occur as both aggregates, exhibiting curved grain boundaries and are granoblastic in texture. Biotite grains occur as flakes of various dimensions and forms euhedral inclusions in garnet porphyroblasts (Fig. 5d, f). Subhedral to anhedral biotite crystals (0.16 mm average) which are commonly altered to chlorite (Fig. 5d). They display iron oxide and quartz inclusion. Magnetite crystals (0.24–1 mm) occur as inclusions in biotite porphyroblasts. Garnet porphyroblasts (0.23–3 mm) are rich in quartz inclusions. Subhedral amphibole crystals (0.2–1.5 mm) are associated with biotite, magnetite, garnet and quartz. Secondary chlorite flakes (0.16 mm average) result from alteration of biotite. Very few pyrite grains were observed; they are euhedral to subhedral crystals (0.1–1 mm) and are associated with magnetite, garnet and quartz. The garnet BIF shows amphibolite facies mineral assemblage, which is made up of quartz, magnetite garnet, amphibole and biotite.

Geochemistry

Major elements

The whole-rock major element data of Nkout West deposit are presented in Table 1. The result shows that Fe_2O_3 and SiO_2 are the main components of the studied samples with contents ranging from 82.2 to 99.9 wt% (Fig. 6).

The samples with high contents of iron and silica are the magnetite BIF in which these two components have values greater than 88.9 wt%, similar to pure chemical sediments (James 1954). The Al_2O_3 content in magnetite BIF is generally low (0.13–0.82 wt%) except sample WH3-2 which has a value of 1.65 wt%. This magnetite BIF also shows very low TiO_2 (0.06 wt%) contents. CaO and MgO contents are slightly high, ranging between 0.33–1.7 and 1.52–7.56 wt%, respectively. K_2O and Na_2O contents are very low and, in most cases, are less than the detection limit (0.01 wt%). The P_2O_5 concentration is low (average 0.09 wt%) in all the magnetite BIF samples.

The garnet BIF shows high SiO_2 (50.80–54.50 wt%) and relatively low Fe_2O_3 (31.50–38.10 wt%) contents when compared with the magnetite BIF (38.80–52.50 wt% SiO_2 and 41.90–57.40 wt% Fe_2O_3). The Al_2O_3, K_2O and MgO contents are high, ranging between 5.33–9.54, 2.30–3.05, and 2.17–2.89 wt, respectively (Fig. 6), as well as the TiO_2 (0.17–0.26 wt%) and P_2O_5 (0.08–0.10 wt%) contents. A strong negative correlation exists between Fe_2O_3 and Al_2O_3 ($r^2 = 0.81$; Fig. 7b) and between Fe_2O_3 and TiO_2 ($r^2 = 0.84$; Fig. 7d); and a strong positive correlation exists between Al_2O_3 and TiO_2 ($r^2 = 0.80$; Fig. 7c), suggesting detrital input in the studied garnet BIF samples.

Table 1 Major elements geochemical composition (wt%) and element ratios of Nkout West BIF

Magnetite BIF										Garnet BIF				
wt%	WH4-5	WH4-8	WH4-10	WH4-2	CH7-1	CH7-2	CH24-1	CH24-2	CH24-3	CH7-3	CH7-6	WH3-6	WH3-9	WH4-3
SiO_2	45.5	40	42.5	38.8	43.1	38.6	40.3	41.9	56	51.8	60.7	52.5	54.5	50.8
TiO_2	0.03	0.03	0.01	0.02	0.01	0.02	0.06	0.01	0.02	0.33	0.35	0.26	0.21	0.17
Al_2O_3	0.72	0.82	0.17	0.7	0.16	0.74	1.59	0.13	0.47	8.85	10.8	9.54	7.25	5.33
Fe_2O_3	50.4	55.5	57.4	55.3	54.5	54.6	52.1	55.1	38.1	28.3	20	31.5	32.7	38.1
MgO	3.04	2.48	1.52	2.18	1.93	2.53	2.03	1.92	5.35	2.85	1.49	2.2	2.17	2.89
MnO	0.09	0.11	0.08	0.12	0.11	0.13	0.06	0.05	0.16	0.11	0.09	0.25	0.13	0.17
Na_2O	0.07	0.07	0.02	0.07	0.3	0.21	0.03	0.05	0.06	1.52	0.19	0.2	0.32	0.22
K_2O	0.29	0.15	0.02	0.13	0.08	0.19	0.54	0.05	0.05	0.99	2.86	3.05	2.79	2.3
CaO	1.04	1.35	1.04	1.68	2.25	2.08	1.37	1.38	0.8	4.59	0.85	1.94	0.68	1.25
Cr_2O_3	0.01	0.01	0.01	0.01	0.01	0.01	0.01	0.01	0.01	0.03	0.01	0.02	0.02	0.01
P_2O_5	0.03	0.11	0.09	0.12	0.07	0.03	0.12	0.1	0.11	0.18	0.05	0.1	0.08	0.1
LOI	−1.1	−1.29	−1.39	−1.07	−1.15	−0.93	−0.23	−1.08	−0.43	0.47	1.1	−0.15	0.11	0.58
Total	100.12	99.34	101.47	98.06	101.37	98.21	97.98	99.62	100.7	100.02	98.49	101.41	100.96	101.92
Fe/Ti	1680	1850	5740	2765	5450	2730	868	5510	1905	86	57	121	156	224
Si/Fe	0.90	0.72	0.74	0.70	0.79	0.70	0.77	0.76	1.47	1.83	3.03	1.66	1.66	1.33
Al/Ti	24.00	27.33	17.00	35.00	16.00	37.00	26.50	13.00	23.50	26.81	30.85	36.69	34.52	31.35
Si/Al	63.194	48.78	250.00	55.42	269.37	52.16	25.34	322.30	119.14	5.85	5.62	5.50	7.51	9.53
Fe/Al	70.00	67.68	337.64	79.00	340.62	73.78	32.76	423.84	81.06	3.19	1.85	3.30	4.51	7.14

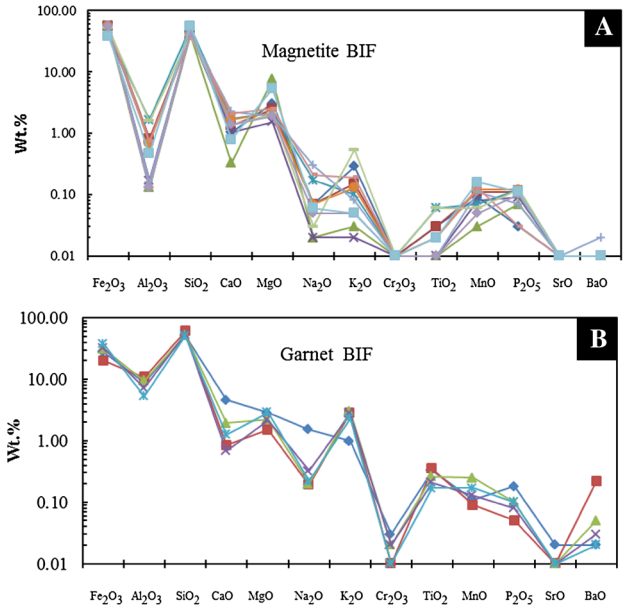

Fig. 6 Major elements compositions of Nkout West BIF (**a**) magnetite BIF and (**b**) garnet-BIF

Trace elements

The trace element compositions of the studied metamorphosed BIF show significant variations in the samples (Table 2).

The magnetite BIF shows low but variable Ba (0.26–3.52 ppm), Sr (0.259–0.69 ppm), Cu (0.05–1.11 ppm), Zn (0.78–1.94 ppm), and Pb (0.605–1.94 ppm) contents. The Co/Zn and Ni/Zn ratios vary from 0.04–0.22 to 0.29–1.23, respectively. Zr content is very low and shows insignificant to null correlation that exists between Zr and Al_2O_3 and TiO_2 (Fig. 8). The concentrations of High-Field Strength Elements (HFSE) are extremely low: Th (0.005–0.066 ppm), Zr (0.001–0.004 ppm), V (0.80–1.08 ppm), Sc (0.02–0.13 ppm) and Hf (0.001 ppm)) The garnet BIF is enriched in large ion lithophile element (LILE), such as Ba (15.55–37.40 ppm) and Rb (7.90–16.55 ppm), and depleted in HFSE such as Zr, Hf, Th and U (Fig. 8b). A weak positive correlation exists between Zr and Al_2O_3 (r^2 = 0.391; Fig. 8a) and between Zr and TiO_2 (r^2 = 0.107; Fig. 8b), when compared with the magnetite BIF.

Rare Earth Elements

The REE content of magnetite BIF shows ΣREE values ranging from 0.59 to 2.40 ppm. The Post-Archean Australian Shale (subscript PAAS)-normalized REE pattern (Fig. 9a) shows LREE depletion (La/Yb_{PAAS} = 0.22–1.53, average = 0.58) relative to HREE (Tb/Yb_{PAAS} = 0.81–0.96, average = 0.88); positive Eu anomaly (Eu/Eu^*_{PAAS} = 1.06 – 2.29, average 1.86) and negative Ce anomalies (Ce/Ce^*_{PAAS} = 0.86 – 0.94, average; 0.90) and slight positive Y anomaly. However, Bau and Dulski (1996) have proposed the use of $(Ce/Ce^*)_{PAAS}$ versus

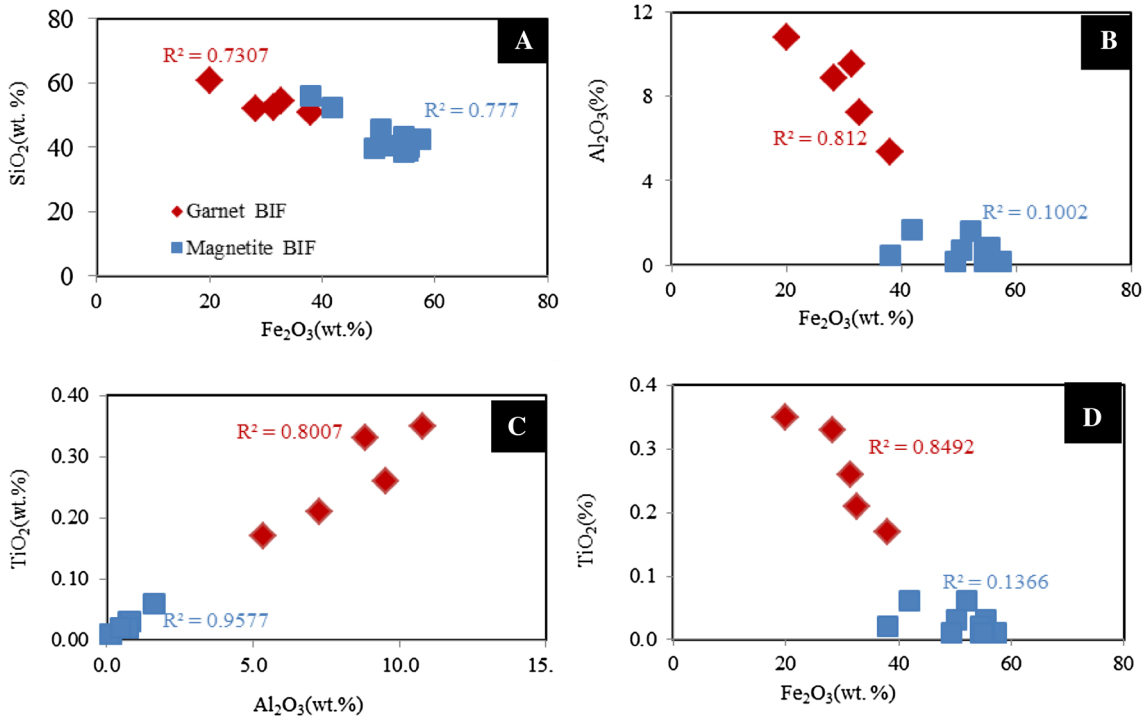

Fig. 7 Variation diagram of Fe_2O_3 and SiO_2 (**a**), Fe_2O_3 and Al_2O_3 (**b**), TiO_2 and Al_2O_3 (**c**), Fe_2O_3 and TiO_2 (**d**). Oxides of Al, Si, and Ti portray a negative gradient with increasing Fe_2O_3

Table 2 Trace and rare earth element compositions (ppm) and element ratios of Nkout West BIF

	Magnetite BIF									Garnet BIF				
	WH4-5	WH4-8	WH4-10	WH4-2	CH7-1	CH7-2	CH24-1	CH24-2	CH24-3	CH7-3	CH7-6	WH3-6	WH3-9	WH4-3
Trace (ppm)														
Ba	3.52	1.13	0.5	1.79	177.5	3.86	12.75	3.33	0.96	30.1	169	37.4	15.55	28.2
Cd	0.002	bdl	0.002	0.002	0.001	0.001	0.001	0.001	0.001	0.001	0.001	bdl	bdl	0.002
Co	0.245	0.172	0.135	0.076	0.069	0.071	0.303	0.086	0.131	0.958	0.425	0.329	0.283	0.277
Cr	13.6	7.61	8.17	3.67	6.16	5.61	4.71	5.76	5.68	4.95	4.67	8.56	7.19	4.09
Cu	0.38	0.6	0.37	bdl	1.04	0.59	1.54	0.24	0.47	5.89	6.08	0.06	0.11	0.53
Hf	bdl	bdl	bdl	bdl	0.001	0.001	0.001	0.001	0.001	0.001	0.001	bdl	0.001	bdl
Li	4.72	0.32	0.3	0.78	0.1	0.09	1.87	0.13	0.44	1.58	2.9	1.28	0.88	12.6
Mn	136	79.2	79.2	35.1	53.5	57.4	78.8	40	48.6	11.5	5.17	69.4	63.2	28.5
Mo	0.129	0.07	0.076	0.01	0.04	0.032	0.017	0.033	0.038	0.007	0.01	0.073	0.071	0.004
Nb	bdl	bdl	bdl	bdl	0.001	0.001	0.001	0.001	0.001	0.001	0.001	bdl	bdl	bdl
Ni	2.1	0.9	1.06	0.09	0.31	0.31	1.14	0.21	0.47	2.75	0.43	1.8	1.6	1.02
Pb	0.122	0.037	0.034	0.058	0.012	0.027	0.032	0.046	0.148	0.178	0.558	0.158	0.605	0.539
Rb	12.35	1.62	0.149	1.635	0.332	0.883	13.35	0.375	0.244	8.19	19.4	16.55	7.9	29.9
Sr	0.336	0.694	0.652	0.259	5.15	2.9	1.99	0.402	0.207	2.29	1.21	0.655	0.848	0.303
Th	0.067	0.024	0.011	0.031	0.024	0.043	0.073	0.021	0.023	0.225	0.319	0.296	0.276	0.068
U	0.015	0.03	0.01	0.156	0.005	0.015	0.046	0.129	0.035	0.132	0.191	0.112	0.058	0.078
V	1.08	0.98	0.97	0.8	0.93	0.94	1	0.99	0.92	1.4	1.55	1.66	1.12	1.07
W	0.013	0.011	0.026	0.018	0.008	0.011	0.009	0.006	0.006	0.006	0.007	0.033	0.013	0.01
Y	0.357	0.196	0.343	0.303	0.323	0.178	0.661	0.775	0.237	0.107	0.037	0.139	0.06	0.115
Zn	1.71	0.78	0.79	1.61	0.32	0.9	1.65	0.67	1.78	1.71	1.52	1.31	1.97	2.2
Zr	0.004	0.001	0.001	0.002	0.001	0.001	0.005	0.002	0.001	0.012	0.003	0.006	0.009	0.001
K/Rb	38.704	104.938	255.034	103.976	198.795	137.033	119.85	224	270.492	150.183	140.722	116.616	169.62	101.003
Th/U	2.331	0.797	1.078	0.197	2.7	2.841	1.591	0.16	0.652	1.705	1.675	2.643	2.726	0.871
Co/Zn	0.143	0.221	0.171	0.047	0.216	0.079	0.184	0.128	0.074	0.56	0.28	0.251	0.144	0.126
REE (ppm)														
La	0.558	0.175	0.076	0.108	0.179	0.109	0.344	0.199	0.14	1.87	2.65	0.897	1.555	0.565
Ce	0.857	0.321	0.16	0.215	0.297	0.157	0.6	0.377	0.302	2.99	4.69	1.82	3.1	1.06
Pr	0.086	0.036	0.021	0.026	0.032	0.016	0.068	0.05	0.039	0.274	0.473	0.197	0.334	0.11
Nd	0.34	0.143	0.149	0.122	0.127	0.076	0.287	0.229	0.185	0.789	1.555	0.65	1.14	0.369
Sm	0.045	0.029	0.022	0.028	0.024	0.01	0.072	0.065	0.037	0.07	0.187	0.104	0.145	0.048
Eu	0.022	0.012	0.017	0.01	0.014	0.006	0.033	0.027	0.008	0.016	0.044	0.021	0.038	0.013
Gd	0.046	0.029	0.041	0.038	0.033	0.018	0.093	0.082	0.037	0.041	0.056	0.058	0.067	0.031
Tb	bdl	bdl	bdl	bdl	bdl	bdl	0.013	0.012	bdl	bdl	bdl	bdl	bdl	bdl
Dy	0.04	0.025	0.039	0.037	0.034	0.016	0.083	0.078	0.037	0.021	0.009	0.042	0.021	0.021

Table 2 (continued)

	Magnetite BIF								Garnet BIF				
	WH4-5	WH4-8	WH4-10	WH4-2	CH7-1	CH7-2	CH24-1	CH24-2	CH24-3	CH7-3	CH7-6	WH3-6	WH3-9	WH4-3
Ho	0.009	0.006	0.009	0.009	0.009	0.004	0.02	0.019	0.007	0.004	0.001	0.006	0.002	0.004
Er	0.026	0.017	0.025	0.023	0.024	0.016	0.057	0.062	0.021	0.011	0.003	0.014	0.004	0.01
Tm	0.003	0.002	0.004	0.003	0.003	0.002	0.007	0.007	0.003	0.002	0.001	0.001	0.001	0.001
Yb	0.027	0.015	0.025	0.024	0.022	0.019	0.06	0.045	0.018	0.01	0.005	0.011	0.003	0.012
Lu	0.004	0.002	0.004	0.004	0.003	0.003	0.008	0.006	0.003	0.001	0.001	0.002	0	0.001
∑REE	2.07	0.818	0.596	0.654	1.126	0.632	2.405	2.033	1.078	6.21	9.716	3.83	6.416	2.249
Y/Ho	39.667	32.667	39.425	35.647	38	43.415	33.384	41.005	35.909	26.098	31.083	23.966	26.043	30.263
$(La/Yb)_{PAAS}$	1.534	0.843	0.223	0.334	0.609	0.421	0.425	0.325	0.564	14.353	37.551	5.955	33.7	3.469
$(Tb/Yb)_{PAAS}$	0	0	0	0	0	0	0.811	0.962	0	0	0	0	0	0
Ce/Ce*	0.901	0.934	0.923	0.926	0.905	0.872	0.904	0.866	0.946	0.96	0.963	0.997	0.989	0.977
Pr/Pr*	0.903	0.947	0.768	0.927	0.936	0.82	0.927	0.975	0.927	1.014	0.996	1.027	1.01	1
Eu/Eu*	2.276	2.005	2.625	1.392	2.29	1.922	1.907	1.749	1.063	1.433	1.99	1.27	1.823	1.601
Y/Y*	1.467	1.24	1.454	1.322	1.472	1.713	1.271	1.566	1.186	0.9	0.863	0.671	0.638	0.999

bdl below detection limit

$(Pr/Pr^*)_{PAAS}$ diagram to discriminate the 'true' from 'false' Ce anomaly in BIF as a result of possibly anomalous abundance of La. In this diagram, the magnetite BIF plots in the field of La anomaly (Fig. 10). Its corresponding chondrite-normalized pattern shows LREE enrichment and HREE depletion and null to slightly positive Eu anomaly representing little fractionation of REE (Fig. 9b).

The REE content of garnet BIF is relatively high (2.24–9.17 ppm) when compared with magnetite BIF. The REE pattern of garnet BIF shows strong LREE enrichment ($La/Yb_{PAAS} = 3.46–37.55$, average = 19.00) and HREE depletion (Fig. 9c), and positive Eu anomaly ($Eu/Eu^*_{PAAS} = 1.27–1.89$, average = 1.62). It plots in the field of positive La anomaly on the Ce/Ce* vs. Pr/Pr* diagram (Fig. 10). The corresponding chondrite-normalized REE diagram of garnet BIF shows LREE enrichment and HREE depletion, positive Eu anomaly (1.19–1.41), indicating little REE fractionation (Fig. 9d).

Pb–Pb geochronology

Pb isotopic data obtained from magnetite BIF are presented in Table 3. The majority of the Pb concentration of the studied samples ranged intrinsically between 2.0 and 6.0 ppm. The uranogenic Pb-isotopic ratio $^{206}Pb/^{204}Pb$ and $^{207}Pb/^{204}Pb$ ranges from 21.82 to 74.77, and from 16.4 to 26.01, respectively, while the thorogenic Pb-isotopic ratio ($^{208}Pb/^{204}Pb$) varies between 37.99 and 68.

The two-stage model of Stacey and Kramers (1975) is compared with our Pb data in the Pb-isotopic composition plots. Figure 11 presents the initial uranogenic (Fig. 11a, b) and thorogenic (Fig. 11c) diagrams with various Pb-isotope ratios in studied samples. The primary growth curve adopted is equivalent to the two-stage Pb evolution curve of Stacey and Kramers (1975) while the isochron line is considered as the secondary isochron (Fig. 11). Our Pb isotopic data plot above the second-stage average crustal Pb evolution curve ($\mu = 9.74$, Stacey and Kramers 1975, Fig. 11b). The data form a linear array and show a systematic change in Pb-isotopic composition of the analysed magnetite BIF. The Pb–Pb data show some limit of the isotopic composition and a relatively scattered characteristic at the less radiogenic end of the linear array.

In the first stage, the Pb–Pb data plot below the Stacey and Kramers (1975) growth curve, whereas in the second stage, it plots above the growth curve and lies on the less radiogenic end of the trend.

Faure (1977) proposed that the slope of the linear array of the $^{207}Pb/^{204}Pb$ versus $^{206}Pb/^{204}Pb$ diagram can be used to determine the age of the rock and to calculate the $^{238}U/^{204}Pb$ ratio (μ value); it is equivalent to the difference between the measured ratio ($^{206}Pb/^{204}Pb$)m and the intercept ratio ($^{206}Pb/^{204}Pb$)ì divided by the slope of the isochron. The regression line fitting for the study yields a

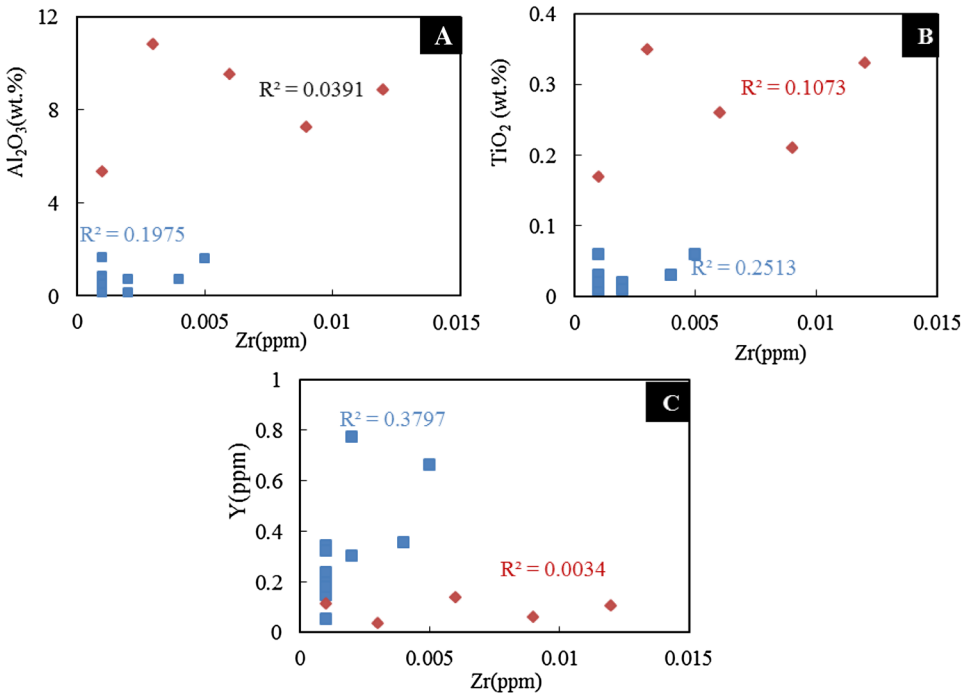

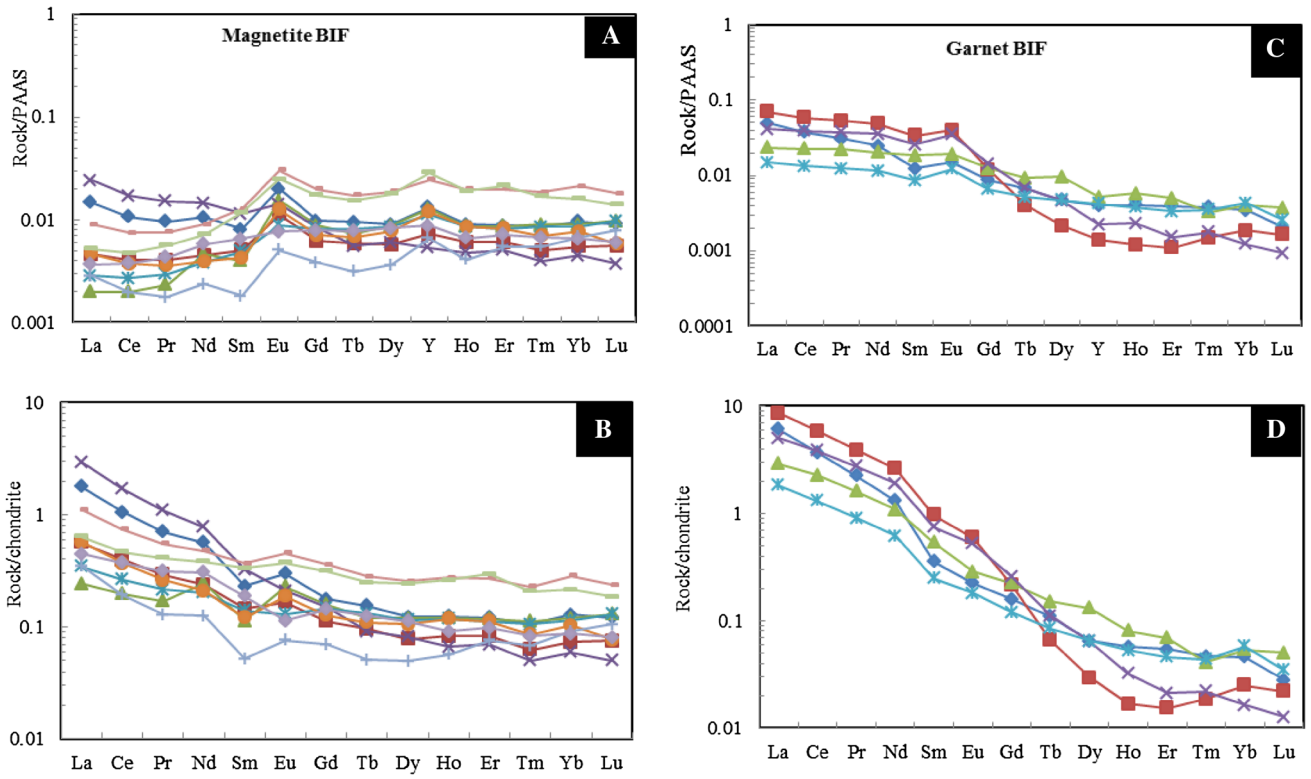

Fig. 8 Relationship between Al_2O_3 (**a**), TiO_2 (**b**), Hf (**c**) and Y (**d**) with Zr in Nkout West BIF (symbols as in Fig. 7.)

Fig. 9 REE pattern for the studied Nkout West BIF. **a**, **b** Post-Archean Australian Shale (PAAS), normalized after Taylor and McLennan (1985). **c**, **d** Chondrite normalized after Boynton (1984)

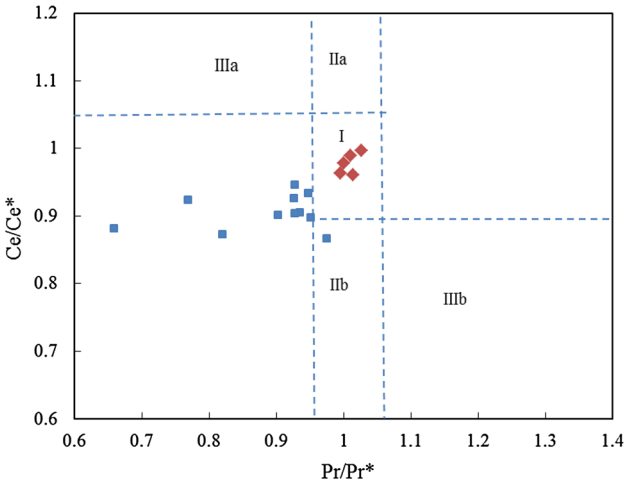

Fig. 10 Pr/Pr* vs. Ce/Ce* diagram (after Bau and Dulski 1996) for the Nkout West BIF. Field I: neither Ce nor La anomaly, field IIa: positive La anomaly, no Ce anomaly, field IIb: negative La anomaly, no Ce anomaly, field IIIa: positive Ce anomaly, field IIIb. Symbols are as in Fig. 7

slope R = 0.519 ± 0.096 (at 95% confidence level, 1σ precision input error calculation of 0.1%, Fig. 11c). The Pb–Pb data from banded iron formation from Nkout west show a secondary isochron that defined an apparent age value of 2679 ± 89 Ma (MSWD = 5.6, Fig. 11b) and the obtained μ value for this study is 15.22.

Discussion

Petrography and metamorphic evolution

Nkout BIF shows planar fabrics, defined by the orientation of recrystallized minerals such as garnet, amphibole, magnetite, quartz, chlorite and biotite. It consists of bands with different mineral assemblages and proportions.

The light bands are mainly composed of recrystallized quartz, whereas the dark bands are mainly made up of quartz, iron and silicate minerals. These minerals are coarse grained and show granoblastic textures with inter-granular triple junctions, confirming metamorphic recrystallization. The original structures from the sedimentary protolith are not preserved within the metamorphic grade, suggesting that metamorphism was not accompanied by only single deformation phases neither metamorphic event. This is confirmed by different foliation generations, recrystallization and mineral inclusions in garnet porphyroblasts (Fig. 12).

The mineral phase relations and microstructures show at least four metamorphic events. These events are: prograde (M_1), and peak metamorphic (M_2), post-peak decompression (M_3) and retrograde (M_4) conditions.

The M_1 prograde metamorphic stage assemblage is represented by inclusions of biotite ($Bt\text{-}_1$), quartz ($Qtz\text{-}_1$), and magnetite ($Mag\text{-}_1$), within M_2 peak metamorphic stage garnet porphyroblasts ($Grt\text{-}_2$) (Fig. 12a, b). This mainly demonstrates the inclusion minerals in the garnet porphyroblasts which form the internal schistosity (Si). These minerals that show spiral inclusion trail suggest the existence of shearing during their formation.

The M_2 peak metamorphic event is marked by inclusion garnet ($Grt\text{-}_2$) + biotite ($Bt\text{-}_2$) + quartz ($Qtz\text{-}_2$) + magnetite ($Mag\text{-}_2$) within the matrix of the rock (Fig. 12a, b). This was developed by the involvement of fluid. The peak metamorphic conditions (M_2) outlasted the most intense fabric forming event (D_2), and the growth of these assemblages continued after the main D_2 fabric. This fabric is defined by garnet ($Grt\text{-}_2$), magnetite ($Mag\text{-}_2$), biotite ($Bt\text{-}_2$) and quartz ($Qtz\text{-}_2$) alignment within the foliation matrix and is in relation to the S_2 fabric and cross cut the internal schistosity (Si).

The M_3 post-peak metamorphic event is characterized by decompression with the appearance of amphibole ($Amp\text{-}_3$) which forms relatively large crystal grains of different shapes

Table 3 Pb isotope data of Nkout West magnetite BIF

Sample	$^{206}Pb/^{204}Pb$	±1σ	$^{207}Pb/^{204}Pb$	±1σ	$^{208}Pb/^{204}Pb$	±1σ
WH4-F1	24.01	0.0034	16.55	0.0019	38.83	0.0040
WH4-F2	32.04	0.0043	18.29	0.0021	43.87	0.0068
WH4-F3	21.82	0.0026	16.4	0.0017	38.34	0.0039
WH4-F4	22.86	0.0029	16.83	0.0018	39.28	0.0039
WH4-F5	24.38	0.0031	16.97	0.0019	39.52	0.0039
WH4-F6	32.28	0.0043	18.11	0.0020	43.59	0.0046
WH4-F7	21.89	0.0035	16.07	0.0019	37.99	0.0041
WH4-S1	28.04	0.0028	17.22	0.0017	44.64	0.0044
WH4-S2	27.47	0.0027	16.91	0.0016	40.72	0.0040
WH4-S3	42.46	0.0138	20.27	0.0042	46.72	0.0116
WH4-S6	43.44	0.0145	20.05	0.0038	47.21	0.0111
WH4-S7	74.77	0.0133	26.01	0.0038	68.12	0.0101
WH4-S8	51.68	0.0095	21.51	0.0030	47.95	0.0055

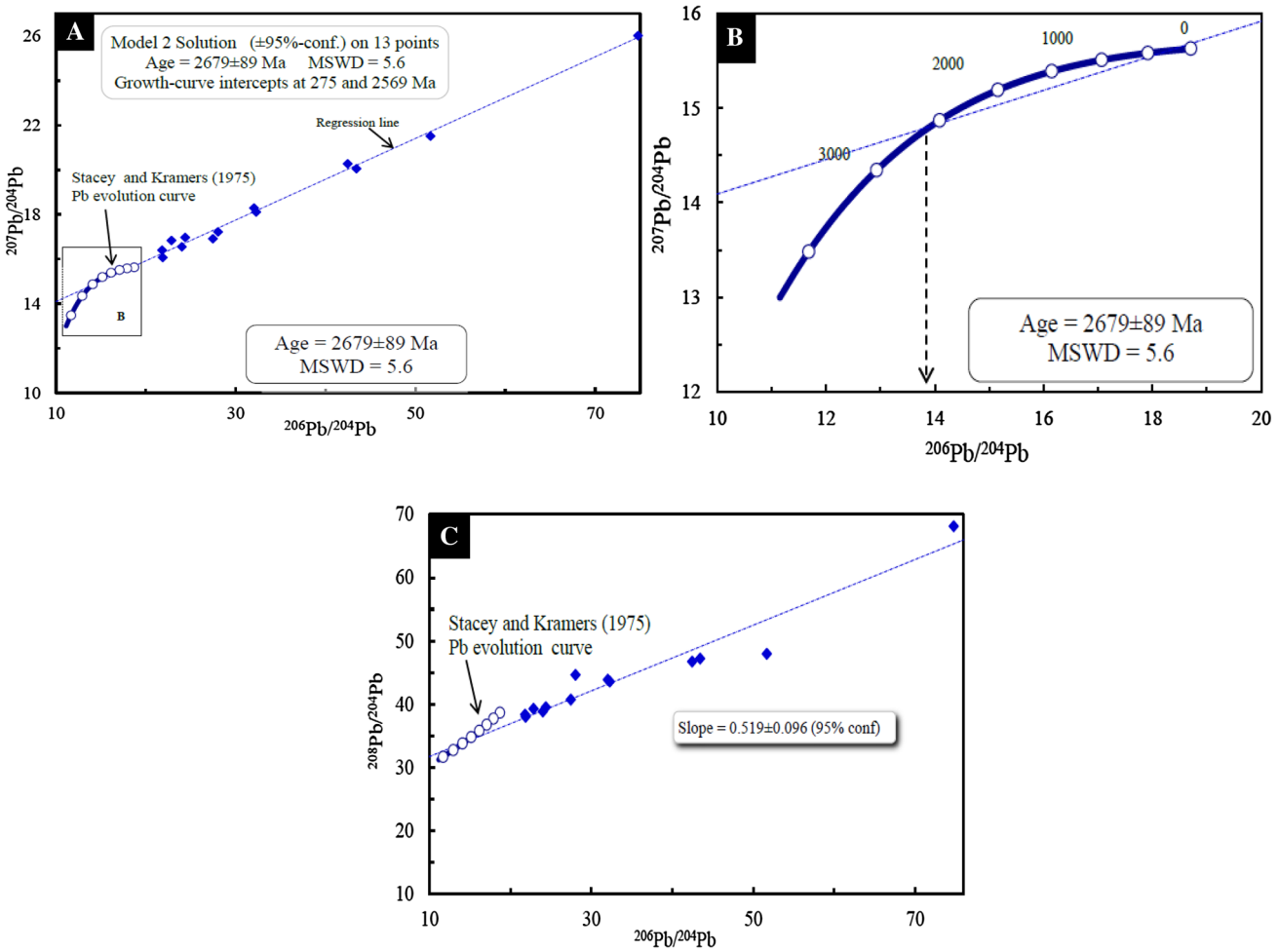

Fig. 11 **a** $^{207}Pb/^{204}Pb$ versus $^{206}Pb/^{204}Pb$ for Nkout West BIF. Isochron age is assumed at 1st stage evolution and Pb isotopic composition at 4.5 Ga. **b** $^{207}Pb/^{204}Pb$ versus $^{206}Pb/^{204}Pb$ for Nkout West BIF. Isochron age is assumed at 2nd stage evolution and Pb isotopic composition at 3.7 Ga. **c** $^{208}Pb/^{204}Pb$ versus $^{206}Pb/^{204}Pb$ for Nkout West. **d** BIF (calculations were done using isoplot 4.15 software of Ludwig (2011), with input error of 0.1% (1σ) for all isotopic ratios, with Stacey and Kramers (1975) model)

and the production of inclusion-free new garnet (Grt-$_3$) in the rock matrix (Fig. 12c, d).

The last metamorphic conditions (M_4) were reached and characterized by cooling, reflecting the textures which is marked by the fracturing of inclusion-free garnet (Grt-$_4$) and the recrystallization of biotite (Bt-$_4$) and quartz (Qtz-$_4$) (Fig. 12e, f). The recrystallization appears in only very small abundance. They were probably formed during the third (D_3) deformational event and are restricted mainly to late fractures of D_4. However, remobilization of sulfides (pyrite) mineral took place later and was possible because of the occurrence of certain minerals at the last and later stage of metamorphic event. In summary, garnet porphyroblasts show dimensional fabric such as slightly rotated inclusion trails, implying that garnet growth was during prograde metamorphism (M_2) which was contemporaneous with either D_2 or D_3 deformational events. Retrograde metamorphism probably occurred during the end of the third (D_3) deformational event and is restricted mainly to late fractures of D_4.

The stated mineral assemblage and metamorphic evolution indicate that the metamorphic grade in the Nkout area has reached the amphibolite facies conditions. Previous works have revealed that the Ntem Complex had experienced multiple deformational events and regional metamorphism with the *T–P* peak conditions at 750 °C, 5–6 Kb (Tchameni et al. 2010; Lerouge et al. 2006). Teutsong et al. (2017) have recently reported granulite facies mineral assemblage in the Bikoula BIFs, whereas Ganno et al. (2016, 2017) showed that the Kouambo and Zambi BIFs (Nyong series) have suffered greenschist to amphibolite facies metamorphism. Thus, Nkout West BIFs as other iron formations in the Ntem Complex were metamorphosed to various grades, ranging from amphibolite to granulite facies conditions.

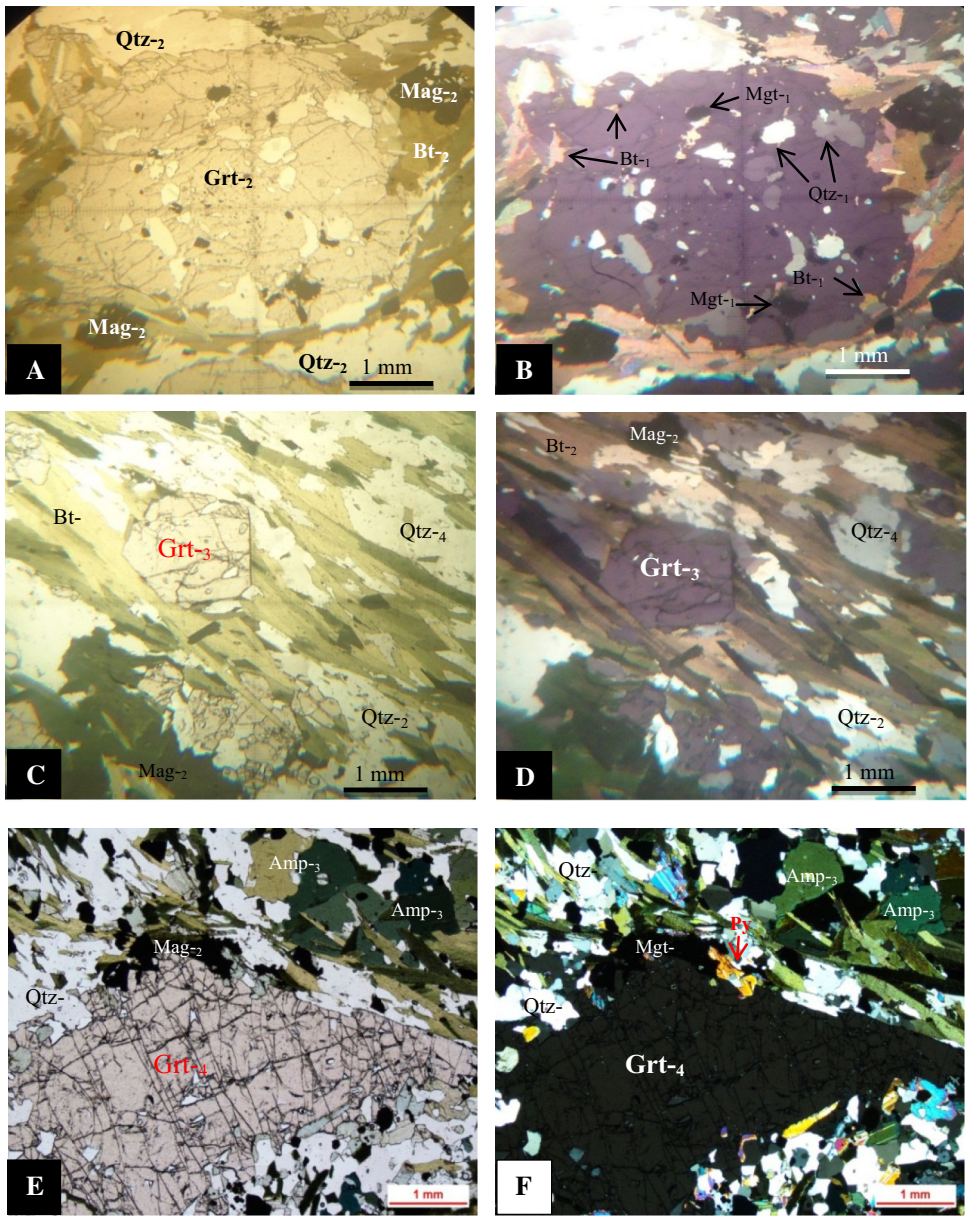

Fig. 12 Mineral assemblages in the Nkout BIF showing different metamorphic events, plane-polarized light (PPL) and cross-polarized light (XPL). **a**, **b** Inclusion garnet porphyroblast (Grt-$_2$) in association with biotite (Bt-$_2$) + quartz (Qtz-$_2$) + magnetite (Mag-$_2$); note the inclusion minerals such as biotite (Bt-$_1$), quartz (Qtz-$_1$), and magnetite (Mag-$_1$) in garnet porphyroblast; **c**, **d** inclusion-free garnet porphyroblast (Grt-$_3$); **e**, **f** fracturing inclusion-free garnet porphyroblast (Grt-$_4$) in association with amphibole (Amp-$_3$)

Effects of metamorphism

The banded iron formations, especially those of Archean and Paleoproterozoic ages, have undergone various grades of metamorphism (Klein 2005; Rosière et al. 2008). Trendall and Blockley (1970) argued that the metamorphism transformed the primary banded structures in BIF to metamorphic foliation. Also, because the mineralogy is controlled by the wall rock chemical composition, the metamorphism could be responsible for the partial redistribution of chemical components in the rock. Therefore, chemical compositions of metamorphosed BIFs are commonly used in the literature to depict the effects of metamorphism.

LILEs such as Ba, K, Rb, Th, and U are considered to be mobile during diagenetic and metamorphic processes and, thus, are good indicators to detect the effects of metamorphism in the BIF (Lan et al. 2014; and references therein). K/Rb ratio is high in high-grade metamorphic rocks (> 500 for granulite) and very low in unmetamorphosed rocks (230 for igneous rock and 200 for shale) (Rudnick et al. 1985; Bauernhofer et al. 2009).

The average K/Rb ratio of the Nkout West BIF is low, 169.07 and 135.62 for magnetite BIF and garnet-rich BIF, respectively, similar to unmetamorphosed rocks (Rudnick et al. 1985). The stable behaviour of LILE in Nkout West BIF suggests that the metamorphosed BIF have kept original chemical compositions during post-depositional

processes. Based on these results, the geochemical composition of the studied BIF can be used to constrain the origin and depositional environment of the Nkout West deposit.

Detrital input

The petrographic study of the Nkout West BIF reveals that the iron formation is well banded and displays granoblastic micro-texture (Fig. 5). Iron formation was defined for the first time as chemical sediments formed by precipitation of iron and silica component from solutions, consisting of a mixture of seawater with hydrothermal fluids (James 1954). The major composition of iron formation with mainly iron oxides and silica supports this definition (Trendall 2002). However, not all BIFs are made up of pure chemical sediments, but some are commonly contaminated by clastic components (Bau and Dulski 1996; Basta et al. 2011 and references therein). The Al_2O_3, NaO_2, K_2O and TiO_2 contents are mainly hosted in silicates and are usually used as contamination input tracers. Such impurities in terrigenous sediments are carried by rivers or winds from weathered pre-existing rock, or deposited by volcanic activities (Klein and Beukes 1992) or pelagic sediments (Lascelles 2007). A strong positive correlation between Al_2O_3 and TiO_2 has been reported for BIF worldwide (Ewers and Morris 1981; Basta et al. 2011; Yang et al. 2015) and is attributed to clastic input. Moreover, detrital component in BIF could be gauged through elevated concentrations of HFSE (e.g. Zr, Hf, Ta, and Th) and ∑REE (McLennan et al. 1993; Bau 1993; Bolhar et al. 2004).

In the Nkout area, the garnet BIF has higher average contents of Al_2O_3 (8.35 wt%), TiO_2 (0.26 wt%), K_2O (2.39 wt%) when compared with magnetite BIF, however, indicating clastic contamination (Lascelles 2007; Basta et al. 2011), whereas the magnetite BIF shows high SiO_2 and Fe_2O_3 contents, similar to pure chemical sediments. Also, its low Al_2O_3, TiO_2 and ∑REE (average 1.44) contents are indicative of the absence of detrital components (Klein 2005). From the above, we propose that Nkout West magnetite BIF is detritus free, whereas garnet BIF has a significant amount of clastic materials. Similar result was recently reported from Bikoula BIF located some 50 km Northwest of Nkout deposit (Teutsong et al. 2017).

The origin of the Nkout West BIFs

BIF is well known to be chemical sediments mainly composed of iron and silica. Some authors have attributed the origin of Fe and Si in BIF to the weathering of continental rocks (Holland 1984; Manikyamba et al. 1993; Kholodov and Butuzova 2001), while others are in the opinion that it was derived from the leaching of basaltic rocks from the ocean floor (Beukes and Klein 1990; Klein and Beukes 1992; Bau and Möller 1993). Huston and Logan (2004); Klein (2005) argued that the Fe and Si were precipitated in solutions composed of hydrothermal fluids admixing with seawater, arising from the fact that the REE pattern of BIF have pronounced positive Eu anomaly. Proposed methods for distinguishing between seawater, hydrothermal, biogenic and detrital sources are based on the mineralogical and geochemical compositions.

Hydrothermal fluid shows high Fe/Ti, Fe/Al and Si/Al ratios because Al^{3+} and Ti^{4+} are insoluble in sea water and resistant to hydrothermal alteration (Gurvich 2006). The studied magnetite BIF displays average Fe/Ti (3102.42), Fe/Al (173.73) and Si/Al (140.19) ratios, similar to sediments with predominantly hydrothermal components (Barrett 1981). The average Fe/Ti, Fe/Al and Si/Al ratios of the garnet BIF (128.78, 4.00 and 5.85, respectively) are very low when compared with that of magnetite BIF. Bonatti (1975), Choi and Hariya (1992) have proposed the use of Si vs. Al binary diagram to discriminate hydrothermal metal-rich deposit from hydrogenous deposit. The magnetite BIF plots mainly in the hydrothermal field confirming their high Si/Al ratio, whereas the garnet BIF plots in the hydrogenous field (Fig. 13a). Pure hydrothermal deposit contains little Al and high Al/Ti ratio (Marchig et al. 1982). The relative high content of Al_2O_3 (average = 8.35 wt%) in garnet BIF justified its hydrogenous nature.

The predominantly hydrothermal origin of magnetite-rich BIF is confirmed by the Fe/Ti vs. Al/(Al + Fe + Mn) diagram (Barrett 1981), where it plots close to modern metalliferous hydrothermal sediments and far away from modern pelagic-terrigenous sediments (Fig. 13b). This diagram shows that the garnet BIF has low hydrothermal component (< 70%).

Toth (1980) has proposed the use of Co/Zn ratio to detect the hydrothermal input of chemical sediments. According to this author, hydrothermal deposits show low Co/Zn ratio (0.15), whereas hydrogenous deposits display high Co/Zn ratio (2.5). The average Co/Zn ratio in the study is 0.14 for magnetite BIF, 0.27 for garnet BIF. These ratios are consistent with trace metal of predominantly hydrothermal sources (magnetite BIF), or with minor hydrogenous components (garnet BIF).

Hein et al. (1990), Usui and Someya (1997) argued that hydrogenous deposits show high ∑REE while the ∑REE of hydrothermal deposits are very low. In addition, the hydrothermal solution has a chondritic Y/Ho ratio (28), positive Eu anomaly, LREE enrichment relative to HREE while sea water is characterized by LREE depletion and HREE enrichment, positive Y anomaly and super-chondritic Y/Ho ratio (> 44) (Bau and Dulski 1999).

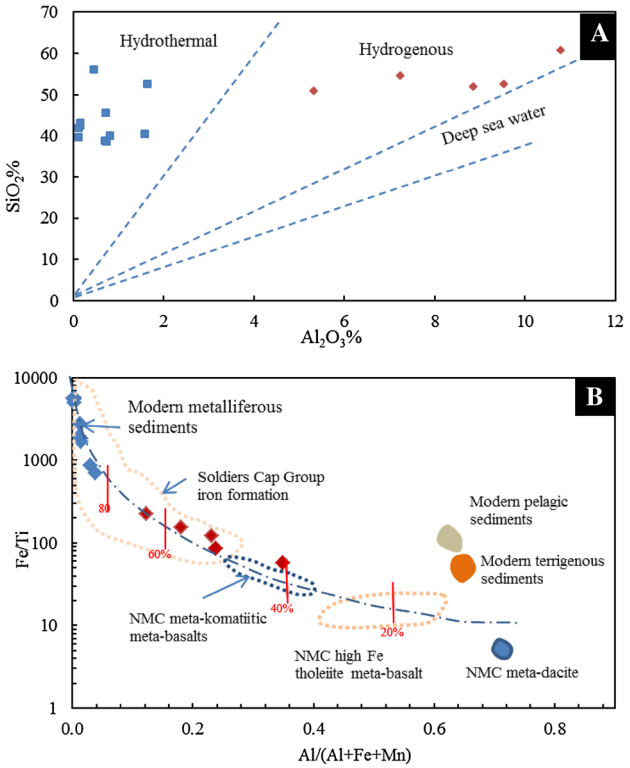

Fig. 13 **a** Si vs. Al discrimination diagram of samples from Nkout area plotted in the field of hydrothermal and hydrogenous deposit. **b** Fe/Ti vs. Al/(Al + Fe + Mn) discrimination diagram shows the hydrothermal input and volcanic-clastic components in the hydrothermal sediment (after Hatton and Davidson 2004).The curve represents mixing of East Pacific Rise deposits (EPR) with pelagic sediments (PC) the percentage indicate the approximate amount of EPR in the mixture (adopted from Barrett 1981). The compositions for mean upper continental crust (UC, Taylor and McLennan 1985), Red Sea hydrothermal deposits (RS, Marchig et al. 1982) and the Cyprus umber (CU). Symbols are as in Fig. 7

The PAAS-normalized REE pattern of the Nkout West BIF shows that the magnetite BIF displays both positive Eu and Y anomalies ($Eu/Eu^*_{PAAS} = 1.8$; $Y/Y^*_{PAAS} = 1.3$) and depletions in LREE, similar to unmetamorphosed Superior-type BIF worldwide (Beukes and Klein 1990; Bau and Dulski 1996; Klein 2005; Planavsky et al. 2010). These characteristics also suggest that the metamorphism that affected the Nkout West BIF did not alter the REE-Y composition. However, the magnetite BIF also exhibits slight positive Y anomaly, which is the signature inherited from sea water. Evans (1978) proposed that Yttrium (Y) could be detected in fluid-related alkaline volcanic rocks and Y/Ho fractionation occurs in aqueous complexes as REEs are been transported. The slight positive Y anomaly in the Nkout west BIF, therefore, suggests a volcanic input. Their average Y/Ho ratio of 36.93 falls between hydrothermal (28) and seawater (> 44), therefore, suggests the mixture of hydrothermal solution and sea water.

The garnet BIF shows positive Eu anomaly and negative Y anomaly and chondritic Y/Ho ratio (27.49) also suggests crustal input material.

Both samples (magnetite BIF, garnet BIF) display no Ce anomalies due to the positive La anomaly (Fig. 11). Bau and Dulski (1996) have proposed that the absence of true Ce anomaly may be related to anoxic conditions that led Fe^{2+} to be oxidized to Fe^{3+}, but not sufficient for Ce^{3+} to be oxidized to Ce^{4+}. Planavsky et al. (2010) reported the absence of true-negative Ce anomaly in Archean and Paleoproterozoic iron formation and argued that microbially mediated Fe oxidation was the main process during their deposition. Therefore, we propose that the lack of true Ce anomaly in Nkout West BIF reflects the absence of free oxygen in the Ntem basin, leading to anaerobic microbial Fe^{2+} oxidation.

Metamorphic resetting age

The whole-rock Pb–Pb dating was applied on magnetite BIF samples. On the uranogenic diagram (Fig. 12a), the regression line does intercept the Stacey and Kramers (1975) growth curve. The secondary isochron Pb data yield Pb–Pb isochron age of 2679 Ma. The whole-rock Pb–Pb analyses present MSWD > 1; indicating a significant scatter plot data (Brooks et al. 1968, 1972; York 1969). Actually, the scatter of the Pb data plots at the low-radiogenic end of the trend indicates that there was mobility and/or heterogeneity.

The heterogeneity of the radiogenic isotope signature within the same rock group may reflect the variable degree of crustal contamination at initial differences in U/Pb source ratio or post-depositional processes such as metamorphism or weathering (Rosholt et al. 1973, Barton et al. 1986). Not much is known on the effect of weathering on U/Pb systems in BIF. But many authors have suggested that U could be lost in oxidizing ground water while Pb is retained in heamatite and goethite (Rosholt et al. 1973). Armstrong (1986) demonstrated that U loss is strictly geological and does not affect Pb–Pb systematics. Many authors (Barton et al. 1986; Moorbath et al. 1973) have indicated that in low-grade metamorphic rocks, whole-rock Pb–Pb isotope systems is stable but could be reset in high-grade metamorphic rocks.

Therefore, the Pb–Pb age of 2679 Ma can either correspond to the depositional age or the age of complete isotope resetting during metamorphic event, which remobilized the Pb isotope of the Nkout West BIF. Although there exists a relative elevated measure of Pb–Pb ratios in this study, which could support the age of complete isotopic resetting during metamorphism, similar elevated Pb–Pb ratios have been obtained in other BIF deposits worldwide [e.g. Kraaipan BIF, South Africa (Anhaeusser and Walraven 1997); Minas deposit, Quadrilatero Ferrifero, Brazil (Babinski et al. 1995)] have been interpreted as the BIF depositional age. The Nkout West metamorphosed BIF is

characterized by the preservation of primary sedimentary features and pure chemical composition. Thus, one may be tempted to say that the 2679 Ma Pb–Pb data present the minimum depositional age of Nkout West iron formation, inferring a Neoarchean age.

The differences in Pb composition in rocks have been applied to understand the source of magma or hydrothermal interaction, and subsequent crystallization and deposition. Tosdal et al. (1999) argued that the low Pb concentrations (1–2 ppm or less) characterize magmatic or hydrothermal system relative to crustal source rocks (10–30 ppm). Nkout Pb composition is roughly on average of <4.0 ppm possibly reflecting a hydrothermal Pb source. However, the heterogeneous nature in the isotopic composition may support a slight crust involvement (fluid-rock interaction) of Pb source.

In the Congo craton, metamorphosed BIF-hosted iron deposits are widespread. The first attempt for dating of BIF was made by Chombong and Suh (2013), who used SHRIMP U/Pb on zircon method to date metadacitic rocks intercalated with BIF, at Njweng area (Mbalam iron deposit). With this indirect method, they reported $^{207}Pb/^{206}Pb$ age of 2883 ± 20 Ma, interpreted as either the age of crystallization of the dacite or the age of initial BIF deposition in the Congo craton, pointing to the Mesoarchean age of the Ntem Complex BIF. Tchameni et al. (2000) have reported that Pb–Pb zircon evaporation age is 2666 ± 2 Ma and 2687 ± 3 Ma on high-K granitoid from the Ntem complex, and attributed these ages to tectono-thermal events, which follow the Archean accretion and differentiation of the North West Congo craton. The results obtained in this study point to the existence of Neoarchean metamorphic event in the Ntem complex.

Conclusion

The following conclusions were made from the geologic, geochemical and geochronological study of the Nkout West iron deposit in the Ntem Complex:

1. Three types of BIF including magnetite BIF, garnet BIF, and garnet-amphibole BIF were petrographically distinguished on the mineralogical basis. They are strongly deformed and were metamorphosed under medium (amphibolite) metamorphic grade, resulting in crystallized magnetite and quartz.
2. The Nkout West BIF is made up of mainly oxide facies with Fe_2O_3 and SiO_2 being the two main components with content >82.2 wt%, which suggests that it is typically a chemical sedimentary rock. The low Al_2O_3, TiO_2, Y, Nb, Zr and Th concentrations in the magnetite BIF suggest detritus-free chemical sediments, whereas their high corresponding concentrations in the garnet metamorphosed BIF indicate clay-rich contaminated input.
3. The Post-Archean Australian Shale (subscript PAAS)-normalized REE pattern of the Nkout West magnetite BIF typically shows LREE-depleted patterns relative to HREE, positive La and $Y(Y/Y^*_{PAAS} = 1.3)$ anomalies, and relatively high Y/Ho ratios (36.93), a characteristic similar to that of modern seawater. Their positive Eu anomaly indicates the involvement of hydrothermal fluid. The slight positive Y anomaly in the Nkout BIF, therefore, suggests a slight volcanic input. The garnet BIF shows positive Eu, and negative Y anomalies and chondritic Y/Ho ratio (27.49). The lack of true Ce anomaly in the Nkout West BIF reflects the absence of free oxygen in the Ntem basin, leading to anaerobic microbial Fe^{2+} oxidation.
4. The whole-rock direct Pb–Pb data yielded an isochron age of 2679 Ma interpreted as the Neoarchean metamorphic resetting age.

Acknowledgements This study is a part of the senior author's Ph.D. thesis at the University of Yaoundé I. The authors would like to express their gratitude to the management staff of 'IMIC/CAMINEX SA' for the permission to collect diamond drill core samples from the Nkout West deposit and logistic facilities during field work. We are thankful to Professor A. Von Quadt and one anonymous reviewer for their helpful and suggestive comments. This is the contribution of IGCP 646 project.

References

Anderson KFE, Frances W, Rollinson GK, Charles JM (2014) Quantitative mineralogical and chemical assessment of the Nkout iron ore deposit, southern Cameroon. Ore Geol Rev 62:25–39

Anhaeusser CR, Walraven F (1997) Polyphase crustal evolution of the Archean Kraaipan granite-greenstone terrane, Kraapvaal Craton, South Africa. Economic Geology Research Unit, ISBN 1868381935

Armstrong, RA (1986) Geochronological studies on Archaean and Proterozoic formations of the foreland of the Namaqua Front and possible correlates on the Kaapvaal Craton. Ph.D thesis, University of the Witwatersrand, Johannesburg

Babinski M, Chemale F Jr, William RVS (1995) The Pb/Pb age of the Minas Supergroup carbonate rocks, Quadrilátero Ferrífero, Brazil. Precambrian Res 72:235–245

Barley ME, Pickard AL, Hagemann SG, Folkert SL (1999) Hydrothermal origin for the 2 billion year old Mount Tom Price giant iron ore deposit, Hamersley Province, Western Australia. Mineral Deposita 34:784–789

Barrett TJ (1981) Chemistry and mineralogy of Jurassic bedded chert overlying ophiolites in the North Appenines, Italy. Chem Geol 34:289–317

Barton ES, Armstrong RA, Cornell DH, Welke HJ (1986) Feasibility of total-rock Pb–Pb dating of metamorphosed banded iron formation: the Marydale Group, Southern Africa. Chem Geol 59:255–271

Basta FF, Maurice AE, Fontbote L, Favarger P (2011) Petrology and geochemistry of the banded iron formation (BIF) of Wadi Karim

and Um Anab, Eastern Desert, Egypt: implications for the origin of Neoproterozoic BIF. Precambrian Res 187:277–292

Bau M (1993) Effects of syn- and post-depositional processes on the rare-earth element distribution in Precambrian iron-formations. Eur J Mineral 5:257–267

Bau M, Dulski P (1996) Distribution of yttrium and rare-earth elements in the Penge and Kuruman Iron Formation, Transval Supergroup, South Africa. Precambrian Res 79:37–55

Bau M, Dulski P (1999) Comparing yttrium and rare earths in hydrothermal fluids from the Mid-Atlantic Ridge: implications for Y and REE behaviour during near-vent mixing and for the Y/Ho ratio of Proterozoic seawater. Chem Geol 155:77–90

Bau M, Möller P (1993) Rare earth element systematics of the chemically precipitated component in Early Precambrian iron-formations and the evolution of the terrestrial atmosphere-hydrosphere-lithosphere system. Geochim Cosmochim Acta 57:2239–2249

Bauernhofer AH, Hauzenberger CA, Wallbrecher E, Muhongo S, Hoinkes G, Mogessie A, Opiyo-Akech N, Tenczer V (2009) Geochemistry of basement rocks from SE Kenya and NE Tanzania: indications for rifting and early Pan-African Subduction. Int J Earth Sci 98:1809–1834

Bekker A, Slack JF, Planavsky N, Krapez B, Hofmann A, Konhauser KO, Rouxel OJ (2010) Iron formation: the sedimentary product of a complex interplay among mantle, tectonic, oceanic and biospheric processes. Econ Geol 105:467–508

Beukes NJ, Klein C (1990) Geochemistry and sedimentology of a facies transition from microbanded to granular iron-formation in the early Proterozoic Transvaal Supergroup, South Africa. Precambrian Res 47:99–139

Bolhar R, Kamber BS, Moorbath S, Fedo CM, Whitehouse MJ (2004) Characterization of Early Archean chemical sediments by trace element signatures. Earth Planet Sci Lett 222:43–60

Bonatti E (1975) Metallogenesis at oceanic spreading centers. Ann Rev Earth Planet Sci 3:401–433

Boynton WV (1984) Geochemistry of rare earth elements: meteorite studies. In: Henderson P (ed) Rare earth element geochemistry. Elsevier, New York, pp 63–114

Brooks C, Wendt I, Harre W (1968) A two-error regression treatment and its application to Rb–Sr and initial Sr87/Sr86 ratios of younger Variscan granitic rocks from the Schwarzwald massif, southwest Germany. J Geophys Res 73:6071–6084

Brooks C, Hart SR, Wendt I (1972) Realistic use of two error regression treatments as applied to rubidium–strontium data. Rev Geophys Space Phys 10:551–577

Caen Vachette M, Vialette Y, Bassot JP, Vidal P (1988) Apport de la géochronologie à la connaissance de la géologie gabonaise. Chron Rech Min 491:35–54

Choi JH, Hariya Y (1992) Geochemistry and depositional environment of Mn oxide deposits in the Tokoro Belt, northeastern Hokkaido Japan. Econ Geol 87:1265–1274

Chombong NN, Suh CE (2013) 2883 Ma commencement of BIF deposition at the northern edge of Congo craton, southern Cameroon: new zircon SHRIMP data constraint from metavolcanics. Episodes 36:47–57

Evans JL (1978) The geology and geochemistry of the Dyke Lake area (parts of 23J/8, 9), Labrador. Mineral Development Division, Newfoundland Department of Mines and Energy, vol 39, pp 74–78

Ewers WE, Morris RC (1981) Studies of the Dales George member of the Brockman Iron Formation, Western Australia. Econ Geol 76:1929–1953

Faure G (1977) Principles of isotope geology. Wiley, New York, p 464

Ganno S, Ngnotue T, Kouankap NGD, Nzenti JP, Notsa FM (2015) Petrology and geochemistry of the banded iron-formations from Ntem complex greenstones belt, Elom area, Southern Cameroon: implications for the origin and depositional environment. Chem Erde 75:375–387

Ganno S, Moudioh C, Nzina NA, Kouankap Nono GD, Nzenti JP (2016) Geochemical fingerprint and iron ore potential of the siliceous itabirite from Palaeoproterozoic Nyong Series, Zambi area, Southwestern Cameroon. Resour Geol 66(1):71–80

Ganno S, Njiosseu TEL, Ngnotué T, Kouankap NGD, Nzenti JP (2017) A mixed seawater and hydrothermal origin of superior-type banded iron formation (BIF)-hosted Kouambo iron deposit, Palaeoproterozoic Nyong Series, Southwestern Cameroon: constraints from petrography and geochemistry. Ore Geol Rev 80:860–875

Ganno S, Tsozué D, Kouankap Nono GD, Tchouatcha MS, Ngnotué T, Gamgne Takam R, Nzenti JP (2018) Geochemical constraints on the origin of mineralized banded iron formation from the Meyomessi area, Archaean Ntem Complex (Congo Craton), southern Cameroon. Resour Geol 68(3):287–302

Goodwin AM (1991) Precambrian geology: the dynamic evolution of the continental crust. Academic Press, New York, pp 1–666

Gross GA (1983) Iron-formation in fold belts marginal to the Ungava craton. In: Trendall AF, Morris RC (eds) Iron formation: facts and problems. Elsevier, Amsterdam, pp 253–294

Gross GA, McLeod CR (1980) A preliminary assessment of the chemical composition of iron-formation in Canada. Can Mineral 18:223–229

Gurvich EG (2006) Metalliferous sediments of the world ocean: fundamental theory of deep-sea hydrothermal sedimentation. Springer, Berlin, p 416

Hatton O, Davidson G (2004) Soldiers Cap Group iron-formations, Mt. Isa Inlier, Australia, as windows into the hydrothermal evolution of a base-metal-bearing Proterozoic rift basin. Aust J Earth Sci 51:85–106

Hein JR, Schulz MS, Kang JK (1990) Insular and submarine ferromanganese mineralization of the Tongap-Lau region. Mar Min 9:305–354

Holland HD (1984) The chemical evolution of the atmosphere and oceans. Princeton University Press, Princeton, pp 582–589

Huston DL, Logan GA (2004) Barite, BIFs and bugs: evidence for the evolution of the Earth's early hydrosphere. Earth Planet Sci Lett 220:41–55

Ilouga CDI, Suh CE, Ghogomu RT (2013) Textures and rare earth elements composition of banded iron formations (BIF) at Njweng prospect, Mbalam Iron Ore District, Southern Cameroon. Int J Geosci 4:146–165

James HL (1954) Sedimentary facies of iron-formations. Econ Geol 49:235–293

James HL (1992) Precambrian iron-formations: nature, origin, and mineralogical evolution from sedimentation to metamorphism. In: Wolf KH, Chilingarian GV (eds) Diagenesis III. Developments in sedimentology. Elsevier, Amsterdam, pp 543–589

Kholodov VN, Butuzova GY (2001) Problems of iron and phosphorus geochemistry in the Precambrian. Lithol Min Resour 36(4):291–302

Klein C (2005) Some Precambrian banded iron-formations (BIFs) from around the world: their age, geologic setting, mineralogy, metamorphism, geochemistry and origin. Am Mineral 90:1473–1499

Klein C, Beukes NJ (1992) Time distribution. In: Schopf JW, Klein C (eds) stratigraphy, sedimentologic setting, and geochemistry of Precambrian iron-formation, in the proterozoic biosphere: a multidisciplinary study. Cambridge University Press, New York, pp 139–146

Lan TG, Fan HR, Santosh M, Hu FF, Yang KF, Yang YH, Liu YS (2014) U–Pb zircon chronology, geochemistry and isotopes of the Changyi banded iron formation in eastern Shandong Province: constraints on BIF genesis and implications for Paleoproterozoic tectonic evolution of the North China Craton. Ore Geol Rev 56:472–486

Lascelles DF (2006) The Mount Gibson banded iron formation-hosted magnetite deposit: two distinct processes for the origin of high-grade iron ore. Econ Geol 101:651–666

Lascelles DF (2007) Black smokers and the Archean environment: uniformitarian model for the genesis of iron-formations. Ore Geol Rev 32:381–411

Lerouge C, Cocherie A, Toteu SF, Milesi JP, Penaye J, Tchameni R, Nsifa NE, Fanning CM (2006) Shrimp U/Pb zircon age evidence for paleoproterozoic sedimentation and 2.05 Ga syntectonic plutonism in the Nyong Group, South-western Cameroon: consequences for the eburnean-transamazonian belt of NE Brazil and central Africa. J Afr Earth Sci 44:413–427

Li X-H, Chen Y, Li J, Yang C, Ling X-X, Tchouankoue JP (2016) New isotopic constraints on age and origin of Mesoarchean charnockite, trondhjemite and amphibolite in the Ntem Complex of NW Congo Craton, southern Cameroon. Precambrian Res 276:14–23

Ludwig KR (2011) Isoplot 3.00—a geochronological toolkit for excel. Berkely Geochronology Center, p 67 **(special publication 4)**

Manikyamba C, Balaram V, Naqvi SM (1993) Geochemical signatures of polygenetic origin of the banded iron formation (BIF) of Archean Sandur greenstone belt (schist belt), Karnataka nucleus, India. Precambrian Res 61:137–164

Marchig V, Gundlach H, Möller P, Schley F (1982) Some geochemical indicators for discrimination between diagenetic and hydrothermal metalliferous sediments. Mar Geol 50:241–256

Maurizot P, Abessolo A, Feybesse JL, John et Lecomte P (1986) Étude de prospection minière du Sud-Ouest Cameroun. Synthèse des travaux de 1978 à 1985, rapport BRGM 85 CMR 066

McLennan SM, Hemming S, McDanniel DK, Hanson GN (1993) Geochemical approaches to sedimentation, provenance, and tectonics. In: Johnsson MJ, Basu A (eds) Processes controlling the composition of clastic sediments, vol 285. Geological Society of America, Special Paper, pp 21–40

Moorbath S, O'Nions RK, Pankhurst RJ (1973) Early Archaean age for the Isua Iron Formation, West Greenland. Nature 245:138–139

Ndime Ekah N, Ganno S, Soh Tamehe L, Nzenti JP (2018) Petrography, lithostratigraphy and major element geochemistry of Mesoarchean metamorphosed banded iron formation-hosted Nkout iron ore deposit, north western Congo craton, Central West Africa. J Afr Earth Sci 148:80–98

Nédélec A, Nsifa EN, Martin H (1990) Major and trace element geochemistry of the Archaean Ntem plutonic complex (South Cameroon): petrogenesis and crustal evolution provenance of detritus for the Nyong Group. Precambrian Res 47:35–50

Nsoh FE, Agbor TA, Etame J, Suh EC (2014) Ore-textures and geochemistry of the Nkout iron deposit South East Cameroon. Sci Technol Dév 15:43–52

Nzenti JP, Barbey P, Macaudière J, Soba D (1988) Origin and evolution of the late Precambrian high-grade Yaounde gneisses (Cameroon). Precambrian Res 38:91–109

Penaye J, Toteu SF, Tchameni R, Van Schmus WR, Tchakounte J, Ganwa A, Minyem D, Nsifa EN (2004) The 2.1 Ga West Central African Belt in Cameroon: extension and evolution. J Afr Earth Sci 3:159–164

Planavsky N, Bekker A, Rouxel OJ, Kamber B, Hofmann A, Knudsen A, Lyons WT (2010) Rare earth element and yttrium compositions of Archaean and Paleoproterozoic Fe formations revisited: new perspectives on the significance and mechanisms of deposition. Geochim Cosmochim Acta 74:6387–6405

Pouclet A, Tchameni R, Mezger K, Vidal M, Nsifa EN, Shang CK, Penaye J (2007) Archaean crustal accretion at the northern border of the Congo Craton (South Cameroon), the charnockite-TTG link. Bull Geol Soc Fr 178:331–342

Poulton SW, Fralick Philip W, Canfield Donald E (2010) Spatial variability in oceanic redox structure 1.8 billion years ago. Nat Geosci 3(7):486–490

Pufahl PK (2010) Bio-elemental sediments. In: James NP, Dalrymple RW (eds) Facies models 4, 4th edn. Geological Association of Canada, St. John's, pp 477–504

Rosholt JN, Zartman RE, Nkomo LT (1973) Lead isotope systematics and uranium depletion in the Granite Mountains, Wyoming. Bull Geol Soc Am 84:989–1002

Rosière CA, Spier CA, Rios FJ, Suckau VE (2008) The itabirites of the Quadrilátero Ferrífero and related high-grade iron ore deposits: an overview. In: Hagemann S, Rosière CA, Gutzmer J, Beukes NJ (eds) Banded iron formation-related high-grade iron ore. Reviews in economic geology, vol 15, pp 223–254

Rudnick RL, McLennan SM, Taylor SR (1985) Large ion lithophile elements in rocks from high-pressure granulite facies terrains. Geochimica Cosmochimica Acta 49:1645–1655

Shang CK, Satir M, Siebel W, Taubald H, Nsifa EN, Westphal M, Reitter E (2001) Genesis of K-rich granitoids in the Sangmelima region, Ntem complex (Congo craton), Cameroon. Terra Nova 5:60–63

Shang CK, Satir M, Siebel W, Nsifa NE, Taubald H, Liegeois JP, Tchoua FM (2004) Major and trace element geochemistry, Rb-Sr and Sm-Nd systematics of the TTG magmatism in the Congo Craton: case of the Sangmelima region, Ntem complex, southern Cameroon. J Afr Earth Sci 40:61–79

Shang CK, Liégeois JP, Satir M, Frisch W, Nsifa EN (2010) Late Archaean high-K granite geochronology of the northern metacratonic margin of the Archaean Congo Craton, Southern Cameroon: evidence for Pb-loss due to non-metamorphic causes. Gondwana Res 475:1–19

Soh Tamehe L, Nzepang Tankwa M, Wei CT, Ganno S, Ngnotue T, Kouankap Nono GD, Simon SJ, Zhang JJ, Nzenti JP (2018) Geology and geochemical constrains on the origin and depositional setting of Kpwa-Atog Boga banded iron formations (BIFs), northwestern Congo craton, southern Cameroon. Ore Geol Rev 95:620–638

Soh Tamehe L, Wei CT, Ganno S, Simon SJ, Kouankap Nono GD, Nzenti JP, Lemdjou YB, Lin NH (2019) Geology of the Gouap iron deposit, Congo craton, southern Cameroon: implications for iron ore exploration. Ore Geol Rev 107:1097–1128

Spier CA, de Oliveira SB, Rosiere CA (2003) Geology and geochemistry of the Aguas Claras and Pico Iron Mines, Quadrilatero Ferrifero, Minas Gerais, Brazil. Mineral Deposita 38:751–774

Spier CA, de Oliveira SMB, Sial AN, Rios FJ (2007) Geochemistry and genesis of the banded iron formations of the Caue Formation, Quadrilatero Ferrıfero, Minas Gerais, Brazil. Precambrian Res 152:170–206

Stacey JS, Kramers JD (1975) Approximation of terrestrial lead isotope evolution by two-stage model. Earth Planet Sci Lett 26:207–221

Suh CE, Cabral A, Shemang EM, Mbinkar L, Mboudou GGM (2008) Two contrasting iron-ore deposits in the Precambrian mineral belt of Cameroon, West Africa. Explor Min Geol 17:197–207

Suh CE, Cabral AR, Ndime E (2009) Geology and ore fabrics of the Nkout high-grade haematite deposit, southern Cameroon. Smart Sci Explor Min 1:558–560

Taylor SR, McLennan SM (1985) The continental crust: its composition and evolution. Blackwell, London, pp 1–328

Tchameni R, Mezger K, Nsifa NE, Pouclet A (2000) Neoarchaean evolution in the Congo craton: evidence from K rich granitoids of the Ntem complex, Southern Cameroon. J Afr Earth Sci 30:133–147

Tchameni R, Mezger K, Nsifa NE, Pouclet A (2001) Crustal origin of Early Proterozoic syenites in the Congo Craton (Ntem Complex), South Cameroon. Lithos 57(1):23–42

Tchameni R, Pouclet A, Mezger K, Nsifa EN, Vicat JP (2004) Monozircon and Sm-Nd whole rock ages from the Ebolowa greenstone belts: evidence for the terranes older than 2.9 Ga in the Ntem

complex (Congo craton, South Cameroon). J Cameroon Acad Sci 4(3):213–224

Tchameni R, Lerouge C, Penaye J, Cocherie A, Milesi JP, Toteu SF, Nsifa EN (2010) Mineralogical constraint for metamorphic conditions in a shear zone affecting the Archean Ngoulemakong tonalite, Congo craton (southern Cameroon) and retentively of U–Pb SHRIMP zircon dates. J Afr Earth Sci 58:67–80

Teutsong T, Bontognali TRR, Ndjigui PD, Vrijmoed JC, Teagle D, Cooper M, Vance D (2017) Petrography and geochemistry of the Mesoarchean Bikoula banded iron formation in the Ntem complex (Congo craton), Southern Cameroon: implications for its origin. Ore Geol Rev 80:267–288

Tosdal RM, Wooden JL, Bouse RM (1999) Pb isotopes, ore deposits, and metallogenic terranes, Application of radiogenic isotopes to ore deposit research and exploration. Rev Econ Geol 12:1–28

Toteu SF, Van Schmus WR, Penaye J, Nyobe JB (1994) U–Pb and Sm–Nd evidence for Eburnean and Pan-African high-grade metamorphism in cratonic rocks of southern Cameroon. Precambrian Res 67:321–347

Toteu SF, Penaye J, Poudjom Djomani YH (2004) Geodynamic evolution of the Pan-African belt in Central Africa with special reference to Cameroon. Can J Earth Sci 41:73–85

Toteu SF, Penaye J, Deloule E, Van Schmus WR, Tchameni R (2006) Diachronous evolution of volcano-sedimentary basins, North of the Congo Craton: insights from U–Pb ion microprobe dating of zircons from the Poli, Lom and Yaounde Groups (Cameroon). J Afr Earth Sci 44:428–442

Toth JR (1980) Deposition of submarine crusts rich in manganese and iron. GSA Bull 91(1):44–54

Trendall AF (2002) The significance of iron-formation in the Precambrian stratigraphic record. Int Assoc Sedimentol Spec Publ 33:33–66

Trendall AF, Blockley JG (1970) The iron formations of the Precambrian Hamersley Group Western Australia with special reference to the crocidolite. Geological Survey of Western Australia Bulletin, Perth

Usui A, Someya M (1997) Distribution and composition of marine hydrogenetic and hydrothermal manganese deposits in the northwest Pacific. In: Nicholson K, Hein JR, Buhn B, Dasgupta S (eds) Manganese mineralization: geochemistry and mineralogy of terrestrial and marine deposits. Geological Society London, Special Publication 119, pp 177–198

Yang X-Q, Zhang Z-H, Duan S-G, Zhao X-M (2015) Petrological and geochemical features of the Jingtieshan banded iron formation (BIF): a unique type of BIF from the Northern Qilian Orogenic Belt, NW China. Ore Geol Rev 63:418–443

York D (1969) Least-squares fitting of a straight line with correlated errors. Earth Planet Sci Lett 5:320–324

Young GM (2013) Precambrian supercontinents, glaciations, atmospheric oxygenation, metazoan evolution and an impact that may have changed the second half of Earth history. Geosci Front 4:247–261

Zhai M, Santosh M (2011) The early Precambrian odyssey of the North China Craton: a synoptic overview. Gondwana Res 20:6–25

Zhai MG, Santosh M (2013) Metallogeny of the North China Craton: link with secular changes in the evolving Earth. Gondwana Res 24:275–297